NASA Contractor Report 185218

Saturated Fluorescence Measurements of the Hydroxyl Radical in Laminar High-Pressure Flames

Campbell D. Carter, Galen B. King, and
Normand M. Laurendeau

Purdue University
West Lafayette, Indiana

February 1990

NASA

National Aeronautics and
Space Administration

TABLE OF CONTENTS

LIST OF SYMBOLS

English Symbols

Symbol	Description	Units
A	Parameter in Chan-Daily-Crosley model	cm
A	Integrated absorption	cm^{-1}
a	Line broadening parameter	--
A_f	Einstein coefficient for the observed fluorescence transition	s^{-1}
$A(i,j)$	Einstein coefficient for spontaneous emission from energy level i to energy level j	s^{-1}
A_ν	Spectral absorption	--
B	Function in Chan-Daily-Crosley model	cm^2
B_{lu}	Einstein coefficient for absorption from level l to level u	cm^3-cm^{-1}/J-s
B_{ul}	Einstein coefficient for stimulated emission from level u to level l	cm^3-cm^{-1}/J-s
c	Speed of light	cm/s
d	Laser probe diameter	cm
$E(i)$	Energy of rotational level i	cm^{-1}
F_1 and F_2	Notation for spin split rotational energy levels	--
f	Parameter in Chan-Daily-Crosley model	--
f_B	Change in the Boltzmann fraction relative to the calibration condition	--
f_b	Fraction of population in the excited electronic state quenched to the vibrational bath levels ($v'' > 0$)	--
$\langle F_c \rangle$	Spatially-averaged depletion of the laser-coupled levels	--
f_c	Fluorescence calibration factor	cm^{-3}/V
f_e	Fluorescence correction factor for linewidth variation relative to the calibration condition	--
F_{lB}	Boltzmann fraction of lower laser-coupled level	--

Symbol	Description	Units
f_v	Ratio of rate coefficients for (1) transfer from $v'' > 0$ to $v'' = 0$ and (2) electronic quenching (Q_e)	--
f_Q	Fluorescence quenching correction factor	--
FWHM	Full width at half maximum	--
g_l	Degeneracy of rotational level l	--
g_u	Degeneracy of rotational level u	--
$g(i)$	Degeneracy of rotational level i	--
$g(\nu)$	Normalized slit function	$1/cm^{-1}$
H	Height of monochromator slit image at the laser beam	cm
h	Plank constant	J-s
I_f	Fluorescence intensity	W/cm^2-sr
I_f^0	Fluorescence intensity at coordinates (y=0,z=0)	W/cm^2-sr
I_L	Laser irradiance	W/cm^2
I_L^P	Laser irradiance at the beam center line and temporal peak	W/cm^2
J	Rotational quantum number. J'' and J' are the respective rotational quantum numbers in the ground and excited electronic states.	--
K	Absorption parameter	--
k	Boltzmann constant	J/K
$k(\nu)$	Absorption coefficient	cm^{-1}
l	Lower laser-coupled rotational level	--
L_{eff}^x	Effective path length for absorption	cm
m	Mass of species of interest	g
N	Rotational quantum number. N'' and N' are the respective rotational quantum numbers in the ground and excited electronic states.	--
N_c	Population in the collisionally-excited rotational energy levels	$1/cm^3$
n_G	Number of ground-state rotational levels modelled	--
N_l	Population of the lower laser-coupled rotational energy level	$1/cm^3$
N_l^0	Population of the lower laser-coupled rotational energy level at equilibrium	$1/cm^3$
$n_l(\nu)$	Spectral population of the lower laser-coupled rovibronic level	$1/cm^3$-cm^{-1}

Symbol	Description	Units
$n_l^0(\nu)$	Spectral population of the lower laser-coupled rovibronic level at equilibrium	$1/cm^3\text{-}cm^{-1}$
N_u	Population of the upper laser-coupled rovibronic level	$1/cm^3$
$\hat{N}_u$	Normalized population of the upper laser-coupled rovibronic level	--
$n_u(\nu)$	Spectral population of the upper laser-coupled rovibronic level	$1/cm^3\text{-}cm^{-1}$
N_T	Total species population	$1/cm^3$
P	Pressure	atm
Q_C	Frequency of dephasing collisions	s^{-1}
Q_D	Frequency of Doppler-changing non-quenching collisions	s^{-1}
$Q_e(i,j)$	Rate coefficient for electronic quenching from level i to level j	s^{-1}
$Q_e(i)$ or Q_e	Rate coefficient for electronic quenching from level i	s^{-1}
Q_{eff}	Effective rate coefficient for collision-induced transfer from excited rotational level u	s^{-1}
$Q_r(i,j)$	Rate coefficient for rotational energy transfer from level i to level j	s^{-1}
$Q_r(i)$ or Q_r	Rate coefficient for rotational energy transfer from level i	s^{-1}
$Q_v(i,j)$	Rate coefficient for vibrational energy transfer from level i to level j	s^{-1}
$Q_v(i)$ or Q_v	Rate coefficient for vibrational energy transfer from level i	s^{-1}
r	Radial distance from laser beam center line	cm
S_f	Fluorescence signal	V
$S_{f,m}$	Fluorescence signal at maximum laser power	V
T	Temperature	K
t	Time	s
t_p	Time at which the laser pulse peaks	s
u	Upper laser-coupled rotational level	--
v	Vibrational quantum state. v'' and v' are the respective vibrational states in the ground and excited electronic states.	--
$V(y;a)$	Voigt function	--
$\overline{v}_q$	Average relative velocity between species of interest and species q	cm/s
W	Width of monochromator slit image at the laser beam	cm

Symbol	Description	Units
w	Halfwidth of the laser irradiance profile	cm
W'	Saturation parameter	--
W_p'	Saturation parameter at the laser beam center line and temporal peak	--
W_r'	Relative saturation parameter	--
W_ν' and W_y'	Spectral saturation parameter as a function of frequency ν or nondimensional frequency y, respectively	--
W_{lu}	Rate coefficient for laser absorption from level l to level u	s^{-1}
W_{lu}^{p}	Rate coefficient for absorption (from levels l to u) at the laser beam center line and temporal peak	--
W_{ul}	Rate coefficient for stimulated emission from level u to level l	s^{-1}
x	Lateral distance across laser beam	cm
x_i	Mole fraction of i-th species	--
$Y(y;a)$	Normalized line profile	$1/cm^{-1}$
y	Nondimensional frequency	--
y_{Lm}	Nondimensional central frequency of the m-th laser mode	--
Δy_{Lm}	Nondimensional spectral separation of the laser modes	--
y_{Lc}	Nondimensional central frequency of the laser spectral profile	--

Greek Symbols

Symbol	Description	Units
α_{sat}	Degree of saturation	--
α_{sat}^{p}	Degree of saturation at the laser beam center line and temporal peak	--
Γ	Function in Chan-Daily-Crosley model	--
γ	Local depletion of the laser-coupled levels	--
$2\gamma_i$	Broadening coefficient for the i-th collision partner	cm^{-1}/atm
δ	Absolute uncertainty	--
ϵ	Relative uncertainty	--
ζ_G	Ratio of the B-parameter in the ground electronic state to that in the excited state	--

Symbol	Description	Units
η	Efficiency of the fluorescence detection system, which incorporates (1) the efficiency the fluorescence optics (including the lenses, mirrors, and grating), (2) the spectral efficiency (i.e., the fraction of the spectral profile passed by the exit slit), and (3) the sensitivity of the PMT (V/W).	V/W
θ	Parameter in Chan-Daily-Crosley model	--
λ	Wavelength	nm
ν	Frequency	cm^{-1}
ν_0	Central frequency of the transition of interest	cm^{-1}
ν_f	Central frequency of the observed fluorescence transition	cm^{-1}
ν_{Lm}	Central frequency of the m-th laser mode	cm^{-1}
$\Delta\nu_{Lm}$	Spectral separation of the laser modes	cm^{-1}
ν_{Lc}	Central frequency of the laser spectral profile	cm^{-1}
$\Delta\nu_C$	Collisional linewidth (FWHM)	cm^{-1}
$\Delta\nu_D$	Doppler linewidth (FWHM)	cm^{-1}
$\Delta\nu_L$	Laser linewidth (FWHM)	cm^{-1}
$\Delta\nu_N$	Natural linewidth (FWHM)	cm^{-1}
$\Delta\nu^*$	Monochromator resolution	cm^{-1}
ρ_0	Energy density of the central mode of the laser spectral profile	J/cm^3
ρ_m	Energy density of the m-th laser mode	J/cm^3
ρ_ν	Spectral energy density	J/cm^3-cm^{-1}
$\sigma_e(i,j)$	Collisional cross section for electronic quenching from level i to level j	cm^2
$\sigma_e(i)$ or σ_e	Collisional cross section for the total electronic quenching from level i (for a specific species)	cm^2
$\sigma_r(i,j)$	Collisional cross section for rotational energy transfer from level i to level j	cm^2
$\sigma_r(i)$ or σ_r	Collisional cross section for the total rotational energy transfer from level i (for a specific species)	cm^2
$\sigma_m^q(i,j)$	Cross section (for transfer from level i to level j) describing collisions with species q and energy transfer mode m (with m = e, v, or r)	cm^2
ϕ	Parameter in Chan-Daily-Crosley model	--
ϕ	Equivalence ratio	--
Ω	Solid angle	sr

ABSTRACT

We have investigated theoretically and experimentally the efficacy of laser-saturated fluorescence (LSF) for OH concentration measurements in high-pressure flames. Using a numerical model describing the interaction of hydroxyl with nonuniform laser excitation, we have studied the effect of pressure on the validity of the *balanced cross-rate* model and the sensitivity of the depopulation of the laser-coupled levels to the ratio of rate coefficients describing (1) electronic quenching to $^2\Sigma^+(v''>0)$ and (2) vibrational relaxation from $v''>0$ to $v''=0$. At sufficiently high pressures and near-saturated conditions, the total population of the laser-coupled levels reaches an asymptotic value, which is insensitive to the degree of saturation. When the ratio of electronic quenching to vibrational relaxation is small and the rate coefficients for rotational transfer in the ground and excited electronic states are nearly the same, the balanced cross-rate model remains a good approximation for all pressures. When the above ratio is large, depopulation of the laser-coupled levels becomes significant at high pressures, and thus the balanced cross-rate model no longer holds. Under these conditions, however, knowledge of the depletion of the laser-coupled levels can be used to correct the model.

A combustion facility for operation up to 20 atm was developed to allow LSF measurements of OH in high-pressure flames. Using this facility, we achieved partial saturation in laminar high-pressure (≤ 12.3 atm) $C_2H_6/O_2/N_2$ flames. To evaluate the limits of the balanced cross-rate model, we compared absorption and calibrated LSF measurements at 3.1 and 6.1 atm. The fluorescence voltages were calibrated with absorption measurements in an atmospheric flame and corrected for their finite sensitivity to quenching with (1) estimated quenching rate coefficients and (2) an *in situ* measurement from a technique employing two fluorescence detection geometries. While the absorption and calibrated fluorescence measurements compare well at 3.1 atm, the OH fluorescence values are ~25% below the absorption measurements at 6.1 atm, indicating an effective error of ~25% in the balanced cross-rate model. We anticipate that with atmospheric-pressure fluorescence calibration and a measurement or a reasonable estimate of the quenching correction factor, one can measure OH concentrations within ±50% at pressures up to 10 atm.

CHAPTER 1

INTRODUCTION

1.1 Background

Measurements of flame species by optical methods, such as laser-induced fluorescence (LIF), have proved valuable in elucidating chemical and physical processes occurring in combustion environments (Eckbreth, 1988). Fluorescence measurements are relevant to the study of a broad range of practical combustion topics including turbulent flames, engine knock, pollutant formation, and flame stability. Linear fluorescence methods are particularly useful for turbulent flames, where 2-D images of *relative* species concentrations can yield insight into the complex interaction between chemistry and the flow field. In comparison, laser-saturated fluorescence (LSF), which is currently limited to point-wise or perhaps 1-D measurements, is attractive because it can provide reliable *absolute* species concentrations. Moreover, unlike linear fluorescence, LSF measurements are insensitive to the rate coefficients for both laser excitation and collisional de-excitation. As a consequence, *in situ* calibration of the fluorescence signal is not necessary: a calibration factor determined in one flame (through techniques such as Rayleigh scattering or absorption) can more easily be applied to other flames where calibration is more difficult or perhaps impossible [e.g., turbulent or sooting flames (Lucht et al., 1984, 1985; Drake et al., 1984, 1985)].

Since LSF was first proposed as a combustion diagnostic (Piepmeier, 1972a; Daily, 1977), it has been used to detect the diatomic molecules C_2 (Baronavski and McDonald, 1977; Mailander, 1978), MgO (Pasternack et al., 1978), CN (Bonczyk and Shirley, 1979; Verdieck and Bonczyk, 1981), CH (Mailander, 1977; Bonczyk and Shirley, 1979; Verdieck and Bonczyk, 1981; Kohse-Hoinghaus et al., 1983, 1984; Takubo et al., 1983), OH (Lucht et al., 1978, 1983, 1984, 1985; Kohse-Hoinghaus, 1983, 1984, 1986; Drake et al., 1984, 1985; Salmon and Laurendeau, 1985a, 1985b) and NH (Salmon et al., 1984) in subatmospheric and atmospheric flames. Initial experiments (Pasternack et al., 1978; Bonczyk and Shirley, 1978; Verdieck and Bonczyk, 1981) showed significant disagreement between fluorescence and independent absorption measurements. Later, however, Lucht et al.

(1983) and Salmon and Laurendeau (1985a) compared LSF measurements of OH concentration (calibrated using Rayleigh scattering) with independent absorption measurements in low-pressure (72 torr) laminar $H_2/O_2/Ar$ flames and demonstrated that saturation can be used to obtain accurate number densities (±15-25%) under these conditions.
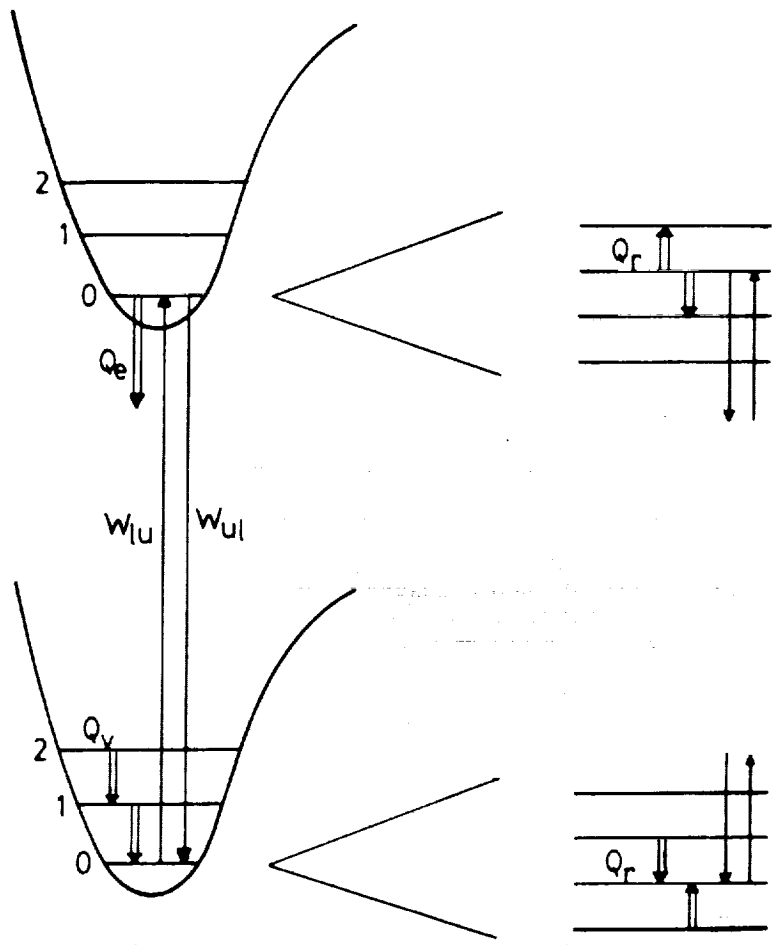
Figure 1.1   Energy level structure and population transfer mechanisms. W_{lu} and W_{ul} are the rate coefficients for absorption and stimulated emission, respectively. Q_r, Q_v, and Q_e are the rate coefficients for rotational relaxation, vibrational relaxation, and electronic quenching, respectively.

In a typical experiment employing LSF, molecules initially in a rotational level within the lowest vibrational level of the ground electronic state are excited through absorption to a rotational level in the $v' = 0$ level of an excited electronic state (Fig. 1.1). Spontaneous emission, stimulated emission, and the collisional energy exchange processes--rotational relaxation, vibrational relaxation, and electronic quenching--transfer population from the *upper* laser-coupled level to other

rovibronic levels of the excited and ground electronic states. Likewise, in the ground state, the *lower* laser-coupled level is re-populated by these same process. The rate equation describing the population of the upper laser-coupled level is

$$\frac{dN_u}{dt} = N_l W_{lu} - N_u (W_{ul} + Q_{eff})$$ (1.1)

where N_u and N_l are the instantaneous populations of the upper and lower laser-coupled levels, respectively, and W_{lu} and W_{ul} are the respective rate coefficients for absorption and stimulated emission. Q_{eff}, the effective rate coefficient for collisional depopulation of the directly-excited level, includes contributions from rotational and vibrational energy transfer, electronic quenching and spontaneous emission. When the population of the directly-excited rotational level peaks during laser excitation, steady-state conditions apply, and we can write

$$\frac{N_u}{N_l} = \frac{1}{g_l/g_u + Q_{eff}/W_{lu}}$$ (1.2)

where g_l and g_u are the respective degeneracies of levels l and u and $g_u W_{ul} = g_l W_{lu}$. In general, the population N_u can be related to N_l^0, the desired unperturbed population of level l, by

$$N_u + N_l = (1 - \gamma) N_l^0$$ (1.3)

The population N_l^0 is related to the species number density through the Boltzmann fraction, and the parameter $1 - \gamma$ is the fraction of the original population remaining in the laser-coupled levels and is determined by the collision environment (i.e., the temperature and concentrations of the collision partners for the molecule of interest). Combining Eqs. (1.2) and (1.3) gives

$$N_u = \frac{g_u}{g_l + g_u} N_l^0 (1 - \gamma) \alpha_{sat}$$ (1.4)

where α_{sat}, the degree of saturation, is given by

$$\alpha_{sat} = \left[1 + \frac{g_u/(g_l + g_u)}{W'} \right]^{-1}$$ (1.5)

and $W' \equiv W_{lu}/Q_{eff}$ is the saturation parameter. We note that when $g_u = g_l$ and $W' \geq 10$, then $\alpha_{sat} \geq$ 95%.

The fluorescence signal is given by the integral of the local excited-state population over the imaged volume; i.e.,

$$S_f = \frac{hc\nu_f A_f}{4\pi}(\eta\Omega)\int_V N_u(x,y,z)dV \quad , \tag{1.6}$$

where ν_f (cm^{-1}) is the frequency of the observed transition, A_f (s^{-1}) is the Einstein coefficient for spontaneous emission, η is the net efficiency of the detection system, and Ω is the solid angle defined by the collection optics. When the unperturbed number density N_l^0 does not vary throughout the imaged volume, we can solve for this quantity and obtain

$$N_l^0 = \frac{g_l + g_u}{g_u} \frac{4\pi S_f}{hc\nu_f A_f(\eta\Omega)\int_V (1-\gamma)\alpha_{sat}dV} \quad . \tag{1.7}$$

By rearranging this equation we obtain

$$\langle F_c \rangle \equiv \frac{\int_V (1-\gamma)\alpha_{sat}dV}{\int_V \alpha_{sat}dV} = \frac{g_l + g_u}{g_u} \frac{4\pi S_f / N_l^0}{hc\nu_f A_f(\eta\Omega)\int_V \alpha_{sat}dV} \quad , \tag{1.8}$$

which represents the spatially-averaged fraction of population remaining in the laser-coupled levels. Note that insofar as W_{lu} is independent of x (e.g., along the beam center line), $\langle F_c \rangle$ reduces to 1 − γ. The influence of the spatial profile of the laser beam and the degree to which γ deviates from zero complicates LSF measurements. These complications become more important at high pressure.

1.2 Contents of Report

In this report, we focus on the efficacy of the LSF method for measurement of OH concentration in high-pressure flames. In particular, we have investigated theoretically and experimentally the validity of the *balanced cross-rate model* (Lucht et al., 1980), which Lucht et al. (1983) and Salmon and Laurendeau (1985a) used successfully at low pressure to relate the measured quantity N_u to the unperturbed number density N_l^0. In essence, the model states that the laser-coupled levels experience approximately no net depletion; i.e.,

$$N_u + N_l \approx N_l^0 \quad . \tag{1.9}$$

The utility of this model, as opposed to Eq. (1.3), is that it requires no knowledge of the collisional environment; consequently, fluorescence measurements can be related more easily to the desired

species number density. When Eq. (1.9) cannot be used due to depletion of the laser-coupled levels and this depletion cannot be accurately measured, LSF can lose much of its attractiveness over linear fluorescence methods.

In the following chapter, we review the literature, with a focus on recent studies involving laser-saturated fluorescence. This review also describes some alternate methods for making quenching-insensitive concentration measurements in flames. Chapters 3 through 7 contain papers which have been published, recently submitted, or are in preparation for publication in refereed journals. In Chapter 3, which was published in *Applied Optics* (Carter et al., 1987), we perform a feasibility study on the application of LSF to the measurement of OH concentration in high-pressure flames. Using a numerical model for the collisional dynamics of the OH molecule under nonuniform laser excitation, we investigate the effect of pressure on the validity of the balanced cross-rate model and the sensitivity of the depopulation of the laser-coupled levels to the ratio of rate coefficients describing (1) electronic quenching to the ground-state vibrational levels for which $v'' > 0$ and (2) vibrational relaxation from $v'' > 0$ to $v'' = 0$.

In Chapter 4, we describe the experimental apparatus. This includes a description of the high-pressure combustion facility, which we have developed in the course of this work and which will be used in future high-pressure combustion studies employing spectroscopic methods; this section of Chapter 4 was published in the *Review of Scientific Instruments* (Carter, et al., 1989). In Chapter 5, we present relative concentration measurements of OH in lean premixed $C_2H_6/O_2/N_2$ flames at high-pressure (P ≤ 12.6 atm). For this experiment we made no explicit use of saturation of the transition; rather, we were interested in the feasibility of probing the reaction zone in high-pressure laminar flat flames, thereby potentially allowing the study of high-pressure flame chemistry. We also discuss problems encountered using LIF under these conditions. This chapter has been accepted for publication as a short communication in *Combustion Science and Technology*.

In Chapter 6, we describe experiments to evaluate the efficacy of LSF for OH concentration measurements in high-pressure combustion environments. In addition to demonstrating that saturation is possible in high-pressure $C_2H_6/O_2/N_2$ flames, we evaluate the limits of the balanced cross-rate model, Eq. (1.9), by comparing absorption and calibrated LSF measurements up to a pressure of ~6 atm. The fluorescence measurements are calibrated with absorption measurements at 1 atm, and in this way, we compare $\langle F_c \rangle_P$, the spatially-averaged population fraction of the

laser-coupled levels at pressure P, to $\langle F_c \rangle_1$, the population fraction at atmospheric pressure. We also present absolute OH concentration profiles for lean flames at about 1, 3, 6, 9 and 12 atm; to our knowledge, these are the first high-pressure absolute concentration measurements of OH performed with LIF. Chapter 7 describes the use of a method suggested by Cottereau (1986) for making quenching-independent measurements with LSF. This technique employs two detection geometries, including two monochromators. The ratio of the resulting fluorescence signals can be used to correct the fluorescence signals for their finite sensitivity to quenching. Finally, Chapter 8 presents conclusions and recommendations for future work with LSF.

CHAPTER 2

LITERATURE REVIEW

2.1 Laser-Saturated Fluorescence

Utilization of laser-saturated fluorescence (LSF) as a diagnostic tool for concentration measurements was initially proposed by Piepmeier (1972a), who noted that saturation of an atomic transition would have the benefit of greatly increasing the fluorescence emission, while reducing the dependence of the emission on changes in laser irradiance and collisional quenching. Daily (1977) also realized the potential of the LSF technique to circumvent the so-called quenching problem, thus allowing concentration measurements of atomic and molecular species in complex reacting flows. Because of their simpler energy level structure and larger absorption cross section, saturated fluorescence was initially applied to atoms, with the majority of experiments using sodium (Lucht et al., 1983; Alkemade, 1985).

The LSF method has been applied to the diatomic molecules C_2, CN, CH, MgO, OH, and NH. The aim of the initial experiments (see Table 2.1) was to make absolute concentration measurements in flames; some of the deficiencies of these experiments included the following:

1. an inability to adequately determine experimental parameters such as effective probe volume, photomultiplier gain, and detection efficiency;

2. the use of a relatively high pressure, i.e., 1 atm, and excitation with laser pulses of long temporal width, e.g. $\geq 1\mu s$, which can enhance noncyclic processes such as laser-induced photochemistry and the population of bath energy levels;

3. the lack of spectral, temporal, and spatial resolution, thus making absolute concentration measurements difficult if not impossible.

Furthermore, as observed by Lucht (1981), since none of these experiments used more than one flame condition, the dependence of the saturated fluorescence measurements on collisional de-excitation could not be assessed.

Table 2.1   Initial experiments with laser-saturated fluorescence.

Molecule	Investigators
C_2	Baronavski and McDonald (1977)
	Mailander (1978)
CH	Mailander (1978)
	Bonczyk and Shirley (1979)
	Verdieck and Bonczyk (1981)
CN	Bonczyk and Shirley (1979)
	Verdieck and Bonczyk (1981)
MgO	Pasternack et al. (1978)
OH	Lucht et al. (1978)

In 1980, Lucht et al. (1980b) used a set of rate equations, each describing the population of a rotational level in either the $X^2\Pi(v''=0)$ or $A^2\Sigma^+(v'=0)$ states of the OH molecule, to determine the validity of the so-called balanced cross-rate model, which states that the population in the laser-coupled levels remains approximately constant (and equal to the initial population of the lower level), since the rates of transfer into and out of the coupled levels are balanced. That is,

$$N_u + N_l \approx N_l^0 \quad , \qquad\qquad (2.1)$$

where N_u and N_l are the respective populations in the upper and lower laser-coupled levels and N_l^0 is the initial population of level l. For the simulated conditions of the burnt-gas region in an atmospheric-pressure H_2/air flame, they found that with a nanosecond pulse-length laser, the depopulation of the laser-coupled levels is small.

By employing the balanced cross-rate model, Lucht et al. (1981,1983) subsequently verified experimentally that saturation of a molecular transition could yield accurate, absolute number densities in low-pressure flames. Saturation of OH molecules was effected in flat laminar subatmospheric H_2/O_2 flames (diluted with either Ar or N_2) by using a Nd:YAG-pumped dye laser with a pulse energy of ~4 mJ at ~310 nm and a nominal pulse length of 10 ns. To resolve the temporal peak of the fluorescence pulse and thereby ensure steady-state conditions as well as

8

obtain a fluorescence signal at peak saturation, the 350 ps window of a 1-GHz sampling oscilloscope was positioned at the temporal maximum of the fluorescence signal. The small spectral ($\sim$2 cm^{-1}) and spatial (45 μm $\times$ 3 mm) windows, provided by the monochromator exit and entrance slits, respectively, enhanced the observed saturation. By pumping the $P_1(5)$ and $Q_1(10)$ lines (and observing fluorescence from the $R_1(3)$ and $P_1(11)$ transitions, respectively) Lucht et al. (1983) were able to achieve a degree of saturation estimated at 90-95%. This value, however, was uncertain because the degree of saturation is difficult to estimate owing to nonuniform illumination of the sampling volume (Salmon and Laurendeau, 1985a).

The detection parameters for the LSF measurements were obtained using Rayleigh scattering (Lucht, 1981). The depth of the scattering volume, assumed to be equivalent to the height of the volume, was estimated by opening the entrance slit until the signal became constant; the depth of the fluorescence probe volume was also obtained in this way. To evaluate the efficacy of the LSF method and the calibration procedure employing Rayleigh scattering, the fluorescence measurements, each an average of 1200 laser shots, were compared with absorption measurements at 72 torr in lean, stoichiometric, and rich $H_2/O_2/Ar$ flames. Figure 2.1 shows profiles of OH number density for the lean flame determined from LSF and absorption measurements, and the results from a calculation using a one-dimensional code for reacting flows (Peterson, 1981). The OH concentrations derived from the $Q_1(10)/P_1(11)$ excitation/detection scheme were 30% higher than values from the $P_1(5)/R_1(3)$ scheme; the profile shown in Fig. 2.1 is the average of the two curves. The saturated fluorescence measurements were also corrected using a factor obtained by matching the uncorrected measurement at the peak of the absorption profile with the corresponding absorption concentration. At this peak, the LSF (uncorrected) and absorption measurements were within 15%; however, the estimated path length was an important source of uncertainty in the absorption measurements. In addition to the absolute concentration measurements, Lucht et al. (1983) showed that over the range of 30 to 242 torr (in an $H_2/O_2/N_2$ flame), the ratio of number densities from saturated fluorescence and absorption was approximately constant, which shows that sensitivity to quenching has been reduced significantly.

Lucht et al. (1982) also made temperature measurements in the 72-torr, $H_2/O_2/Ar$ flames described above using the LSF method. As with concentration measurements with LSF, each excitation/fluorescence line pair should have good spectral isolation in absorption and emission; an additional constraint is that the two lower laser-coupled rotational levels must have a large energy difference to reduce the sensitivity to systematic errors. Lucht et al. (1982) determined two
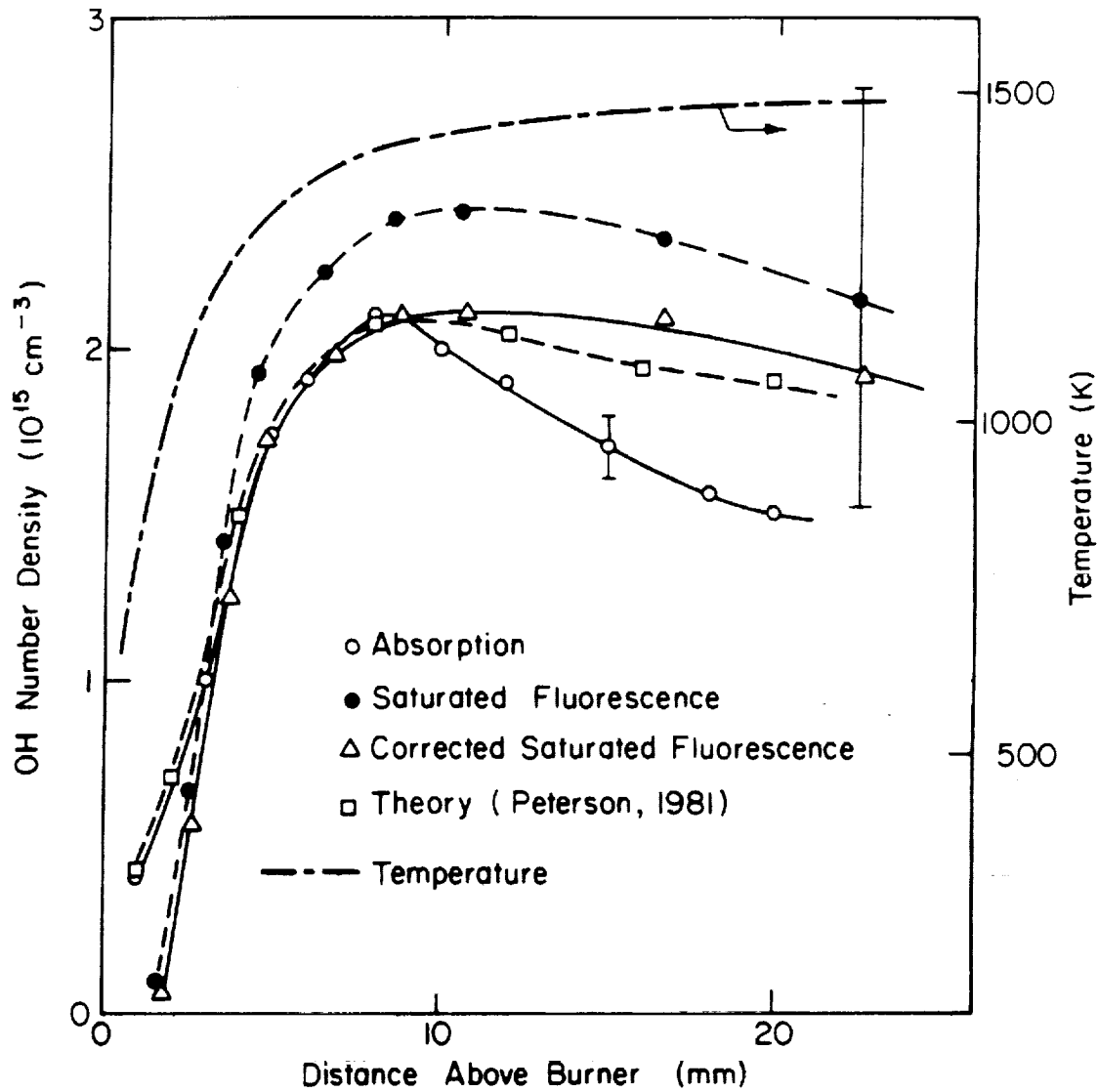
Figure 2.1 Hydroxyl number density profiles in a lean $H_2/O_2/Ar$ flame at a pressure of 72 torr and an equivalence ratio of 0.6 (Lucht et al., 1981). The error bar on the absorption curve corresponds to the standard deviation of the OH number densities calculated from ten absorption lines.

temperature profiles from LSF in each of the lean, stoichiometric, and rich flames using the following excitation/detection transitions: (a) $P_1(5)/R_1(3)$ and $Q_1(13)/P_1(14)$; (b) $Q_1(10)/P_1(16)$ and $Q_1(13)/P_1(14)$. The temperature profiles from LSF were compared with those calculated from absorption and thermocouple measurements and from the one-dimensional chemical kinetics code (Peterson, 1981). In the burnt-gas region of the lean and stoichiometric flames, temperatures determined from scheme (a) consistently gave values 100-200 K higher than those from the other methods, while measurements from scheme (b) yielded temperatures in good agreement with those from absorption, thermocouples and numerical computation. However, in the burnt-gas region of the rich flame, both LSF schemes gave temperatures higher than those obtained with thermocouples and the calculations.

Based on the above experiments, Lucht et al. (1983) postulated that a significant source of error in the LSF measurements could arise from polarization effects. In an anisotropic magnetic or electric field, the total angular momentum J of a molecule is spatially quantized, and as a consequence, under excitation by a linearly polarized source, fluorescence from the pumped level can be significantly polarized. However, Altkorn and Zare (1984) show that for an isotropic molecular distribution of the J vectors, saturation decreases the degree of polarization. Furthermore, collisions also reduce the fluorescence polarization, though both Doherty and Crosley (1984) and Zizak et al. (1986) observed polarized fluorescence from the directly-excited level in atmospheric-pressure flames.

Kohse-Hoinghaus et al. (1983,1984) used the LSF method to measure CH and OH concentrations in a laminar premixed C_2H_2/O_2 flame at 10 torr. To obtain concentrations from the measured fluorescence signal, they (1) used the balanced cross-rate model and (2) solved analytically the rate equation describing N_U [Eq. (1.1)] for a rectangular laser irradiance pulse,

$$I_L = I_L^p \qquad 0 < t < \tau_L \qquad (2.2)$$

$$I_L = 0 \qquad t \geq \tau_L \ .$$

where I_L^p is the peak irradiance produced by the laser system and τ_L was chosen so that the rectangular pulse had the same energy flux (J/cm^2) as the actual pulse. Comparing the results from this model with one which used a more realistic laser pulse showed that this model approximates well the saturation characteristics of a two-level system. The effective saturation volume,

$$V_{eff} = \int (N_u/N_i^0)dx\,dy\,dz \ , \qquad (2.3)$$

11

was then obtained using the irradiance distribution of the laser and the analytical expression for N_u. This method does not make explicit use of the saturation condition, $W' \gg 1$; rather, Kohse-Hoinghaus et al. (1983,1984) extracted the effective quenching rate Q_{eff} by monitoring the fluorescence decay. The success of this model is, of course, due in part to the reduced sensitivity of V_{eff} to the modelling parameters [e.g., the energy density (J/cm^3) under saturated conditions]. Kohse-Hoinghaus et al. (1983,1984) verified their procedure by demonstrating good agreement between the number density of OH determined from LSF and that measured from a fluorescence method suggested by Stepowski and Cottereau (1979).

To build a data base of OH concentration measurements (for later comparison with calculated values), Kohse-Hoinghaus et al. (1986) applied their saturated fluorescence technique to lean and rich laminar premixed $H_2/O_2(/Ar)$, CH_4/O_2, and C_2H_2/O_2 flames at low pressure (30 and 72 torr). To calibrate the fluorescence signals, they employed two independent methods: (1) measuring a signal of known intensity produced by scattering the laser beam from a ground quartz disk; (2) measuring Raman scattering from the Q branch of N_2. The two methods gave the same calibration constant within 5%. As explained above, this saturated fluorescence approach relies on a measurement of Q_{eff}, the effective quenching rate; in the 30 torr flames, the variation of Q_{eff} with position and equivalence ratio was less than 30%. In addition to the concentration measurements, Kohse-Hoinghaus et al. (1986) measured temperature profiles in each of the flames using laser-induced fluorescence (LIF). This was accomplished by delaying the fluorescence measurements--relative to the laser pulse--until thermalization of the excited-state rotational population had occurred; in the 72 torr flame, for example, Kohse-Hoinghaus et al. waited 60 ns to collect fluorescence. Comparison of the OH concentration profile in the $H_2/O_2/Ar$ flame (at 72 torr) to calculated values (using the measured temperature profile) show good agreement.

Lucht et al. (1985) applied the LSF method to measurement of OH in near-sooting and sooting, flat, laminar, atmospheric-pressure $CH_4/O_2/N_2$ flames. The LSF signals were calibrated using a combined absorption/fluorescence method applied in a lean flame ($\phi = 0.78$), where the OH concentration was much greater; the LSF method could then be used to determine number densities in three rich flames ($\phi = 1.68$, 1.85, and 2.02). With the absorption/fluorescence technique (Fig. 2.2), the total number density, N_T, at position x is determined from the path-integrated number density by

$$N_T(x) = \frac{1}{L_{eff}^x} \int_{-\infty}^{\infty} N_T(\xi)d\xi \quad , \tag{2.4}$$

12

where, L_{eff}^x, the effective path length for fluorescence measurements at position x, is derived from the radial dependence of the normalized OH fluorescence signal, i.e.,

$$L_{eff}^x = \int_{-\infty}^{\infty} S_f(\xi)/S_f(x)d\xi \quad .$$ (2.5)

Lucht et al. (1985) used the $Q_1(8)$ and $P_1(9)$ lines for excitation and detection, respectively, since the population in the ground-state rotational level varies only 10% between 1000 and 2600 K. For the rich flames, the principal source of interference--which determined the detection limit--for the fluorescence measurements was rotational Raman scattering from N_2, which was observable as a consequence of the small OH concentration.
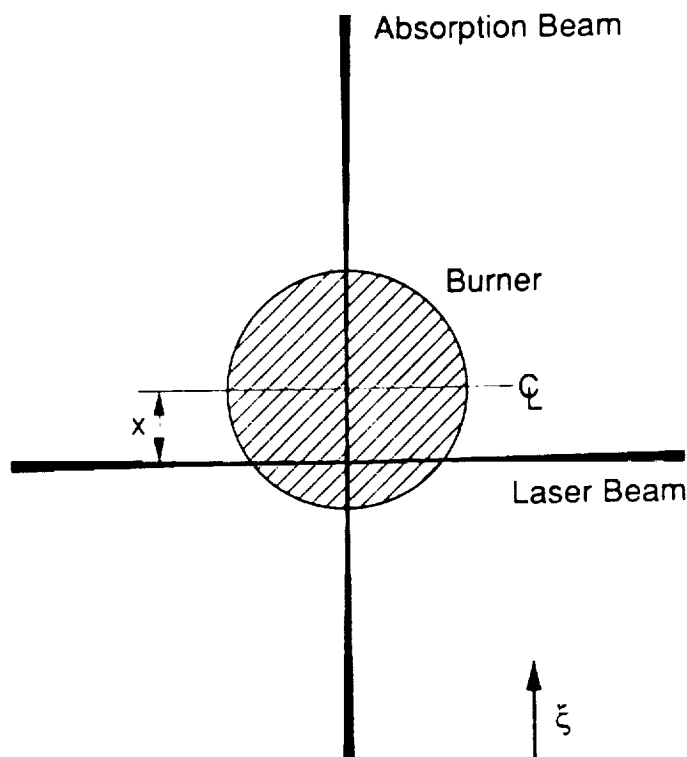
Figure 2.2   Absorption/fluorescence sampling geometry.

A single-shot, LSF method has also been developed for application in turbulent flames (Lucht et al., 1984; Drake et al., 1984). Hydroxyl concentration measurements were made at atmospheric pressure in an H_2/air, turbulent, diffusion flame with a spatial and temporal resolution of ~0.1 mm^3 and ~2 ns, respectively, and an estimated accuracy of ±30%. As with the experiments in the rich $CH_4/O_2/N_2$ flames, the $Q_1(8)/P_1(9)$ excitation/detection line pair was used to minimize the

13

dependence of N_i^0 on temperature. The calibration factor for the measurements in the turbulent flames was obtained by replacing the nonpremixed burner with a laminar flat-flame burner and comparing a concentration determined from the combined absorption/fluorescence method with the relative concentration determined from the signal-averaged, LSF method. Probability density functions of OH concentration from the laminar flame gave a relative standard deviation of about 7%; attenuating the fluorescence signal by a factor of 10 increased this figure to 25%, implying that the precision of the single-shot data was limited by the number of photons collected. Examination of the radial profiles of OH concentration in the laminar diffusion flames led Lucht et al. (1984) to also conclude that at least in these flames, variation in the index of refraction was not great enough to cause significant beam steering or defocusing. The LSF technique was then used to make absolute concentration measurements in laminar (Reynolds number, Re = 660), transitional (Re = 1600), and turbulent (Re = 8500) diffusion flames. These measurements confirmed, for the first time, the existence of a superequilibrium concentration of OH in turbulent nonpremixed flames.

Drake et al. (1985) used these OH concentration measurements to compare the LSF method with planar laser-induced fluorescence (PLIF) measurements. With PLIF, one expands the laser radiation into a sheet and then detects fluorescence from the molecules in the plane of the beam. In this experiment, fluorescence was detected with a 100 by 100 photodiode array camera system, which imaged a 30 x 30 mm area of the flame and gave a spatial resolution of 0.3 x 0.3 x 0.4 mm. The PLIF measurements were calibrated at the peak of the average fluorescence intensity by the corresponding average OH concentration obtained with LSF. Once normalized in this way, the agreement between average concentrations of OH from PLIF and LSF was surprisingly good in the laminar, transitional, and turbulent flames, with the only significant disagreement occurring in the fuel rich portion of the flame zone, where the electronic quenching rate (and therefore the fluorescence yield) may change significantly. This conclusion was strengthened by calculations of the variation in quenching as a function of the mixture ratio for an H_2/air diffusion flame. These calculations--using published collision cross sections and assumed temperature dependencies--showed that indeed under these conditions the net electronic quenching rate is sensitive to the local mixture ratio in the rich region of the flame. In the turbulent flame, agreement between measurements of the rms fluctuations in OH concentration from the two methods was also very good; in the laminar and transitional flames, however, the rms fluctuations measured by PLIF gave values about twice those from LSF. Drake et al. (1985) suggested that the higher

fluctuations in the laminar and transitional flames resulted from noise in the PLIF detection system; the fluctuations of OH concentraion in the turbulent flame, however, were sufficient to overcome the noise in the detection system.

Salmon et al. (1984) applied the LSF method to measurement of NH concentration in a laminar, premixed, $CH_4/N_2O/Ar$ flat flame at a pressure of 50 torr. As with the previous experiments of Lucht et al. (1983,1984,1985), they used the balanced cross-rate model to relate the population in the upper laser-coupled level to the population originally in the lower laser-coupled level. Excitation of rotational transitions in the $A^3\Pi-X^3\Sigma^-(0,0)$ band of NH was accomplished by Raman shifting the frequency-doubled output of the Nd:YAG-pumped dye laser system; this gave a pulse energy of about 2.5 mJ at 337 nm. Salmon et al. used the $P_1(5)/R_1(3)$, $P_1(7)/R_1(5)$, and $P_1(11)/R_1(9)$ excitation/detection line pairs, and optical detection parameters were determined with Rayleigh scattering measurements. In addition, for accurate calibration using Rayleigh scattering, they made corrections to the fluorescence measurements to account for poor saturation in the wings of the laser profile (Salmon et al., 1985a). The resulting number densities were compared with those calculated from the absorption/fluorescence method. At the peak NH concentration, measurements from absorption and LSF agreed to within about 20%.

Salmon and Laurendeau (1985a), in the first paper of a two-part study, presented a calibration technique for LSF using Rayleigh scattering. The technique, which eliminates the dependence of LSF on absorption measurements, makes use of an Abel transformation to extract $\epsilon_f(0,0)$, the fluorescence emission at the beam center line, from $I_f(y)$ [$\equiv \int \epsilon_f(x,y)dx$], the fluorescence intensity profile, i.e.,

$$\epsilon_f(0,0) = \left\{ -\frac{1}{\pi r}\frac{d}{dr}\left[\int_r^R \frac{I_f(y)y\,dy}{\sqrt{(y^2-r^2)}} \right] \right\}_{r=0} , \qquad (2.6)$$

where r is the distance from the beam center line and R is the extent of the measured fluorescence intensity profile. The new calibration method was applied to LSF measurements of OH concentration in a 72 torr $H_2/O_2/Ar$ flame; these measurements were compared with those determined from the combined absorption/fluorescence method described above, though the effective path length was determined only at 5 mm above the burner. The absorption and LSF measurements showed good agreement (within ±10%) to a height of ~8 mm; thereafter, the two concentration measurements showed increasing disagreement. Salmon and Laurendeau (1985a) attributed this deviation to entrainment of the N_2 guard flow. Presumably, then, this disagreement between the LSF and

absorption measurements would be reduced by determining the effective path length L_{eff} at heights greater than 8 mm. Salmon and Laurendeau (1985a) also noted that the good agreement between number densities derived from absorption and LSF suggests that the fluorescence was not significantly polarized; however, they did not measure the degree of polarization.

In their second paper, Salmon and Laurendeau (1985b) presented an investigation of the effects of nonuniform irradiance of the laser probe volume on LSF measurements. Using a measured Rayleigh scattering profile and the assumption of an axisymmetric laser irradiance profile, they deduced that the spatial dependence of the irradiance could be described with a Gaussian or a quasi-Lorentzian function. To model the saturation effects within the probe volume, they employed both a steady-state two-level and a time-dependent four-level model--two levels describing the laser-coupled levels and two levels describing neighboring rotational levels in the respective ground and excited electronic states. Salmon and Laurendeau were able to compare the relative saturation along the center line of the laser beam with that averaged throughout the probe volume for spatial excitation profiles described with Gaussian and quasi-Lorentzian functions. The saturation behavior and the sensitivity to the center-line laser irradiance determined from the experimental data of Lucht et al. (1981, 1983) were bracketed by the curves calculated using the Gaussian and quasi-Lorentzian excitation functions. Salmon and Laurendeau noted that failure to account for the effect of the wings can lead to erroneous results when the transition is assumed to be well-saturated and the measurements are calibrated by a method that does not give an absolute number density (e.g., Rayleigh scattering).

To test the validity of the balanced cross-rate model, Salmon and Laurendeau (1985b) proposed constructing curves of $I_f(0)/\epsilon_f(0,0)$, the effective depth of the probe volume at the beam center line, versus W_{lu}/Q_{eff}, prepared by (1) varying the laser irradiance (and thus W_{lu}) at constant pressure and (2) varying the pressure (and thus Q_{eff}) at constant laser irradiance. This effective depth, D_c^{*}, is proportional to the spatially-averaged population fraction remaining in the laser-coupled levels,

$$D_c^{*} = \int (1 - \gamma)\alpha_{sat}(x,0)dx \quad . \tag{2.7}$$

Here, $1 - \gamma$ is the fraction of the original population remaining in the laser-coupled levels and α_{sat} is the degree of saturation,

$$\alpha_{sat} = \left[1 + \frac{g_u/(g_l + g_u)}{W'} \right]^{-1} \quad , \tag{2.8}$$

16

where $W' \equiv W_{lu}/Q_{eff}$ is the saturation parameter. Consequently, for the same saturation parameter the ratio of D_c^* at two different pressures gives the ratio of the spatially-averaged population fraction (see Eq. 1.8), i.e.,

$$\frac{[D_c^*]_1}{[D_c^*]_2} = \frac{\left[\int (1-\gamma)\alpha_{sat}dx / \int \alpha_{sat}dx\right]_1}{\left[\int (1-\gamma)\alpha_{sat}dx / \int \alpha_{sat}dx\right]_2} \equiv \frac{[<F_c>]_1}{[<F_c>]_2} \ . \qquad (2.9)$$

The ratio of $\langle F_c \rangle$ as a function of pressure to $\langle F_c \rangle$ at the calibration condition, and not the magnitude of $\langle F_c \rangle$, is perhaps the more important parameter, since the variation of this ratio with collisional environment increases the uncertainty of any number density measurement (when the calibration and the desired measurements are performed under different conditions). One difficulty with this approach, however, is assuring that W_{lu}/Q_{eff} is constant at different pressures, since the nature of the broadening changes from predominantly Doppler (heterogeneous) broadening at 1 atm to a combination of collisional (homogeneous) and Doppler broadening at higher pressures. Hence, with increasing pressure, one cannot assure that W_{lu}/Q_{eff} will remain constant when I_L/Q_{eff} is kept constant. A similar qualitative approach is to simply compare the shape of the saturation curves at different pressures. At pressures where depletion of the laser-coupled levels is significant, a decrease in the slope of the curve at a high degree of saturation may be observable.

Using a rate-equation model, Campbell (1984a,1984b) simulated the dynamics of the OH molecule for excitation of an isolated transition in the (0,0) and (0,1) bands of the $A^2\Sigma^+-X^2\Pi$ electronic transition. The model included about 40 rotational energy levels in each of the three lowest vibrational levels (v=0,1,2) of the ground and excited electronic states. The resulting 232 rate equations were solved and N_u, the population determined from the multilevel model, was compared to $N_{u,2}$, the population predicted from the simple two-level model (i.e., the balanced cross-rate model). The conditions for the calculations simulated the burnt-gas region of a stoichiometric CH_4/air flame at 2000 K. Though collisional energy exchange processes in the hydroxyl molecule have been studied extensively, in general, they are not yet described well by theory or experiment. Therefore, Campbell studied the sensitivity of the ratio of populations $N_u/N_{u,2}$ to the rate coefficients describing the various collisional energy exchange processes (i.e., electronic quenching and rotational and vibrational relaxation). The results show that prediction of species number densities with the balanced cross-rate model can result in significant errors, particularly at pressures of 1 atm and above. However, because Campbell used low excitation energies for many

17

of his cases, predicted errors using the two-level model arise from both depopulation of the laser-coupled levels and a low degree of saturation. Nevertheless, Campbell's (1984a) results show that the depopulation of the laser-coupled levels can be significant for high pressure or for long temporal pulse lengths.

Cottereau (1986) suggested an alternative procedure which accounts for spatially-nonuniform saturation. This technique, which could be used for single-shot LSF measurements, requires two monochromators for the detection of the fluorescence--one with the slit axis parallel (scheme A) and the other with the slit axis perpendicular (scheme B) to the laser beam axis--to measure the fluorescence. The two detection schemes yield different saturation functions, with the geometry having the slit axis parallel to the beam axis giving the higher degree of saturation for equivalent slit dimensions (Daily, 1978). For scheme A, the fluorescence signal can be obtained by combining Eqs. (1.4)-(1.6). Thus,

$$S_{fA} = C N_i^0 (\eta_A W_A \Omega_A) \int_0^\infty 2 \pi r \frac{(1-\gamma) W'(r)/W_p' \, dr}{W'(r)/W_p' + g_u/[W_p'(g_l + g_u)]} \quad , \quad (2.10)$$

while for scheme B the signal is similarly given by

$$S_{fB} = C N_i^0 (\eta_B H_B W_B \Omega_B) \int_0^\infty 2 \frac{(1-\gamma) W'(r)/W_p' \, dr}{W'(r)/W_p' + g_u/[W_p'(g_l + g_u)]} \quad , \quad (2.11)$$

where C accounts for constants such as the Einstein A-coefficient, η_A and η_B are the net efficiencies of the respective fluorescence detection systems, Ω_A and Ω_B are the solid angles of fluorescence collection for the two geometries, and W_A, H_B and W_B are the relevant probe dimensions for the two geometries. Consequently, the ratio of the two relationships is a function only of the center-line saturation parameter, W_p', the spatial dependence of the saturation parameter, $W'(r)/W_p'$, and the ratio of the detection parameters for the two geometries, K; i.e.,

$$\frac{S_{fA}}{S_{fB}} = f \left\{ W_p' ; \frac{I_L(r)}{I_L(0)} ; K \right\} \quad , \quad (2.12)$$

where the relationship

$$\frac{I_L(r)}{I_L(0)} \approx \frac{W'(r)}{W_p'} \quad (2.13)$$

has been used. Insofar as the detection parameters and $I_L(r)/I_L(0)$, the spatial dependence of the laser irradiance, remain constant, S_{fA}/S_{fB} depends only on the center-line saturation parameter. Applying this method requires the following procedure.

1. Select a flame and calibrate the fluorescence signals from both geometries (with measurements from absorption spectroscopy or Rayleigh scattering, for example).

2. In the calibration flame, generate saturation curves for the two geometries by varying the laser irradiance, being careful not to change the spatial dependence of I_L. Since the relative laser irradiance is approximately equivalent to the relative saturation parameter, W_r', when Q_{eff} is constant, the curve S_{fA}/S_{fB} versus I_L defines the calibration function $W_r'(S_{fA}/S_{fB})$. This function should be defined over the range of expected values of W_r'.

3. At the condition of interest, measure S_{fA} and S_{fB}; from the calibration curve $W_r'(S_{fA}/S_{fB})$ determine the value of W_r'. With this value and either saturation curve $S_{fA}(W_r')$ or $S_{fB}(W_r')$, determine the fractional change in fluorescence intensity due to the change in the relative saturation parameter. This value (for geometry A or B) is then used to correct the fluorescence signal (from geometry A or B) for any change in the saturation parameter between the calibration flame and the flame of interest.

Thus, at the condition of interest, the number density N_T is given by

$$N_T = S_f f_c f_Q \cdot \prod_i^N f_i \quad , \tag{2.14}$$

where f_c (cm^{-3}/V) is the calibration factor (determined in step 1), f_Q is the quenching correction factor, which accounts for the fractional change in W_r', and the f_i are additional correction factors (for variations in Boltzmann fraction, etc.). Use of this technique is discussed in detail in Chapter 7.

2.2 Other Methods

We now discuss alternate optical methods for quantitative detection of molecular species such as OH in practical combustors; like LSF, these methods potentially circumvent the so-called quenching problem. First, Barlow et al. (1989a,1989b) reported single-shot measurements of OH using simultaneous linear LIF and vibrational Raman-scattering of H_2, O_2, N_2, and H_2O (using the Stokes bands) in nonpremixed turbulent jet flames. The N_2 anti-Stokes and Rayleigh scattering

signals were monitored; flame temperatures could then be calculated from the N_2 Raman measurements or more accurately from the ideal gas law, by using the total number density derived from the Raman measurements. Two lasers, with colinear beams, were used: (1) DIANA, a flash-lamp-pumped dye laser (λ = 532 nm, with 1 J for each 2-μs pulse) for the scattering measurements, and (2) a Nd:YAG-pumped, frequency-doubled dye laser for the OH fluorescence measurements. To ensure operation in the linear fluorescence regime, Barlow et al. employed a large beam diameter at the probe volume and excited the $S_{21}(8)$ transition [of the ($v'=0,v''=0$) band] using ~0.1 mJ per pulse. Rather than monitoring the P- or Q-branches, they detected the weaker R-branch to reduce fluorescence trapping; the peak fluorescence signals in the turbulent flame corresponded to ~600 photoelectrons. In addition, part of the UV laser beam was split off and sent to a laminar flame where the fluorescence was monitored to ensure that the laser wavelength was centered on the $S_{21}(8)$ line. The 10 signals (6 scattering, 2 fluorescence, and 2 photodiode signals) were each recorded with a gated integrator, and the signals were then processed with a computer.

To accurately calculate OH number densities, correction factors were applied to the recorded fluorescence signals (on a shot-by-shot basis) to account for variations in quenching and the ground state Boltzmann fraction. In addition Barlow et al. (1989a, 1989b) applied a correction factor for the average amount of fluorescence trapping; this was estimated from horizontal fluorescence scans across the turbulent flame. This problem could be avoided by exciting transitions in the (1,0) band and detecting (1,1) band fluorescence; however, sufficient quenching data is not available for the $A^2\Sigma^+$ ($v=1$) state. To correct the fluorescence yield for changes in electronic quenching, Barlow et al. fit collisional cross sections calculated by Garland and Crosley (1986) to a relationship of the form

$$\sigma(T) = A_1 + A_2 e^{-T/1000} + A_3 e^{-T/2000} \tag{2.15}$$

where T (K) is the flame temperature. The resulting quenching correction factor was small when the flame was locally lean and increasingly large when the flame was locally fuel-rich.

Andresen et al. (1988) discussed the potential of reducing the sensitivity of LIF measurements to quenching by exciting the molecule of interest to a fast predissociating state. Predissociation is a process whereby a molecule undergoes a radiationless transition from a discrete state to a continuous state--one corresponding to dissociation--at the same energy (Herzberg, 1950). Sensitivity to quenching is reduced when the time for predissociation is short compared to the time for collisional quenching. Though Andresen et al. (1988) focus on the efficacy of this approach for

temperature measurements, the same technique could be applied to concentration measurements as well. In particular, Andresen et al. (1988) suggest that a KrF excimer laser, with a tunable range from 248.0 to 248.9 nm, could be used to detect the OH, O_2, and H_2O molecules. With the high energies per pulse of excimer lasers (e.g., 400 mJ/pulse in a bandwidth of 0.5 cm^{-1} with their KrF laser), 2-D concentrations or temperatures could be obtained even while exciting very weak transitions. For OH, the KrF laser was employed to excite a number of transitions in the $A^2\Sigma^+ \leftarrow X^2\Pi$ (3,0) band; flame temperatures were obtained from excitation spectra, while monitoring fluorescence only from the (3,2) P-, Q-, or R-branch transitions originating from the directly-excited rotational level. To minimize polarization effects, fluorescence was measured from (1) P- or R-branch transitions when a Q-branch transition was excited or (2) a Q-branch transition when P- or R-branch transitions were excited. Andresen et al. (1988) note that accurate single-shot temperature measurements may be possible with O_2 and OH by excitation of two closely-lying lines. For instance, they observe that the $P_2(8)$ ($\lambda = 248.457$ nm) and the $R_1(15)$ ($\lambda = 248.476$ nm) lines of OH could be excited simultaneously with a broad-band excimer laser; because the ground states of these transitions are separated by ~3000 cm^{-1}, the method offers good sensitivity to temperature. However, measurements of OH fluorescence spectra show some rotational and vibrational energy transfer within the $^2\Sigma^+$ state in H_2/O_2 and C_4H_{10}/O_2 flames, demonstrating that the fluorescence measurements are somewhat sensitive to quenching. In addition, with an assumed temperature and rotational energy transfer cross section (in the $v'=3$ state), Andresen et al. estimated the predissociation time to be 100 ps. Predissociation times for the $^2\Sigma^+$, $v' = 5$ and 6 states have been determined to be less than 10 ps (Carlone and Dalby, 1969).

Schwarzwald et al. (1987,1988) reported measurements of quenching lifetimes for OH (1987,1988) and CN (1988) in atmospheric-pressure flames with a streak camera and a home-built picosecond laser. The laser system included an excimer laser (delivering 8 ns pulses at 308 nm), which pumped a quenched transient dye laser (QTDL). The 200-ps pulses from the QTDL laser then pumped a distributed feedback dye laser (DFDL); the resulting laser pulses had a temporal width of 20-40 ps and a bandwidth of 0.003 nm. Wavelength tuning the laser system over a range of several nm was achieved via rotation of a mirror system in the DFDL (Schwarzwald et al., 1988). The output of the DFDL was then frequency doubled using a β-BaB$_2$O$_4$ crystal, yielding an energy of 15 μJ for OH excitation and 5 to 20 μJ for CN excitation. For OH, fluorescence lifetimes, which were averaged over 50 to 100 laser shots, of the $N = 5$ rotational level in the $^2\Sigma^+$ state were ~2 ns over a range of equivalence ratios and throughout the burnt-gas region in premixed CH$_4$/air flat

21

flames. Though this method can be applied to laminar high-pressure (≥ 1 atm) flames to correct fluorescence yields for quenching variations, it cannot currently be applied to turbulent flames, since single-shot fluorescence lifetime measurements are required.

Elzinga et al. (1987) and Fiechtner et al. (1988,1989) described the asynchronous optical sampling (ASOPS) method, which unlike fluorescence techniques uses a coherent beam to carry the signal. The ASOPS method is similar to the conventional pump/probe technique, but it employs two dye lasers (a pump and a probe laser), each of which is synchronously-pumped by the second harmonic of a mode-locked Nd:YAG laser. By mode-locking the two Nd:YAG lasers at slightly different frequencies, the picosecond pulses of the pump and probe lasers walk in and out of phase at the beat frequency. This provides a method whereby sub-nanosecond events are mapped into the millisecond regime, thus obviating the need for fast detection electronics. The method not only allows measurement of collisional quenching rates, but also a means to make quenching-corrected concentration measurements on a time scale shorter than that for turbulent fluctuations. One goal of this work is to detect important flame radicals such as OH, though to date detection only of rhodamine B (Elzinga et al., 1987) and sodium (Fiechtner et al., 1988; 1989) has been reported. Recent experiments (Fiechtner et al. 1989) used mode-locking frequencies of ~82 MHz and a beat frequency of ~10 kHz to measure the quenching rate coefficient of the 3P state of sodium in a laminar $C_2H_4/O_2/N_2$ flame. The pump and probe beams were crossed at ~5°, resulting in an estimated interaction length of 0.5 mm. In one arrangement, the pump laser was tuned to the $3S_{1/2} \rightarrow 3P_{3/2}$ transition (589.0 nm), while the probe laser was tuned to the $3P_{1/2} \rightarrow 5S_{1/2}$ transition (615.4 nm). To increase the signal-to-noise ratio a dual-photodiode voltage-subtraction detector (i.e., a differential detector) was used. A portion of the probe beam (A) was picked off before interaction with the pump beam in the flame. Its intensity (measured by one of the photodiodes) was then adjusted to equal the intensity of the signal-carrying probe beam (beam B, measured by the other photodiode) with no sodium present in the flame; to derive the absorption signal, the intensity of beam A was then subtracted from that of beam B. Using this differential detector and a digitizing oscilloscope, Fiechtner et al. (1989) were able to measure quenching rate coefficients by averaging only 256 decay curves. A typical value for this flame was $1.8 \times 10^9 \, s^{-1}$, with the average decay curve exhibiting 0.4% relative error.

CHAPTER 3

FEASIBILITY OF HYDROXYL CONCENTRATION MEASUREMENTS
BY LASER-SATURATED FLUORESCENCE IN HIGH-PRESSURE FLAMES

3.1 Introduction

Since laser-saturated fluorescence (LSF) was first proposed as a combustion diagnostic (Piepmeier, 1972; Daily, 1977), the method has been used to detect the diatomic molecules C_2 (Baronavski and McDonald, 1977), MgO (Pasternack et al., 1977), CN (Verdieck and Bonczyk, 1981), CH (Verdieck and Bonczyk, 1981; Kohse-Hoinghaus et al., 1983), OH (Kohse-Hoinghaus et al., 1983; Lucht et al., 1983; Salmon and Laurendeau, 1985a), and NH (Salmon et al., 1984) in atmospheric and subatmospheric flames. Although initial experiments disagreed with absorption measurements by factors of two or more, recent experiments provide results which show agreement within 15-25% (Lucht et al., 1983; Salmon and Laurendeau, 1985a; Salmon et al., 1984).

The saturated fluorescence method is attractive because, in principle, one can eliminate a primary difficulty of linear fluorescence--the dependence of the fluorescence signal on both the collisional environment and the laser power fluctuations. In typical laboratory experiments using nonsooting laminar flat flames, one can usually calibrate fluorescence measurements using absorption, and thus the LSF method offers no substantial advantage. For nonpremixed flames, planar fluorescence (which is a linear technique because of the low irradiance of the expanded beam) can provide 2-D images of the reaction zone in a single laser shot (Lee et al., 1986). However, in turbulent flames, particularly in rich conditions (Drake and Pitz, 1985), characterization of the collisional environment can be difficult if not impossible. Consequently, the LSF method is valuable for quantitative concentration measurements in such practical systems.

Although saturated OH fluorescence has been applied at atmospheric pressure to sooting laminar flames (Lucht et al., 1985) and to turbulent nonpremixed flames (Drake et al., 1984; Lucht et al., 1984), the method requires further study for application in complex high-pressure combustion environments. In this chapter, we present the results of a numerical investigation into the effect of

pressure on the efficacy of the balanced cross-rate model and thus on the potential for saturated fluorescence measurements at pressures > 1 atm. So that the sole collision partner for the OH radical is H_2O, we performed the calculations for the burnt-gas region of a stoichiometric H_2/O_2 flame at 2000 K.

3.2 Adequacy of the Rate-Equation Approach

The rate-equation approach, which we have used to model the excitation dynamics of the OH molecule, is conceptually as well as mathematically simpler than the quantum-mechanical density-matrix approach. Unfortunately, modelling the excitation process with rate equations fails to account for optical nutations which can arise during excitation by coherent radiation. Such coherent transients, i.e., oscillations of the excited-level population, will not be observed when (1) the effective coherence time of the excitation source is short compared to the reciprocal of the absorption or stimulated emission rate coefficient (Altkorn and Zare, 1984), or (2) the characteristic time for damping is short compared to the smallest time interval which can be resolved with the detection system (Macomber, 1968). A second complication is that our rate-equation approach fails to deal with the distribution of modes characteristic of Nd:YAG-pumped dye lasers. When the distribution of energy among the modes varies either from pulse to pulse or during an individual pulse, fluctuations in the excited-level population can occur. This is particularly true at subatmospheric pressure since the linewidth of the excited transition is narrow and primarily Doppler broadened.

At sufficiently low pressure, the characteristic time for damping is long, and thus the rate-equation approach might not be expected to adequately model the population in the laser-coupled energy levels. However, as observed by Altkorn and Zare (1984), the utility of the rate equations is not as limited as the above criteria suggest. First, because the spatial profile of pulsed dye lasers is inhomogeneous, the integration of fluorescence across the probe volume will usually mask coherent effects. Second, averaging of the fluorescence signal over many laser shots will also mask fluctuations in the excited-state population, thus ensuring the adequacy of the rate-equation approximation even in cases where it is inappropriate for individual laser shots.

At higher pressures the collision frequency rises; hence, the characteristic time for damping decreases and the transition linewidths are broadened. One important consequence is that the population of the excited level becomes less sensitive to the distribution of mode intensities since more modes are now connected to the excited transition. A second consequence is that the larger

number of exciting modes decreases the effective coherence time of the laser. A third consequence is that with the greater collision frequency, oscillations in the excited-state population are more quickly damped out. Thus, with increasing pressure, the rate-equation approach more closely approximates the density-matrix approach. We also note that Lucht et al. (1984) have made single-shot LSF measurements of OH concentration in a laminar, atmospheric, H_2/air flame. Examination of the measured probability density function demonstrates that significant fluctuations, owing to either coherent effects or variations in the modal intensity distribution, were not present at the peak of the fluorescence pulse.

3.3 The LSF Method

During laser excitation, molecules initially in a rotational energy level within the lowest vibrational level of the ground electronic state are excited through absorption to a rotational level in the ground vibrational level of an excited electronic state. Spontaneous emission, stimulated emission, and collisional energy-exchange processes--rotational relaxation, vibrational relaxation, and electronic quenching--transfer population from the directly-excited rotational level to other rotational levels in the upper and the ground electronic states (Fig. 3.1).

The rate equation for the population of the upper laser-coupled level is

$$\frac{dN_u}{dt} = N_l W_{lu} - N_u (W_{ul} + Q_{eff}) \quad , \tag{3.1}$$

where N_l and N_u are the populations of the lower and upper laser-coupled rotational levels, respectively, W_{lu} and W_{ul} and are the respective rate coefficients for absorption and stimulated emission, and Q_{eff} is the effective rate coefficient for depopulation of the directly-excited level by both collisional-processes and spontaneous emission. Upon laser excitation, the population peaks and steady-state conditions apply, so that Eq. (3.1) becomes

$$\frac{N_u}{N_l} = \frac{1}{g_l/g_u + Q_{eff}/W_{lu}} \quad , \tag{3.2}$$

where g_u and g_l are the respective degeneracies of the upper and lower laser-coupled levels and $g_u W_{ul} = g_l W_{lu}$.

The population of the laser-coupled levels can be related to the unperturbed population N_l^0 of the lower laser-coupled level by

25
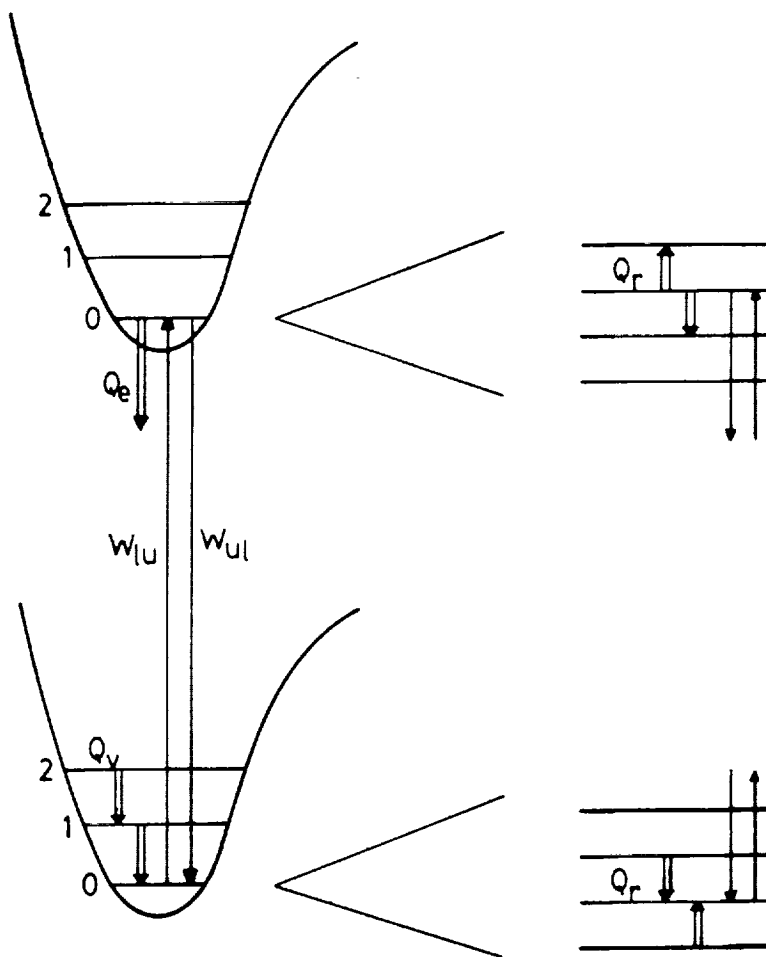
Figure 3.1   Energy level structure and population transfer mechanisms. W_{lu} and W_{ul} are the rate coefficients for absorption and stimulated emission, respectively. Q_r, Q_v, and Q_e are the rate coefficients for rotational relaxation, vibrational relaxation, and electronic quenching, respectively.

$$N_u + N_l = (1 - \gamma)N_l^0 \quad .$$
(3.3)

Here, $1 - \gamma$ is the fraction of the original population remaining in the laser-coupled levels, and N_l^0

is related to the desired species number density through the Boltzmann fraction. At low pressures,

$\gamma \approx 0$ and Eq. (3.3) reduces to the familiar balanced cross-rate model, $N_u + N_l \approx N_l^0$ (Salmon and

Laurendeau, 1985; Lucht et al., 1980). Combining Eqs. (3.2) and (3.3) yields

$$N_u = \frac{g_u}{g_l + g_u} N_l^0 (1 - \gamma)\alpha_{sat} \quad ,$$
(3.4)

where α_{sat}, the degree of saturation, is

$$\alpha_{sat} = \left[1 + \frac{g_u / (g_l + g_u)}{W'} \right]^{-1} \quad . \tag{3.5}$$

and the saturation parameter W' is given by

$$W' = W'_{lu} / Q_{eff} \quad . \tag{3.6}$$

Equation (3.4) demonstrates that the species number density can now be calculated from N^0_l by determining N_u from the measured fluorescence signal and accounting for α_{sat} and γ.

Because the spatial irradiance profile of the laser is nonuniform, the population in the upper laser-coupled level will vary with position. Consequently, the fluorescence intensity across the entrance slit to the monochromator must be expressed through an appropriate integral of N_u. Figure 3.2 shows the fluorescence collection volume as determined by the image of the monochromator entrance slit along the laser beam. For this geometry, the fluorescence intensity (W/cm²-sr) across the image of the slit is given by

$$I_f(y, z) = \frac{hc\nu_f A_f}{4\pi} \int N_u(x, y, z) dx \quad . \tag{3.7}$$

where ν_f (cm⁻¹) is the frequency of the observed transition, A_f (s⁻¹) is the rate coefficient for spontaneous emission, and $N_u(x,y,z)$ is the local number density of the upper laser-coupled level. If the dimensions of the slit imaged on the laser beam are small compared to the characteristic dimensions for the radial and longitudinal variation in laser irradiance, then the fluorescence intensity can be taken as approximately uniform across the monochromator slit [i.e., $I_f(y,z) \approx I^0_f \equiv I_f(0,0)$]. Under these conditions, Eqs. (3.4) and (3.7) can be combined to obtain

$$N^0_l = \frac{g_l + g_u}{g_u} \cdot \frac{4\pi I^0_f}{hc\nu_f A_f \int (1 - \gamma)\alpha_{sat} dx} \quad . \tag{3.8}$$

where $\int(1 - \gamma)\alpha_{sat}dx$ is the effective depth of the collection volume (i.e., the depth for which the fluorescence signal is equivalent to that resulting from complete saturation and no depopulation from the laser-coupled levels) (Salmon and Laurendeau, 1985). Hence, Eq. (3.8) finally expresses the unperturbed number density N^0_l as a function of the measured fluorescence intensity I^0_f.

Further understanding can be gained by rearranging Eq. (3.8) to give

27
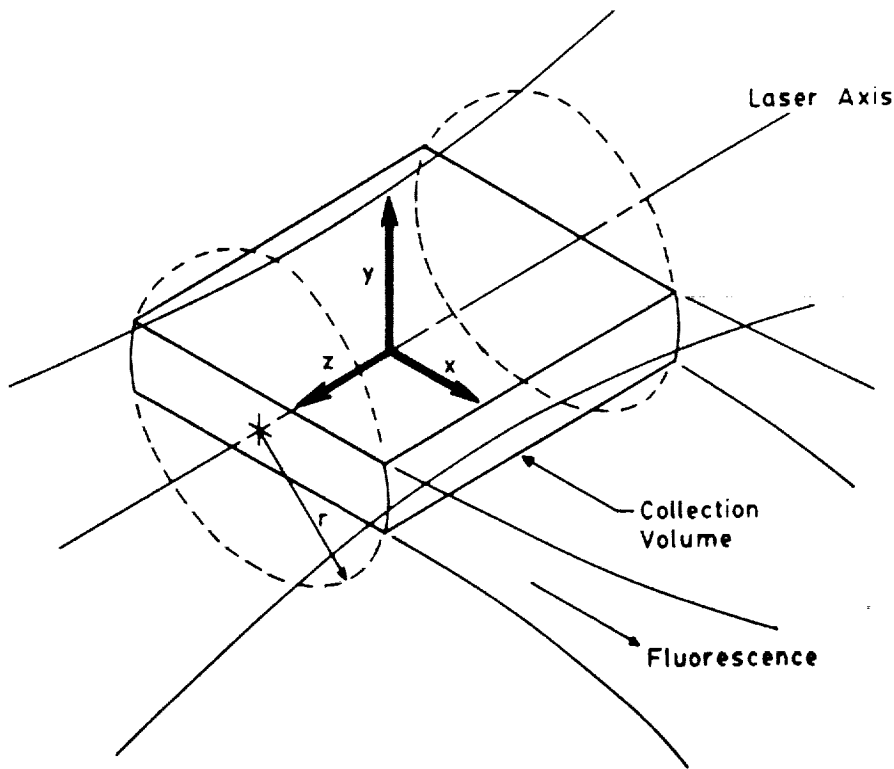
Figure 3.2   Geometry of the fluorescence collection volume.

$$\frac{\int (1-\gamma)\alpha_{sat}dx}{\int \alpha_{sat}dx} \cdot N_l^0 = \frac{g_l + g_u}{g_u} \cdot \frac{4\pi I_j^0}{hc\nu_j A_j \int \alpha_{sat}dx} \quad . \qquad (3.9)$$

The right-hand side of Eq. (3.9) does not depend explicitly on the depopulation of the laser-coupled

levels. Rather, depletion is reflected in a decrease in I_j^0, and because N_l^0 is unaffected, $\langle F_c \rangle \equiv$

$[\int(1-\gamma)\alpha_{sat}dx/\int\alpha_{sat}dx]$ represents the spatially-averaged population fraction remaining in the

laser-coupled levels. Along the center line of the laser irradiance profile, $\langle F_c \rangle$ reduces to $1 - \gamma$,

which is equivalent to the ideal case of a spatially-uniform irradiance profile.

The parameter $1 - \gamma$ is approximately unity, and thus the balanced cross-rate model is valid

at time τ, if the integrated population transfer rates into (R_{in}) and out of (R_{out}) the laser-coupled

levels are balanced, i.e.,

$$\int_0^\tau (R_{in} - R_{out})dt \approx 0 \quad . \qquad (3.10)$$

28

For an ideal two-level system, $R_{in} = R_{out}$, and Eq. (3.10) holds exactly; however, for real multilevel systems, the rates are not likely to equal one another. Hence, those processes which transfer population to levels other than the laser-coupled levels complicate the use of LSF for measurement of species concentrations.

Whereas rotational energy transfer in the ground electronic state replenishes the laser-coupled levels, rotational transfer in the excited electronic state depletes the laser-coupled levels. Rotational transfer to the nearby rotational levels of the excited state provides additional pathways for electronic quenching to the ground state. Those molecules quenched into the $v'' = 0$ level are again part of the rotational reservoir for the laser-coupled levels; however, the molecules quenched to the $v'' > 0$ levels may cascade slowly to the ground vibrational level, thus further depleting the laser-coupled levels. Consequently, the fractional depopulation γ is sensitive to the rate coefficient for rotational energy transfer in the excited electronic state for two reasons. First, an increase in Q_r, the rate coefficient for transfer from the upper laser-coupled level, further populates the surrounding rotational manifold resulting in a depletion of the $v'' = 0$ level and therefore the laser-coupled levels. Second, an increase in $Q_r(u)$ provides more molecules that can be quenched to the $v'' > 0$ levels, again resulting in a depletion of the laser-coupled levels.

The condition for saturation at any location is given by $W' \gg 1$. Thus, from Eqs. (3.4) and (3.5), $\alpha_{sat} \to 1$ and

$$N_u \approx \frac{g_u}{g_l + g_u}(1 - \gamma)N_l^0 \quad . \tag{3.11}$$

When $W' \geq 10$ and $g_u = g_l$, the degree of saturation is greater than 95%. Also, when the spectral irradiance profile of the laser is broad compared to the absorption profile, the saturation parameter is nearly proportional to the ratio of laser irradiance (W/cm^2) to pressure, and therefore the laser irradiance must increase approximately linearly with pressure to maintain the same degree of saturation. For example, with an $H_2/O_2/Ar$ flame at atmospheric pressure and a laser pulse containing ~ 4 mJ of energy, the maximum saturation parameter achievable along the center line of the beam with our Molectron Nd:YAG/dye laser system and a focused spot size of about 0.4 mm is estimated to be 40 (Salmon and Laurendeau, 1985b). To ensure that at peak excitation $W' \geq 10$ in this flame at pressures above about 4 atm, we would need to increase the laser irradiance by decreasing the focused spot size of the beam.

3.4 Laser-Excitation Dynamics

We have modeled the population transfer between and within the $A^2\Sigma^+$ and the $X^2\Pi$ vibrational manifolds of OH using a linear system of rate equations. The upper electronic manifold is described by a single vibrational level, $v' = 0$, containing 29 rotational levels ($N' = 0$ to $N' = 14$; $J' = N' \pm 1/2$). The lower electronic manifold has two vibrational levels, one being the $v'' = 0$ level, containing 26 rotational levels $N'' = 1$ to $N'' = 13$; $J'' = N'' \pm 1/2$), and the other being a vibrational bath level v'' > 0 with no rotational levels. Modelling the $v'' > 0$ levels as a single level is a consequence of the dearth of experimental and theoretical data describing quenching into and vibrational transfer within and out of the $v'' > 0$ levels of the hydroxyl molecule at flame temperatures.

A general FORTRAN 77 program, compatible with the Cyber 205 at Purdue University, was written to set up the Jacobian matrix describing the system of 56 rate equations for this model. To account for the effect of the temporal and spatial dependence of the irradiance for a laser pulse, the rate equations are integrated temporally for each specified spatial location. The spatially-averaged population fraction in the laser-coupled levels, $\langle F_c \rangle$, can then be obtained from

$$< F_c > = \frac{g_l + g_u}{g_u} \frac{\int (N_u/N_l^0)dx}{\int \alpha_{sat} dx} \quad . \tag{3.12}$$

which is derived by combining Eqs. (3.7) and (3.9).

For the rotational levels not coupled by the laser ($i{\neq}u,l$) the generalized rate equation at any location is

$$\frac{dN(i)}{dt} = \sum_j [N(j)Q(j,i)] - N(i)\sum_j Q(i,j) \quad , \tag{3.13}$$

where i and j refer to all energy levels in both the upper and lower electronic states. $Q(i,j)$, the rate coefficient for transfer from level i to level j, is the sum of rate coefficients for spontaneous emission, electronic quenching, rotational relaxation, and vibrational relaxation,

$$Q(i,j) = A(i,j) + Q_e(i,j) + Q_r(i,j) + Q_v(i,j) \quad . \tag{3.14}$$

The above rate coefficients are nonzero only when levels i and j are physically connected. For example, the rate coefficient for spontaneous emission $A(i,j) \neq 0$ only when level i is radiatively coupled to level j.

Similarly, for the upper laser-coupled level ($i=u$) the local rate equation is

$$\frac{dN(u)}{dt} = \sum_j [N(j)Q(j,u)] + N(l)W'_{lu} - N(u) \left[\sum_j Q(u,j) + W'_{ul} \right] \quad . \quad (3.15)$$

Comparing Eqs. (3.1) and (3.15), the effective rate coefficient for depopulation of the upper laser-coupled level is given by

$$Q_{eff} = \sum_j Q(u,j) - \frac{1}{N(u)} \sum_j N(j)Q(j,u) \quad . \quad (3.16)$$

For the lower laser-coupled level (i=l),

$$\frac{dN(l)}{dt} = \sum_j [N(j)Q(j,l)] + N(u)W'_{ul} - N(l) \left[\sum_j Q(l,j) + W'_{lu} \right] \quad . \quad (3.17)$$

3.4.1 Rotational Relaxation Model

Lengel and Crosley (1977) initially suggested empirical equations for rotational energy transfer in OH at room temperature, and later, Chan and Daily (1980) modified these equations for use at flame temperatures. Recently, Lucht et al. (1986) further modified the relations and provided parameters for collisions with water vapor (Table 3.1), which were derived from a comparison of experimental spectra and synthetic spectra generated with a dynamic model similar to the one described in this paper. The comparison employed experimental spectra from excitation of the $P_1(2)$, $P_1(5)$, $R_2(4)$, and $Q_1(10)$ lines of OH in an $H_2/O_2/N_2$ flame (Dieke and Crosswhite, 1962).

The empirical equations describing the collisional cross section for upward rotational transfer from level i to level j [E(j) > E(i)] are

$$\sigma_r(i,j) = B[N'(i)]g(j)\exp[\Gamma(\Delta N', \Delta J') - A(300/T)^\theta \Delta E] \quad (3.18)$$

for transfer with $\Delta N' \neq 0$, and

$$\sigma_r(i,j) = fB[N'(i)]g(j)(T/300)^\phi \quad (3.19)$$

for transfer with $\Delta N' = 0$. Briefly, $B[N'(i)]$ (cm^2) accounts for the variation in cross section with initial rotational quantum number $N'(i)$, $\Gamma(\Delta N', \Delta J')$ accounts for changes in the quantum numbers N' and J' during collisions, and A (cm) and θ determine the dependence of the cross section on the energy difference ΔE (cm^{-1}) between levels i and j. For the $\Delta N' = 0$ case, the constant f corrects the $B[N'(i)]$ values and ϕ accounts for the influence of flame temperature. Though these parameters were determined for rotational energy transfer in the excited electronic state, we use them to describe rotational transfer in the ground electronic state, since the rotational constants for these two states are nearly the same for the hydroxyl radical.

31

Table 3.1 Optimized rate parameters for rotational transfer in $A^2\Sigma^+$ ($v=0$) OH for collisions with H_2O (Lucht et al., 1986).[a]

A = 0.0060 cm	f = 0.10	θ = 0.7		ϕ = 0.8
N' or ΔN'	B [N'] 10^{-16} cm^2	$\Gamma(\Delta N'=\Delta J')$	$\Gamma(\Delta N \neq \Delta J')$	σ_r(i) 10^{-16} cm^2
0	1.60	--	--	85
1	1.60	1.40	-0.50	117
2	1.45	1.20	-1.00	145
3	1.30	0.30	-1.30	167
4	1.20	-0.25	-1.50	184
5	1.20	-1.20	-2.00	204
6	1.00	-1.90	-2.50	203
7	0.85	-3.00	-3.00	194
8	0.70	-3.80	-3.80	176
9	0.50	-4.70	-4.70	148
10	0.40	-6.00	-6.00	122
11	0.40	-6.00	-6.00	108
12	0.40	-6.00	-6.00	102
13	0.40	-6.00	-6.00	92
14	0.40	-6.00	-6.00	66

[a] σ_r(i), the total cross section for rotational transfer from level i $[\sigma_r(i) = \sum_{j \neq i} \sigma_r(i,j)]$, is calculated from the listed parameters and a temperature of 2000 K.

The collisional rate coefficient for any population transfer process is related to the respective cross section by

$$Q_m(i,j) = \sum_q N_q \sigma_m^q(i,j) \bar{v}_q \quad , \tag{3.20}$$

where N_q (cm^{-3}) is the number density of the collision partner q, σ_m^q (i,j) (cm^2) is the cross section for collisions with species q, $\bar{v}_q$ (cm/s) is the average relative velocity between OH and species q, and the subscript m denotes the mode of energy transfer (e, r, v). Note that Eq. (3.20) accounts for the influence of pressure on the LSF signal through the number density N_q. For upward rotational relaxation, Q_r(i,j) is obtained by substitution of Eqs. (3.18) or (3.19) into Eq. (3.20), and for downward rotational transfer, the rate coefficients are calculated using the principle of detailed balancing with a translational temperature of 2000 K.

3.4.2 Electronic Quenching Model

To our knowledge, the distribution of electronic quenching to the vibrational energy levels of the ground electronic state of the hydroxyl radical is not adequately described by theory or experiment. Thus, to study this distributive effect, we formulate electronic quenching as a function of the parameter f_b, the fraction of molecules quenched to the vibrational bath level. For transfer to $v'' > 0$,

$$Q_e(i,b) = f_b Q_e(i) \quad . \tag{3.21}$$

and for transfer to $v'' = 0$,

$$Q_e(i,j) = (1 - f_b)Q_e(i)/n_G \quad , \quad j \neq b \tag{3.22}$$

where $Q_e(i)$ is the total rate coefficient for electronic quenching from rotational level i in the excited electronic state, and n_G is the number of rotational levels in $v'' = 0$. Thus, we assume that quenching is equally likely to each rotational level of $v'' = 0$. Copeland et al. (1985) have measured the dependence of quenching on rotational level for $A^2\Sigma^+$ ($v'=0$) OH with several collision partners at room temperature. However, the effect of flame temperature on the observed rotational-level dependence is uncertain. Hence, we use quenching rate coefficients that are independent of N'.

Fairchild et al. (1983) measured electronic quenching cross sections for collisions of OH with several species at elevated temperatures ($\sim$1000-1500 K). We have extrapolated the average cross section for collisions with H_2O, $\sigma_e = 26.3 \times 10^{-16}$ cm² at about 1200 K, to a temperature of 2000 K by using the approach of Drake and Pitz (1985),

$$\sigma_e(2000) = \sigma_e(1200)(1200/2000)^{1/2} \quad . \tag{3.23}$$

The resulting cross section for electronic quenching is 20×10^{-16} cm²; the rate coefficient Q_e is obtained from σ_e via Eq. (3.20).

3.4.3 Vibrational Relaxation Model

The existing experimental data for vibrational energy transfer within the OH molecule are from studies of the $A^2\Sigma^+$ state (Schofield, 1979; German, 1976; Lengel and Crosley, 1978; Smith and Crosley, 1983). Consequently, as with rotational relaxation, one can only infer rate coefficients for vibrational transfer in the ground $^2\Pi$ state. In an experiment performed at room temperature, Lengel and Crosley (1978) determined cross sections for vibrational transfer in the excited state of OH due to collisions with atomic and diatomic species. They suggest that energy transfer between OH and

the diatomic collision partners takes place during long-lived collisions, resulting in efficient transfer of vibrational energy (e.g., with N_2 as the collision partner, $\sigma_V \approx 24.7 \times 10^{-16}$ cm² for $v'' = 1 \rightarrow 0$ transfer). Recently, Crosley and Smith (1983) investigated vibrational transfer in the burnt-gas region of a CH_4/air flame (T = 1900 K) and deduced the Q_V/Q_e ratio for $A^2\Sigma^+$ ($v''=1\rightarrow0$) as a function of rotational quantum number N' in v' = 1. The values of Q_V/Q_e were found to decrease with increasing N', ranging from about 0.65 at N' = 1 to about 0.4 at N' = 15.

Because of the uncertainty in the cross sections for electronic quenching to the $v'' = 0$ level and for vibrational transfer in the ground state of OH, we found it convenient to express the rate coefficient for vibrational relaxation from the bath level to the $v'' = 0$ level in terms of the parameter f_v and the quenching rate coefficient Q_e. As with quenching to $v'' = 0$, we assume that the population transfer is independent of the rotational level in $v'' = 0$; therefore,

$$Q_v(b, j) = f_v Q_e / n_c \quad . \tag{3.24}$$

Consequently, the effect of quenching to the $v'' > 0$ vibrational levels is qualitatively described by the parameters f_b and f_v. Because the path by which molecules excited to the upper electronic state return to the $v'' = 0$ level of the ground electronic state can be complicated, we do not attempt to attach a strong physical meaning to that portion of the dynamic model describing the bath level. If, for instance, the distribution of OH molecules quenched to the ground electronic state changed to favor the higher vibrational levels, the net rate of population transfer back to $v'' = 0$ might decrease, resulting in a larger population in the vibrational bath level and thus a greater depopulation of the directly-excited levels.

3.4.4 Excitation Model

The frequencies of the OH transitions for spontaneous emission are tabulated in Dieke and Crosswhite (1962), and the associated rate coefficients for spontaneous emission, A(i,j), are taken from Dimpfl and Kinsey (1979). For each of the computational runs, the transition is excited with a pulse described by a Gaussian dependence in both space and time,

$$W_{lu}(x,t) = W_{lu}^p \exp(-x^2/r_w^2)\exp[-(t - t_p)^2/t_w^2] \quad . \tag{3.25}$$

Here, x is the lateral distance from the center line of the irradiance profile (see Fig. 3.2), t_p is the time at which the pulse peaks, and W_{lu}^p is the peak rate coefficient for excitation. The spatial and temporal halfwidths, r_w and t_w, respectively, were chosen to be consistent with our laser system (r_w = 0.2 mm, t_w = 1.8 ns). Temporal integration of the rate equations was performed with the

routine DGEAR (IMSL, Houston, TX). Since the spatial dependence of the excitation function is Gaussian, a Gauss-Hermite quadrature formula with a 20th degree Hermite polynomial (Korn and Korn, 1968; Abramowitz and Stegun, 1968) was used for spatial integration of $N_u(x)$ and $\alpha_{sat}(x)$.

In principle, the peak excitation rate coefficient can be related to the spontaneous emission rate coefficient, $A(u,l)$, and the peak irradiance of the focused laser beam by assuming, for example, a Lorentzian spectral profile that is much greater than the absorption linewidth [Salmon and Laurendeau, 1985b; see also Eq. (6.14)]; however, we have made no attempt here to determine the excitation rate coefficient from the irradiance of our laser system. Instead, we specify a peak center-line saturation parameter $W_p{}' = W^p_{lu}/Q_{eff} \geq 10$, which assures that at $x = 0$ and $t = t_p$ the transition is well saturated.

3.5 Test of Rotational Relaxation/Electronic Quenching Models

Recently, Zizak et al. (1986) measured the relative excited-state, rotational-level population of OH in the burnt-gas region of three atmospheric, laminar, premixed flames using linear, laser-induced fluorescence (see Table 3.2). The distribution of population among the rotational levels depended strongly on the directly-excited level but was relatively independent of temperature and flame type. Given the relative, steady-state populations in the rotational levels of $A^2\Sigma^+$ ($v'=0$), Zizak et al. (1986) determined the ratio between N_u, the population in the directly-excited level, and N_c, the total population of the neighboring rotational levels. The ratio N_u/N_c characterizes the collisional processes in the excited state, and therefore comparison of these experimental values to calculated N_u/N_c values for the simulated H_2/O_2 flame provides a test of the reasonableness of our models for electronic quenching and rotational relaxation.

The rotational distributions for the simulated H_2/O_2 flame were obtained at atmospheric pressure and at the temporal and spatial peak of the excitation pulse. As with the experimentally determined distributions, the calculated populations had reached their steady-state values. Note that since the relative steady-state populations, $N(i)/N(u)$, are determined solely by the collisional rate coefficients for v', there is no difference between relative rotational distributions produced under linear and saturated conditions.

Figure 3.3 shows the variation in the calculated and experimental values of N_u/N_c with the excited $F_1(N')$ levels. The uncertainty in the calculated N_u/N_c ratio due to the limited number of rotational levels ($0 \leq N' \leq 14$) increases with the pumped quantum number; therefore, we performed the calculations only for $N' \leq 12$. Also shown in Fig. 3.3 are similar measurements made by Smith

35
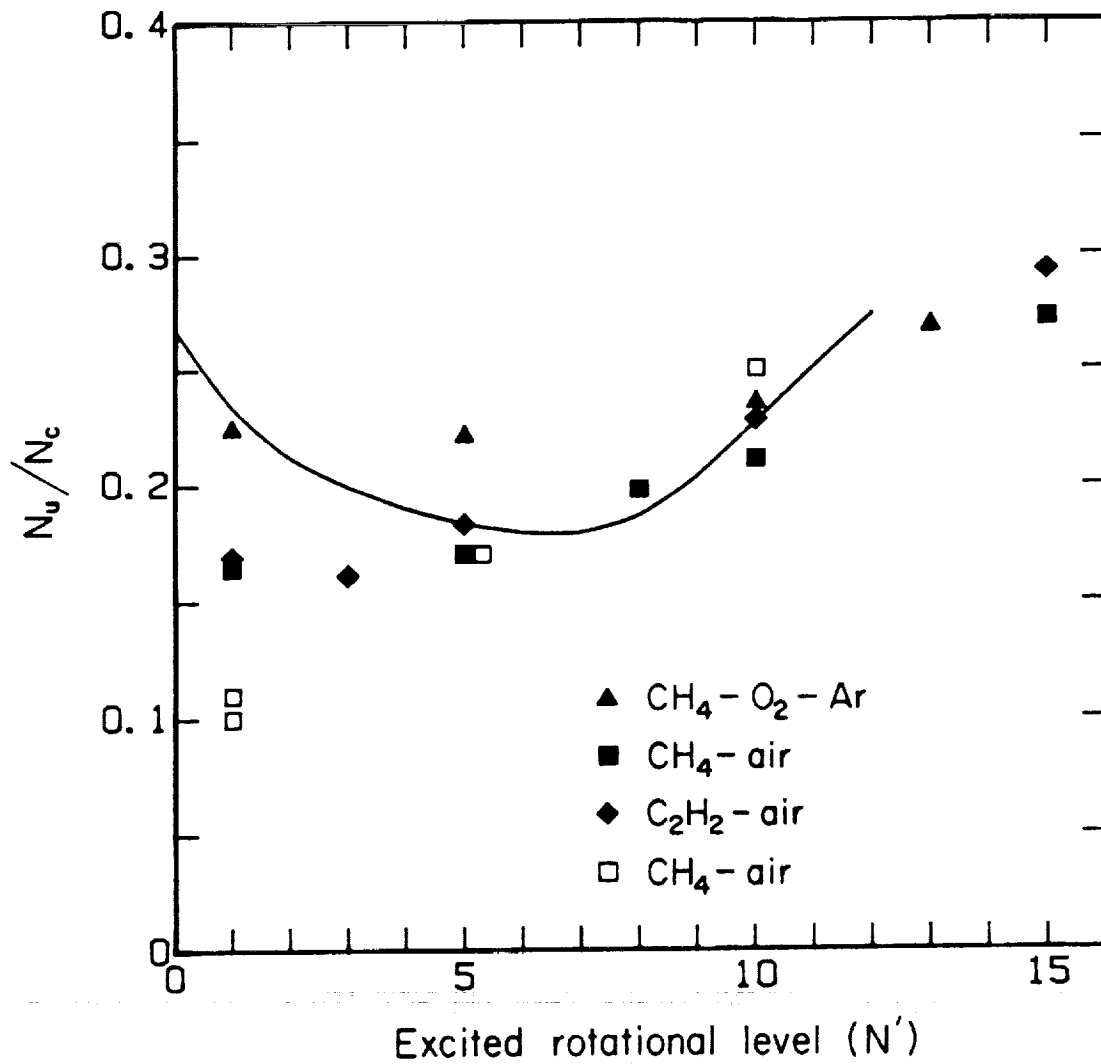
Figure 3.3   Comparison of calculated and experimental ratios (see Table 3.2) of the population in the directly-excited level, N_u, to the total population of the collisionally-excited, neighboring rotational levels, N_c, as a function of the pumped rotational level. The closed symbols are the data of Zizak et al. (1986), while the open symbols are the data of Smith and Crosley (1981).
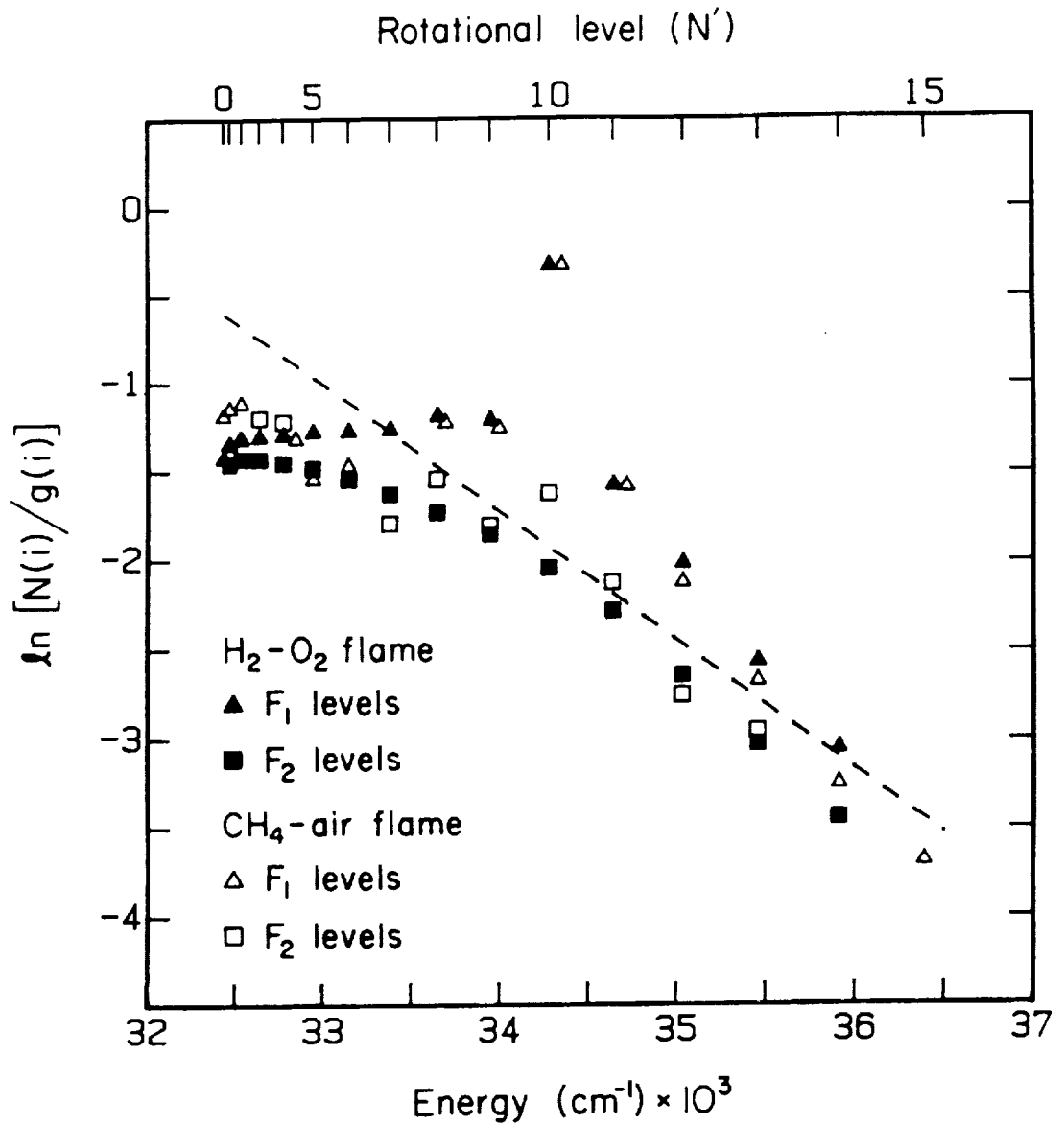
Figure 3.4   Comparison of the relative rotational-level populations in the simulated H_2/O_2 flame and in the experimental CH_4/air flame (Zizak et al., 1986) for excitation of the $Q_1(10)$ line. The Boltzmann distribution at 2000 K is shown by the dashed line. For comparative purposes, the experimental distribution has been normalized so that for the excited $F_1(10)$ level, $N_u^{exp} = N_u^{calc}$.

Table 3.2   Flames used for comparison of the
calculated and experimental ratios N_u/N_c.[a]

Flame	ϕ	T (K)
CH_4/air[b]	1.1	1950
$CH_4/O_2/Ar$[b]	1.0	1950
C_2H_2/air[b]	1.25	2380
CH_4/air[c]	0.86	1900
H_2/O_2	1.0	2000

[a] The equivalence ratio is denoted by ϕ.
[b] Zizak et al. (1986)
[c] Smith and Crosley (1981)

and Crosley (1981) in a CH_4/air flame (see Table 3.2). For $N' \geq 5$, the calculated and experimental values compare well, both showing a rise in N_u/N_c with increasing N'. However, for low N', considerable differences exist in the experimental data among the different flames. The higher N_u/N_c values for the simulated H_2/O_2 and experimental $CH_4/O_2/Ar$ flames might be related to the lack of N_2 compared to the CH_4/air and C_2H_2/air flames. Since N_u/N_c is sensitive to the $Q_e/\sum_{j \cdot u} Q_r(u,j)$ ratio, N_u/N_c could increase at lower N' owing to enhanced quenching or reduced rotational relaxation.

In Fig. 3.4, we compare the relative rotational-level populations from the experimental CH_4/air flame (Zizak et al., 1986) with the populations from the simulated H_2/O_2 flame for excitation of the $Q_1(10)$ line. The calculated populations agree well with those measured by Zizak et al. (1986). For excitation of low N' levels, the populations do not agree as well, which is expected from comparison of the calculated and experimental N_u/N_c values in Fig. 3.3. In general, however, the good agreement between our calculated results and the experimental data of Zizak et al. (1986), as demonstrated in Figs. 3.3 and 3.4, provides confidence in the utility of the dynamic model for analysis of the laser-saturated fluorescence method at high pressure.

3.6 Results and Discussion

The following calculations were carried out for excitation of the $P_1(5)$ transition [$\sigma_r(u) = 184 \times 10^{-16}$ cm^2]. Figure 3.5 shows the temporal dependence along the center line of the excitation profile for (1) the normalized number density in the directly-excited level, (2) the population fraction in the laser-coupled levels, and (3) the normalized excitation rate coefficient. The assumed conditions correspond to atmospheric pressure, a peak center-line saturation parameter $W_p' = 10$, and no

quenching to the vibrational bath level (f_b = 0). For convenience, the number density of the directly-excited level is normalized so that at peak excitation (t = t_p), the normalized population equals the population fraction 1 – $\gamma(0,t_p)$. Hence, from Eq. (3.4),

$$\frac{\tilde{N}_u}{\alpha^P_{sat}} = \frac{g_l + g_u}{g_u} \frac{N_u/N_l^0}{\alpha^P_{sat}} = \frac{(1-\gamma)\alpha_{sat}}{\alpha^P_{sat}} \quad , \tag{3.26}$$

where α^P_{sat} is the degree of saturation at the temporal and spatial peak of the irradiance pulse.

Figure 3.5 shows that under the above conditions, the population of the upper laser-coupled level approaches steady state while the excitation rate coefficient is still increasing. At the peak of the excitation pulse where the LSF signal is monitored, about 92% of the population remains in the two laser-coupled levels at the center line. Thus for f_b = 0 and atmospheric pressure, the model shows that to a good approximation the balanced cross-rate model can be used for OH measurements.

Figure 3.6 demonstrates the spatial dependence at the temporal peak of the excitation pulse for (1) the normalized number density in the directly-excited level, (2) the degree of saturation, (3) the population fraction in the laser-coupled levels, and (4) the normalized excitation rate coefficient at the same conditions as in Fig. 3.5. Because of the large value of W_p', the number density in the directly-excited level remains near its center-line value at substantial lateral distances. As shown by Eq. (3.26), the spatial profile of $\tilde{N}_u / \alpha^P_{sat}$ is dominated by the behavior of α_{sat}, which approaches 96% at the center line of the spatial irradiance profile. The normalized number density and the degree of saturation are equivalent at large lateral distances since $\gamma \rightarrow 0$.

To investigate the effect of pressure on the balanced cross-rate model, we computed the population fraction remaining in the laser-coupled levels as a function of pressure for a constant value of the saturation parameter. Figure 3.7 shows the value of 1 – γ at the temporal and spatial peak of the irradiance profile for four of the cases summarized in Table 3.3. At lower pressures, the populations in the vibrational bath level and in the rotational levels of the excited electronic state increase with increasing pressure. The result is a depletion of the $v'' = 0$ manifold with increasing pressure, and hence a depletion of the laser-coupled levels.

Figure 3.7 also shows that as pressure is increased, the population N_u + N_l = (1 – γ) N_l^0 approaches an asymptotic value which depends on the ratio f_b/f_v. This assertion is confirmed by comparing cases C and D, which have different absolute values of f_b and f_v but the same ratio f_b/f_v.
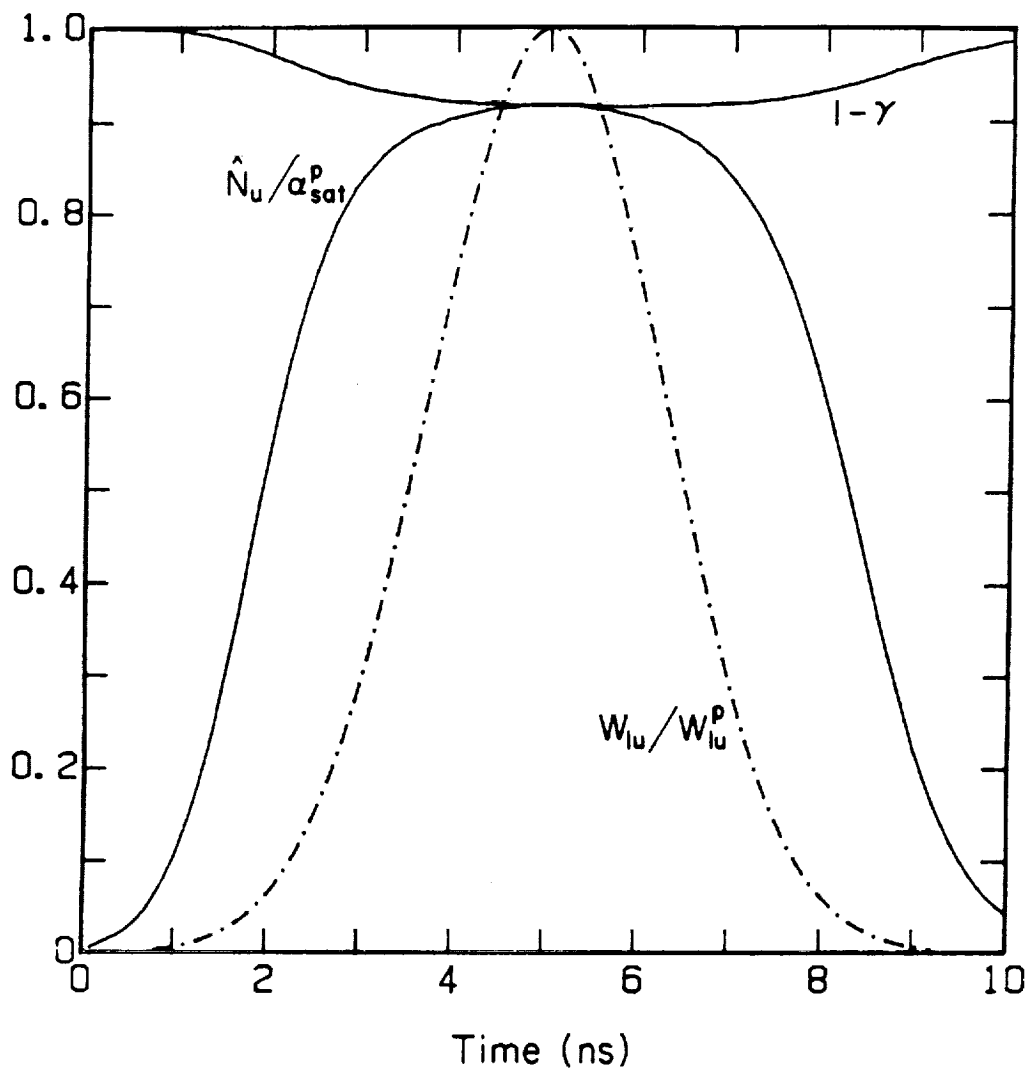
Figure 3.5 Temporal dependence along the center line for (1) the normalized population, $\hat{N}_u(0,t)/\alpha_{sat}^p$, (2) the population fraction in the laser-coupled levels, $1 - \gamma(0,t)$, and (3) the normalized excitation rate coefficient, $W_{lu}(0,t)/W_{lu}^p$, at conditions corresponding to atmospheric pressure, a peak center-line saturation parameter of $W_p' = 10$, and no quenching to the bath level ($f_b = 0$).
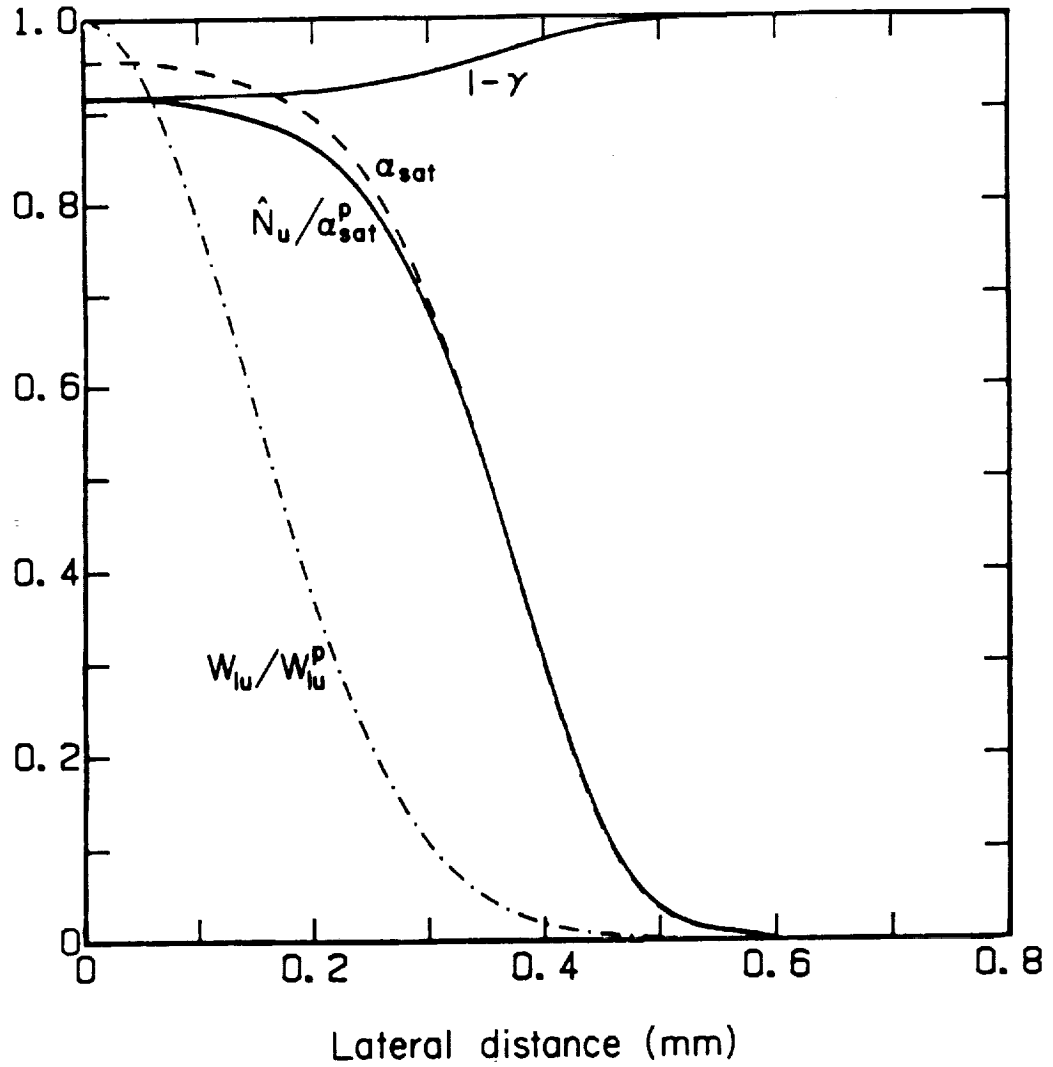
Figure 3.6   Spatial dependence at the temporal peak of the excitation pulse for (1) the normalized population, $\hat{N}_u(x,t_p)/\alpha_{sat}^p$, (2) the degree of saturation, $\alpha_{sat}(x,t_p)$, (3) the population fraction in the laser-coupled levels, $1 - \gamma(x,t_p)$, and (4) the normalized excitation rate coefficient, $W_{lu}(x,t_p)/W_{lu}^p$, at the same conditions as in Fig. 3.5.
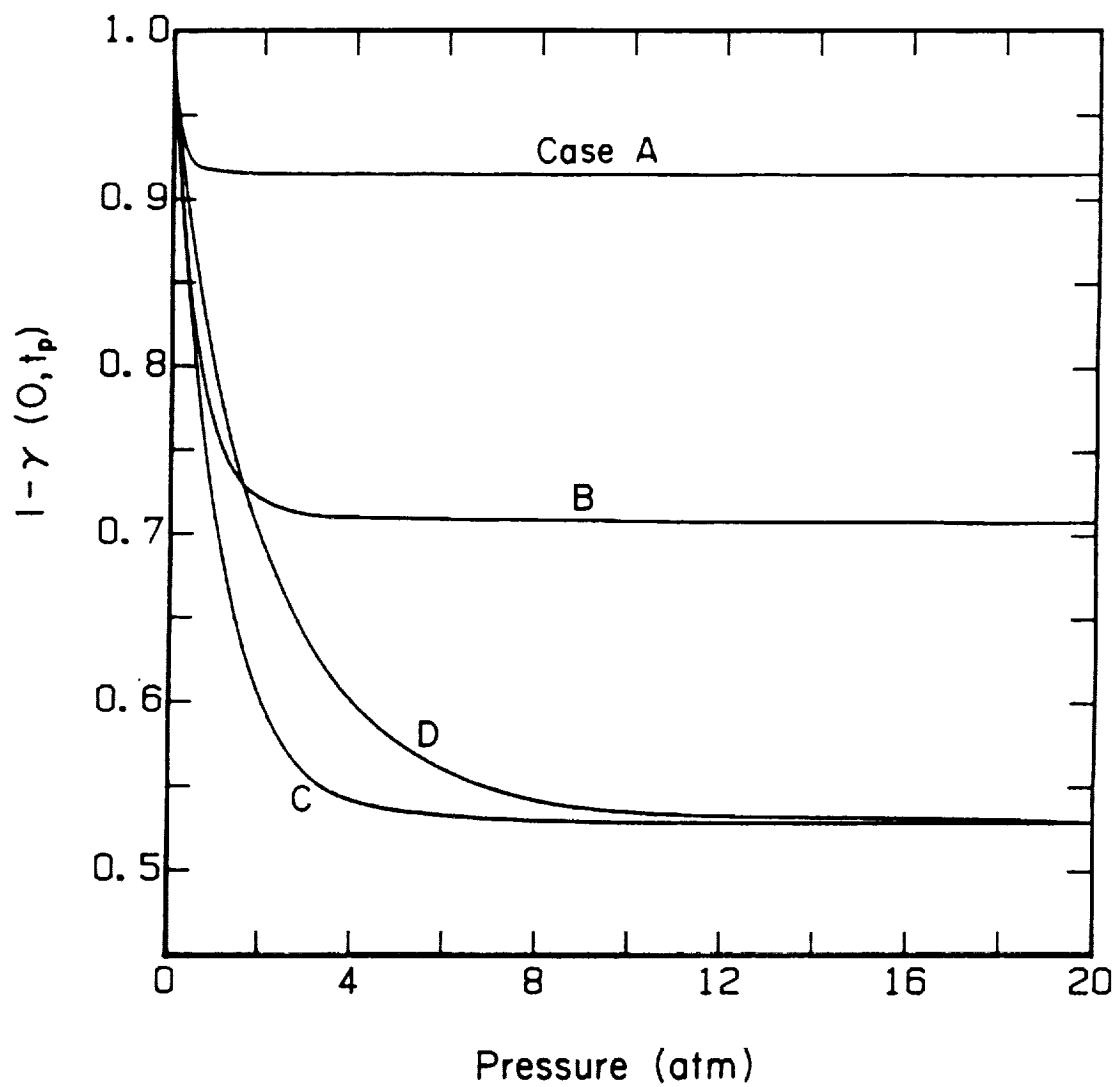
Figure 3.7   Dependence of $1 - \gamma(0,t_p)$, the population fraction at the temporal and spatial peak of the irradiance profile, on pressure for cases A, B, C, and D (see Table 3.3).

Table 3.3 Summary of cases describing depopulation of the laser-coupled levels for $P_1(5)$ excitation.[a]

Case	f_b	f_v	W_p'	$1 - \gamma(0,t_p)$	$\langle F_c(t_p)\rangle$
A	0	--	10	0.92	0.93
B	0.50	0.25	10	0.71	0.75
C	0.50	0.10	10	0.53	0.58
D	0.25	0.05	10	0.53	0.58
E	0.50	0.10	100	0.52	0.55

[a] The parameters $1 - \gamma(0,t_p)$ and $\langle F_c(t_p)\rangle$ are the respective asymptotic values of the center-line and spatially-averaged population fraction in the laser-coupled levels at peak excitation (see Figs. 3.7 and 3.8).

The asymptotic value is attained when the vibrational bath level and the rotational levels of the excited electronic state reach a sufficiently high population that the rates for transfer into and out of the laser-coupled levels are equal. When the transition is well saturated, as happens when W_p' > 10, the asymptotic value of $1 - \gamma$ is insensitive to W_p'; this is borne out by the comparison between cases C and E of Table 3.3.

Figure 3.8 shows the effect of a Gaussian irradiance profile on the spatially-averaged population fraction in the laser-coupled levels for cases A, B, and C. The degree of saturation decreases with increasing distance from the center line of the irradiance profile (see Fig. 3.6); consequently, the population in the laser-coupled levels away from the center line more closely represents the unperturbed population in the ground state. Hence, the spatially-averaged depopulation is less than the depopulation at the center line of the irradiance profile. The resulting increase in the asymptotic value for the spatially-averaged population in the laser-coupled levels is detailed in Table 3.3. Because of the greater center-line saturation in case E, the spatial dependence of α_{sat} more closely approximates that resulting from spatially uniform excitation; thus, the effective population fraction more closely approximates the population fraction along the center line.

Figure 3.9 shows the asymptotic value of both the spatially-averaged and center-line population fractions as a function of the ratio f_b/f_v for W_p' = 10. Depopulation of the laser-coupled levels clearly becomes more problematic as f_b/f_v increases; however, the sensitivity of the population fraction to changes in the ratio f_b/f_v decreases with larger f_b/f_v. As f_b/f_v increases, population within $v'' > 0$ increases; depletion of the laser-coupled levels follows since replenishment via rotational transfer is limited by depletion of $v'' = 0$.
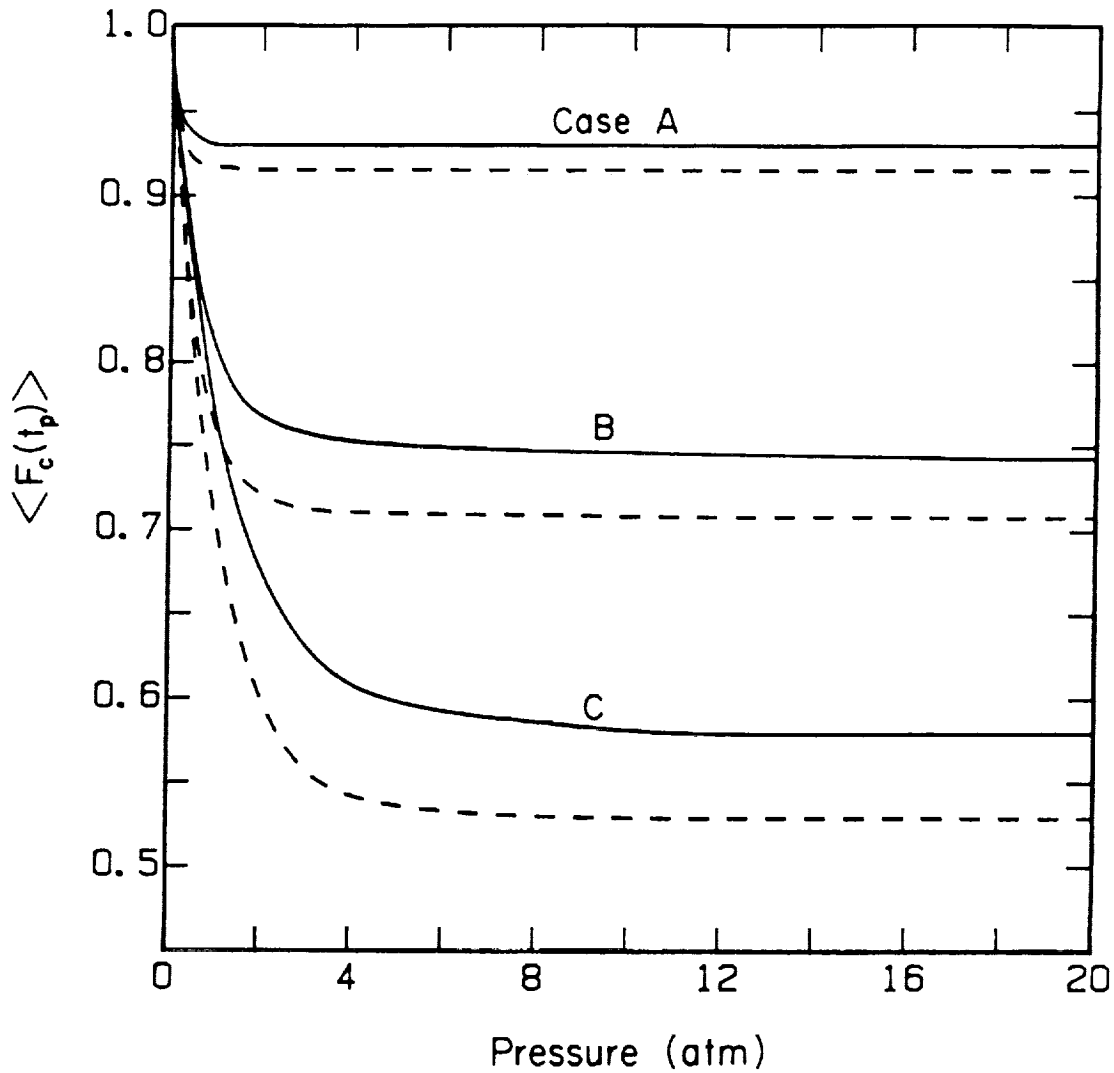
Figure 3.8   Dependence of $\langle F_c(t_p) \rangle$, the spatially-averaged population fraction at the temporal peak of the irradiance profile, on pressure for cases A, B, and C (see Table 3.3). The population fraction at the center line, 1 - $\gamma(0,t_p)$ (---), from Fig. 3.7 is included for comparison.
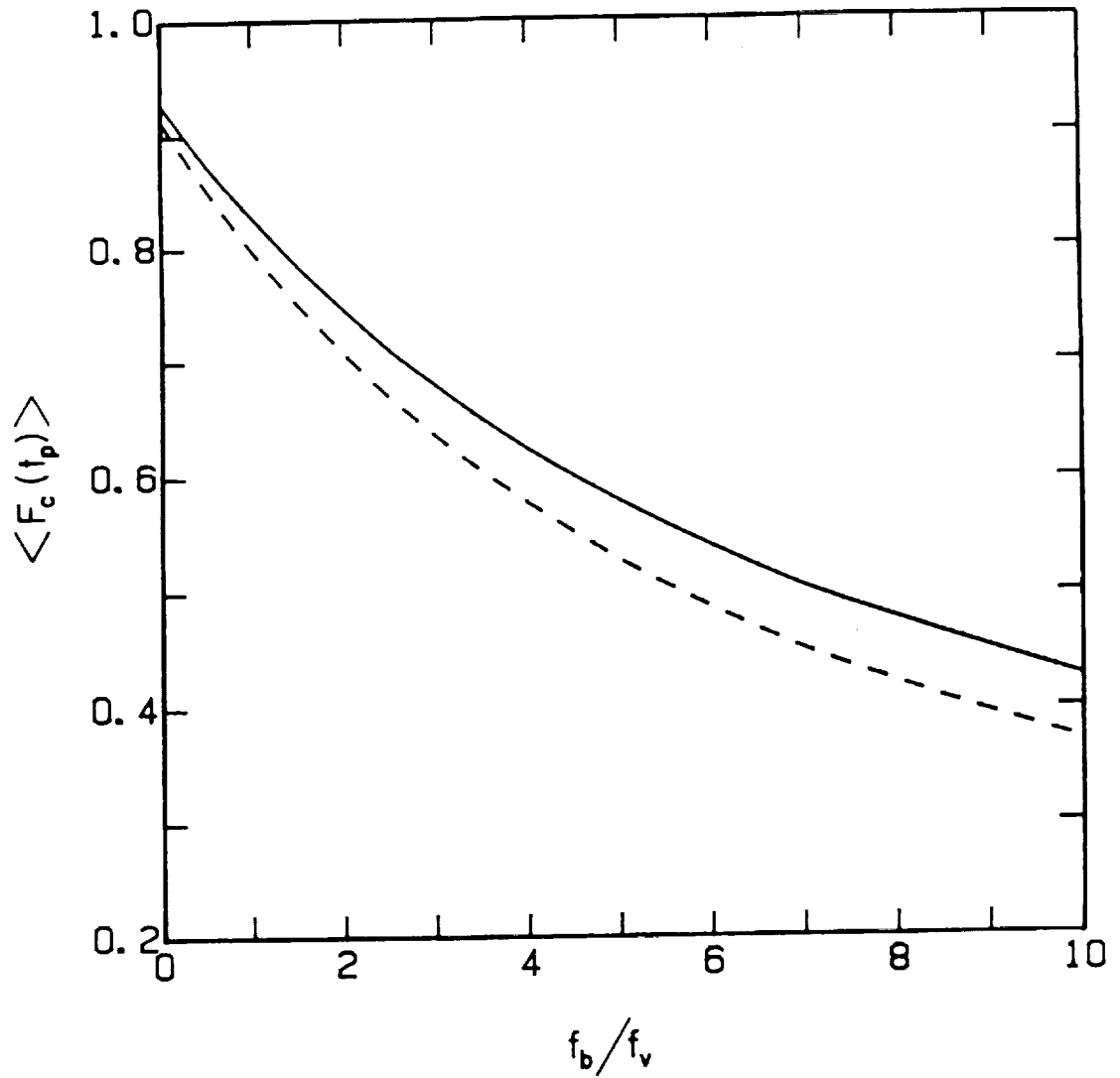
Figure 3.9   Dependence of $\langle F_c(t_p)\rangle$, and $1 - \gamma(t_p)$ (---), the respective spatially-averaged and center-line values of the population fraction, on the ratio f_b/f_v for $W_p' = 10$.

The results in Fig. 3.9 for large f_b/f_v values are in qualitative agreement with those of Campbell (1984), who used a similar dynamic model to show that prediction of species number densities with the balanced cross-rate model can result in significant errors at higher pressures. However, because Campbell (1984) used lower values of the saturation parameter for many of his cases (e.g., $W_p' \approx 1$), predicted errors using the two-level model arise from both depopulation of the laser-coupled levels and a low degree of saturation. Our approach has been to assure that the transition is well saturated and then to determine the depopulation. The error resulting from the balanced cross-rate model at the center line, $\gamma(t_p)$, and averaged throughout the probe volume, $1 - \langle F_c(t_p)\rangle$, is shown in Figs. 3.7 through 3.9.

Table 3.4   Sensitivity of the population fraction to changes in rate coefficients for rotational energy transfer in the ground electronic state.[a]

f_b/f_c	ζ_G	$1 - \gamma(0, t_p)$	$\langle F_c(t_p)\rangle$
0	0.5	0.68	0.72
	1.0	0.92	0.93
	2.0	1.10	1.09
2	0.5	0.56	0.61
	1.0	0.71	0.75
	2.0	0.81	0.84
5	0.5	0.44	0.50
	1.0	0.53	0.58
	2.0	0.59	0.64

[a] ζ_G is the ratio of the B-parameter in the ground state to that in the excited electronic state [Eqs. (3.18) and (3.19); Table 3.1]. The parameters $1 - \gamma(0,t_p)$ and $\langle F_c(t_p)\rangle$ are the respective asymptotic values of the center-line and spatially-averaged population fraction in the laser-coupled levels at peak excitation ($W_p' = 10$; see Figs. 3.7 and 3.8).

Depletion of the laser-coupled levels may also occur via reduced rate coefficients for rotational transfer in the ground electronic state compared to the excited state. Table 3.4 summarizes the sensitivity of the asymptotic center-line and spatially-averaged population fractions to variations in the rate coefficients for rotational transfer in the ground state. Note that at high pressure, overpopulation of the laser-coupled level can occur if the influence of the vibrational bath levels is small ($f_b/f_v \approx 0$) and if the effective rate coefficient for rotational replenishment of the ground state is substantially larger than that for rotational depletion in the excited state. At lower pressure, where

the time scale for collisional depopulation is longer than that for excitation (t_w), the deviation from $N_u + N_l = N_?^0$ will be small. At sufficiently high pressure, where the time scale for collisional depopulation is much shorter than t_w, the population fraction in the directly-excited levels reaches an asymptotic value before the temporal peak of the laser pulse.

Figure 3.10 shows the spatially-integrated, temporal profiles of the normalized population in the upper laser-coupled level for case A. This normalized population is equivalent to $\langle F_c(t_p) \rangle$ at peak excitation ($t = t_p = 5$ ns). When polarization effects are small (Altkorn and Zare, 1984), such profiles are proportional to the measured fluorescence signal. Because the depopulation for case A is small, little difference exists in the profiles at the various pressures. At 0.1 atm, the peak of the fluorescence profile lags the excitation peak; however, as pressure increases, the profiles more closely follow the excitation pulse.

The spatially-integrated population profiles for case C are shown in Fig. 3.11. The effect of depopulation of the laser-coupled levels is evident, and as with case A, the profile at 0.1 atm lags the excitation pulse. However, at 1 atm, the population profile peaks before the excitation pulse. This behavior occurs when the characteristic time for collisional depopulation of the laser-coupled levels is comparable to the characteristic time for excitation. When the characteristic collisional time is much shorter than t_w, depopulation of the laser-coupled levels occurs earlier in the irradiance pulse, as demonstrated by the fluorescence profile at 10 atm.

The effect of depleting the laser-coupled levels is much more distinctive along the center line, as shown in Fig. 3.12 for case C. As pressure increases and the characteristic time for collisional depopulation becomes much smaller than t_w, the saturated value of $N_u + N_l$ is approached, which flattens the temporal population profile. The flat temporal profile at 10 atm shows that the center-line population fraction has reached its asymptotic value (see Fig. 3.7), and no further depopulation of the laser-coupled levels will occur with increasing pressure.

The effect of depopulation on the excited-state rotational levels at the spatial and temporal peak of the irradiance profile is shown in Fig. 3.13. For convenience, we show only the populations in the F_1 levels, and lines are drawn between the rotational-level populations. As with the temporal profiles described above, the population in the upper laser-coupled level decreases with increasing pressure. At pressures of 1 atm and above, the relative populations [i.e., $N(i)/N(u)$] are at steady state. For $N' > 4$, the populations have an approximately Boltzmann distribution, but with a temperature ($\sim$1130 K) lower than the ground-state rotational temperature of 2000 K. Similar

47
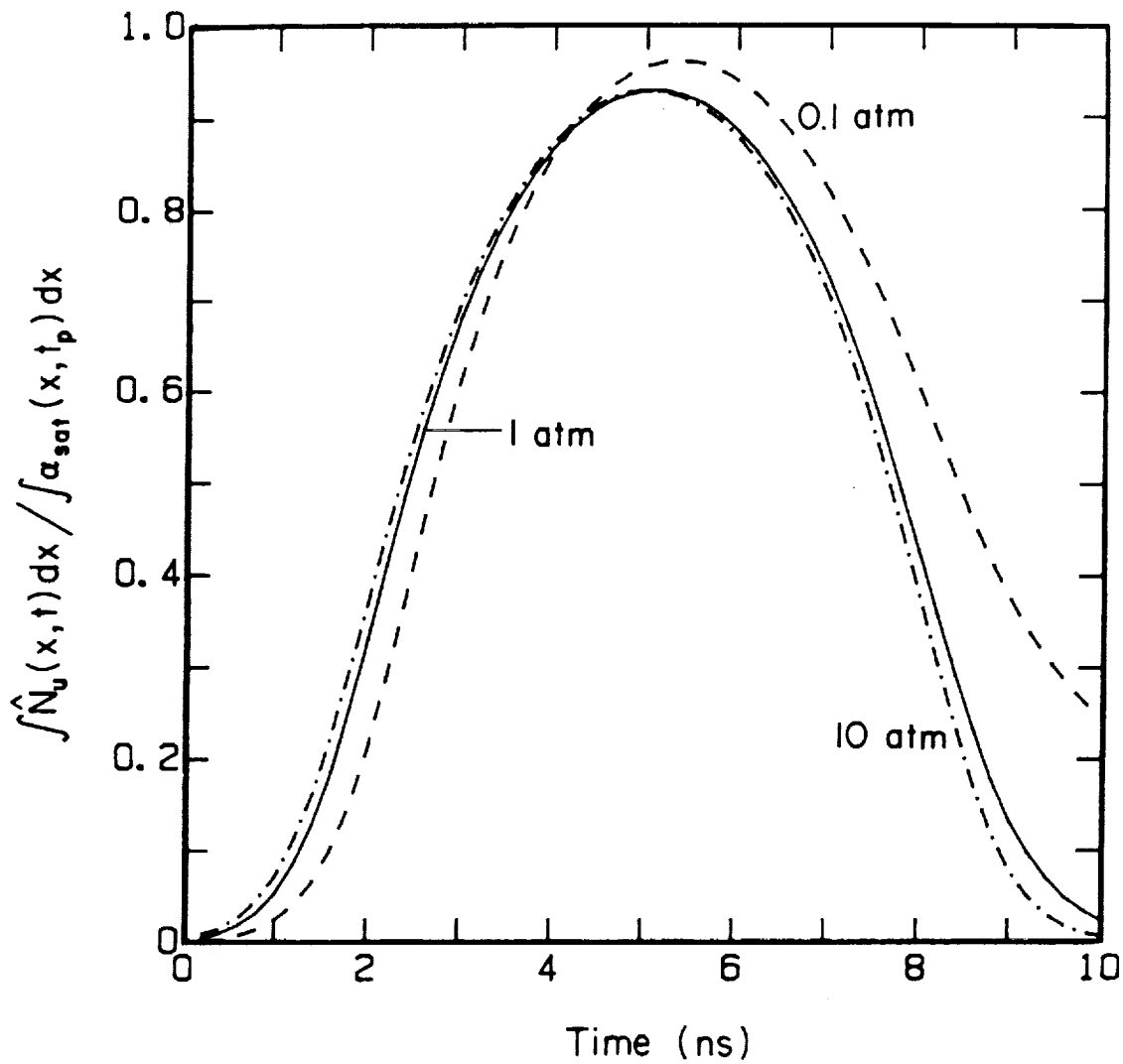
Figure 3.10   Temporal profiles of the spatially-integrated, normalized population in the upper laser-coupled level for case A at pressures of 0.1, 1, and 10 atm.
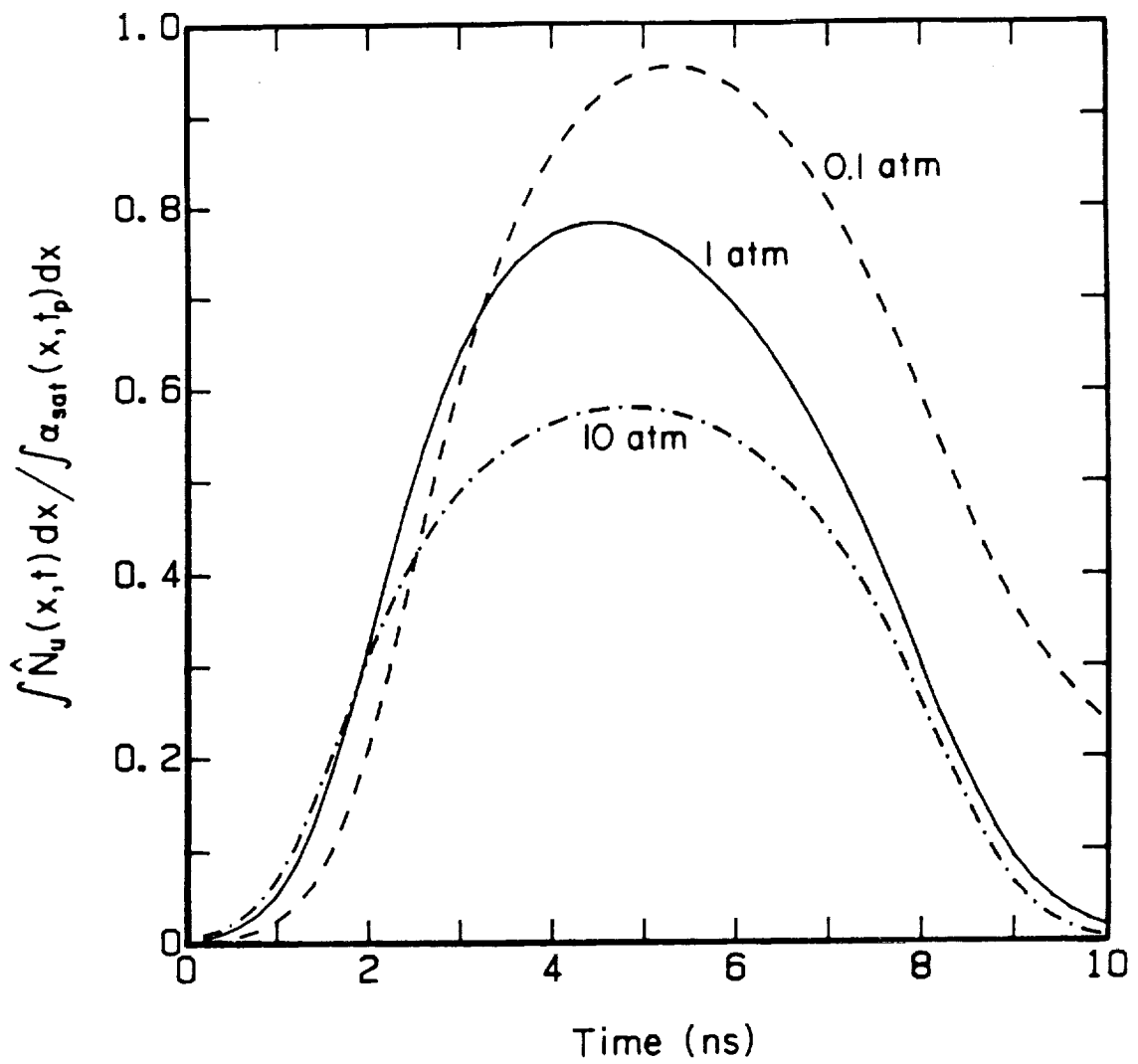
Figure 3.11   Temporal profiles of the spatially-integrated, normalized population in the upper laser-coupled level for case C at pressures of 0.1, 1, and 10 atm.

49
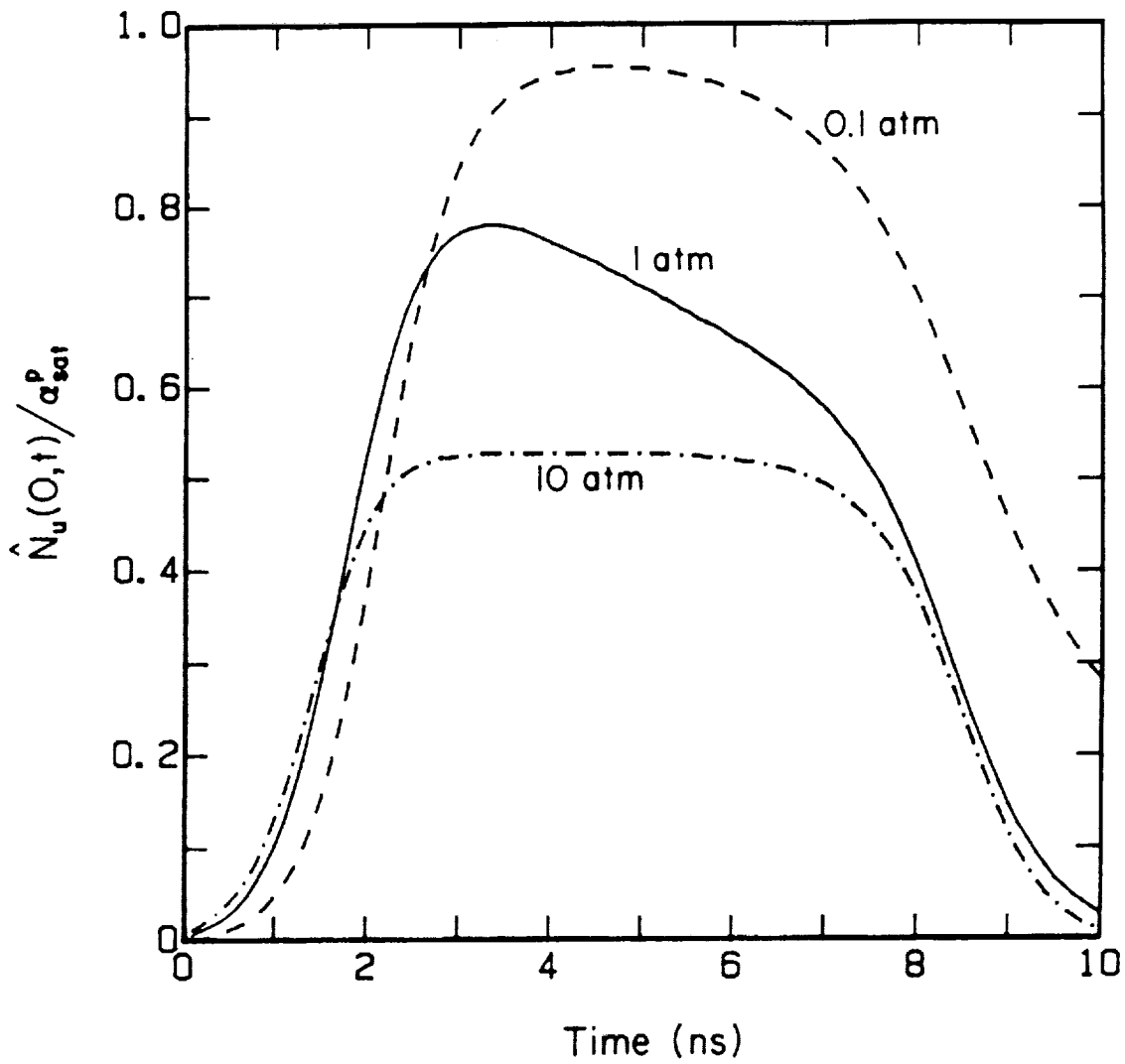
Figure 3.12 Temporal profiles of the center-line, normalized population in the upper laser-coupled level for case C at pressures of 0.1, 1, and 10 atm.
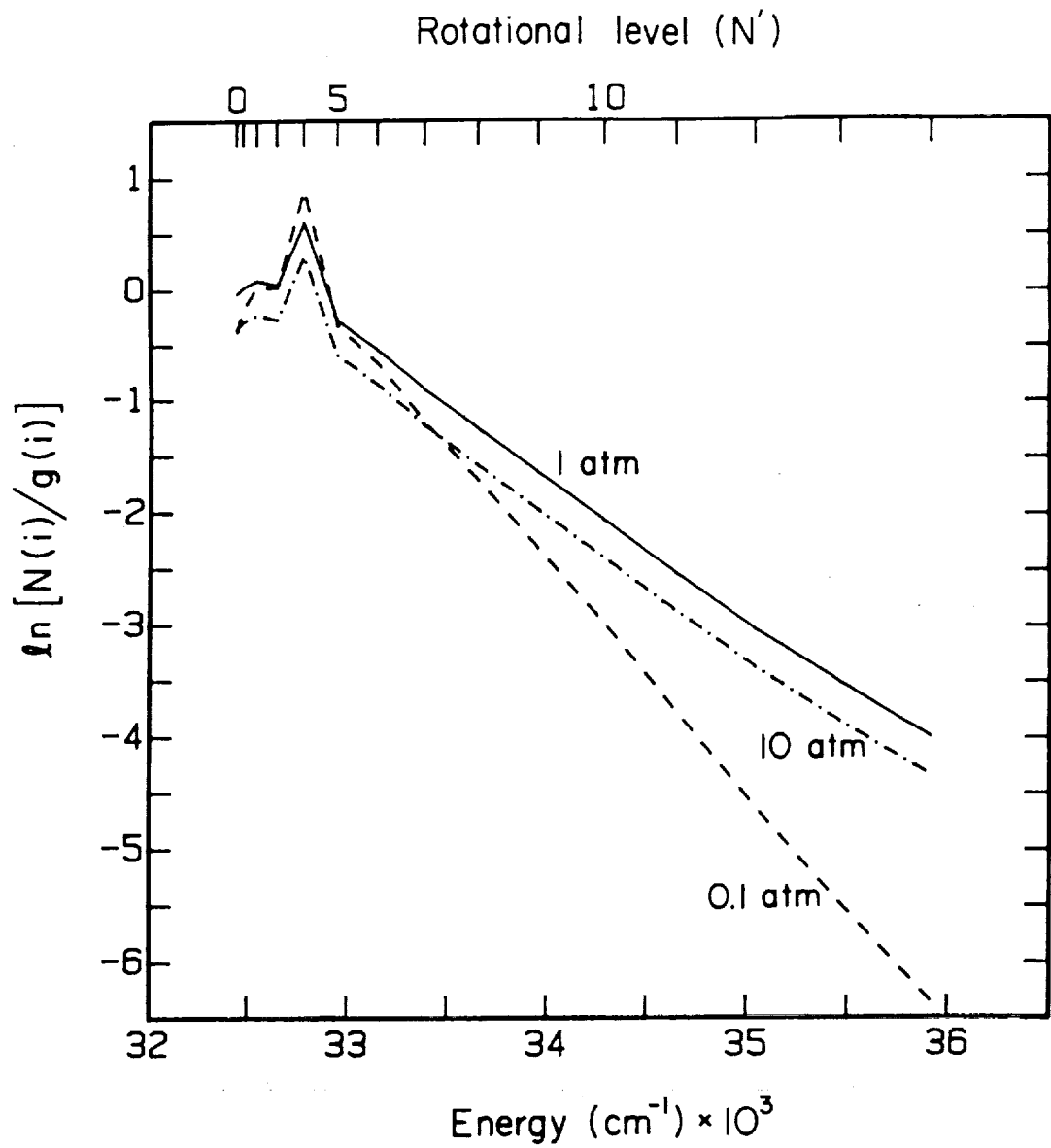
Figure 3.13   Rotational-level populations of the F_1 component at the spatial and temporal peak
of the irradiance profile for case C at pressures of 0.1, 1, and 10 atm.

distributions were obtained by Zizak et al. (1986) for excitation of transitions with $N' = 5$. At pressures above ~5 atm, where the population fraction in the directly-excited levels has reached its asymptotic value, the population distributions coincide.

We now use the results of our analysis to make some important observations regarding the balanced cross-rate model. First, the state-to-state dynamic calculations show that rotational relaxation in the excited state plays only a small role in direct depopulation of the $v'' = 0$ level, even at high pressures (case A). However, rotational relaxation within the excited electronic state can play a larger indirect role by increasing the number of pathways for electronic quenching to the v'' > 0 levels. Second, under conditions where f_b/f_v is small and the rate coefficients for rotational transfer in the ground state are approximately equal to those of the excited state, the balanced cross-rate model should remain a good approximation regardless of pressure. Conversely, for large f_b/f_v ratios, the balanced cross-rate model becomes a poorer approximation at high pressure. Third, at sufficiently high pressure the population of the laser-coupled levels attains an asymptotic value, which is insensitive to both pressure and the saturation parameter. Hence, one would expect that Eq. (3.3) could be used as a modified balanced cross-rate model if $1 - \gamma$ exhibited small sensitivity to both the flame temperature (~1000-2500 K) and the identity of the primary collision partners. For excitation by a nonuniform irradiance profile, Eq. (3.8) shows that the LSF method can be used at high pressure if $\int(1 - \gamma)\alpha_{sat}dx$ (and not $1 - \gamma$ alone) displays low sensitivity to the collision environment.

3.7 Conclusions

We have examined the effect of pressure on the LSF method for measurement of OH concentration. A numerical model of the excitation dynamics of OH has been developed to explore the validity of the balanced cross-rate model at higher pressures. Using this model, we have shown that the depopulation of the laser-coupled levels is sensitive to collisions which depopulate $v'' = 0$ and to rate coefficients for rotational transfer in the ground state which are smaller than those in the excited state. In particular, we have shown that the depopulation of $v'' = 0$, and hence the laser-coupled levels, depends on the probability of (1) electronic quenching to vibrational levels for which $v'' > 0$ and (2) vibrational relaxation to $v'' = 0$. At sufficiently high pressures, regardless of the reason for depopulation, the total population of the laser-coupled levels reaches an asymptotic value, which occurs when the collisionally-excited rotational and vibrational energy levels attain enough population to balance the population transfer rates into and out of the laser-coupled levels.

When $f_b/f_v \leq 1$ and the rotational transfer rate coefficients within the ground and excited states are comparable, the laser-coupled levels are not significantly depopulated, and therefore the balanced cross-rate model is a good approximation at all pressures. However, when f_b/f_v is large, the depopulation of the laser-coupled levels will be significant at higher pressures, and thus the balanced cross-rate model will no longer be valid. At sufficiently high pressures, a modified balanced cross-rate model, Eq. (3.3), could be useful for making measurements of OH concentration if the asymptotic value of the population fraction is insensitive to temperature and the collisional environment.

CHAPTER 4

EXPERIMENTAL APPARATUS

4.1 Combustion Facility for High-Pressure Flame Studies

4.1.1 Introduction

Measurements of flame species by optical methods, such as laser-induced fluorescence (LIF) and coherent anti-Stokes Raman spectroscopy (CARS), have proved valuable in elucidating chemical and physical processes occurring in combustion environments (Eckbreth, 1988). While much developmental work on optical methods has been done in low pressure ($\leq$ 1 atm) flames, most combustors of practical importance operate at high pressure. Since the width of the flame front decreases with increasing pressure, physical probes are even more likely to perturb the flame front; hence utilization of optical methods becomes a necessity for many high-pressure studies. Such measurements could prove useful for a broad range of topics including (1) turbulent flames, (2) engine knock, (3) pollutant formation (e.g., soot and NO production), and (4) flame extinction and stability. In this chapter, we describe a high-pressure combustion facility designed for (1) the development of optical diagnostic methods in high-pressure flames and (2) the study of practical combustion phenomena by optical methods.

In previous work, Flower and Bowman (Flower and Bowman, 1984; Flower, 1986; Flower and Bowman, 1986; Flower, 1988) and Edwards et al. (1985, 1987) have described special facilities designed for optical measurements in high-pressure flames. Flower and Bowman have used laser scattering and attenuation plus laser-Doppler anemometry to study soot production in laminar and turbulent diffusion flames. Their facility includes a rectangular stainless steel chamber, with an optical access port on each of the four sides. The vessel is designed to accommodate flames at pressures to 10 atm, and spatial profiles of the flame are obtained by translating the entire chamber. Edwards et al. (1987) report LIF measurements of OH and CN in solid propellant flames at pressures to 35 atm. The combustor used in this facility is a modification of a high-pressure window bomb,

and it includes a servomechanism to keep the surface of the solid propellant at a constant height during combustion (Edwards et al., 1985). Our design, while emphasizing flexibility and thus allowing a variety of laser diagnostic methods with laminar or turbulent flames, also stresses low cost by employing commercially available components (where practical) in the facility.

4.1.2 High-Pressure Facility

Our high-pressure combustion facility includes (1) the pressure vessel, (2) the burner translation system, (3) two flat-flame burners, and (4) the gas control system. To reduce the cost of the combustion facility, the pressure vessel was constructed from standard stainless steel pipe (AISI 316, schedule 40). The main body of the pressure vessel (Fig. 4.1) is 109 cm long by 20 cm ID, with large diameter slip-on flanges welded to either end and blind flanges for the seals. Copper tubing is coiled around the main body; thus, one can reduce the vessel temperature (if necessary) by flowing water through the tubing.

Four optical access ports, fabricated from 6.4 cm ID pipe and small-diameter slip-on flanges, are welded to the main body; the seals are provided by small-diameter blind flanges, each of which is machined to accommodate a window housing. Each window, 3.8 cm diameter by 1.25 cm thick, is seated in the housing against an O ring and is kept dry and free of particles by flowing dry nitrogen through a system of jets in the housing. The inner face (which holds the window housing) of one blind flange is machined at 10°; thus, for optical measurement techniques such as LIF, this outer flange can be used as the laser beam exit port to keep reflected light away from the sampling volume. On completion, the pressure vessel was hydrostatically tested to 60 atm.

The translation mechanisms are located within the pressure vessel, thus further reducing the cost of the facility since only the burner and not the entire vessel is moved. The vertical translation system uses three Unislide assemblies, which are mounted to the bottom blind flange, and a small stepper motor (Slo-Syn Model M061-FD02) and a timing belt to drive the three units (Fig. 4.2). The Unislide assemblies carry a platform (Fig. 4.3) on which the horizontal translation mechanism and the burner are mounted. Like the vertical system, the horizontal system uses a small stepper motor (Slo-Syn Model M061-FD02) and a timing belt to drive the optical translation stage (Newport model M-420-1S) carrying the burner. The range of movement for the vertical and horizontal systems is about 11 and 2.8 cm, respectively, while the associated single-step resolution (at 200 steps/revolution) is about 2 and 1 μm, respectively. Two linear variable differential transformers
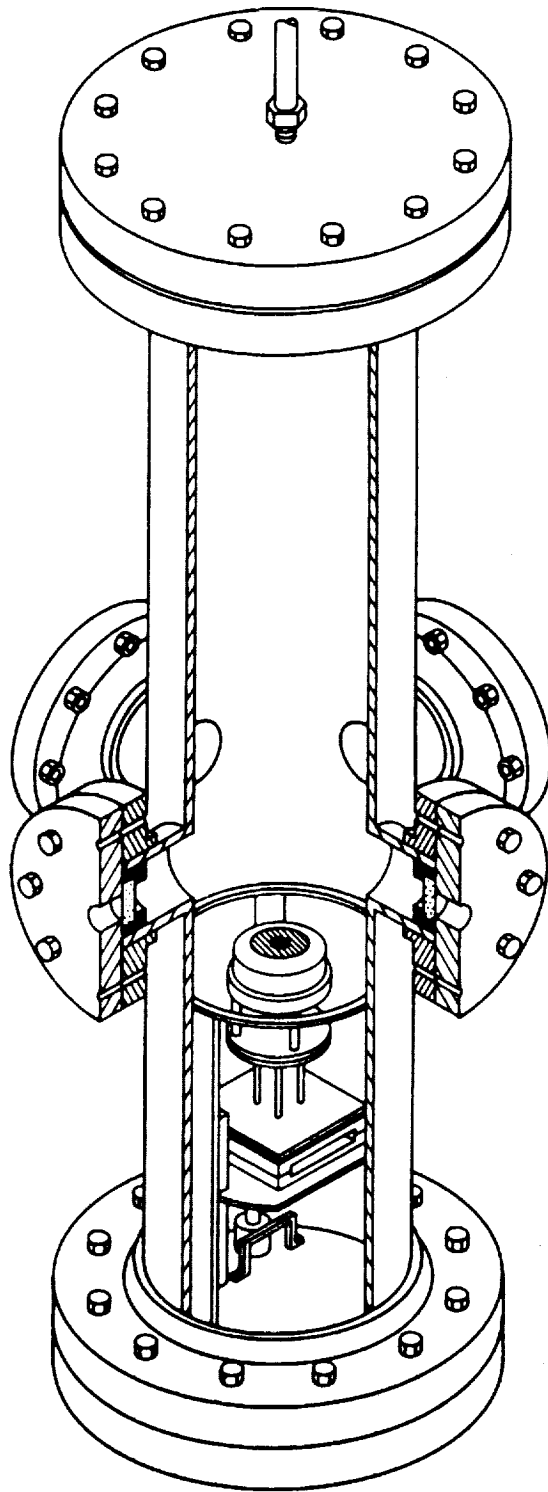
Figure 4.1   Cutaway view of the pressure vessel and components.
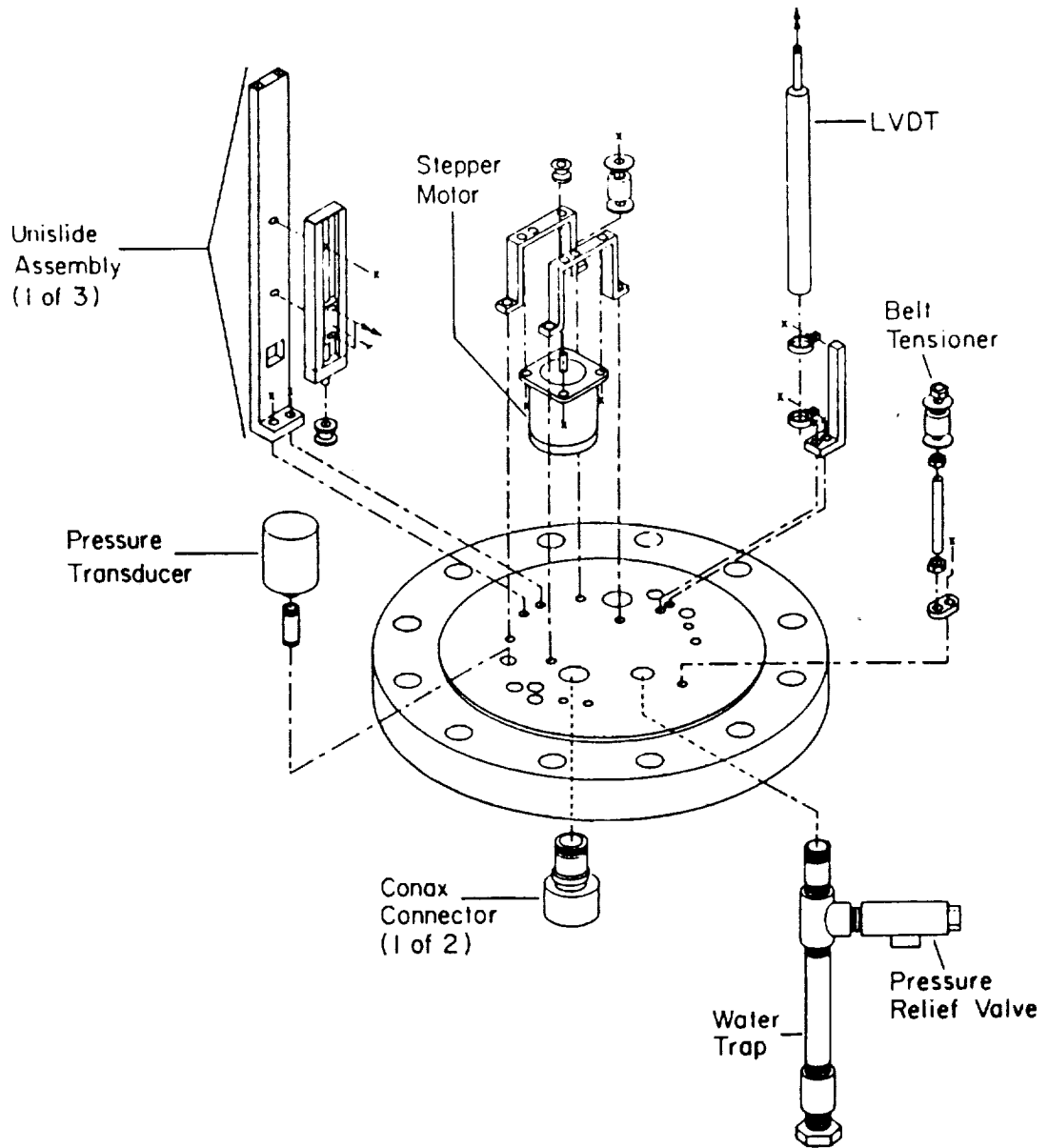
Figure 4.2   Exploded view of bottom flange and components.

Translation Stage

LVDT

Translation
Platform
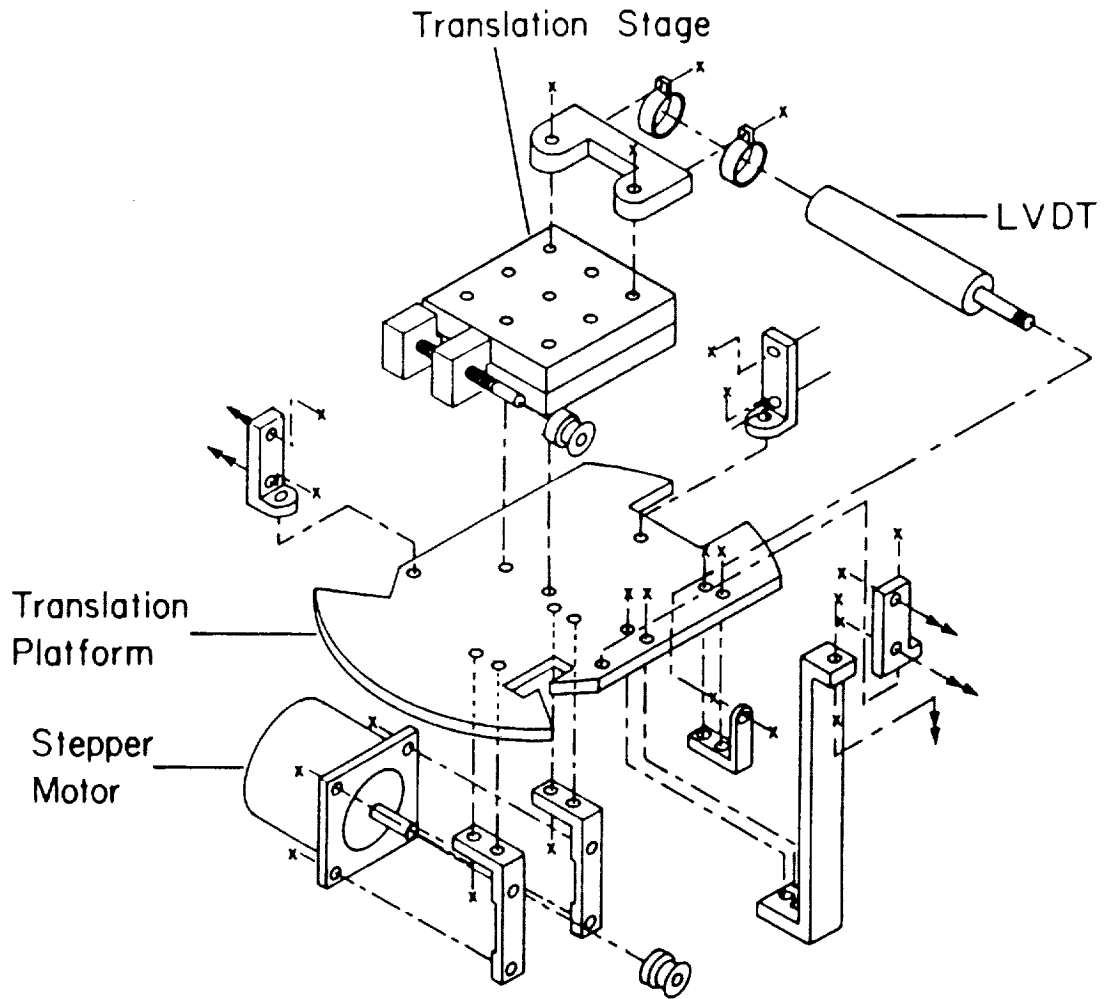
Stepper
Motor

Figure 4.3   Exploded view of horizontal translation system.

58

(LVDTs) are used to monitor the approximate absolute position of the burner; however, to accurately position the burner relative to the selected zero location, the motors are stepped through a microcomputer.

In addition to supporting the translation system, the bottom flange supports an electronic pressure transducer and a pressure relief valve (set for 24 atm) and provides the ports that are used for electrical wiring and fluid connections. Two Conax connectors are used to bring electrical signals to and from the vessel. During operation at high pressure (or even atmospheric pressure), the interior surfaces of the vessel can remain below the dew point, even without cooling the vessel, and thus water vapor from combustion can condense on these surfaces. Because some of the water collects on the bottom flange, We had to (1) isolate exposed electrical wiring from moisture (the wires were stripped to obtain a seal in the Conax connectors) and (2) provide a suitable water trap at the bottom flange. The former was achieved using a silicon elastomer to fill the dead space in the electrical access ports where the wires were exposed and water could collect; the latter was achieved by attaching a closed section of pipe underneath the flange.

The pressure vessel is supported by a steel-frame table; the table also supports optical breadboards located on either side of the vessel. To provide access to the bottom flange and the various components, the pressure vessel is moved by a Unistrut trolley and winch system which mounts to the table. In front of each optical access port is a Lexan shield to protect laboratory personnel should the windows fail.

Though the vessel was designed to accommodate turbulent flames, we have initially used only premixed laminar flames. The primary burner (Fig. 4.4) was constructed especially for us by McKenna Products, Inc. (Pittsburg, CA) and includes a 2.5 cm diameter, water-cooled, sintered bronze flameholder surrounded by a guard ring, also made of sintered bronze, for isolating the flame from the ambient gases. The principal advantage of the cooled bronze flameholder is that it affords a wide range of flow rates for which the flame remains attached to the burner without sustaining damage; additionally, the cooled plug provides a uniform boundary condition which results in a flat flame. Radial LIF measurements of the relative OH concentration at pressures to ~12 atm show that the flame is flat typically to within about ±10% (see Chapter 5). Originally we employed a similar McKenna burner using a stainless steel flameholder. This design was tried
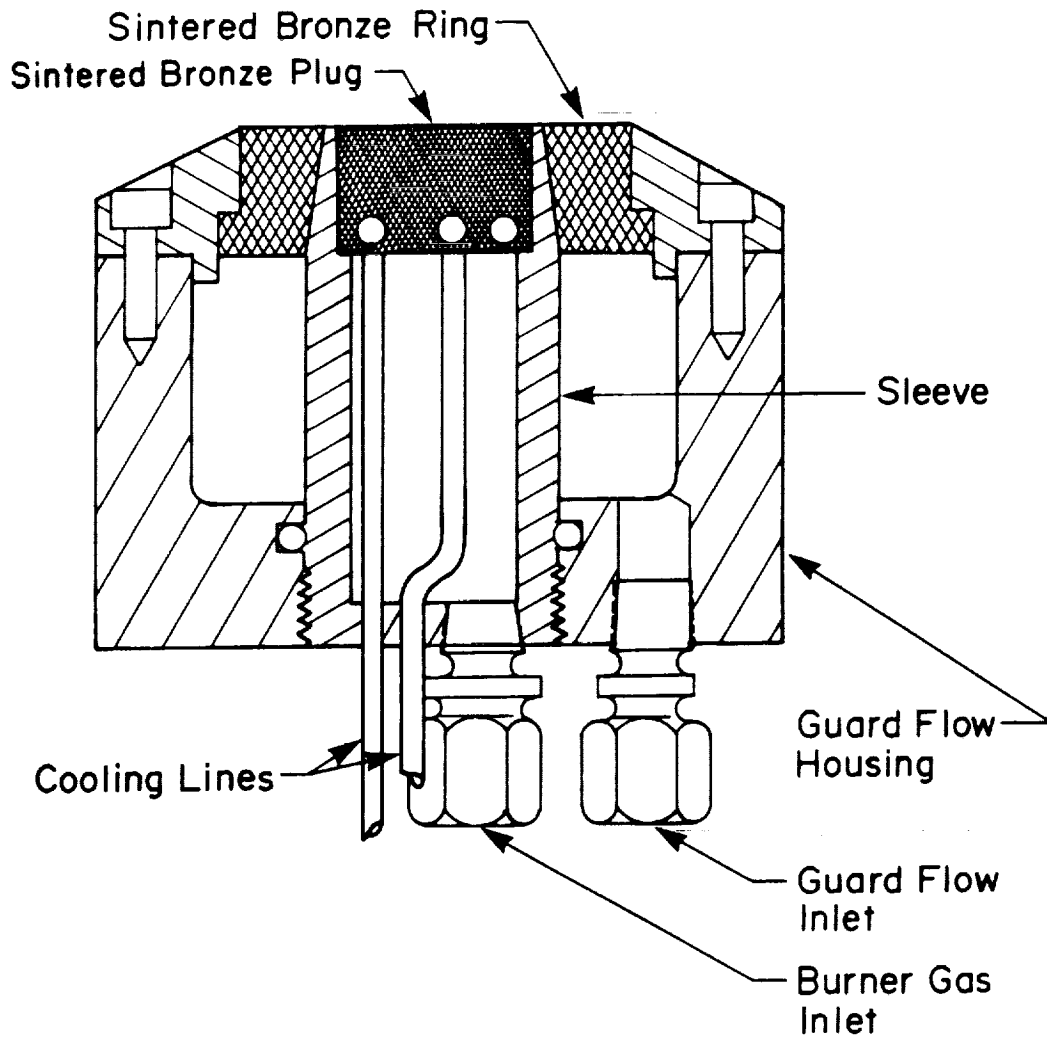
Figure 4.4   McKenna flat flame burner and guard flow housing.
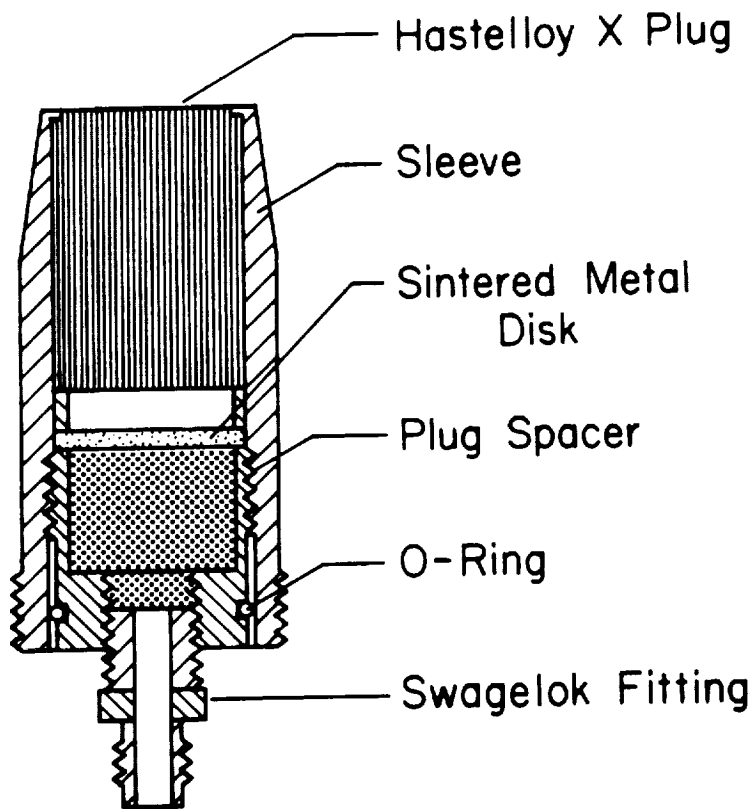
Figure 4.5   Hastelloy flat flame burner.

because a stainless steel plug was assumed to be more durable than the bronze plug; however, as a result of the low thermal conductivity of the stainless steel, the burner was easily damaged by the large heat fluxes which result at high flow rates of the fuel and oxidizer.

The secondary burner (Fig. 4.5) is similar in size and shape to the McKenna burner, but it uses an uncooled hexagonal-pattern plug made of Hastelloy X (a high-temperature, nickel-rich alloy manufactured by Kentucky Metals, New Albany, IN) for flame stabilization. The low surface area of this flameholder (as seen by the flame) makes cooling unnecessary; however, the flame can stabilize below the burner surface since the pore width (~0.8 mm) is not small enough to quench the flame. Though this burner was difficult to use because of its restrictive operating conditions, it did prove to be durable; an added advantage is that the large pore size of this flameholder would allow seeding of the flame.

A significant feature of the observed high-pressure premixed laminar flames is flame jitter--low frequency (~10 Hz) flame oscillations--the amplitude of which increases with pressure for a constant mass flow rate of the combustible mixture. Preliminary measurements at ~6 atm were made using a beam derived from a xenon arc lamp. The small-diameter (~1 mm) beam was first passed through the flame; the beam cross section was then rotated by 90° so that vertical disturbances such as flame jitter would deflect the beam along the horizontal axis. The beam was subsequently focused on the entrance slit of a monochromator, and the beam intensity (passed by the slit), which varied because of flame jitter, was sampled at 1 kHz. These measurements show that the amplitude increases, while the frequency of the oscillations decreases, with decreasing mass flow rate of the combustible mixture.

Flow rates of fuel, oxidizer, diluent, and bath (or guard-ring) gases are metered with four Linde flow control modules (models 15C, 14C, 16C, and 18C, respectively) and an associated Linde readout and control (ROC) box. For each module, a high-pressure regulator is used to control the inlet gas pressure, and a back-pressure regulator is used at the exit to limit the pressure drop. The ROC box is interfaced to an IBM PC-compatible microcomputer via RS 232 ports on the ROC box and the microcomputer, and a special communications program was written to control the flow streams (see Appendix A). In addition to displaying the set and read flow rates (and the vessel pressure), the menu-driven program includes options for (1) setting each flow stream, (2) zeroing all four streams or just the three streams for the flame, (3) making minor adjustments to individual streams or combinations of streams (e.g., fuel and oxidizer or fuel, oxidizer, and diluent), (4) automatically changing the equivalence ratio (according to a prescribed formula), and (5) automatically changing the flow rates of the combustible gases (according to a prescribed formula) in response to pressure changes. This last option is useful even with the McKenna burner since flame stability is enhanced by increasing, with pressure, the mass flow rate of the combustible mixture. We use a formula based on a description of adiabatic flame speed versus pressure of CH_4-air mixtures (Hjima and Takeno, 1986) to scale the mass flow rate of the combustible mixture.

The pressure within the vessel is controlled with a back-pressure regulator (Fairchild Industrial Products, Winston-Salem, NC), which is located on the exhaust line, far enough downstream of the vessel that the gases are sufficiently cool. Typically, during the course of a three-hour experiment, the vessel pressure was held to within 1% of the set point, with only occasional minor adjustments made to the regulator. Upstream of the back-pressure regulator on the exhaust line are a condenser

and water trap; thus, with this trap (and the one underneath the bottom flange), much of the water produced during combustion is eliminated from the pressure vessel. In parallel with this regulator is a valve that can handle large flow rates and can quickly depressurize the vessel. A high-pressure flame is obtained with the following procedure: (1) the burner is lit from an optical access port using a torch; (2) the port is then sealed, a bath-gas flow rate of 20 to 40 slpm is programmed, and the pressurizing option on the interfacing program is selected; and (3) the depressurizing valve is shut, and the back-pressure regulator is adjusted to the desired pressure.

4.1.3 Areas for Improvement

From our experience with the high-pressure combustion facility, we make the following suggestions for an improved design.

1. Using the condenser and water trap on the exhaust line, the water was effectively eliminated from the exhaust system; however, for the pressure vessel a drainage system should be designed to direct the water collecting on the interior surfaces to the trap beneath the bottom flange. This would ensure that the accumulation of water does not interfere with the operation of the burner or the electronic components. (To prevent water that condensed on the top flange from falling on the burner, we attached a steel plate to the burner housing about 15 cm above the burner.)

2. Though the optical translation stage used for horizontal movement is adequate for most purposes, it does exhibit significant side-play; for more accurate positioning of the burner, the current translation stage should be replaced by a system with reduced side-play (for instance a Newport model M-425-1S stage or a linear bearing/shaft arrangement).

3. The width of the burner guard ring (Fig. 4.4) should be reduced to allow a higher velocity of guard flow for the equivalent volumetric flow of gas. This becomes increasingly important at high pressures, since gas consumption can be large. Finally, for modelling purposes (i.e., providing a tractable boundary condition), the grain size of the

63

sintered bronze flameholder (~100 μm) should be reduced, since this dimension should be small compared to the flame stand-off distance (Ferguson and Keck, 1979).

4.2 Spectroscopic Equipment

4.2.1 Fluorescence Experiments

For the LIF experiments (Fig 4.6), the second harmonic (at 532 nm) of a Quanta-Ray DCR-3G Nd:YAG laser is used to pump a PDL-2 dye laser, which includes transversely-pumped oscillator and preamplifier stages along with a longitudinally-pumped amplifier stage. To produce UV radiation, the output of the dye laser is sent to a Quanta-Ray Wavelength Extender (WEX-1), where the light is frequency doubled; the active control circuit of the WEX is used to continuously adjust the angle of the doubling crystal to obtain the maximum doubled output. For the saturated fluorescence measurements (Chapters 6 and 7), we used the fast pulse option of the DCR-3G. A so-called fast pulse was obtained by adjusting the Q-switch delay (relative to the flash-lamp trigger pulse) while monitoring the laser output. A Q-switch delay was used that resulted in two principal temporal modes each about 3 ns in width. (An example of the average temporal dependence of the UV pulse is described below and shown in Fig. 4.10.)

To achieve high conversion efficiency of the 532 nm radiation, the dye laser uses a mixture of Exciton DCM and Sulforhodamine 640 (SR640) dyes. To obtain the optimum mixture, we used the following procedure.

1. Dye concentrations recommended by Quanta-Ray for the oscillator and the amplifier were prepared for both DCM and SR640.

2. Initially, only the DCM solutions were employed, with the PDL-2 lasing at the wavelength of interest (~620 nm).

3. The mixtures of SR640 for the oscillator and amplifier were then added to the DCM mixtures (separately, but for both the oscillator and amplifier) in 50 ml increments while monitoring the laser energy. This was continued for the oscillator and amplifier until in each case the laser energy peaked.

Using this procedure, we obtained a laser energy of about 95 mJ/pulse at 620 nm, with an input energy of about 380 mJ/pulse at 532 nm (an efficiency of ~25%).
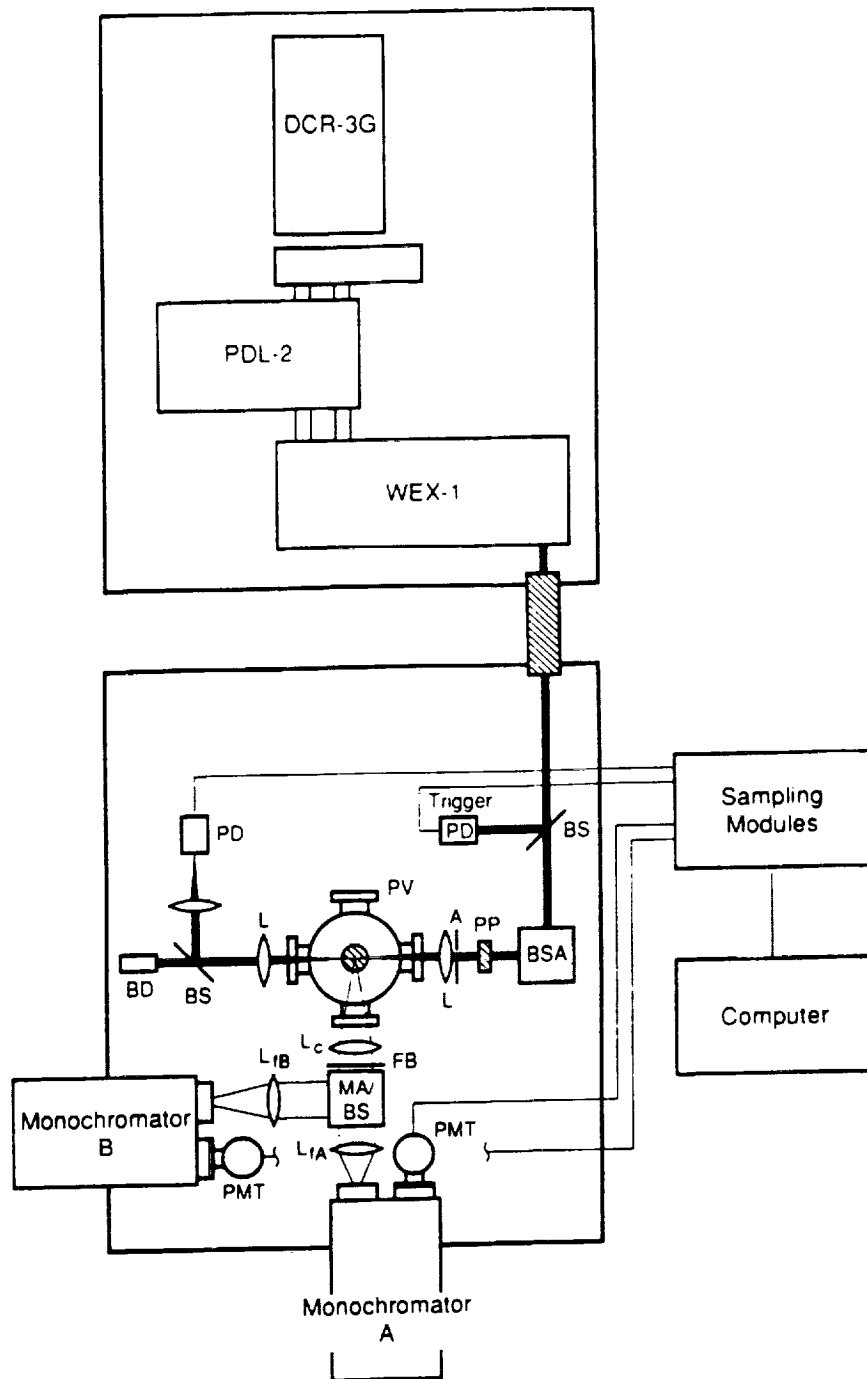
Figure 4.6   Schematic for LIF experiments. Components: A - aperture; BD - beam dump; BS - beam splitter; BSA - beam steering assembly; FB - fluorescence block; L - lens; MA - image rotating mirror assembly; PD - photodiode; PMT - photomultiplier tube; PP - Pyrex plate(s); PV - pressure vessel.
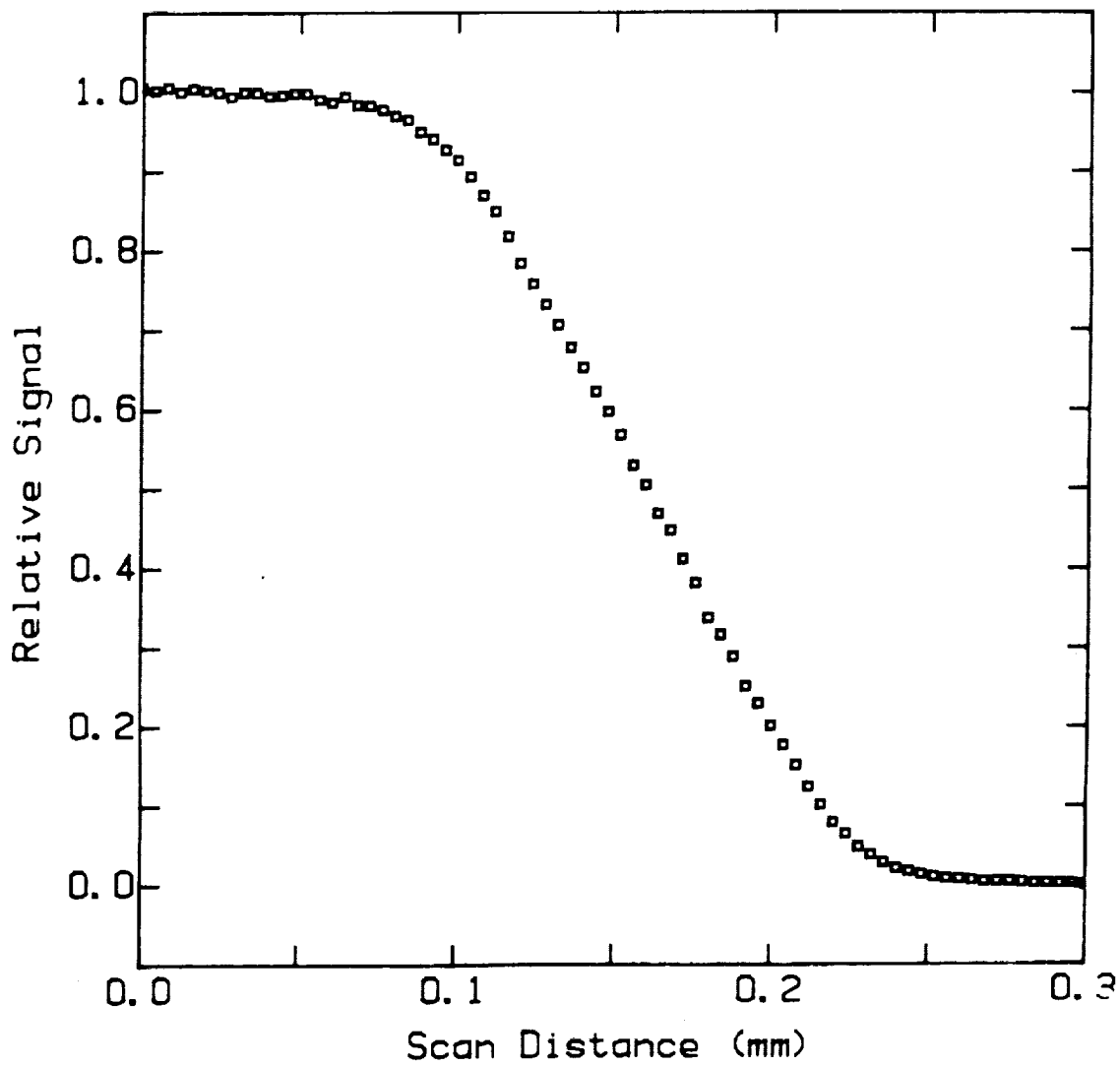
Figure 4.7   Integrated irradiance of UV beam measured by scanning a knife edge across the beam
at the focus.
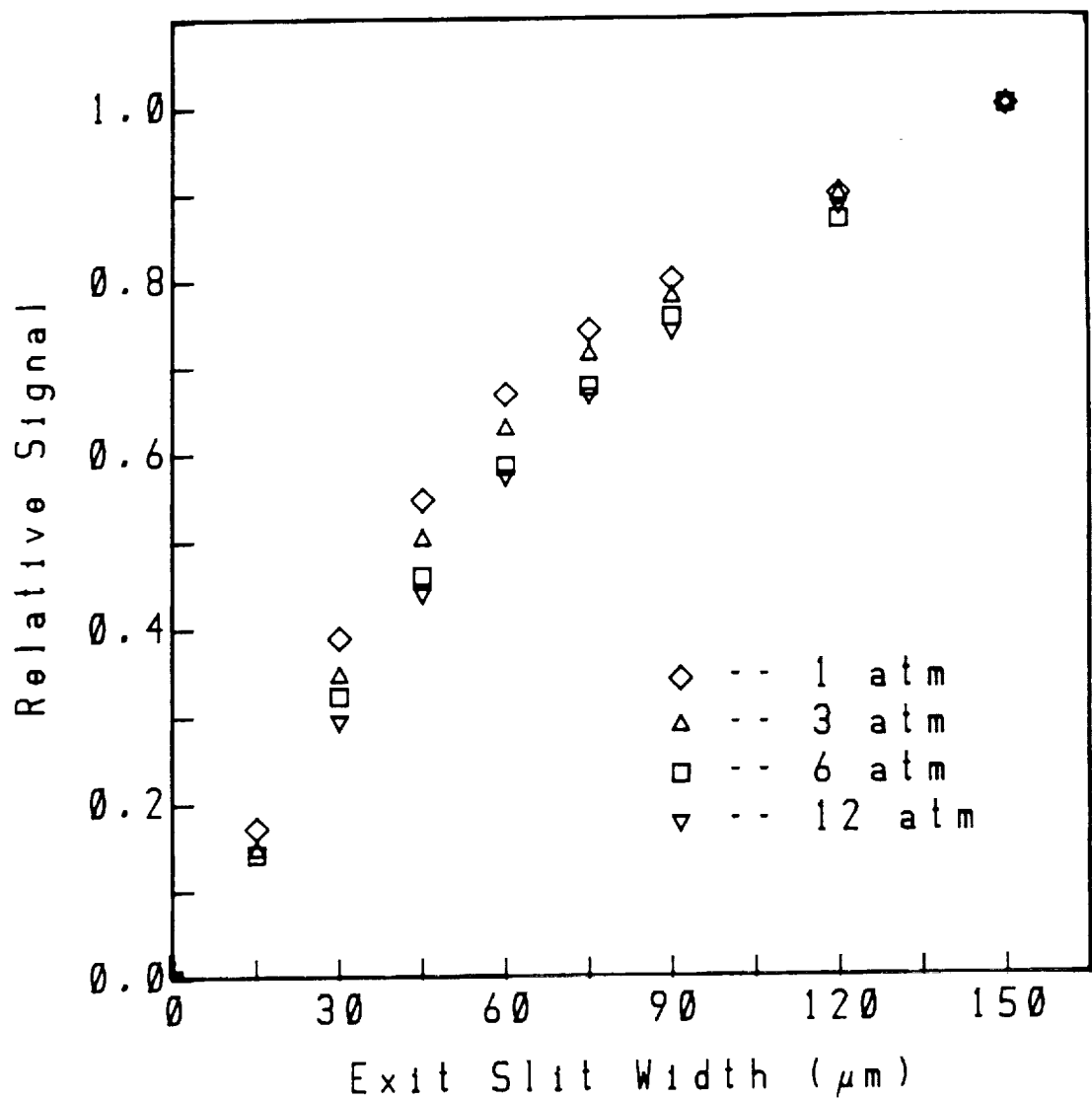
Figure 4.8   Dependence of fluorescence signal of monochromator B on exit slit width and pressure.

A Pellin-Broca prism was used in the WEX to disperse the visible and UV beams after the doubling crystal, and a small portion of either the visible or UV beam was then picked off and directed to the triggering photodiode with a fused silica beam splitter. The UV beam was raised to the appropriate height with a beam steering assembly; the resulting polarization of the radiation was vertical. The beam was attenuated when necessary with Pyrex plates and focused over the burner with a 250 mm focal-length fused silica lens. The approximate spot size of the UV beam over the burner was measured by scanning a knife edge across the focused beam--which had been attenuated with a Pyrex plate. The integrated beam irradiance, $I_{Ly} = \int_{-\infty}^{Y_0} \int_{-\infty}^{\infty} I_L(\hat{x}, \hat{y}) d\hat{x} d\hat{y}$, was then monitored with a photodiode, and an example of a scan is shown in Fig. 4.7. Though I_{Ly} shows good symmetry about the center line, we did observe some nonuniformity in $I_L(x,y)$, the irradiance distribution; at least part of the observed nonuniformity arises in the oscillator of the dye laser. Two additional factors which led to some nonuniformity in the UV beam were (1) slight damage to the doubling crystal and (2) damage to a 180° turning prism in the Quanta-Ray Prism Harmonic Separator (PHS) box (where the 1064 and 532 nm beams are separated).

Fluorescence was collimated with a second 250 mm focal-length lens. In experiments where two monochromators were used, the first reflector of the image rotating mirror assembly was a beam splitter, which allowed part of the fluorescence to pass to monochromator A. The remaining fluorescence was rotated by 90° (with a mirror assembly) and imaged on the entrance slit of monochromator B. Two Spex 3/4 m Czerny-Turner monochromators were used in the experiments: (A) a model 1700 which employed a grating blazed a 1 μm (and was used in third order); (B) a model 1800-II, which employed a grating blazed a 300 nm (and was used in first order). Monochromator B was converted from a spectrometer by fabricating a plate for mounting the exit slit; however, the exit plane was slightly off the position of the focal plane, and as a consequence the image of the entrance slit was blurred at the exit plane. To quantify this effect, the fluorescence signal was measured as a function of exit slit width for the pressures of interest: 1, 3.1, 6.1, 9.2, and 12.3 atm. The results for 1, 3.1, 6.1, and 12.3 atm are shown in Fig. 4.8; the effect of collisional broadening is to further broaden the spectral fluorescence profile, and in comparing the fluorescence signal at different pressures, this broadening must be taken into account.

To align the optics for fluorescence measurements, we devised a simple procedure which does not require opening the vessel (i.e., taking off any of the flanges). This scheme consists of the following steps.

1. In the lens-holding mounts outside the optical access ports, we place iris diaphragms. The lens holders are approximately centered with respect to the ports. The irises are then set at identical heights using a cathetometer (and closing the iris to mark the center).

2. We direct the (attenuated) UV beam through the laser entry and exit ports, using the irises to ensure that the beam passes through the center of both lens holders (and thus the lenses). Also, at this time we adjust the horizontal position of the lens holders to ensure that the beam passes above the center of the burner (when the burner is centered).

3. Through the opposite ports, we direct the beam from a He-Ne laser. The irises are again used to ensure that the beam is level and that it is passing through the center of both lens holders. To ensure the beam crosses the central chord of the burner, we again adjust the horizontal position of the lens holders. Finally, we align the fluorescence optics to so that the He-Ne beam strikes the center of each optic (including those in the monochromator).

By opening the monochromator slits and making only minor adjustments to the collection optics, particularly the collection and focusing lenses, we are then able to find a Rayleigh scattering or fluorescence signal (when the laser is at an appropriate wavelength).

The monochromators employed inexpensive photomultiplier tubes (RCA model 1P28B) specially-wired for fast response (Harris et al., 1976) for detection of the spectrally-resolved fluorescence signals. The average temporal response of each PMT was tested using Rayleigh scattering (Fig. 4.9). These waveforms can be compared to the average temporal signal obtained with a Texas Instruments TIED56 silicon avalanche photodiode (Fig. 4.10), which has a reported temporal response of ~200 ps (Harris et al., 1980). These waveforms were recorded by repetitively scanning in time over the signal, using the 200 ps sampling gate of a Stanford Research Systems fast sampler (SR255), and a scanning voltage supplied by the SR245 computer interface module. The data was then digitized and displayed with the SR245 using the SR265 software package, which also controlled the experiment. The average laser pulse shown in Fig. 4.10 has two temporal modes each with an ~2.5 ns FWHM; this average pulse was obtained consistently from day to day without
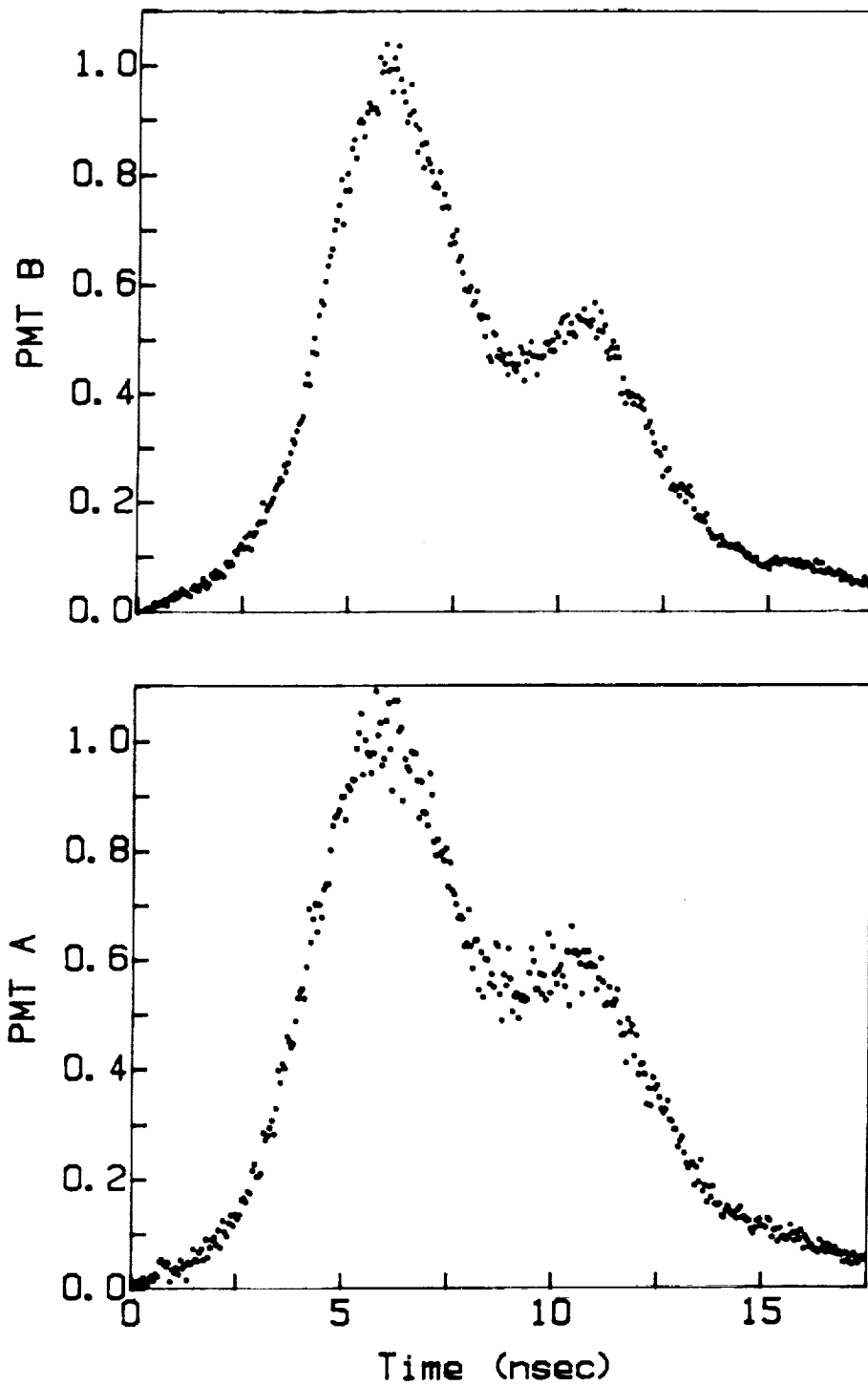
Figure 4.9   Average temporal response of PMT A and B to UV beam using Rayleigh scattering;
the profiles are averages of 45 (PMT A) and 30 (PMT B) temporal scans.
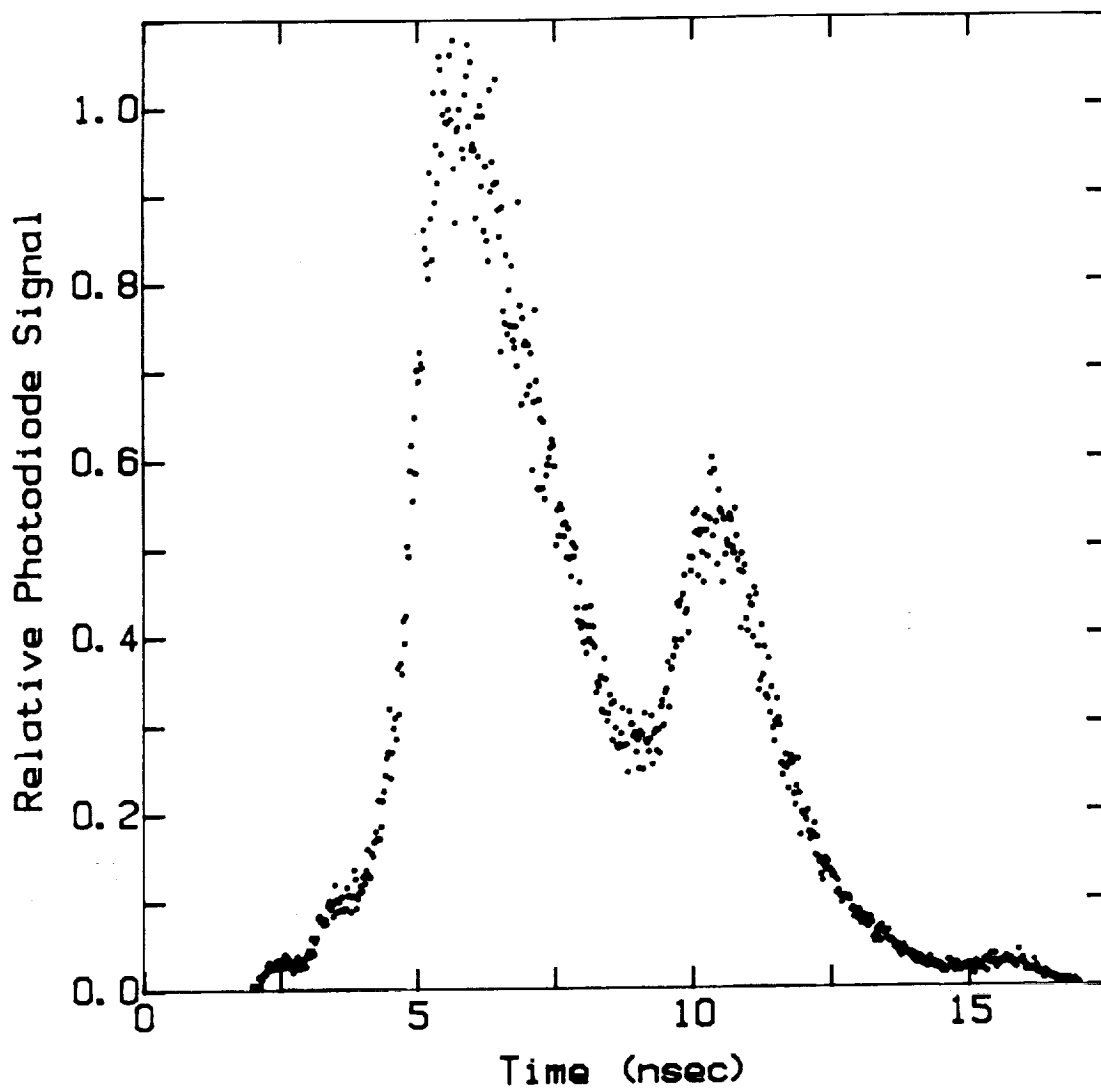
Figure 4.10   Average temporal dependence of the UV beam irradiance measured with silicon avalanche photodiode; the profile is the average of 10 temporal scans.

additional adjustment of the Q-switch delay. Both PMTs, which used a 1000 V supply voltage, show good temporal resolution (Fig. 4.9), though the slower response (compared to that of the fast photodiode) does result in distortion of the waveform.

The linearity of the PMTs and the respective circuits was determined using a Rayleigh scattering signal, which was attenuated with calibrated neutral density filters. The attenuation was progressively decreased, and the subsequent signal was recorded; the results (Fig. 4.11) show that both PMTs have a linear range of about 0.5 V or greater.

In addition to the aforementioned PMTs and fast photodiode, two silicon UV-sensitive PIN photodiodes (Hamamatsu S17722-02) were employed to (1) trigger the detection electronics and (2) monitor the shot-to-shot UV beam energy. These photodiodes were not fast enough to resolve the temporal features of the UV pulse, and consequently they were used only to record the laser energy per pulse rather than the peak laser power. However, because of their large sensitive area, these photodiodes were especially valuable when it was necessary or helpful to measure the integrated beam irradiance (e.g., in the experiment where the knife edge was scanned across the beam). The monitoring photodiode was also used to level and position the burner relative to the laser beam. For both exercises, an aperture in front of the focusing lens can be used to ensure that the beam width is small and approximately constant while crossing the burner. To level the burner, the burner is first translated upward to partially obscure the beam and then translated from side to side while adjusting its tilt; it is considered level when the photodiode signal is approximately constant as the burner is translated horizontally. To find the zero vertical position, the burner is first positioned to totally block the beam. It is then moved downward until the signal at the photodiode is half the unblocked value; this is then recorded on the computer as the zero vertical position of the burner. Though vertical fluorescence profiles taken consecutively (under the same conditions) show little or no shift, the zero position typically varied 50 to 100 μm from day to day.

The PMT and photodiode signals were recorded with gated integrators; for the saturated fluorescence experiments, each PMT signal was resolved with the 200 ps sampling gate of a Stanford Research Systems SR255 fast sampler, which was temporally centered at the peak of the fluorescence pulse using an SR200 gate scanner. The voltage output from the SR255 was then digitized and stored with the SR245 computer interface module and the SR265 software package.
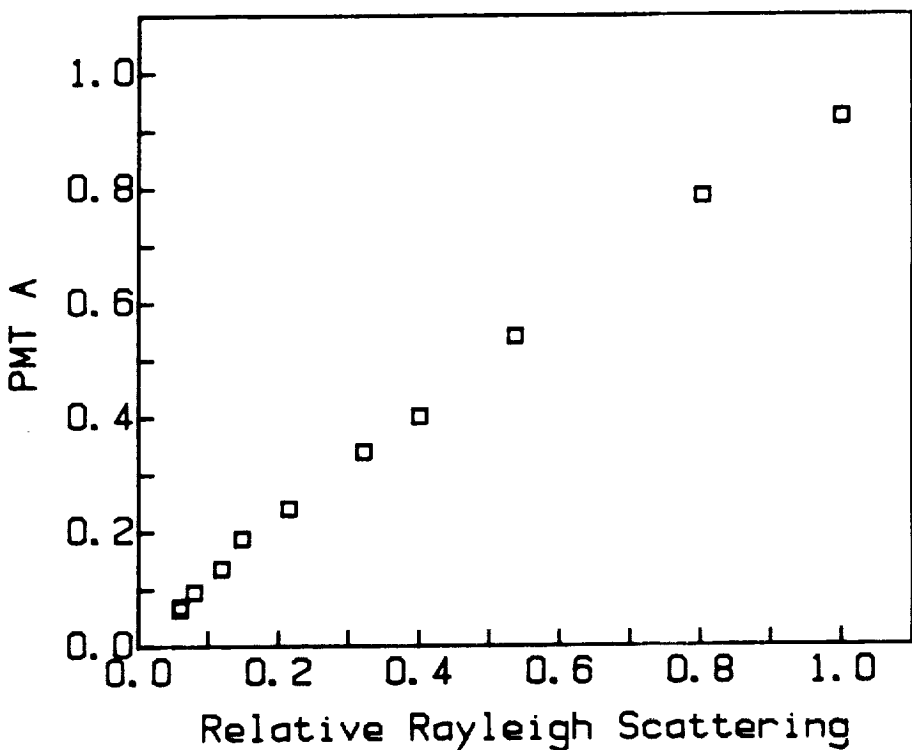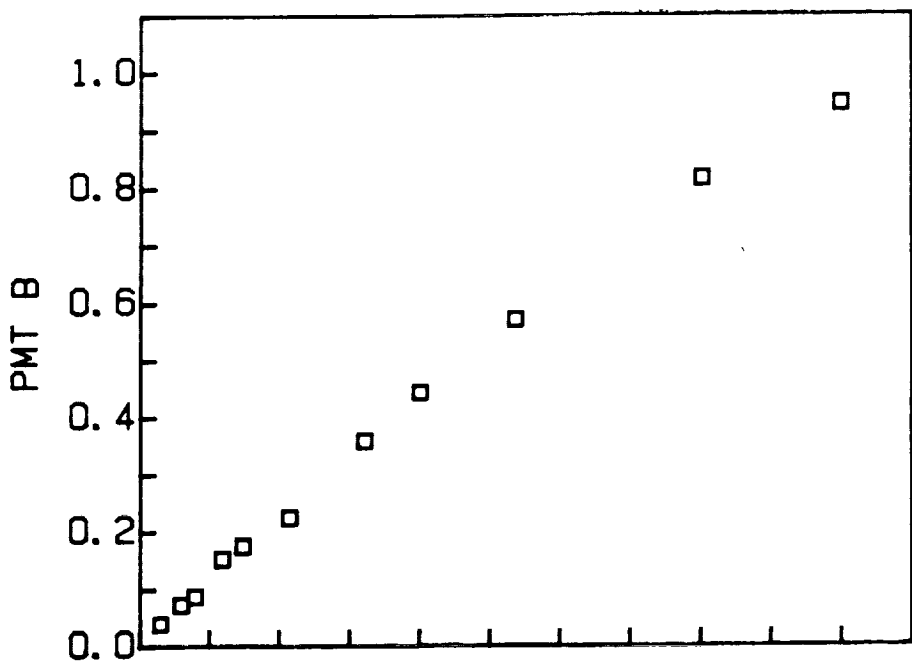
Figure 4.11   Linearity of PMT circuits A (top graph) and B (bottom graph).

For both the monitoring photodiode and the PMTs, when wide-band temporal detection was desired (Chapter 5), we used the SR250 gated integrator and boxcar averager; sampling gates greater than 2 ns could then be selected for detection of the signal.

One of the modifications made to the SR265 software includes a stepper motor interface package. The package consists of two parts: the first, which was written in FORTRAN to be compatible to the SR265 software, displays the menu options; the second communicates with the motor translators through a digital I/O card. This entailed sending to the motor translator box an 8-bit word, specifying the motor and step direction; this section was written in the C programming language for greater speed. Some of the features of the package are listed below.

1. The user can move any motor connected to the two translator boxes. (Up to 16 motors can be addressed.)

2. The user can access a file (supplied by the user), which contains information on the motors and number of steps (for each motor) to be moved after each scan. (A scan is defined as a set of samples taken by the SR245 computer interface.)

3. The user can access a memory file, which keeps track of motor positions relative to a specified zero. A menu command also allows the user to send the motor to its zero position with the backlash of the system automatically removed.

4. The user can specify a motor and the number of steps to be moved after each sample recorded by the SR245 module. Additional options allow the user to (1) reverse the direction of the motor on each subsequent scan (to backtrack over the motor's path) or (2) move the motor back to its zero position before each subsequent scan (so that the scans can be averaged point by point, for example).

The last option is useful in experiments for which one wants to synchronize the movement of a stepper motor with data collection. It can be employed, for example, in scanning (1) a knife edge across the laser beam, (2) the monochromator grating for collection of absorption or fluorescence spectra, and (3) the grating of the dye laser for collection of excitation spectra. The principal limitation with this setup is the maximum stepping frequency of about 200 steps/s; however, this is not a significant limitation for many experiments.

4.2.2 Absorption Experiments

Figure 4.12 shows a schematic of the optical layout for the absorption experiments. The output of a 150-W xenon arc lamp plus two lenses and two apertures were used to produce a collimated beam, which was directed over the center line of the burner; apertures were also used after the burner to minimize detected flame emission. By scanning the burner through the beam, the average beam width was determined to be less than about 200 μm. A Spex 3/4 m monochromator, with a grating blazed at 1 μm (monochromator A described above), was used in 3rd order to resolve the absorption spectra. Spectral scans were obtained by using a specially-designed gearbox (employing an anti-backlash worm gear arrangement) with a 50:1 gear ratio in conjunction with a stepper motor (Slo-Syn Model M061-FD02, which has a single-step resolution of 1.8°). This design--which also included a damper to reduce vibration, especially noticeable at low stepping frequencies--allowed good spectral resolution. Typically, a complete absorption scan consisted of 21000 or 28000 data points (3 or 4 scans each of 7000 points--a limit imposed by the SR265 program). Each scan began before the $P_1(2)$ line (Dieke and Crosswhite, 1962) and ended beyond the $Q_1(15)$ or $P_1(10)$ line (see Table 4.1). Each data point is the result of 30 boxcar samples, using the built-in exponential averager to average individual samples. The computer interface module was then set to sample 1 in 60 boxcar triggers (with a command in the SR245 routine), thus resulting in some correlation (albeit a small one) between consecutive data points. Figure 4.13 gives an example of a typical scan from an atmospheric-pressure flame.

The transmitted light was measured with a PMT using a supply voltage of 700 V; this signal was processed with the SR250, using an enlarged sampling gate of 75 μs (the gate, normally limited to 15 μs, was enlarged by adding a capacitor to the sampling circuit of the SR250 module). The PMT output was connected directly to the SR250 input, which has an input impedance of 1 MΩ, and the boxcar output voltage was tested for a linear dependence on the beam intensity using calibrated neutral density filters to attenuate the beam. Ideally, however, one would use a current-to-voltage conversion circuit to prevent loading of the PMT circuit.

A significant increase in the signal-to-noise ratio of the absorption measurements was obtained by repetitively scanning over a portion of the spectrum and averaging the individual scans. This was accomplished by sending the monochromator stepper motor to its zero position after each scan--which was done automatically by selecting the appropriate option in the motor interface menu. Multiple scans could then be run, and the SR265 routine would continually average the

75
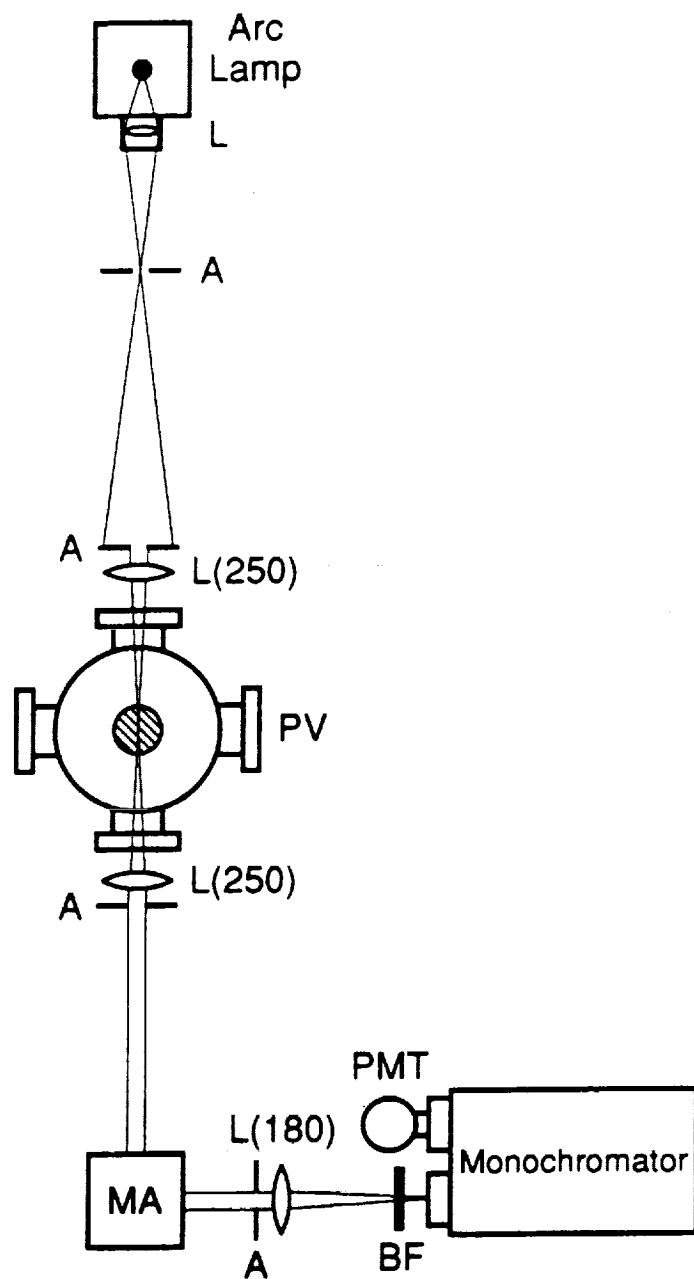
Figure 4.12   Schematic of absorption experiments. Components: A - aperture; BF - bandpass filter; L - lens; MA - image rotating mirror assembly; PMT - photomultiplier tube; PV - pressure vessel.
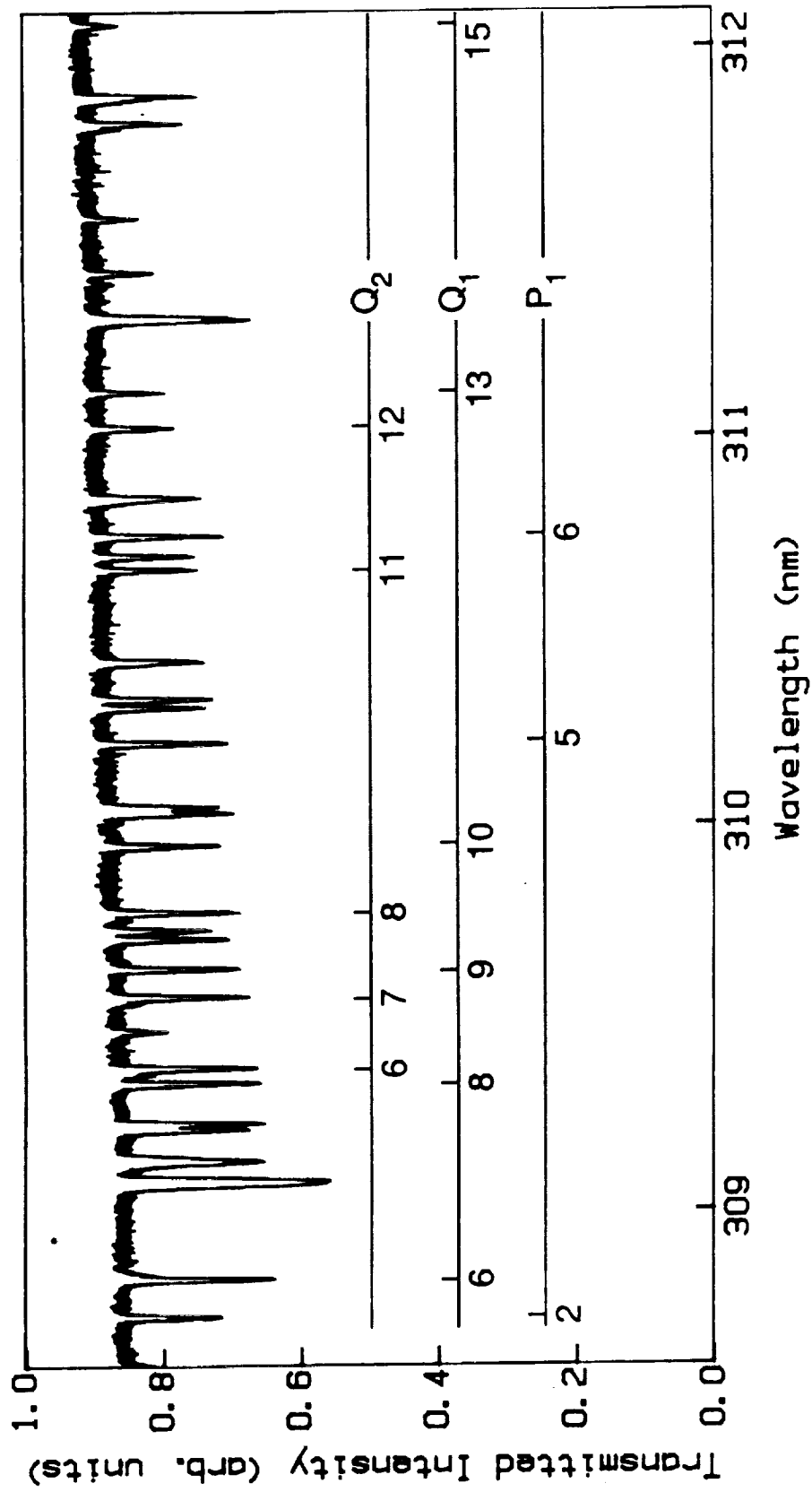
Figure 4.13   Sample absorption spectrum taken in an atmospheric-pressure flame. Identified are the lines that were typically used in the absorption analysis.

Table 4.1 Lines used in absorption analysis.

Line	Wavelength (nm)
$P_1(2)$	308.729
$Q_1(6)$	308.824
$Q_1(8)$	309.329
$Q_2(6)$	309.369
$Q_2(7)$	309.552
$Q_1(9)$	309.624
$Q_2(8)$	309.773
$Q_1(10)$	309.949
$P_1(5)$	310.213
$Q_2(11)$	310.657
$P_1(6)$	310.745
$Q_2(12)$	311.024
$Q_1(13)$	311.113
$Q_1(15)$	312.058
$P_1(9)$	312.485
$P_1(10)$	313.119

results of the current scan with previous scans. An example from an atmospheric-pressure flame is shown in Fig. 4.14, where two profiles of the strong $Q_1(6)$ line are shown: one, a single scan and the other the average of 5 consecutive scans. Typically, the only observable tracking error occurred in going from the first to the second scan; the remaining scans accurately followed the second scan.

To aid in data reduction of the absorption spectra, we again modified the SR265 software package to integrate the absorption profiles; this included the following steps.

1. The user selects a portion of the spectrum that includes the line or lines of interest from the main window containing, for example, a 7000-point scan; this section of the spectrum is then removed to a second window.

2. Control is transferred to the second window, and the user is prompted to make measurements of the baseline by bracketing the region with two cursors.
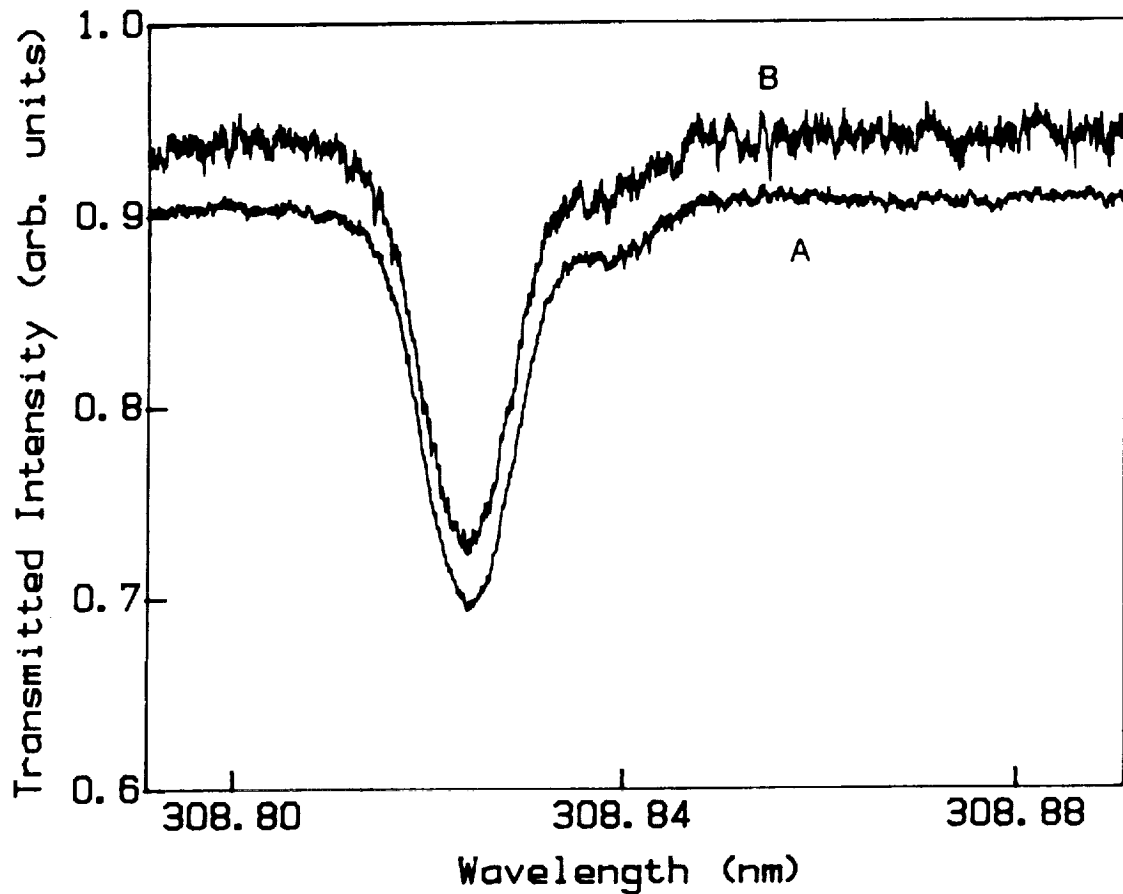
Figure 4.14   Example of improved signal-to-noise ratio in an absorption spectrum obtained by repetitively scanning over the $Q_1(6)$ line in an atmospheric-pressure flame; also included in the scan is the $Q_{12}(6)$ satellite transition. The multiple-scan profile (A), which is the average of 5 consecutive scans, has been offset from the single-scan profile (B) for convenience.

3.   The user is then prompted to make the absorption measurement by again bracketing the region of the spectrum with the two cursors; the program calculates the absorption integral, using the trapezoidal rule.

4.   Finally, control is returned to the main window and the user is prompted to exit the analysis loop or select another portion of the spectrum.

With this software, analysis of absorption spectra is fast and accurate. In particular, with this approach one does not rely on the triangular approximation [i.e., approximating the profile as a triangle (Lucht, 1978; Salmon, 1986a)] for integration of absorption profiles. For this approximation

79

to be valid, (1) the convolution of the transmission functions of the entrance and exit slits should approximate a triangular function, (2) the width of this function should be much greater than the transition linewidth, and (3) the linewidth should have only a small fraction of its total absorption in the wings of the profile. Consequently, while the triangular approximation can be accurate for a predominantly Doppler-broadened profile, its accuracy will decrease with increased collisional broadening.

After having obtained the integrated absorption, the number densities were calculated employing a FORTRAN routine, which *solved* the absorption equation (see Appendix B) using the curve-of-growth method (Lucht, et al., 1978) and fit the data to a Boltzmann curve with a nonlinear least squares algorithm (Salmon, 1986a). The routine also gives the 95% confidence interval for the two parameters, temperature and number density; typical uncertainties for the temperature and number density were 30 to 50 K and 5 to 10%, respectively.

CHAPTER 5

LASER-INDUCED FLUORESCENCE MEASUREMENTS OF OH
IN LAMINAR $C_2H_6/O_2/N_2$ FLAMES AT HIGH PRESSURE

5.1 Introduction

Measurements of flame species by optical methods, such as laser-induced fluorescence (LIF), have proved valuable in elucidating chemical and physical processes occurring in combustion environments (Eckbreth, 1988). Until recently (Edwards et al., 1987; Felton et al., 1988), most work using LIF has been done in low-pressure (≤ 1 atm) flames, though most combustors of practical importance operate at high pressure. Since the width of the flame front decreases with increasing pressure, physical probes are even more likely to perturb the flame front; hence, utilization of optical methods may be a necessity for many high-pressure studies. Such measurements could prove useful for the study of a broad range of topics including (1) turbulent flames, (2) engine knock, (3) pollutant formation (e.g., soot and NO production), and (4) flame extinction and stability. While high-pressure turbulent combustion environments allow analysis of the complex interaction between chemistry and the flow field, high-pressure laminar environments should also have an important role: allowing the study of pressure-dependent flame chemistry. Thus, we have examined laminar flame structure at high pressure using relative LIF measurements of the OH molecule. We describe fluorescence profiles at 4 pressures--3.2, 6.3, 9.5, and 12.6 atm--in flat premixed $C_2H_6/O_2/N_2$ flames, and we discuss problems associated with high-pressure LIF measurements.

5.2 Experimental Apparatus

Our combustion facility, which is designed for study of high-pressure flames by spectroscopic methods (Chapter 4), includes the following: (1) a pressure vessel constructed from standard stainless steel piping components (Fig. 5.1); (2) an electronic gas delivery system, which is interfaced to a microcomputer; (3) a sintered bronze water-cooled burner (2.5 cm in diameter, constructed by McKenna Products, Inc, Pittsburg, CA), which we used without the guard ring to

allow better optical access to the flame; and (4) an internal x-y burner translation system employing stepper motors. The range of movement of the vertical and horizontal translation mechanisms is about 11 and 2.8 cm, respectively, while the associated single-step resolution is about 2 and 1 μm, respectively. Because the motors are stepped through a microcomputer, we can accurately position the burner.

The optical layout for the LIF experiment is shown in Fig. 5.2. The Quanta-Ray PDL-2 dye laser is pumped by the frequency-doubled output of a Quanta-Ray DCR-3G Nd:YAG laser; to produce UV radiation, the output of the dye laser is sent to the Quanta-Ray Wavelength Extender (WEX-1), where the laser light is frequency doubled. The dye laser is normally tuned to the $Q_1(8)$ transition (λ = 309.3 nm) of the $A^2\Sigma^+$-$X^2\Pi(0,0)$ band (Dieke and Crosswhite, 1962); this line was chosen for excitation because the Boltzmann fraction of the lower rotational level varies by only 10% over a temperature range of 1000-2600 K (Lucht et al., 1984). For this experiment, the pulse width and repetition rate of the dye laser were ~8 ns and 10 Hz, respectively.

A small portion of the UV beam is first picked off with a quartz beam splitter and sent to a UV-sensitive photodiode which produces the signal used for triggering the detection electronics. The beam is then raised to the appropriate height with a beam steering assembly; the resulting polarization of the radiation is vertical. The beam is attenuated if necessary with Pyrex plates and then focused over the burner with a 250 mm focal-length fused silica lens giving a focused spot size of ~100 μm. For this experiment, the laser energy after attenuation was ~1 mJ/pulse. With the resulting laser power and the small spot size, we observed partial saturation of the transition, particularly when using a small temporal sampling gate (e.g., 200 ps). Using saturation spectroscopy was not our intention for this experiment, however, and we report further on the saturation behavior of OH at high pressure in Chapters 6 and 7. After leaving the exit port, the beam is collimated, and another portion is picked off and focused on a pinhole aperture in front of a second UV-sensitive photodiode. This photodiode allows us (1) to assess laser power fluctuations and beam steering and (2) to level and position the burner relative to the laser beam. Though vertical fluorescence profiles taken consecutively (under the same conditions) show little or no shift, the zero position typically varied 50 to 100 μm from day to day.

The OH fluorescence is collected with a 250 mm focal-length collimating fused silica lens through a port adjacent to the beam entrance and exit ports; the optical access ports have a limiting f-number of about f/9. The laser axis of the fluorescence sampling volume is then rotated from horizontal to vertical with two mirrors, and the fluorescence is focused on the entrance slit of a Spex
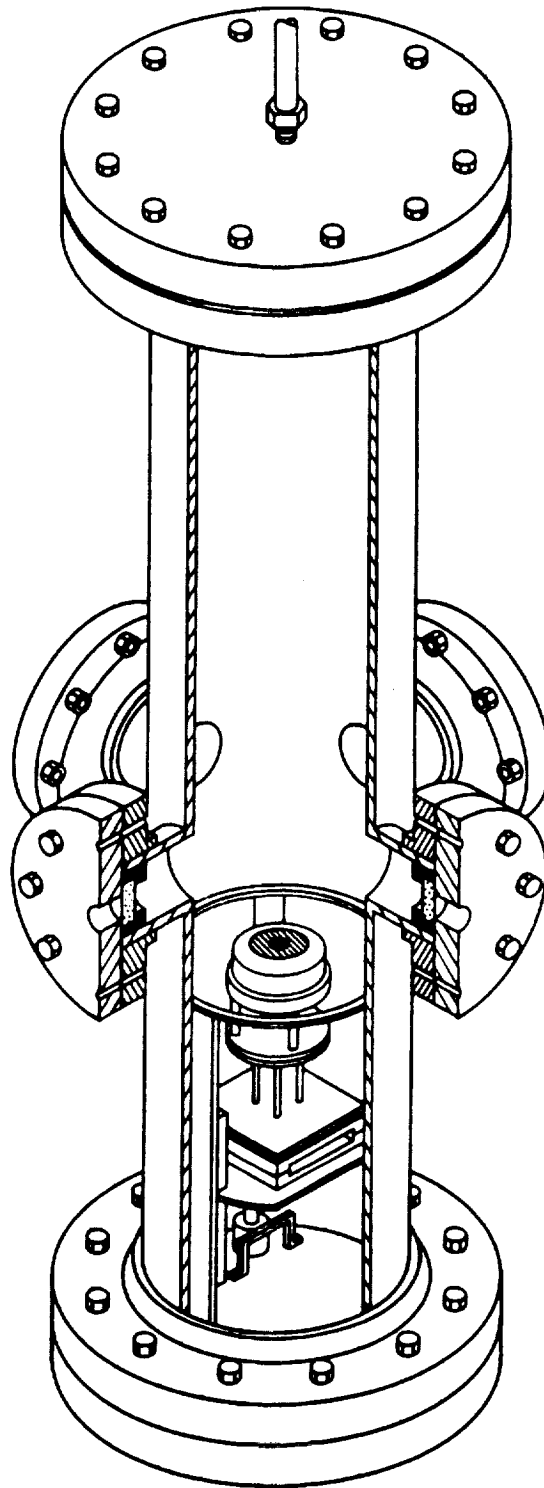
Figure 5.1   Cutaway view of pressure vessel and associated components.
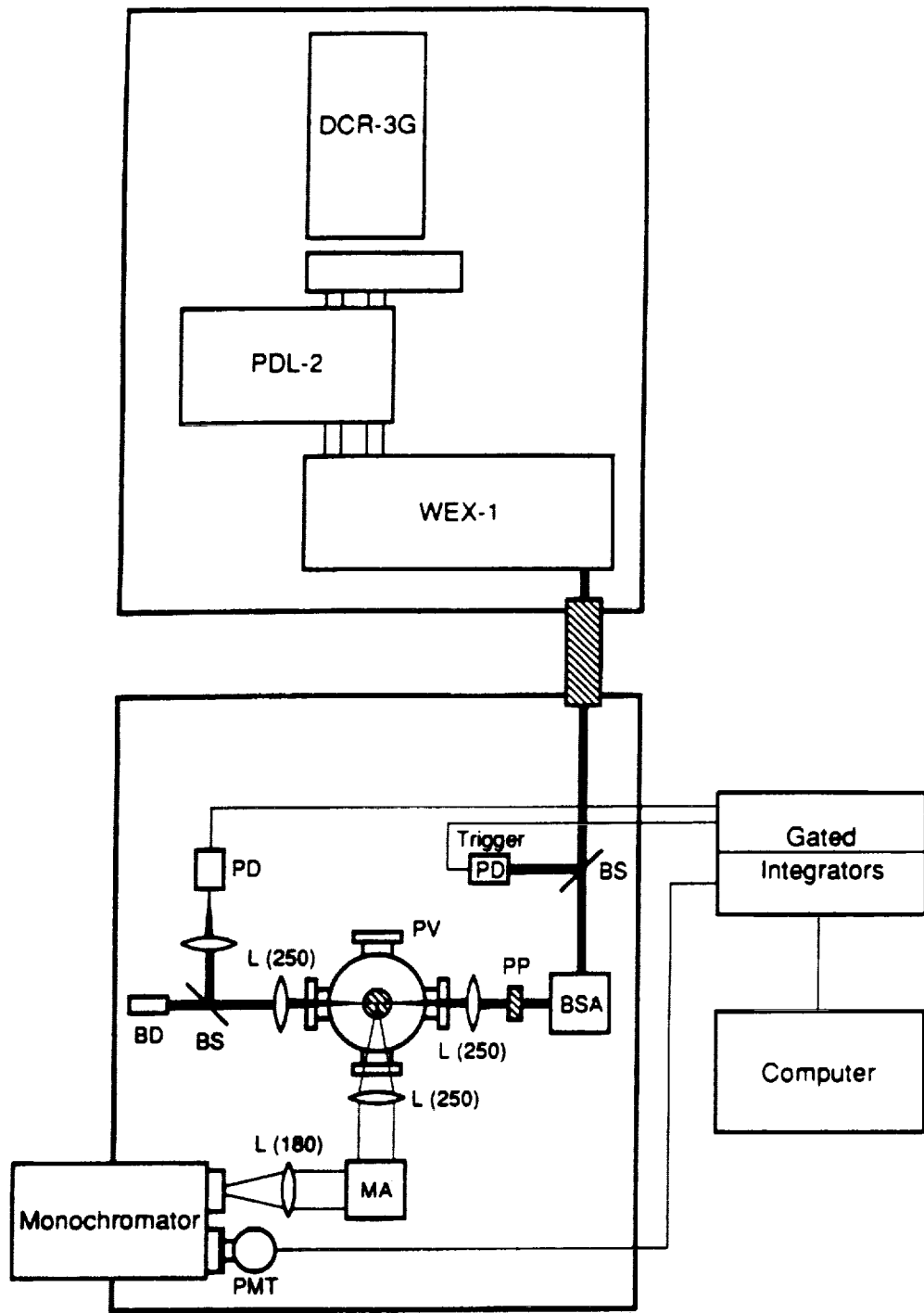
Figure 5.2   Schematic of LIF experiment. Components: BD - beam dump; BS - beam splitter; BSA - beam steering assembly; L - lens; MA - image rotating mirror assembly; PD - photodiode; PMT - photomultiplier tube; PP - Pyrex plate(s); PV - pressure vessel.

3/4 meter monochromator. The fluorescence signal is then detected with an RCA 1P28B photomultiplier, and the resulting electronic signal along with the photodiode signal are processed with two Stanford Research Systems SR250 gated integrators using sampling gates of 6 and 10 ns for the photomultiplier and photodiode signals, respectively (the wider gate for the photodiode reflecting its slower response). The data is then digitized and stored on an IBM PC using the Stanford Research Systems SR245 computer interface and the SR265 software package, which we modified to allow programmed movement of the stepper motors.

5.3 Results and Discussion

A significant feature of the high-pressure flames we observed is flame jitter--low frequency (~10 Hz) flame oscillations--the amplitude of which increases with pressure for a constant mass flow rate of the combustible mixture. We also noticed a reduction in flame noise when using a guard flow (Matsumoto et al., 1982); however, this surrounding flow did not eliminate the flame jitter observed at high pressures. Measurements of the jitter intensity and frequency at 6.3 atm were made using a small-diameter beam produced from a xenon arc lamp. The beam was passed through the flame, and its cross section was rotated by 90° so that vertical disturbances such as flame jitter deflected the beam along the horizontal axis. The beam was subsequently focused on the entrance slit of a monochromator, and the intensity was sampled at 1 kHz. The measurements showed that the amplitude increases, while the frequency of the oscillations decreases, with decreasing mass flow rate of the combustible mixture.

The flame jitter was reduced by placing a screen about 8 mm above the burner surface. We note, however, that the problem of flame jitter is exacerbated by the increase in the index of refraction with pressure; as a result, the laser beam is more likely to be steered away from the fluorescence collection window (as defined by the monochromator entrance slit) at high pressures by fluctuations in the gas density. A similar problem is encountered with spatial gradients in the refractive index: the beam can be displaced relative to the fluorescence collection window as it moves through the flame. This effect was indeed observed near the flame front (where the temperature gradient is large) of these high-pressure flames. The problem is perhaps ameliorated by the one-dimensional geometry of the flame, at least insofar as the laser beam and the entrance slit image are displaced by the same amount. Even when the beam and slit image do not suffer relative displacement, a refractive index gradient can still lead to a spatially distorted LIF profile.

Rather than collecting fluorescence from the entire $(v'=0, v''=0)$ band we used a monochromator to isolate appropriate transitions. Although this approach gives a lower fluorescence signal, it has two advantages: (1) self-absorption can be reduced through selection of the detected line; and (2) detection of Rayleigh scattering or scattering from the burner surface can be eliminated. Though this method proved satisfactory, perhaps a better excitation/detection scheme for our conditions would include (1,0) excitation and (1,1) wide-band detection (Laurendeau and Goldsmith, 1989). In addition to satisfying the criteria of minimal self-absorption and detected scattering, this method does not require a monochromator, thus yielding a higher fluorescence collection efficiency.

We now make the following observations regarding the effect of collisions on our relative fluorescence signals. When rotational equilibrium--that is, steady state of the relative populations of the rotational levels--in the $A^2\Sigma^+(v=0)$ state of OH is established, the ratio of population in the directly-excited rotational level to that in the neighboring rotational levels is insensitive to gas composition and temperature (Smith and Crosley, 1981; Zizak et al., 1986). Thus, we expect that the fluorescence collected from the directly-excited rotational level will be as insensitive to the collisional environment as fluorescence from the entire (0,0) band. In addition, we expect some change in the quenching rate at constant pressure through the reaction zone and from flame to flame insofar as the concentration of quenching species and temperature change. However, as shown in two previous experiments, over the range of mixture ratios and temperatures expected, this variation in electronic quenching may not be large. First, Stepowski and Cottereau (1981), using three low-pressure C_3H_8/O_2 flat flames (equivalence ratios 0.55, 1.0, and 1.25), showed that for a given flame, the net electronic quenching of OH is approximately constant from the burnt-gas zone to below the luminous region. Also, at a constant height above the burner, the variation in quenching rate among the three flames was within about 20% of the maximum value (which was found in the stoichiometric flame). Second, Schwarzwald et al. (1988) measured electronic quenching rates of OH in atmospheric-pressure CH_4/air flat flames (equivalence ratios from 0.77 to 1.43). Not surprisingly, the electronic quenching was approximately constant in the burnt-gas region ($y = 0.5 - 20$ mm) of each flame; in addition, at a constant height ($y = 20$ mm), there was no discernable difference in quenching over the range of equivalence ratios studied.
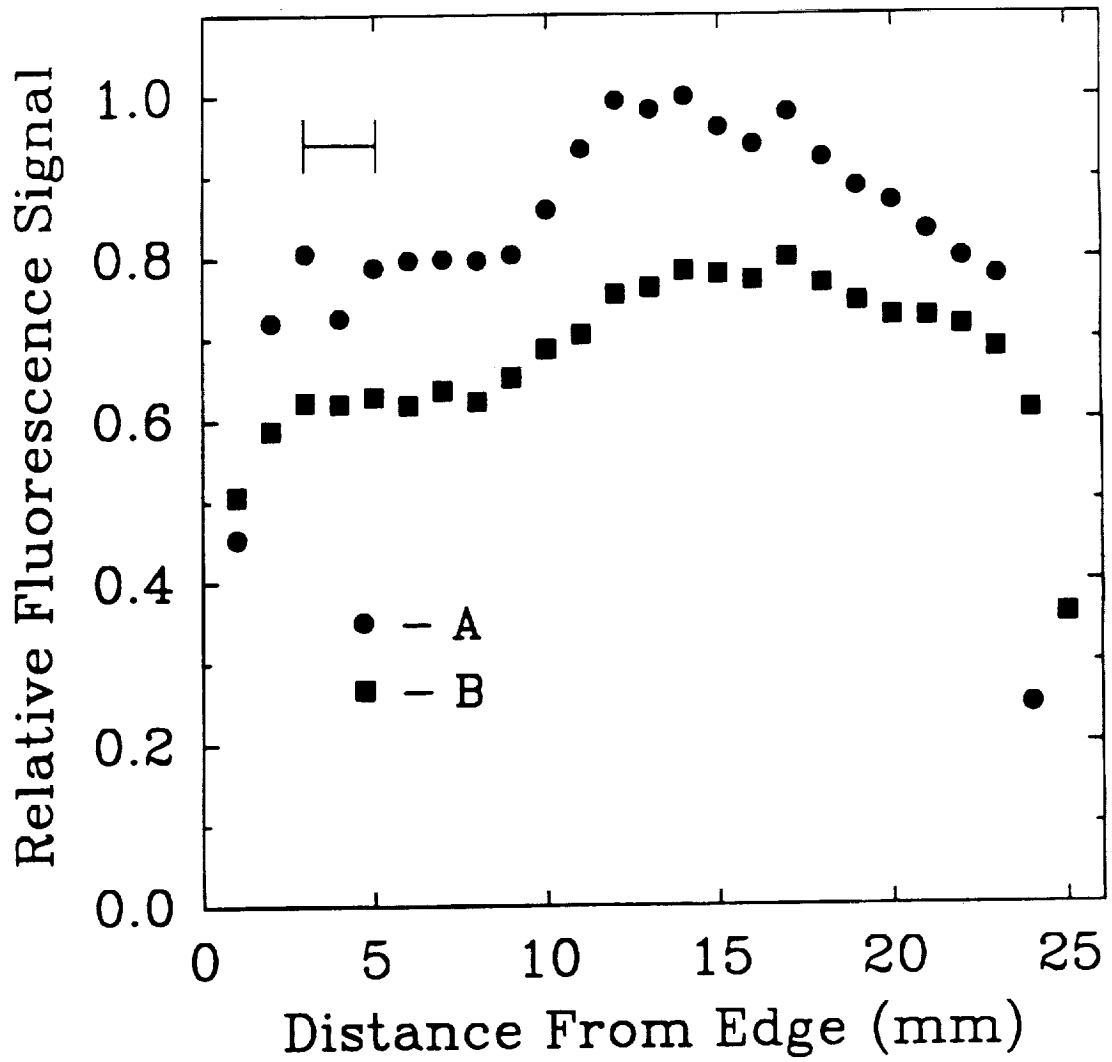
Figure 5.3 Horizontal fluorescence profiles 1.5 mm above the burner at (A) 12.6 and (B) 3.2 atm obtained by detecting the $O_{12}(10)$ transition. The bracketed region denotes the range of horizontal locations for the vertical profiles in Figs. 5.4-5.9.
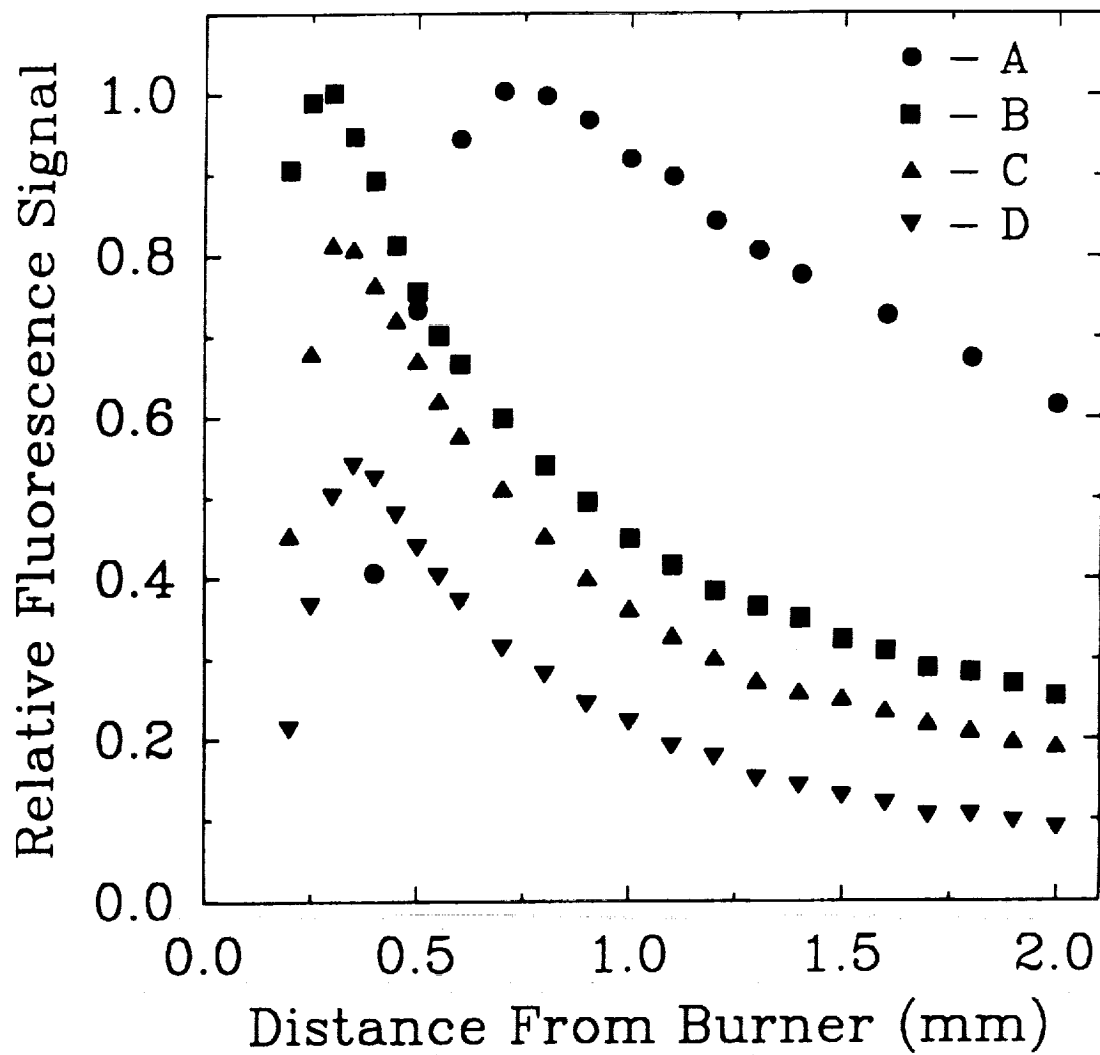
Figure 5.4   Vertical fluorescence profiles at 3.2 atm. Flow rates of $C_2H_6/O_2/N_2$ (slpm): (A) 0.16/0.75/2.2 (1 atm); (B) 0.29/1.17/3.87; (C) 0.23/0.95/3.42; (D) 0.20/0.87/3.11.
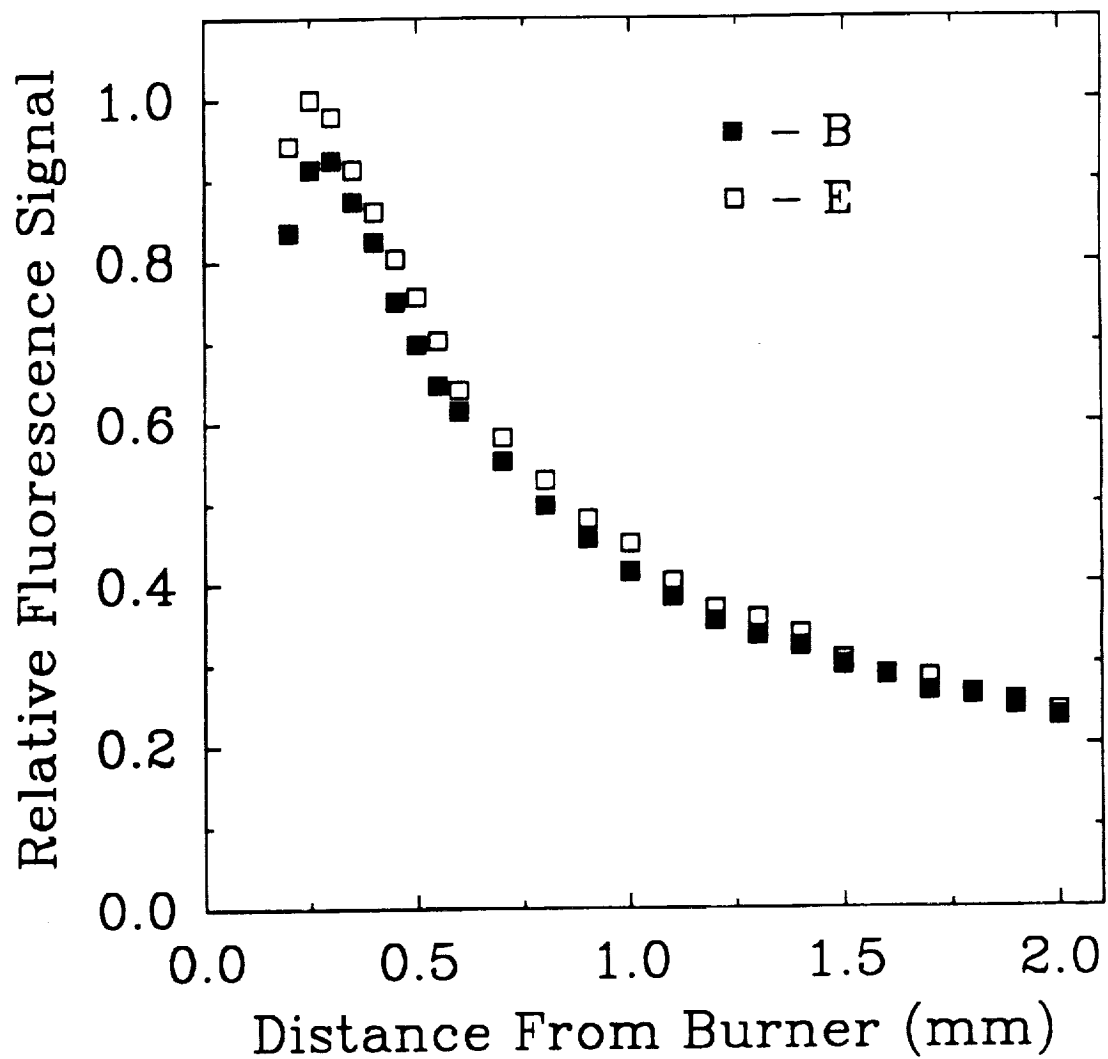
Figure 5.5   Vertical fluorescence profiles at 3.2 atm. Flow rates of $C_2H_6/O_2/N_2$ (slpm): (B) and (E) 0.29/1.17/3.87.

C-2

For each of the following vertical fluorescence profiles, the monochromator was tuned to detect the $P_1(9)$ transition ($\lambda = 312.5$ nm). The entrance and exit slit widths were 30 μm, while the entrance slit height was 2 mm; the resulting spatial resolution is about 42 μm by 2.9 mm, and the theoretical spectral resolution is 0.03 nm. For all measurements shown below, each data point is the average of the fluorescence signal from 600 laser shots. Because self-absorption of the $P_1(9)$ fluorescence was evident in atmospheric-pressure flames, the burner was positioned horizontally such that the laser probe was at the near edge of the flame (about 3-5 mm from the edge of the burner). With this approach, we can reduce the effect of self-absorption on the relative profiles, and we can probe closer to the burner without blocking portions of the fluorescence signal. Normally, we did not probe closer than $\sim$0.35 mm above the burner surface; when measurements closer to the surface were desired, we blocked the lower half of the fluorescence cross section to eliminate vignetting of the fluorescence profile. Using this method, we probed to within $\sim$0.2 mm above the burner. In addition, the flames examined were lean, ranging in equivalence ratio from about 0.54 to 0.94.

Though monitoring the $P_1(9)$ line was satisfactory for the vertical fluorescence profiles, for horizontal profiles the monochromator was tuned to the $O_{12}(10)$ line ($\lambda = 316.5$ nm); this line has a much lower absorption cross section (Dimpfl and Kinsey, 1979), and thus fluorescence from this line is not significantly affected by self-absorption. Figure 5.3 shows typical horizontal fluorescence profiles (which have been scaled for convenience) in the burnt-gas region ($y = 1.5$ mm above the burner) for flames at 3.2 and 12.6 atm. At this height in these flames, the OH concentration gradient is small; consequently, the monochromator slits were opened to 140 μm (for the measurement at 3.2 atm) and 200 μm (at 12.6 atm) to collect more photons per laser shot. Though the fluorescence was primarily from the $O_{12}(10)$ line, the $P_2(14)$ and the $P_1(15)$ lines--which are about equidistant from the $O_{12}(10)$ line--give a small contribution to the total signal. At both pressures, the profiles show a rise in the fluorescence signal at about 1 cm from the burner edge; this nonuniformity, which was always observed in the horizontal profiles, probably results from a defect in the burner design or construction. In addition, at 12.6 atm, the photodiode signal decreased near the far edge of the flame, indicating that the beam was suffering some displacement; the sharp drop in fluorescence at this edge suggests that beam steering was also distorting the relative concentration profile.

Vertical profiles of the relative OH concentration at 3.2 atm are shown in Figs. 5.4 and 5.5; profiles B through D were taken consecutively and are compared to profile A from an atmospheric-pressure flame. At this pressure over a range of flow rates, we were able to probe within the flame reaction zone, where much of the interesting chemistry takes place; we were aided in this effort by our ability to probe very close to the burner surface. For adequate resolution near the flame front of the high-pressure flames, the burner was translated ~50 μm after each data point; away from the flame front the data points are separated by ~100 μm. Comparison between the atmospheric profile and those at 3.2 atm shows, as expected, a significant reduction in the flame thickness (Williams, 1985). Because the flow rates of fuel and oxidizer are below the values at which the minimum stand-off distance is obtained, a decrease in their flow rate increases the stand-off distance (Ferguson and Keck, 1979; Chao and Law, 1988); decreasing the N_2 diluent flow rate, however, has the opposite effect. With the changes in flow rates we find a decrease in the fluorescence signal. At least part of this reduction is probably due to the lower flame temperature [which we would expect from a reduction in the C_2H_6 and O_2 flow rates (Ferguson and Keck, 1979)] and the concomitant decrease in equilibrium and superequilibrium OH; note, however, that a decrease in temperature could also lead to an increase in electronic quenching of the excited OH (Garland et al., 1986; Jeffries, et al., 1988) and hence a decreased fluorescence yield. An additional effect of reducing the flow rate of the mixture is that the diameter of the flame decreases slightly; consequently, when sampling near the edge of the burner, the flame position can change with respect to the probe volume. This may have happened with profile D, where the fluorescence signal is lower than expected in comparison to profiles B and C.

After the completion of each profile, the burner was translated back to the initial position (y = 0.2 mm), with the backlash from the translation system first being removed, and the next set of measurements was begun. Figure 5.5 demonstrates the repeatability of the measurements; curves B and E, which have the same flow rate, were taken consecutively. The small decrease in signal from flame E to B probably results from drift of the laser wavelength from the peak absorption wavelength.

Vertical OH fluorescence profiles taken consecutively in flames at 6.3 atm are shown in Figs. 5.6 and 5.7. With large reductions in the C_2H_6 and O_2 flow rates (and a smaller reduction in the N_2 flow rate) the flame front moves away from the burner; thus for profiles C and D the reaction zone is observable. Profiles A, B, and C were taken consecutively, while profile D (Fig. 5.7) was recorded two days later under the same conditions as C to assess its repeatability. For these measurements,

91
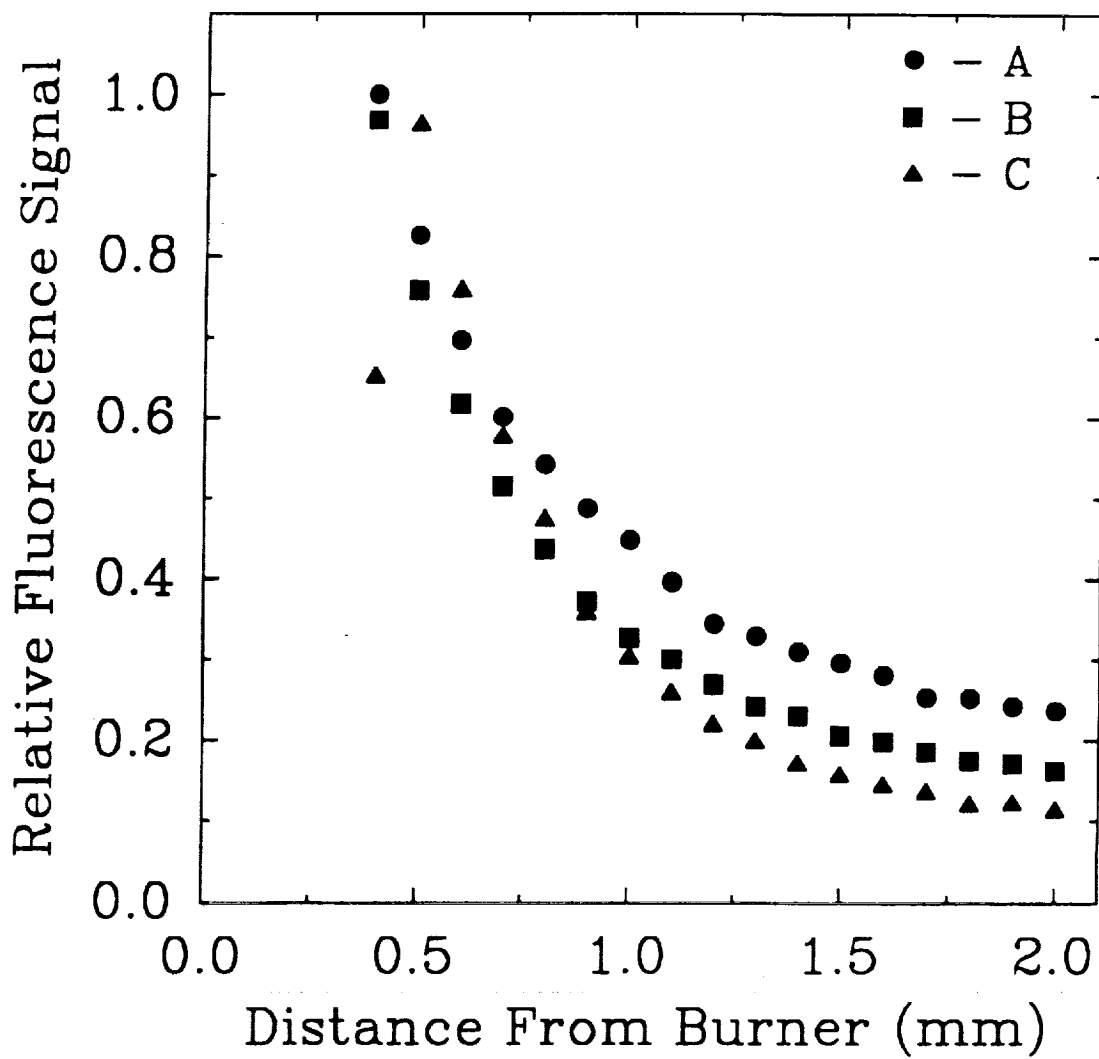
Figure 5.6   Vertical fluorescence profiles at 6.3 atm.   Flow rates of $C_2H_6/O_2/N_2$ (slpm):   (A) 0.38/1.46/6.38; (B) 0.29/1.17/5.63; (C) 0.20/0.86/4.92.
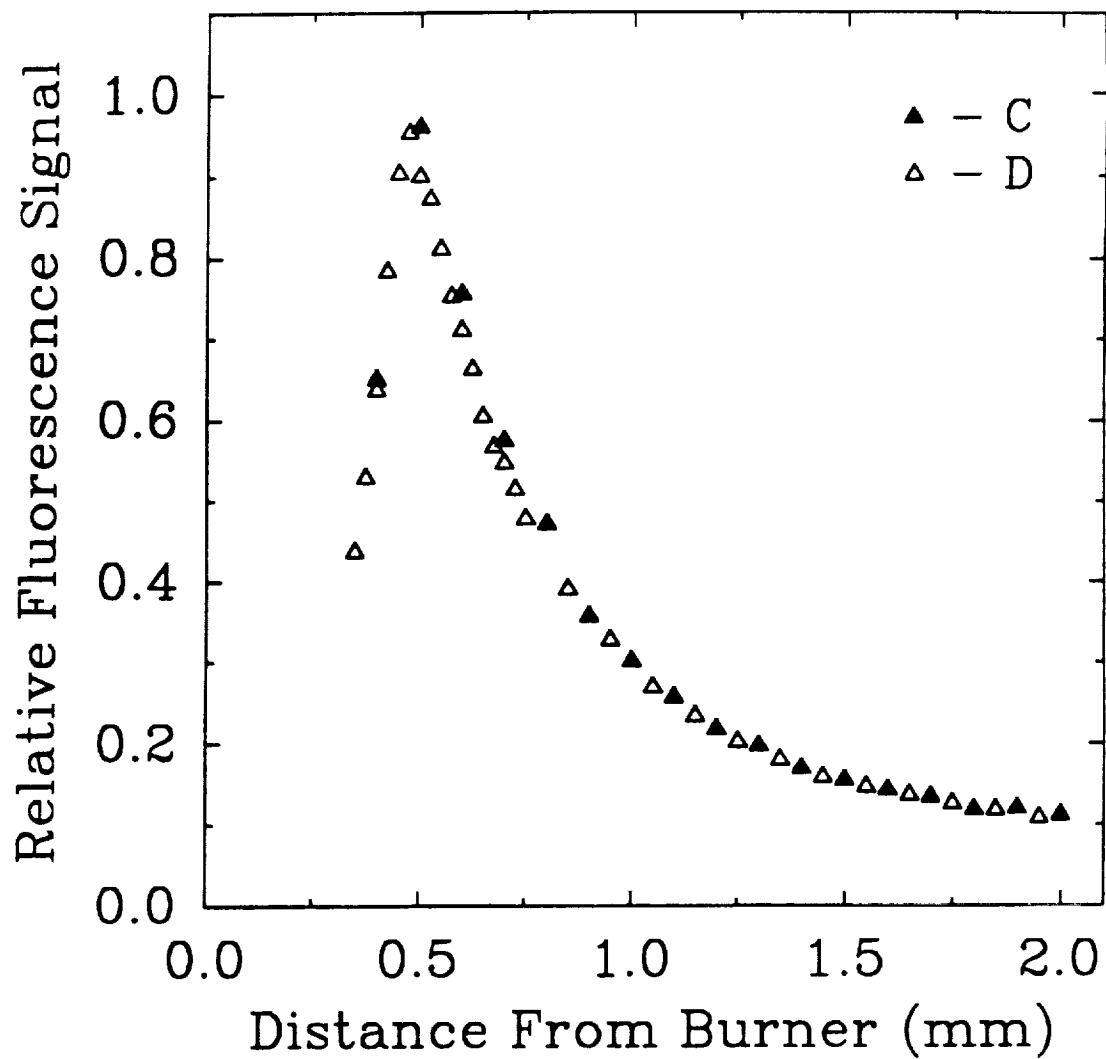
Figure 5.7   Vertical fluorescence profiles at 6.3 atm. Flow rates of $C_2H_6/O_2/N_2$ (slpm): (C) and (D) 0.20/0.86/4.92.
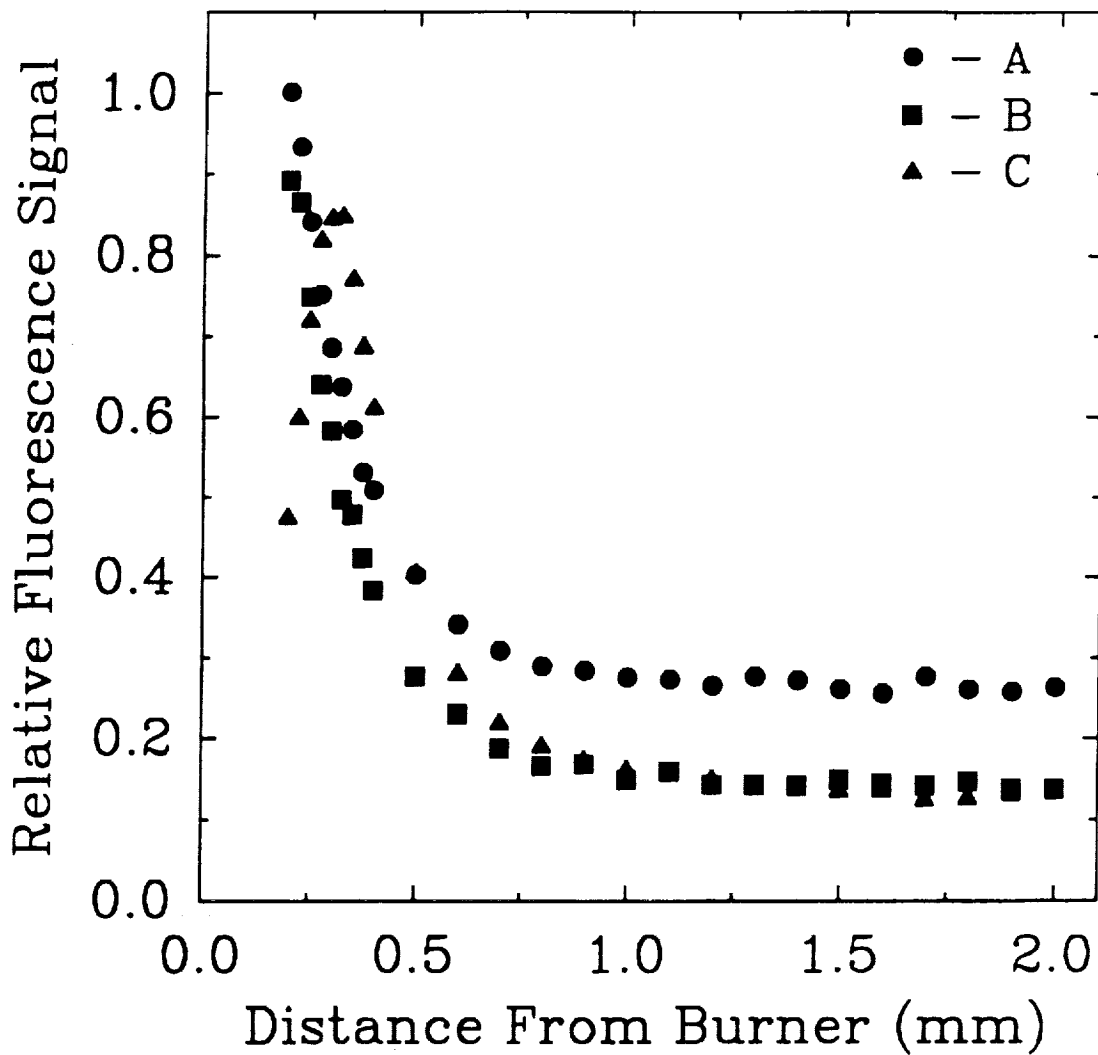
Figure 5.8   Vertical fluorescence profiles at 9.5 atm.   Flow rates of $C_2H_6/O_2/N_2$ (slpm):   (A) 0.54/3.12/10.3; (B) 0.40/2.58/8.06; (C) 0.40/2.58/8.85.
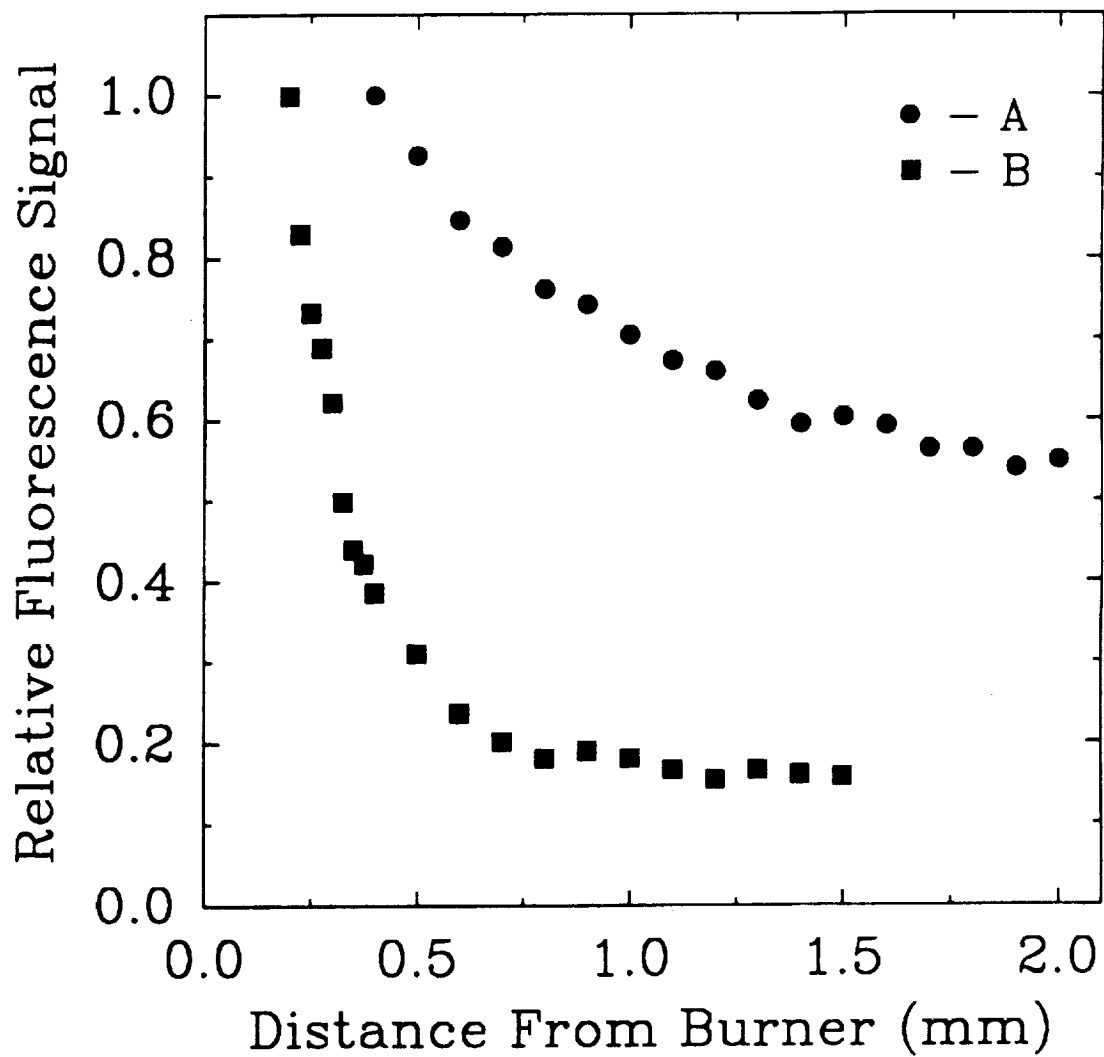
Figure 5.9   Vertical Fluorescence profiles at 12.6 atm.   Flow rates of $C_2H_6/O_2/N_2$ (slpm):   (A) 0.65/2.43/12.2; (B) 0.43/2.20/7.94.

the collection cross section was not blocked; thus the initial height above the burner for profiles A, B, and C is 0.4 mm. For profile D in Fig. 5.7 the initial height is 0.35 mm, and the first 17 points are separated by only ~25 μm. Near the flame front, the shot-to-shot noise of the fluorescence signal for profiles C and D was larger than would be expected from Poisson statistics; this undoubtedly is due in part to the large gradients of temperature and concentration in this region. As noted above, we did observe some displacement of the beam relative to the sampling window. We have made no attempt in these measurements, however, to quantify or remedy this effect.

Profiles from flames at 9.5 atm, which were taken on the same day (with profiles B and C taken consecutively), are shown in Fig. 5.8. Starting with flame B we attempted to probe the reaction zone by slightly increasing the diluent flow rate; the result is shown as profile C. At these conditions, further increase in the diluent flow rate resulted in a wrinkled flame, indicating that the flame was near its blow-off limit. As with measurements at 3.2 atm, the collection cross section was blocked and an initial height of 0.2 mm was used; furthermore, the initial 9 data points are separated by ~25 μm. As expected, flames B and C, differing only slightly in the diluent flow rate, have similar levels of OH in the burnt-gas region. (The flame temperature will decrease with increasing diluent flow, but only weakly since the flame will stabilize further from the burner where its conductive heat loss is less.) As was observed in profiles C and D at 6.3 atm, the noise in the fluorescence signal (for all 3 profiles) at 9.5 atm was significant below about 0.5 mm, where the [OH] gradient is very large. Because of the higher net reaction rate at greater pressure, equilibration also occurs at smaller distances from the burner surface (e.g., < 1.5 mm for OH).

In Fig. 5.9, we show the OH measurements for 2 flames at 12.6 atm; the profiles, which were taken on separate days, have been scaled for convenience. With B the fluorescence cross section was blocked, while for A it was not. As expected, the larger flow rate acts to spread out the recombination zone. These profiles also point to a limitation of this particular burner; the flame stand-off distance may be on the order of the grain size of the sintered metal (~100 μm). Finally, the flames became increasingly unstable with increasing pressure; because we sought quiescent conditions in which to make LIF measurements, this is the highest pressure at which we chose to take data. Nevertheless, higher pressure flames were easily obtained with the McKenna burner.

5.4 Summary

We have presented measurements of relative OH concentration using the LIF method in flat laminar, lean premixed $C_2H_6/O_2/N_2$ flames at 3.2, 6.3, 9.5, and 12.6 atm. At these pressures, we

have measured vertical fluorescence profiles over a range of flow rates of the combustible mixture and have demonstrated that in some cases the reaction zone can be probed. In comparison to atmospheric-pressure flames, we observed that at high pressure the reaction zone was small and accordingly vertical gradients of temperature and concentration could be very large (in the reaction zone, as well as in the recombination zone). One result of the large gradients was an increase in the noise of the fluorescence signal even from small flame disturbances. An impediment to making measurements in these experiments was beam steering (of the laser beam relative to the fluorescence collection window), which arose from flame oscillations and increased with pressure. Because we were interested in making measurements under steady, laminar conditions, we chose not to make measurements in flames above 12.6 atm.

CHAPTER 6

SATURATED FLUORESCENCE MEASUREMENTS OF THE HYDROXYL
RADICAL IN LAMINAR HIGH-PRESSURE $C_2H_6/O_2/N_2$ FLAMES

6.1 Introduction

Measurements of flame species by optical methods, such as laser-induced fluorescence (LIF), have proved valuable in elucidating chemical and physical processes occurring in combustion environments (Eckbreth, 1988). Fluorescence measurements are relevant to the study of a broad range of practical combustion topics including turbulent flames, engine knock, pollutant formation, and flame stability. Linear fluorescence methods are particularly useful for turbulent flames, where 2-D images of *relative* species concentrations can yield insight into the complex interaction between chemistry and the flow field. In comparison, laser-saturated fluorescence (LSF), which is currently limited to point-wise or perhaps 1-D measurements, is attractive because it can provide reliable *absolute* species concentrations. Moreover, unlike linear fluorescence, LSF measurements are insensitive to the rate coefficients for both laser excitation and collisional de-excitation. As a consequence, *in situ* calibration of the fluorescence signal is not necessary: a calibration factor determined in one flame (through techniques such as Rayleigh scattering or absorption) can more easily be applied to other flames where calibration is more difficult or perhaps impossible [e.g., turbulent or sooting flames (Lucht et al., 1984, 1985; Drake et al., 1984, 1985)].

Since LSF was first proposed as a combustion diagnostic (Piepmeier, 1972a; Daily, 1977), it has been used to detect the diatomic molecules C_2 (Baronavski and McDonald, 1977; Mailander, 1978), MgO (Pasternack et al., 1978), CN (Bonczyk and Shirley, 1979; Verdieck and Bonczyk, 1981), CH (Mailander, 1977; Bonczyk and Shirley, 1979; Verdieck and Bonczyk, 1981; Kohse-Hoinghaus et al., 1983, 1984; Takubo et al., 1983), OH (Lucht et al., 1978, 1983, 1984, 1985; Kohse-Hoinghaus, 1983, 1984, 1986; Drake et al., 1984, 1985; Salmon and Laurendeau, 1985a, 1985b) and NH (Salmon et al., 1984) in both subatmospheric and atmospheric flames. Initial experiments (Pasternack et al., 1978; Bonczyk and Shirley, 1978; Verdieck and Bonczyk, 1981) showed significant disagreement

between the fluorescence and independent absorption measurements. Later, however, Lucht et al. (1983) and Salmon and Laurendeau (1985a) compared LSF measurements of OH concentration (calibrated using Rayleigh scattering) with independent absorption measurements in low-pressure (72 torr) laminar $H_2/O_2/Ar$ flames and demonstrated that saturation can be used to obtain accurate number densities ($\pm$15-25%) under these conditions.

In this chapter, we discuss the efficacy of the LSF method for measurement of OH concentration in high-pressure (P > 1 atm) flames. We first describe our efforts to achieve saturation of an OH transition in a series of $C_2H_6/O_2/N_2$ flames. We then test the adequacy of the balanced cross-rate model at high pressure. This model was used successfully by Lucht et al. (1983) and Salmon and Laurendeau (1985a) at low-pressure to relate the population of the laser-coupled rovibronic level in the excited state to the unperturbed population of the laser-coupled rovibronic level in the ground state. In essence, the model states that

$$N_u + N_l \approx N_l^0 \quad . \tag{6.1}$$

where N_u and N_l are the instantaneous populations of the upper and lower laser-coupled rovibronic levels, respectively, and N_l^0 is the unperturbed population of level l. To evaluate the adequacy of Eq. (6.1), we compare absorption and calibrated LSF measurements up to a pressure of ~6 atm. We also present absolute OH concentration profiles for lean flames at about 1, 3, 6, 9, and 12 atm; to our knowledge, these are the first absolute concentration measurements of OH in high-pressure flames made with LIF.

6.2 Theory

During laser excitation the population of the directly-excited rovibronic level N_u peaks and steady-state conditions apply. Thus, from the rate equation describing the upper laser-coupled level (Chapter 3),

$$\frac{N_u}{N_l} = \frac{1}{g_l/g_u + Q_{eff}/W_{lu}} \quad , \tag{6.2}$$

where g_l and g_u are the respective degeneracies of levels l and u, and W_{lu} is the rate coefficient for absorption. Q_{eff}, the effective rate coefficient for collisional depopulation of the directly-excited level, includes contributions from rotational and vibrational energy transfer, electronic quenching and spontaneous emission. In general, the population of N_u can be related to N_l^0 by

$$N_u + N_l = (1 - \gamma)N_l^0 \tag{6.3}$$

where $1 - \gamma$ is the fraction of the original population remaining in the laser-coupled levels, and N_l^0 is related to the species number density through the Boltzmann fraction. Combining Eqs. (6.2) and (6.3) gives

$$N_u = \frac{g_u}{g_l + g_u} N_l^0 (1 - \gamma)\alpha_{sat} \quad , \tag{6.4}$$

where α_{sat}, the degree of saturation, is given by

$$\alpha_{sat} = \left[1 + \frac{g_u/(g_l + g_u)}{W'} \right]^{-1} \quad , \tag{6.5}$$

and $W' \equiv W_{lu}/Q_{eff}$ is the saturation parameter.

The observed fluorescence signal is given by the integral of the local excited-state population over the imaged volume; i.e.,

$$S_f = \frac{hc\,v_f A_f}{4\pi}(\eta\Omega) \int_V N_u(x,y,z)dV \quad , \tag{6.6}$$

where v_f (cm^{-1}) is the frequency of the observed transition, A_f (s^{-1}) is the Einstein coefficient for spontaneous emission, η (V/W) is the net efficiency of the detection system, and Ω (sr) is the solid angle defined by the collection optics. In this experiment, the image of the monochromator entrance slit was rotated by 90° so that the slit width was perpendicular to the direction of travel of the beam (Fig. 6.1). If the dimensions of the slit imaged on the laser beam, H and W, are small compared to variations in the local excited-state number density, then $\int N_u dV = HW\int N_u dx$. When N_l^0 does not vary with the depth of the beam, we can solve for the unperturbed number density via Eq. (6.4) to obtain

$$N_l^0 = \frac{g_l + g_u}{g_u} \frac{4\pi S_f}{hc\,v_f A_f(HW\,\eta\Omega)\int_d (1-\gamma)\alpha_{sat}dx} \quad . \tag{6.7}$$

By rearranging this equation we obtain

$$<F_c> = \frac{\int_d (1-\gamma)\alpha_{sat}dx}{\int_d \alpha_{sat}dx} = \frac{g_l + g_u}{g_u} \frac{4\pi S_f/N_l^0}{hc\,v_f A_f(HW\,\eta\Omega)\int_d \alpha_{sat}dx} \quad , \tag{6.8}$$

which represents the spatially-averaged fraction of population remaining in the laser-coupled levels (Chapter 3). Note that insofar as W_{lu} is independent of x (e.g., along the beam center line), $<F_c>$ reduces to $1 - \gamma$.
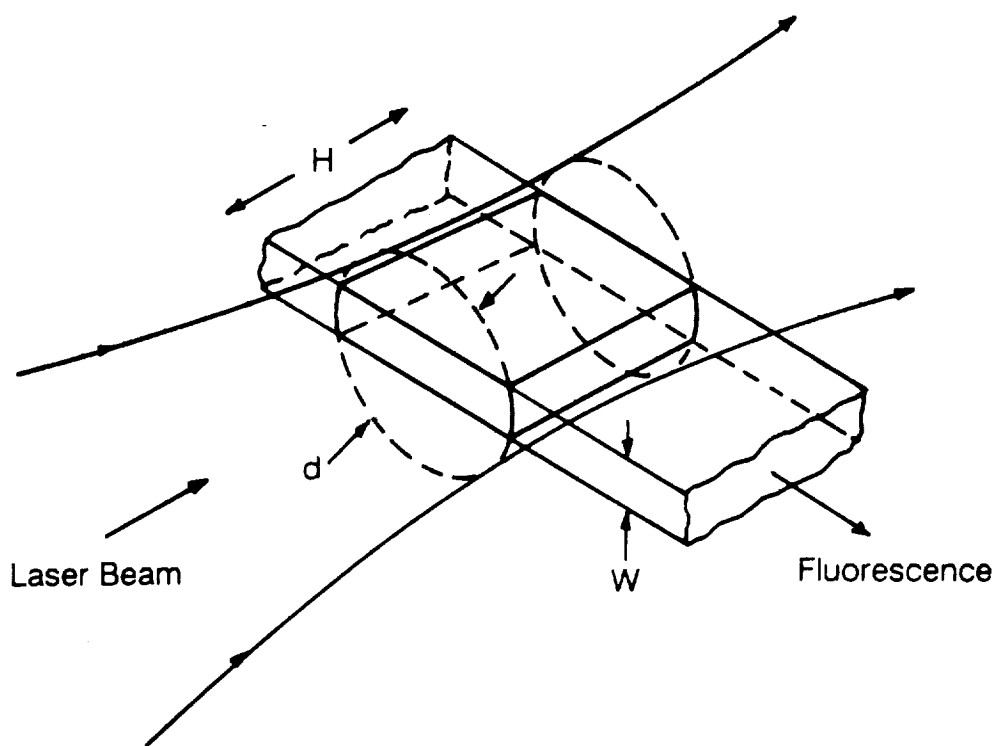
Figure 6.1 Geometry of the fluorescence collection volume.

The parameter $1 - \gamma$ is approximately unity and the balanced cross-rate model is valid when the population transfer rates into (R_{in}) and out of (R_{out}) the laser-coupled levels are balanced, i.e.,

$$\int_0^\tau (R_{in} - R_{out})dt \approx 0 \quad , \tag{6.9}$$

where $t = 0$ and $t = \tau$ represent the start of laser excitation and the observation time, respectively. On the other hand, for the OH molecule with $A^2\Sigma^+ \leftarrow X^2\Pi(0,0)$ excitation, a likely scenario for depletion of the laser-coupled levels includes (1) electronic quenching from $^2\Sigma^+(v'=0)$ to the $^2\Pi(v''>0)$ levels followed by (2) slow vibrational transfer to $v'' = 0$ (Campbell, 1984a; Rensberger et al., 1989; Wysong et al., 1989). Following the approach used in Chapter 3, the rate coefficient for quenching from rovibronic level i to the vibrational bath level (a composite of the $v'' > 0$ levels) is modelled as a fraction f_b of the total population leaving rovibronic level i,

$$Q_e(i,b) = f_b Q_e \quad , \tag{6.10}$$

where we use the notation Q_e instead of $Q_e(i)$, since we assume that the rate coefficient for electronic quenching is independent of rotational level i (Kohse-Hoinghaus et al., 1988). Similarly, the rate coefficient for vibrational transfer from $v'' > 0$ to $v'' = 0$ is expressed as a fraction f_v of Q_e,

$$Q_v(b) = f_v Q_e . \qquad (6.11)$$

When the ratio f_b/f_v is large, the population of the vibrational bath level will be large at high pressures (i.e., when a sufficient number of collisions have taken place), and thus it is likely that the laser-coupled levels will be depleted. Consequently, the balanced cross-rate model will not be strictly valid. However, at sufficiently high pressures, the local depletion $1 - \gamma$ reaches an asymptotic value, which occurs because the collisionally-excited rotational and vibrational energy levels attain sufficient population to balance the population transfer rates into and out of the laser-coupled levels (see Chapter 3). Therefore a modified balanced cross-rate model, Eq. (6.3), could be useful for making concentration measurements if the spatially-averaged population fraction, $\langle F_c \rangle$, is reasonably insensitive to the collisional environment. In other words, by calibrating fluorescence measurements with a method which gives an absolute concentration (e.g., absorption), $\langle F_c \rangle$ is automatically accounted for in the calibration factor. Fluorescence measurements calibrated with a method such as Rayleigh scattering (Salmon and Laurendeau, 1985a, 1985b; Kohse-Hoinghaus, 1983, 1984), however, will be in error by $1 - \langle F_c \rangle$.

6.3 Experimental Apparatus

Our high-pressure combustion facility includes the following: (1) a pressure vessel constructed from standard stainless steel piping components (Fig. 6.2); (2) an electronic gas delivery system, which is interfaced to a microcomputer; (3) a sintered bronze water-cooled flat-flame burner (2.5 cm in diameter) surrounded by a guard ring; and (4) an internal x-y burner translation system employing stepper motors. The range of movement of the vertical and horizontal translation mechanisms is about 11 and 2.8 cm, respectively, while the associated single-step resolutions are about 2 and 1 μm. The motors are stepped using a microcomputer, and thus we can accurately position the burner. Because flow instabilities in the burnt-gas region of the flame increased with increasing pressure, a screen was attached to the burner housing ~8 mm above the burner surface. This provided a significant improvement in flame stability. Further details of the combustion facility are given in Chapter 4.
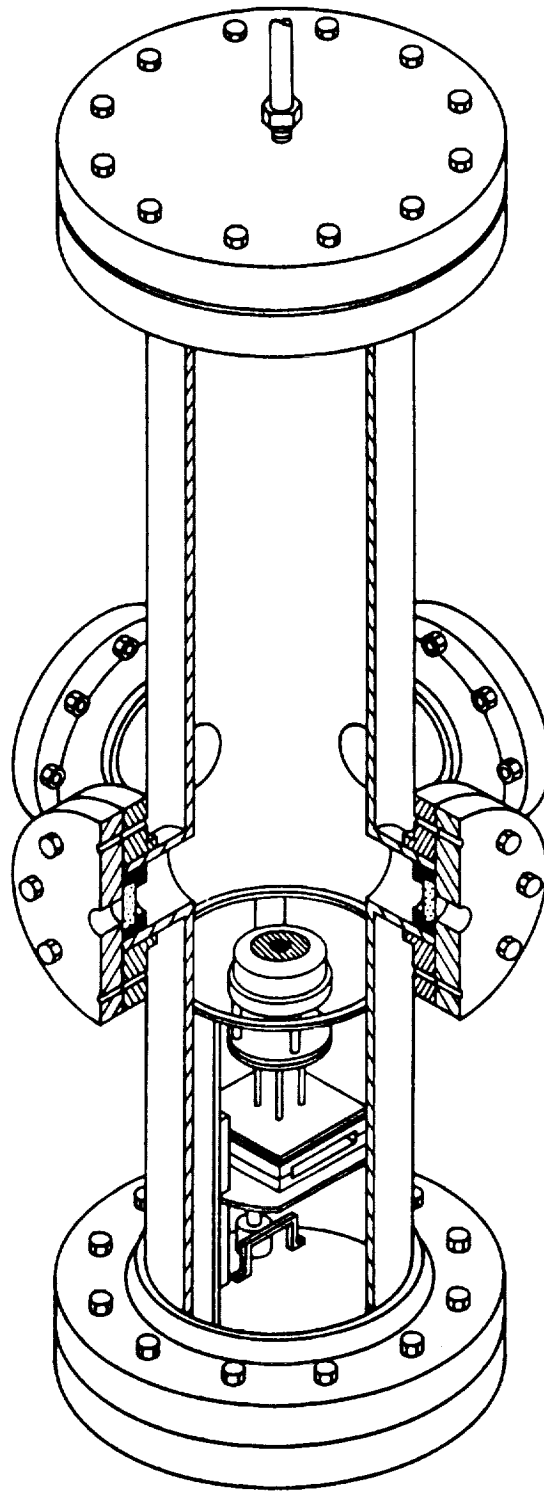
Figure 6.2   Cutaway view of the pressure vessel and components.
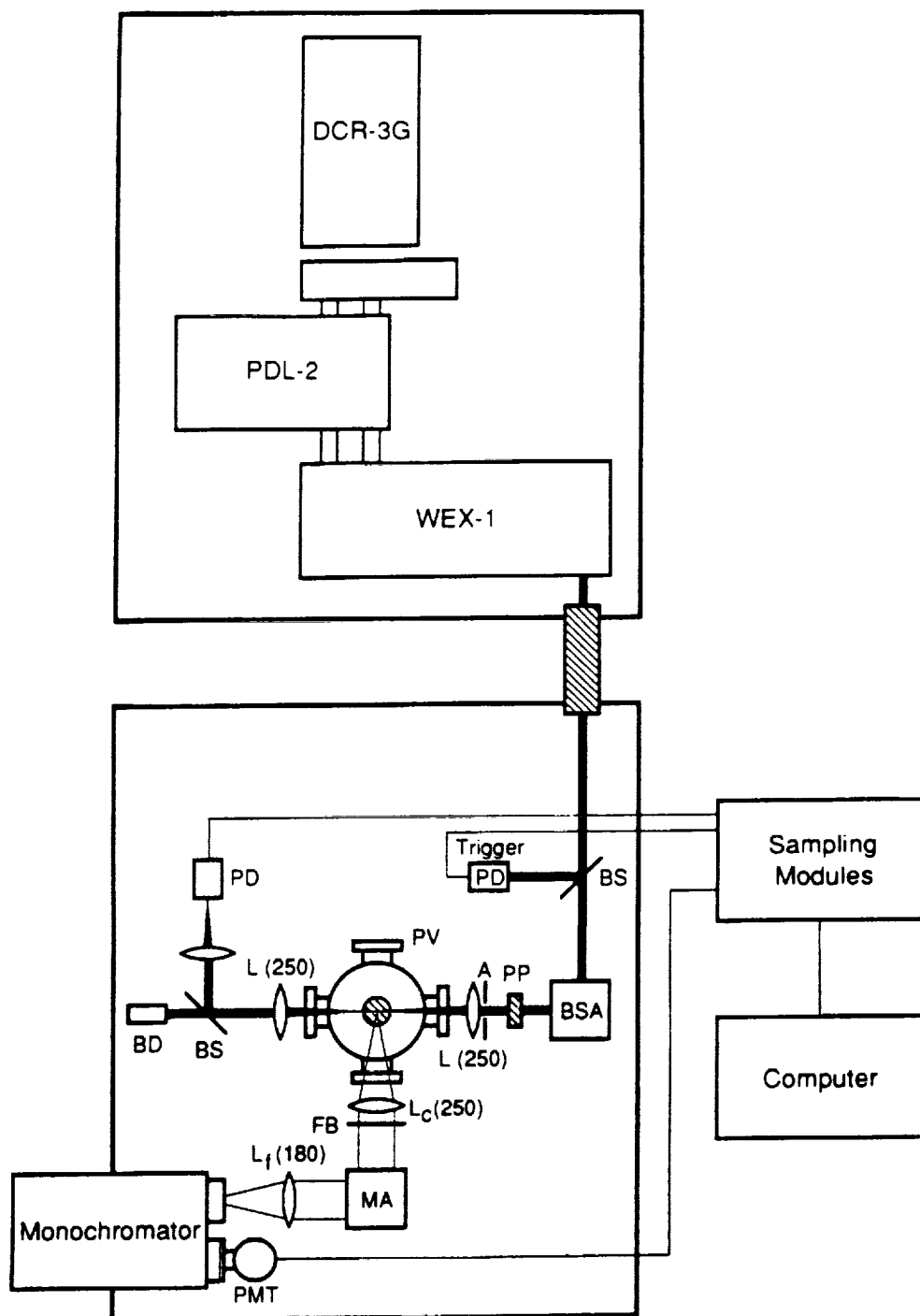
Figure 6.3   Schematic for LSF experiments. Components: A - aperture; BD - beam dump; BS - beam splitter; BSA - beam steering assembly; FB - fluorescence block; L - lens; MA - image-rotating mirror assembly; PD - photodiode; PMT - photomultiplier tube; PP - Pyrex plate(s); PV - pressure vessel.

The optical layout for the fluorescence measurements is shown in Fig 6.3. The second harmonic (at 532 nm) of a Quanta-Ray DCR-3G Nd:YAG laser is used to pump a PDL-2 dye laser, which includes transversely-pumped oscillator and preamplifier stages along with a longitudinally-pumped amplifier stage. To achieve high conversion efficiency of the 532 nm radiation, the dye laser employs a mixture of Exciton DCM and Sulforhodamine 640 dyes. Using this procedure, we obtained a laser energy of ~95 mJ/pulse at 620 nm, with an input energy of ~380 mJ/pulse at 532 nm. The output of the dye laser is frequency doubled in the Quanta-Ray Wavelength Extender (WEX-1). The visible and UV beams are dispersed with a Pellin-Broca prism, with a portion of the visible beam (not shown in Fig. 6.3) used to trigger the detection electronics. We obtained as much as 20 mJ/pulse of UV energy at ~310 nm, though this value dropped to about 15 mJ/pulse over the course of the experiment. The UV beam was raised to the appropriate height with a beam steering assembly; the resulting polarization of the radiation was vertical. The UV beam was also attenuated when necessary with Pyrex plates, and an aperture placed before the focussing lens was used to block scattered radiation. We used a 250-mm focal-length fused silica lens to focus the beam over the burner and a second 250-mm focal-length lens to collimate the beam after the exit port. At the exit port, the vessel window is fixed at a 10° angle so that light reflected from the window surfaces is directed away from the laser probe volume. Finally, a portion of the beam was directed to a silicon UV-sensitive PIN photodiode (Hamamatsu S17722-02), which monitored the shot-to-shot fluctuations of the UV beam energy. Though somewhat slow, this photodiode, because of its large sensitive area, was especially valuable when measuring the integrated beam intensity; for example, we employed this photodiode when positioning the burner relative to the laser beam to determine the burner *zero* position.

Fluorescence was collimated with another 250-mm focal-length lens and was rotated by 90° with a mirror assembly; the fluorescence was then focused on the entrance slit of a 3/4 meter monochromator. For the saturated fluorescence measurements, the slit width and height were 30 μm and 2 mm, respectively; this resulted in a spatial resolution of 42 μm by 2.9 mm. For measurements close to the burner surface, we blocked the lower half of the fluorescence beam prior to the image rotating mirror assembly; thus we could probe close to the burner without vignetting the fluorescence profile. The Spex 1800-II monochromator employed a specially-wired RCA 1P28B photomultiplier tube (Harris et al., 1976) with a 1000 V supply voltage for detection of the spectrally resolved fluorescence signals.
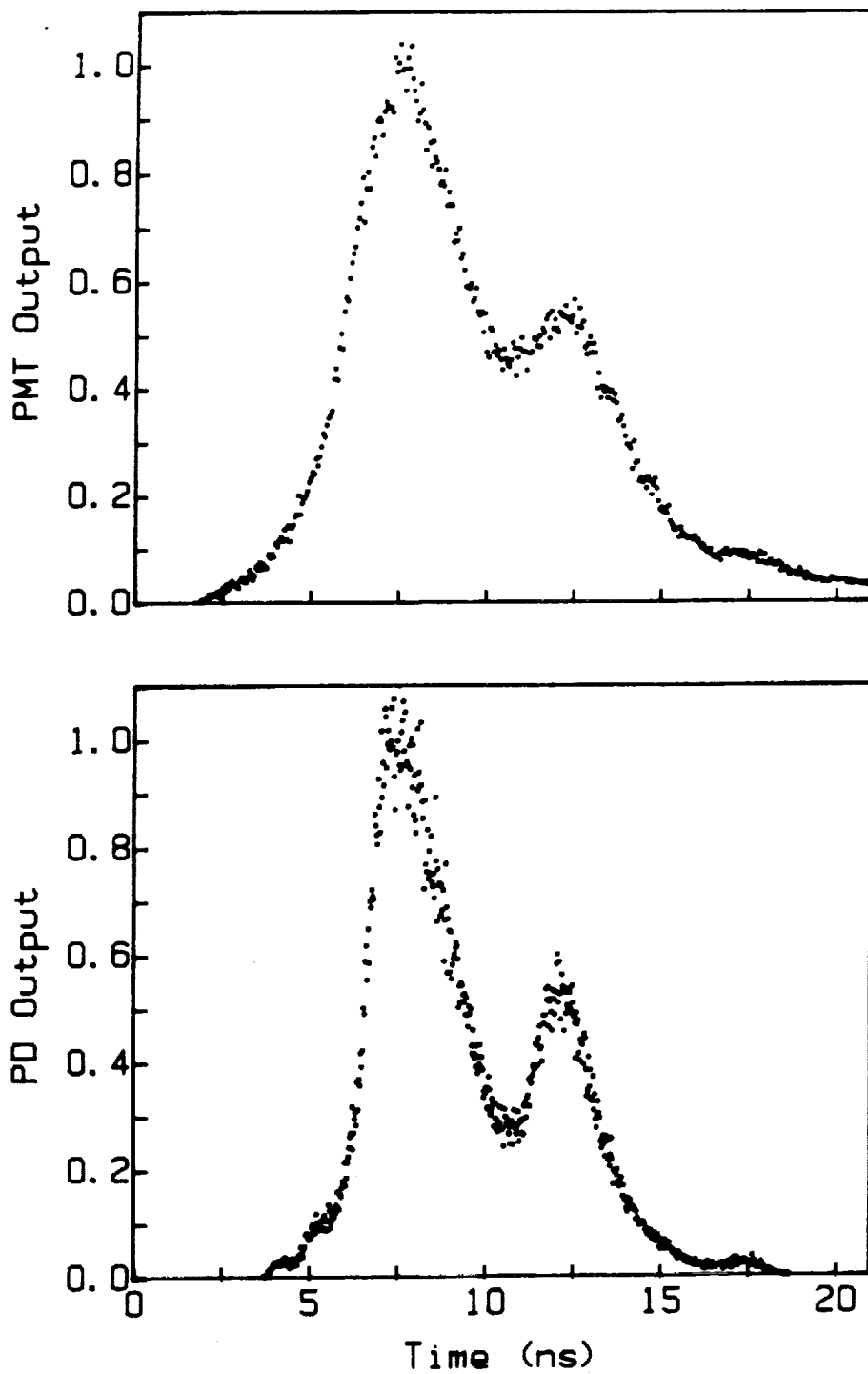
Figure 6.4   Average temporal intensity (30 scans) of the UV beam measured with the photomultiplier tube using Rayleigh scattering (top); average temporal intensity (10 scans) of the UV beam measured with the avalanche photodiode (bottom).

106

The PMT and photodiode signals were recorded with equipment from Stanford Research Systems; for the saturated fluorescence experiments, the PMT signal was resolved with the 200 ps sampling gate of the SR255 fast sampler, which was set at the peak of the fluorescence pulse using an SR200 gate scanner. The voltage output from the SR255 was then digitized and stored with the SR245 computer interface module and the SR265 software package, which we modified to allow programmed movement of laboratory stepper motors. For the PIN photodiode, we used a 10 ns gate of the SR250 gated integrator and boxcar averager.

The average temporal response of the PMT using Rayleigh scattering is compared in Fig. 6.4 to the average intensity profile obtained with a silicon avalanche photodiode (Texas Instruments TIED56), which has a temporal response of ~200 ps (Harris et al., 1980). These waveforms were recorded by repetitively scanning in time over the signal, using the 200 ps sampling gate of the fast sampler (SR255), and a scanning voltage supplied by the SR245 computer interface module. The average laser pulse has two temporal modes, each with ~2.5 ns FWHM. The relative intensity profile recorded by the PMT compares well with that from the avalanche photodiode, though the slower PMT response does result in distortion of the waveform.

The power at the peak of the first temporal lobe can be estimated by dividing the average energy per pulse by the integrated area under the normalized temporal profile (Fig. 6.4); from this procedure, using a pulse energy of 15 mJ, we calculate a peak power of ~3.3×10^6 W. The associated maximum UV irradiance (W/cm^2) can be estimated assuming the spatial dependence of the focused beam is described by an axisymmetric Gaussian function with a FWHM of 110 μm (see Chapter 4). The approximate spot size of the UV beam at the burner was determined by scanning a knife edge through the focused beam; though the spatial irradiance profile could not described perfectly by an axisymmetric Gaussian function, this is a convenient approximation for extracting the center-line irradiance. The resulting peak irradiance is ~2.6×10^{10} W/cm^2. By using this small spot size, we can increase the center-line saturation parameter; however, we also decrease the total number of excited molecules (integrated throughout the probe volume) and therefore the fluorescence signal.

6.4 Results and Discussion

6.4.1 Saturation Measurements

For the fluorescence experiments, we used the $Q_1(8)/P_1(9)$ excitation/detection line pair. These lines are suitable since they are isolated from neighboring lines; in addition, the population of the $N'' = 8$ level varies by only $\sim 10\%$ over 1100 to 2600 K (Lucht et al., 1984). To attenuate the laser intensity, we used Pyrex plates which had been calibrated using Rayleigh scattering. To account for possible variations in transmission with position, we *keyed* the plates, and thus we could place them in the same orientation each time. Because the plates steer the laser beam to different locations in the flame, the fluorescence focusing lens, L_f, was positioned to maximize the signal with each change of attenuation; in addition, a dial gage was used to measure the relative displacement of this lens, which equals (when multiplied by the system magnification) the displacement of the beam in the flame. Thus, in obtaining vertical profiles of OH concentration, we could correct the fluorescence signal, if necessary, for the change caused by beam steering. The five flames used in this study are described in Table 6.1.

Table 6.1   Description of $C_2H_6/O_2/N_2$ flames used in experiments.

Flame	Pressure (atm)	Equivalence Ratio	Dilution Ratio	Total Flow Rate (slpm)
A	0.98	0.77	3.0	3.15
B	3.1	0.76	3.1	4.61
C	6.1	0.91	3.1	6.45
D	9.2	0.92	3.1	8.21
E	12.3	0.92	3.1	8.21

The saturation curve obtained in the atmospheric-pressure flame is shown in Fig. 6.5. When plotted on a log-log scale, we observe that *partial* saturation is achieved over a large range of laser powers. In addition, the slope is approximately constant (within the accuracy of the measurements) on a log-log plot, even with the laser power attenuated by two orders of magnitude. Hence, over a wide range of laser attenuation, the sensitivity to laser fluctuations is 0.18 (versus 1 for linear fluorescence). This is the same sensitivity Salmon and Laurendeau (1985b) report for saturation of OH in a low-pressure (242 torr) $H_2/O_2/Ar$ flame.
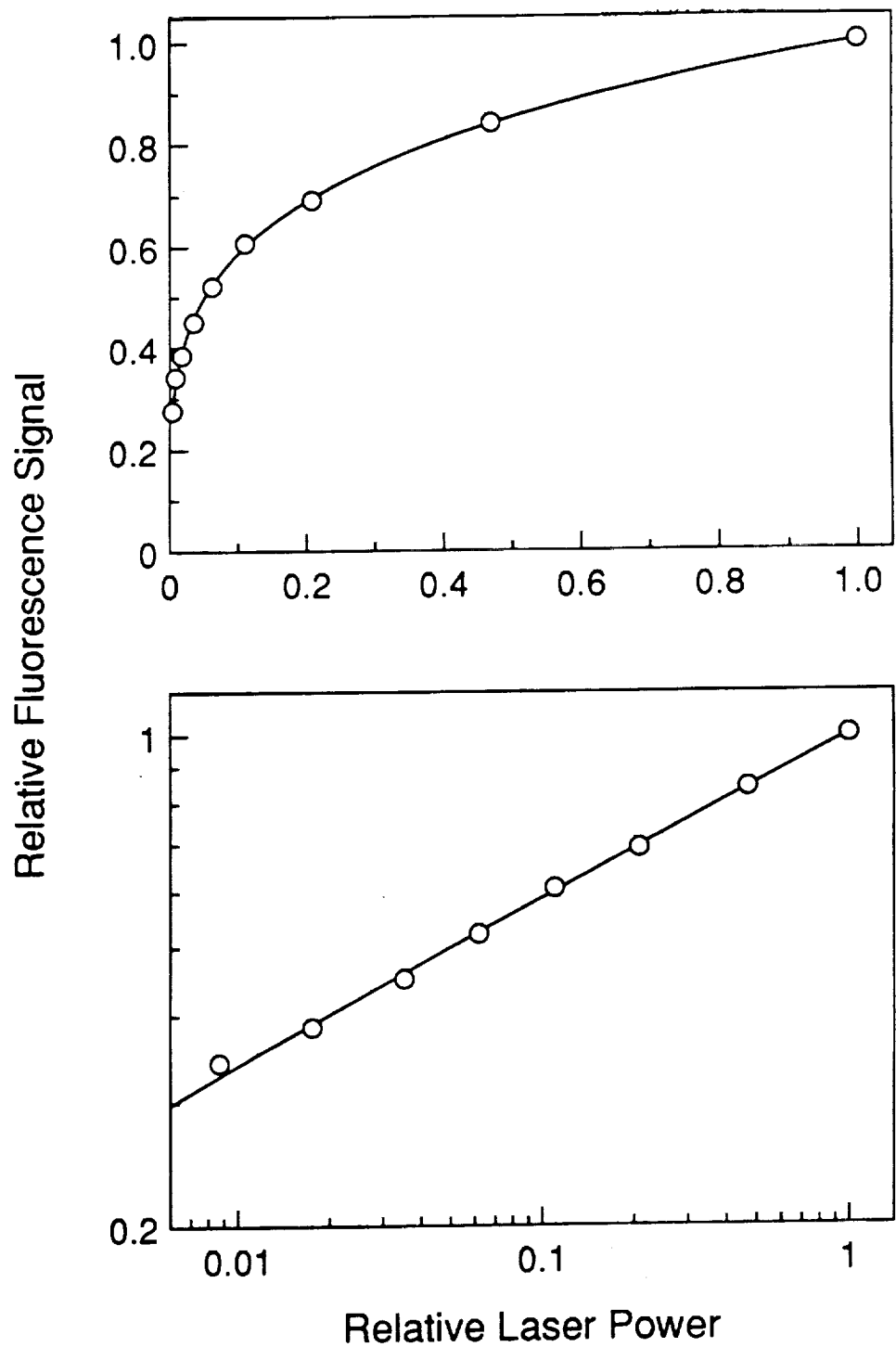
Figure 6.5   Saturation curve for atmospheric $C_2H_6/O_2/N_2$ flame.   The solid line shows the saturation behavior for a simple two-level model using the spatial irradiance function described by Eq. (6.12).

Using a simple two-level model ($\gamma = 0$), the predicted relative saturation curve from Eq. (6.7) becomes

$$\frac{S_f}{S_{f,m}} = \frac{\int_d \alpha_{sat}\, dx}{\int_d \alpha_{sat,m}\, dx} \quad , \tag{6.12}$$

where $S_{f,m}$ refers to the fluorescence signal at maximum laser power and α_{sat} is given by Eq. (6.5). As shown in Fig. 6.5, good agreement between the theoretical and experimental saturation curves results when using the spatial excitation function

$$W_{lu} = \frac{W_{lu}^P}{[1 + (x/w)^2]^{2.2}} \quad , \tag{6.13}$$

where W_{lu}^P is the absorption rate coefficient at the beam center line, x is the displacement from the center line, and w is the beam halfwidth. We should note that with a large center-line saturation parameter, the slope of the saturation curve is especially sensitive to the wings of the spatial irradiance profile and not to the spatial irradiance distribution at the central core of the profile, even though this core contains most of the laser energy.

To obtain a realistic center-line saturation parameter in Eq. (6.5), we used the peak center-line irradiance $I_L^P = 2.6 \times 10^{10}$ W/cm^2. In addition, we employed a dynamic model (see Chapter 3) with suitable rate coefficients for electronic quenching and rotational energy transfer to obtain Q_{eff} (where Q_{eff} is essentially independent of f_v and f_b). For the burnt-gas region of an atmospheric $C_2H_6/O_2/N_2$ flame, the rate coefficient for electronic quenching, Q_e, at ~1750 K (as derived from radiation-corrected thermocouple measurements) was calculated using equilibrium concentrations of the collision partners and the collision cross sections suggested by Garland and Crosley (1986). With this procedure, we calculate a relaxation time for electronic quenching of ~2.2 ns. This compares favorably with the value of ~2 ns measured by Schwarzwald et al. (1988) in atmospheric CH_4/air flames.

To estimate the rate coefficients $Q_r(i,j)$ for rotational energy transfer, we rely on the observation of Zizak et al. (1986), that when rotational equilibrium--steady state among the relative rotational-level populations during the laser pulse--is achieved, the ratio N_u/N_c [where N_c is the population of the collisionally-excited neighboring rotational levels in the $^2\Sigma^+(v=0)$ state] is sensitive to the directly-excited rotational level N_e but apparently insensitive to flame composition and temperature

for larger values of N_e. Since the ratio N_u/N_c is determined by the ratio of rate coefficients for (1) $Q_r(u)$, the total rotational energy transfer from level u and (2) Q_e, the thermally-averaged electronic quenching, we can use the ratio N_u/N_c to estimate $Q_r(u)$. For $N_e = 8$ in the burnt-gas region of a CH_4/air flame, Zizak et al. (1986) found $N_u/N_c \simeq 0.2$; modelling the excitation dynamics in a flame, while using the $Q_r(i,j)/Q_r(u)$--the relative distribution of the rate coefficients--deduced by Lucht et al. (1986) for an $H_2/O_2/N_2$ flame (see Chapter 3), we find that a value of $Q_r(u)/Q_e = 8.4$ gives $N_u/N_c \simeq 0.2$. The resulting effective quenching rate coefficient [Eq. (3.16)] at atmospheric pressure is $Q_{eff} = 2.9 \times 10^9$ s^{-1} at the laser center line.

Table 6.2   Modelling parameters describing $Q_1(8)$ laser excitation and collisional quenching of OH in an atmospheric flame.[a]

E	15 mJ/pulse
P_L	3.3×10^6 W
I_L^P	2.6×10^{10} W/cm^2
ν_0	32328 cm^{-1}
$\Delta\nu_L$	0.5 cm^{-1}
A_{lu}	6.399×10^5 s^{-1}
W_{lu}^P	4.2×10^{13} s^{-1}
Q_{eff}	2.9×10^9 s^{-1}
W_p'	15×10^3

[a] The laser energy used is the value estimated to reach the burner (accounting for optical losses) starting with a beam energy of 18 mJ/pulse.

Finally, assuming the gain curve of the dye laser is described by a Lorentzian profile which is much broader than the absorption linewidth width, we can estimate the saturation parameter as

$$W' = \frac{W_{lu}}{Q_{eff}} = \frac{(g_u/g_l)I_L A_{lu}}{4\pi^2 hc^2 \nu_0^3 \Delta\nu_L Q_{eff}} \quad , \tag{6.14}$$

where ν_0 (cm^{-1}) is the absorption frequency, A_{ul} is the Einstein coefficient for spontaneous emission from level u to l, and $\Delta\nu_L$ (cm^{-1}) is the spectral width (FWHM) characterizing the Lorentzian function. Equation (6.14) gives a peak saturation parameter $W_p' \approx 15 \times 10^3$. The relevant information is summarized in Table 6.2.
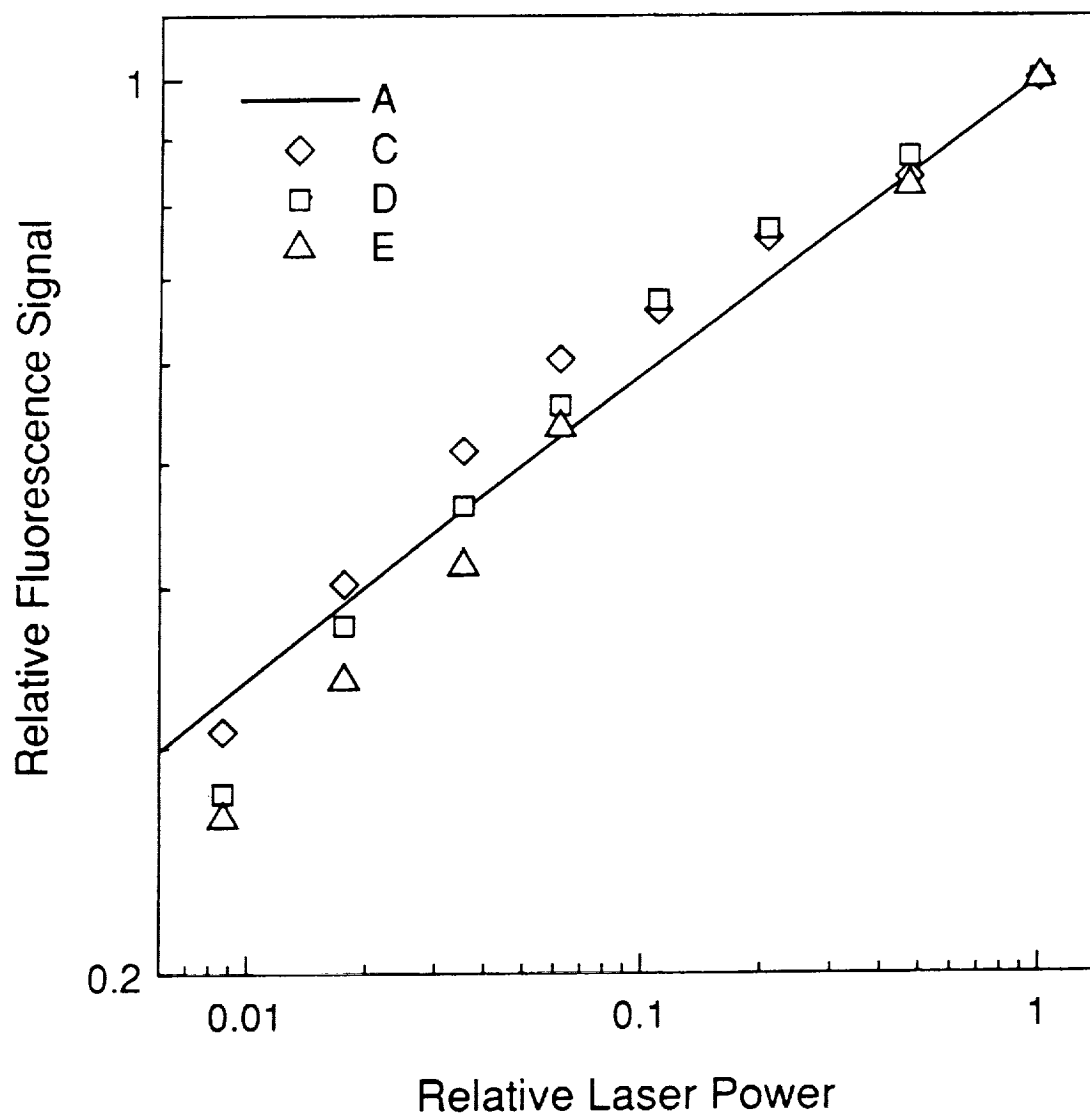
Figure 6.6   Saturation curves for high-pressure $C_2H_6/O_2/N_2$ laminar flames. The curve from the atmospheric flame is shown for comparison.
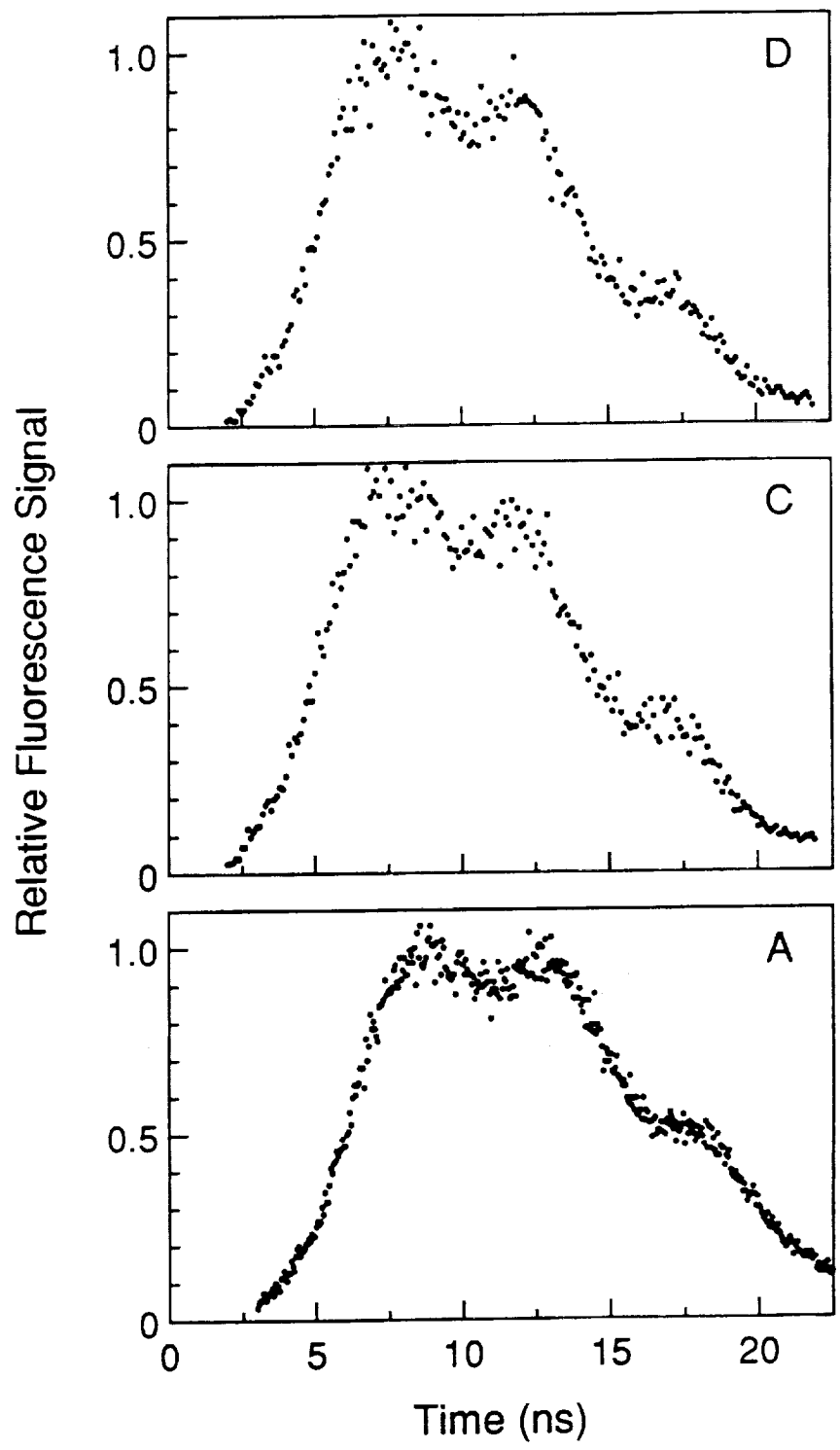
Figure 6.7 Average temporal intensity of fluorescence signal for flames A (30 scans), C (80 scans), and D (80 scans).

113

From Fig. 6.5, we expect that partial saturation will also be obtained over a large range of pressures; this is borne out in Fig. 6.6, which shows saturation curves in three high-pressure flames (see Table 6.1), compared to that obtained in the atmospheric flame. The high-pressure curves show a reduced slope at the highest laser powers; at lower powers, the fluorescence approaches linear behavior and the slope increases. Since the laser-coupled levels are progressively depleted as the laser power is increased, the fluorescence signal does not rise as it otherwise would. Thus, depletion of the laser-coupled levels results in a decreased slope of the saturation curve, both along the center line and averaged throughout the probe volume. Because of masking by the wings of the profile, the spatially-averaged depletion of the laser-coupled levels will always be less than, and perhaps significantly less than, the value along the beam center line (see Chapter 3).

The effect of saturation on the temporal fluorescence profile is shown for flames A, C, and D in Fig. 6.7: the profiles are broadened compared to the laser profile (Fig. 6.4). These profiles also give insight with respect to the depletion of the laser-coupled levels (Salmon and Laurendeau, 1985b). By comparing the relative heights of the two temporal modes, one can estimate the depletion of the laser-coupled levels at the second mode relative to that at the first. One would also need (1) a reliable measurement of the relative intensities of the two laser modes and (2) a saturation curve to describe the sensitivity of the fluorescence signal to W'. Furthermore, with a dynamic model similar to the one we have used, one could perhaps estimate $\langle F_c \rangle$ from the fluorescence profile. Though we do not have a reliable measurement of the temporal dependence of the laser irradiance for these cases, we can compare the profiles taken in flames A and D (since the temporal dependence of the laser was consistent from day to day). From this comparison, we observe that at the second temporal mode, the laser-coupled levels have undergone a spatially-averaged depletion of $\sim$10% at 9.2 atm relative to the second mode in the atmospheric flame.

6.4.2 Fluorescence/Absorption Measurements

To evaluate the efficacy of the balanced cross-rate model [Eq. (6.1)] for predicting number densities, we compare calibrated fluorescence measurements at high pressure with those from absorption. The calibration factor for the high-pressure fluorescence profiles is derived from absorption measurements in the atmospheric-pressure flame (A in Table 6.1). In this way we use the balanced cross-rate model implicitly, since we do not calculate absolute concentrations directly

114

from the fluorescence voltages. At higher pressures, the difference between the calibrated fluorescence and absorption measurements represents the depletion of the laser-coupled level beyond that in the atmospheric flame.

The absorption measurements were performed with a 150-W xenon arc lamp. The small-diameter beam, which was derived with a set of apertures, entered the high-pressure chamber through the optical access port opposite to the fluorescence collection port (Fig. 6.3). The same optics used for fluorescence collection were then used to direct the beam to the monochromator. The effective absorption beam width (i.e., the dimension in the flame stream-wise direction) was measured to be < 200 μm by translating the burner through the beam; the dimension in the horizontal direction was ~1 mm. To accurately calculate the OH number density from the measured integrated absorption (cm^{-1}), we measured an effective absorption path length using horizontal OH fluorescence scans (Fig. 6.8). The total number density, N_T, at radial position x along the absorption path is determined from the path-integrated number density by

$$N_T = \frac{1}{L^x_{eff}} \int_{-\infty}^{\infty} N_T(\xi) d\xi \quad , \tag{6.15}$$

where L^x_{eff}, the effective path length, is derived from the radial dependence of the normalized fluorescence signal, i.e.,

$$L^x_{eff} = \int_{-\infty}^{\infty} S_f(\xi)/S_f(x) d\xi \quad . \tag{6.16}$$

To avoid self absorption--which was evident in the atmospheric flame with the $Q_1(8)/P_1(9)$ excitation/detection scheme--we detected fluorescence from the $O_{12}(10)$ line (while still exciting the $Q_1(8)$ transition). Because of the reduced signal resulting from the smaller A-coefficient, we opened the monochromator entrance and exit slits to 200 μm (250 μm in some cases); consequently, the $P_2(14)$ and $P_1(15)$ lines, which are about equidistant from the $O_{12}(10)$ transition, provide a small contribution to the total signal. In doing this, we increased the sensitivity to Q_{eff}; however, except at the burner periphery, where the temperature change is large, the variation in Q_{eff} with horizontal position should be small. To ensure that the laser probe was similar in diameter to the absorption beam, we used a 1-mm slit height; the resulting probe dimensions were 290 (or 360) μm x 1.4 mm. For flames A, B, and C, horizontal scans were made at two or more vertical positions to assess the variation of L^x_{eff} with distance above the burner. Typically, for the central chord of the burner we found L^x_{eff} to be ~24 mm for x $\simeq$ -9.5 mm (see Fig. 6.8).
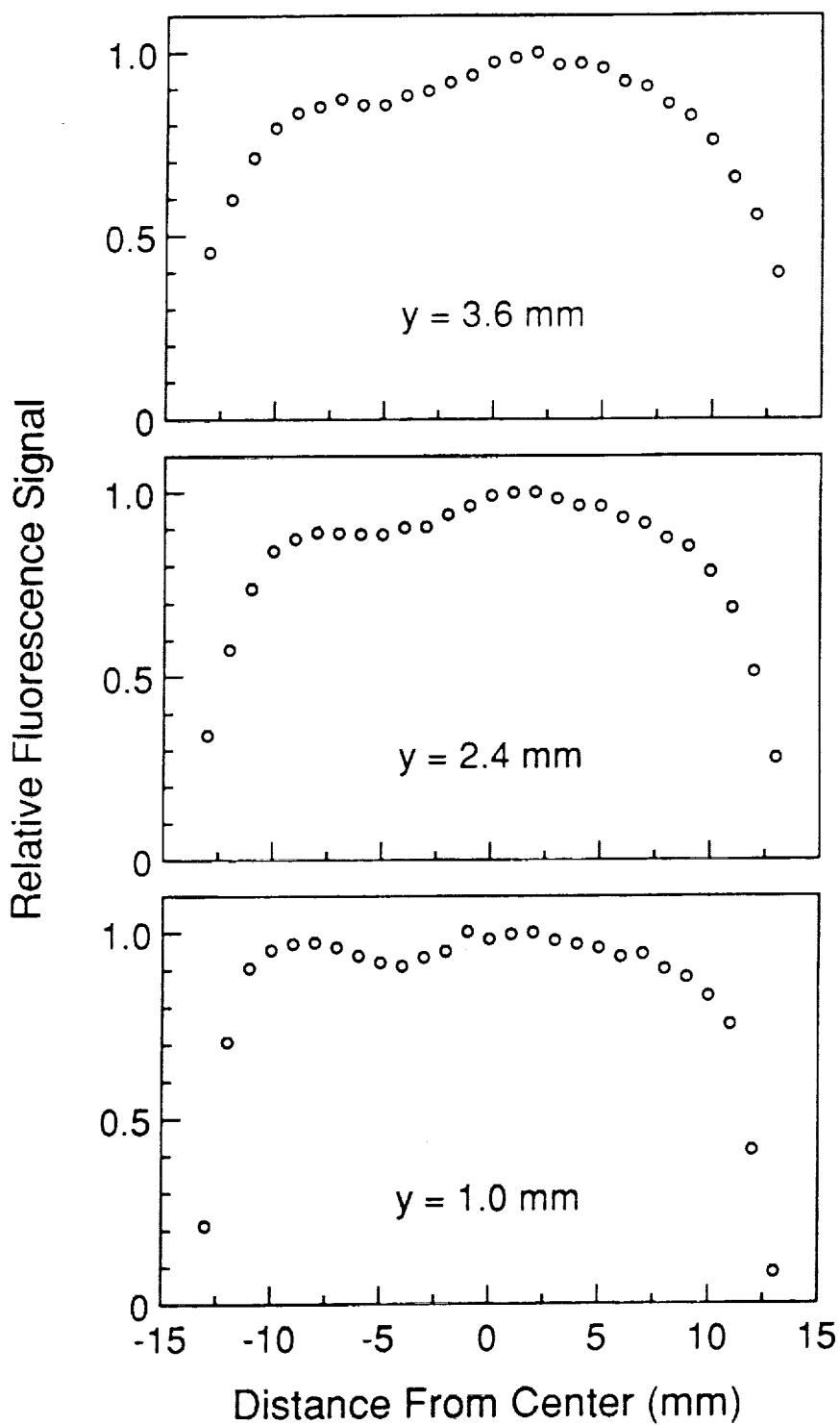
Figure 6.8   Relative horizontal OH fluorescence profiles from the atmospheric flame using $Q_1(8)/O_{12}(10)$ excitation/detection as a function of position above the burner surface. The horizontal position for the vertical profiles is $x \simeq$ -9.5 mm.
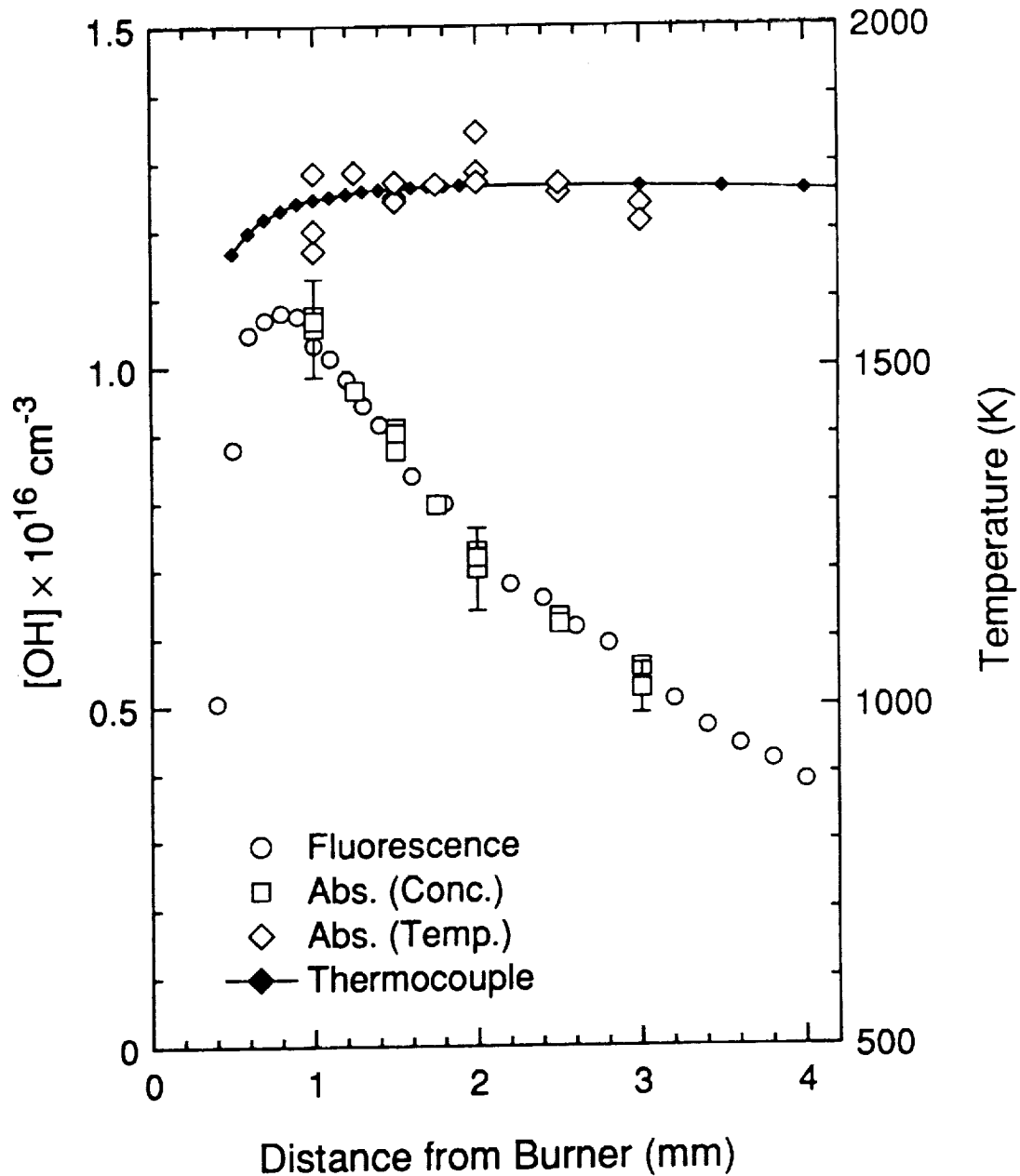
Figure 6.9 Calibration of relative OH fluorescence measurements [$Q_1(8)/O_{12}(10)$ excitation/detection] using absorption measurements in atmospheric-pressure $C_2H_6/O_2/N_2$ flame (flame A in Table 6.1). Multiple data points (for absorption) at the same height represent measurements made on different days. Temperatures from (1) absorption and (2) radiation-corrected thermocouple readings are also shown.

The SR265 software package was modified to integrate the absorption profiles (Chapter 4); with this software, analysis of the absorption spectra is fast and accurate. In particular, one need not rely on the triangular approximation for spectral integration of an absorption line (Lucht et al., 1978). This becomes important at higher pressures, since an increasing fraction of the total absorption occurs in the wings of the profile. When using 10 or more absorption lines (which was typical in flames A and B), the OH number density and temperature could be calculated by using the curve-of-growth method (Lucht et al., 1978), and fitting the integrated absorptions with a nonlinear least-squares algorithm (Salmon, 1986a). This routine also employed the data of Rea et al. (1987, 1989) for calculation of collisional linewidths (see Appendix B).

We now compare the calibrated fluorescence measurements in flames B and C with absorption measurements obtained in these same high-pressure flames. The fluorescence voltages were calibrated using the atmospheric-pressure flame (A) by comparing the relative OH fluorescence profile with the absolute number-density profile measured by absorption (Fig. 6.9). For completeness, we also include OH rotational temperatures calculated from the absorption data and radiation-corrected temperatures from silica-coated thermocouples (see Appendix C). The uncertainties in the absorption concentrations reflect contributions from (1) the least-squares fit (the 2-σ uncertainty which includes the temperature uncertainty), (2) the collisional linewidths, and (3) the path-length measurement. To calculate number densities N_T at higher pressure P, we employ the relation

$$N_T(P) = f_c f_B f_Q(P) f_e(P) \cdot S_f(P) \quad , \qquad (6.17)$$

where f_c (cm^{-3}/V) is the calibration factor, $S_f(P)$ is the fluorescence voltage at pressure P, and the correction factors f_B, f_Q, and f_e describe changes in the fluorescence signal due to variations in the Boltzmann fraction, the effective quenching rate coefficient, and the fluorescence collection efficiency, respectively. The factor f_e accounts for the decrease in detected fluorescence accompanying increased collisional broadening (see Appendix B), which can cause more fluorescence to fall outside the spectral detection window. For our experiment, the problem is perhaps exacerbated by a slight misfocus of the entrance slit image at the exit plane (see Chapter 4); nonetheless, we accounted for this effect by measuring the fluorescence signal as a function of exit slit width in all five flames. The factor f_e is defined as the ratio of fluorescence signals at 30 μm and 90 μm, compared at pressure P and 1 atm (flame A); i.e.,

$$f_e = \frac{[S_f(30 \ \mu m)/S_f(90 \ \mu m)]_1}{[S_f(30 \ \mu m)/S_f(90 \ \mu m)]_P} \quad . \qquad (6.18)$$

Because of the finite slit width (90 μm), f_e probably underestimates the correction factor. When the detected line is well isolated, this correction factor can be reduced or eliminated by increasing the exit slit width with respect to the entrance slit width.

To adequately evaluate the effect of pressure on the efficacy of the balanced cross-rate model, we also correct the fluorescence signal for its dependence on Q_{eff}. We thus estimate the change in Q_{eff} and then determine f_Q from the atmospheric-pressure saturation curve. In principle, this correction factor can be calculated from an *in situ* measurement, employing the method suggested by Cottereau (1986); in Chapter 7, we apply this method to our high-pressure laminar flames. The approach we use here is approximate, since the coupling of the laser and the transition depends on pressure through the frequency of dephasing collisions (Piepmeier, 1972a, 1972b). Consequently, while the atmospheric saturation curve represents the sensitivity to laser power, it only approximates the sensitivity to the collisional environment (see Appendix D). The problem of calculating f_Q is made worse when depletion of the laser-coupled levels accompanies the variation in laser power. Here, we have assumed that at atmospheric pressure, the saturation curve is unaffected by depletion of the coupled levels. To estimate Q_{eff}, we take the same approach described above for the atmospheric-pressure flame. We calculate Q_e [again based on equilibrium concentrations of the collision partners and the respective cross sections suggested by Garland and Crosley (1986)], and we again use $Q_r(u) = 8.4 \times Q_e$. With the dynamic model, we then calculate the ratio $[Q_{eff}]_P/[Q_{eff}]_1$. Not surprisingly, the calculations show that the variation in $[Q_{eff}]_P/[Q_{eff}]_1$ is determined primarily by the pressure ratio for these lean flames. While the error in the calculated value of Q_{eff} might be large, we expect the error in the ratio $[Q_{eff}]_P/[Q_{eff}]_1$ to be small, since the flames are similar in equivalence ratio, dilution ratio, and temperature (in the burnt-gas region). Furthermore, because of saturation, the correction factor f_Q is not sensitive to errors in $[Q_{eff}]_P/[Q_{eff}]_1$. All of the correction factors for the high-pressure flames are summarized in Table 6.3. For comparison, the correction factor f_Q is also calculated from the high-pressure saturation curves; the difference between the two values for P $\leq$ 9.2 atm is $\leq$ 10%.

Figures 6.10 and 6.11 compare fluorescence measurements with absorption measurements for flames B and C, respectively. In addition, in Fig. 6.12, we show hydroxyl concentration profiles for flames D and E. In flames B through E, the reaction zone was not observed; however, under
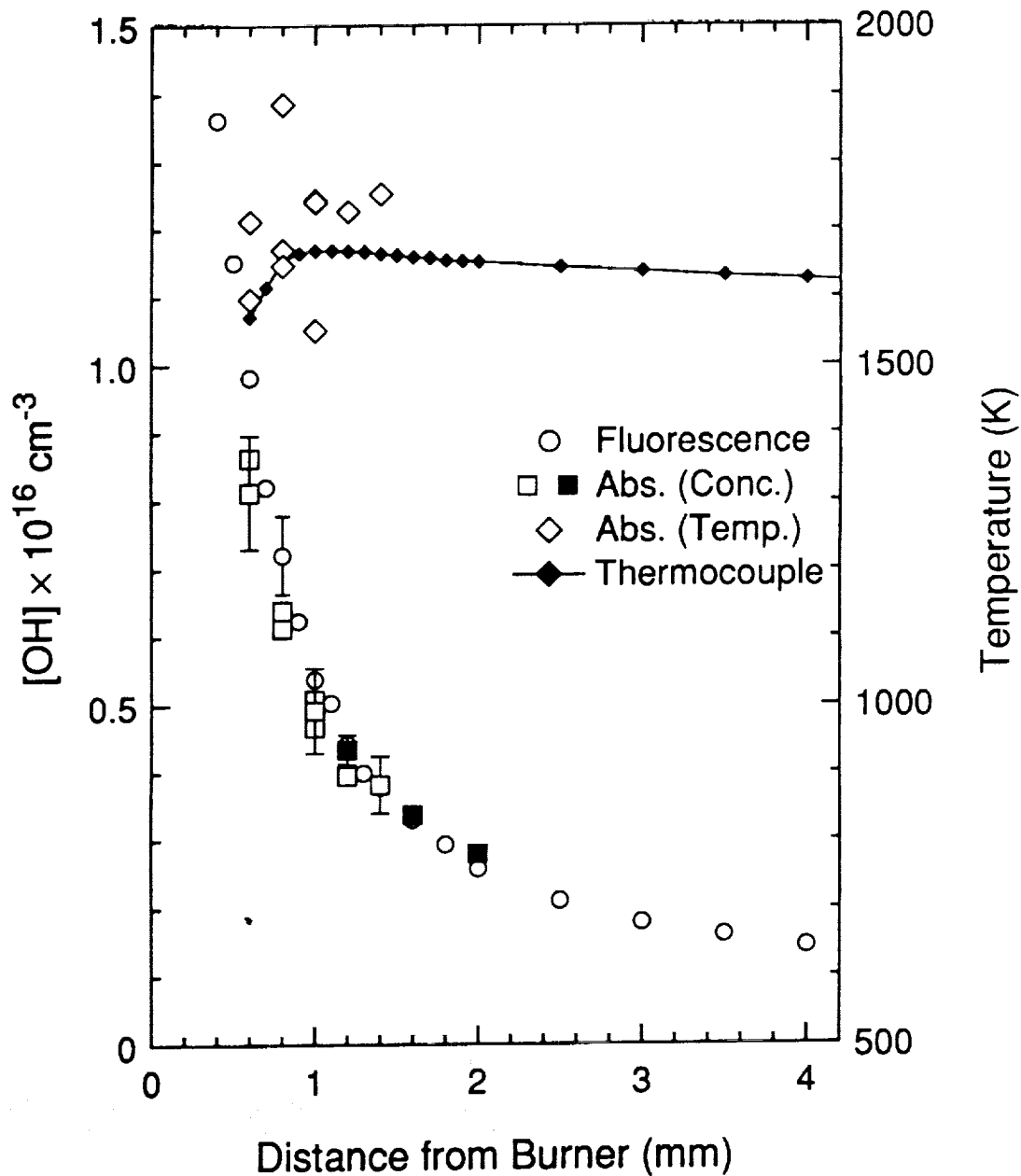
Figure 6.10 Comparison between relative OH fluorescence measurements and absorption measurements in 3.1 atm $C_2H_6/O_2/N_2$ flame (flame B in Table 6.1). The open and closed squares represent absorption measurements using (1) 10 or more lines and (2) only the $Q_1(6)$ and $Q_{12}(6)$ lines, respectively. Temperatures from absorption and radiation-corrected thermocouple readings are also shown.
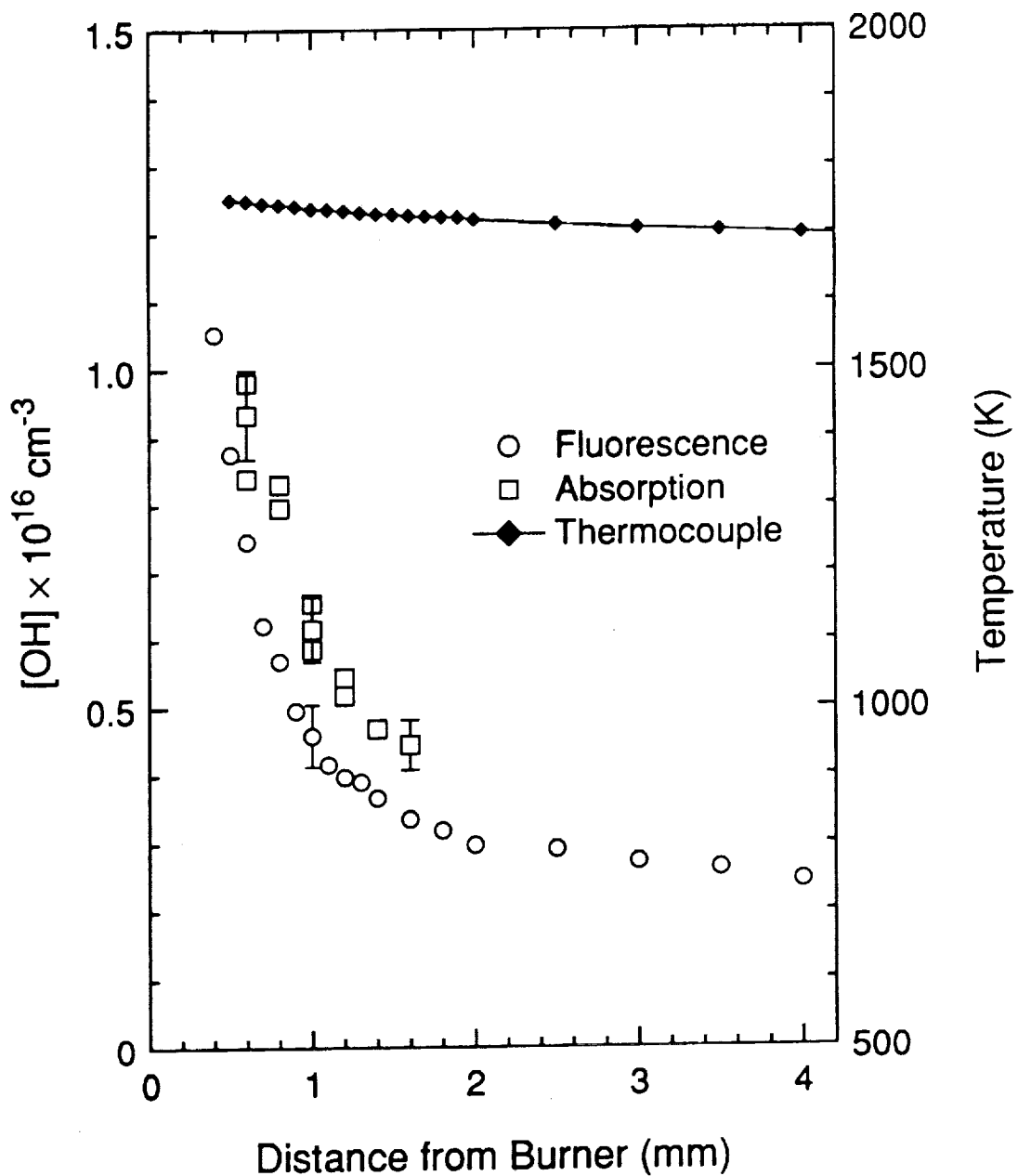
Figure 6.11 Comparison between relative OH fluorescence measurements and absorption measurements in 6.1 atm $C_2H_6/O_2/N_2$ flame (flame C in Table 6.1). The absorption measurements were made using only the $Q_1(6)$ and $Q_{12}(6)$ lines. Radiation-corrected temperatures from a thermocouple are also shown.
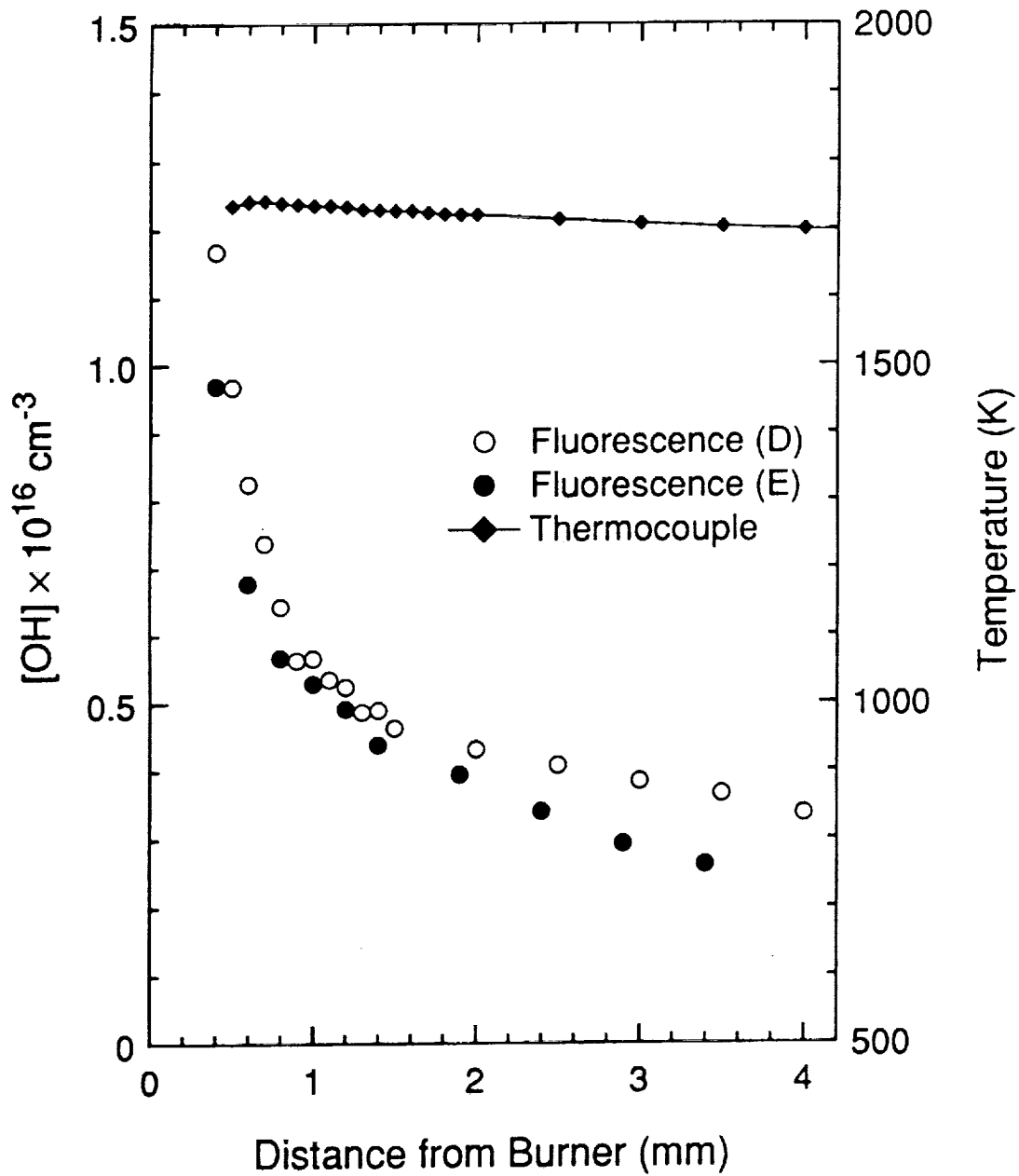
Figure 6.12   Fluorescence measurements for flame D (9.2 atm) and E (12.3, Table 6.1) calibrated from absorption and fluorescence measurements in flame C. Radiation-corrected temperatures from a thermocouple are also shown for flame D.

Table 6.3 Correction factors for high-pressure flames.[a]

Flame	$[Q_{eff}]_P/[Q_{eff}]_1$	f_Q	f_e	f_B
B	3.2	1.30	1.08	1.00
C	6.6	1.56 (1.42)[b]	1.14	1.00
D	10.1	1.70 (1.53)[b]	1.20	1.00
E[c]	~13.5	1.85	1.22	~1.0

[a] Quenching rate coefficients and Boltzmann fractions were based on thermocouple measurements at $y = 1$ mm.

[b] Values for f_Q calculated from the high-pressure saturation data.

[c] Temperatures were not measured for this flame (though the flow rate is the same as for flame D); the value of f_Q is based on the pressure relative to flame D.

certain conditions at high pressure, we were able to probe beneath the flame front (Chapter 5). For flames B and C, the fluorescence voltages were calibrated using the atmospheric flame ($f_c = 1.24 \pm 0.06 \times 10^{16}$ cm^{-3}V^{-1}) and the correction factors shown in Table 6.3. For flames D and E, the fluorescence signals were calibrated by comparing the relative fluorescence profiles to the absorption measurements in flame C ($f_c = 2.92 \times 10^{16}$ cm^{-3}V^{-1}); the correction factors were then calculated relative to flame C (rather than relative to flame A).

Figure 6.10 shows good agreement between the absorption and fluorescence measurements, with the calibrated fluorescence measurements yielding a slightly higher concentration than the absorption measurements. Three of the absorption measurements (indicated in the figure) are the result of repetitively scanning over only the $Q_1(6)$ and the satellite $Q_{12}(6)$ transitions (which was made possible by computer control of the scanning process). This approach was used because flame jitter (which increased with downstream position) and subsequent beam steering reduced the signal-to-noise ratio of the individual absorption lines; the effect of flame jitter is especially evident with the absorption temperatures. With the multiple scans, we increased the signal-to-noise ratio of the absorption measurements, since the $Q_1(6)$ line had the largest absorption of the lines analyzed. To extract the total number density from the integrated absorption, we used temperatures derived from the radiation-corrected thermocouple measurements. The OH absorption uncertainties (Appendix C) indicated in Fig. 6.10 include contributions from the uncertainties in (1) collisional linewidths (2) the effective absorption path

length, (3) the integrated absorption (due to the noise in the profile and baseline) and (2) the temperature (± 50 K). In addition, we show the fluorescence uncertainty, reflecting contributions from drift of the laser frequency (away from ν_0) and the uncertainty in calibration and correction factors.

For flame C, absorption measurements of OH concentration were obtained by averaging over 9 to 34 scans of the $Q_1(6)$ and $Q_{12}(6)$ lines at a given height above the burner. At higher pressure, greater flame instability discouraged us from attempting further absorption measurements. As shown in Fig. 6.11, the calibrated fluorescence measurements in flame C are about 25% below the absorption values. This difference is presumably due to depletion of the laser-coupled levels beyond that in flame A. This conclusion is consistent with results from the high-pressure saturation curves (Fig. 6.6) and the temporal profiles of fluorescence (Fig. 6.7).

Table 6.4   Input parameters for OH dynamic model.[a]

W_{lu}^p	4.2×10^{13} s^{-1}
$Q_r(u)/P$	3.8×10^9 s^{-1} atm^{-1}
Q_e/P	0.45×10^9 s^{-1} atm^{-1}
f_b	0.2
f_v	0.1

[a] In addition to scaling the rate coefficients for rotational energy transfer in the $A^2\Sigma^+$ ($v'=0$) state, the value of $Q_r(u)$ was also used to scale the $Q_r(i,j)$ in the $X^2\Pi$ ($v''=0$) state (see Chapter 3).

Table 6.5   Results of model calculations using the parameters listed in Table 6.4. The center-line and spatially-averaged population fractions are values evaluated at the temporal peak of the excitation pulse.

Pressure (atm)	W_p'	$\langle Fc \rangle$	$1 - \gamma$
1	17.4×10^3	0.90	0.85
6	2.96×10^3	0.80	0.67
12	1.48×10^3	0.71	0.52

Further insights on LSF measurements at high pressure can be obtained by employing the OH dynamic model (see Chapter 3 for details of the model). Input parameters for the model are listed in Table 6.4. The value of f_v appears reasonable for our flame based on recent measurements

of vibrational energy transfer in the $^2\Pi+$ state at *room temperature* (Rensberger et al., 1989; Wysong et al., 1989). The value of f_b is not based on measurements; rather, it was chosen to obtain a large center-line depletion of the laser-coupled levels. We use Eq. (6.13) to describe the spatial dependence of the excitation function and a Gaussian quadrature formula to perform the spatial integration (see Appendix E). The temporal dependence of the excitation pulse is described by a Gaussian function, with a 2.5 ns FWHM. The remaining input parameters are shown in Table 6.4. The calculations were performed for flame pressures of 1, 6, and 12 atm, and the results are shown in Table 6.5.

As noted previously, when $\langle F_c \rangle$ has a small sensitivity to pressure, Eq. (6.3) can be used to relate the measured signal to the unperturbed ground-state population. Despite the large center-line depletion at 12 atm ($\gamma = 0.48$), the relevant spatially-average quantity is $[\langle F_c \rangle_P - \langle F_c \rangle_1]/\langle F_c \rangle_1 = -0.21$. This is the error one would incur at this pressure in using Eq. (6.3), when calibration is performed at 1 atm with absorption or some other method yielding an absolute number density.

6.5 Conclusions

In this chapter, we have demonstrated saturation of the $Q_1(8)$ transition in the (0,0) manifold of the OH molecule in high-pressure flames. In particular, we have obtained saturation curves in $C_2H_6/O_2/N_2$ laminar flames at 1, 6.1, 9.2 and 12.3 atm. Based on these high-pressure curves, saturation could be attained at pressures > 20 atm in $C_2H_6/O_2/N_2$ flames. We have also presented calibrated fluorescence measurements of OH number density at pressures to 12.3 atm; to our knowledge, these are the first absolute concentration measurements of OH obtained at high pressure with LIF. To assess the efficacy of the balanced cross-rate model for high-pressure flames, we have compared LSF measurements, which were calibrated in an atmospheric-pressure flame, to absorption measurements at 3.1 and 6.1 atm. The high-pressure fluorescence signals were corrected for both the fluorescence collection efficiency and the finite sensitivity to Q_{eff}. At 3.1 atm the absorption and fluorescence measurements compare well, with the fluorescence number densities slightly higher than those from absorption. At 6.1 atm, the concentrations given by the LSF measurements are ~25% lower than the absorption values, indicating a depletion of the laser-coupled levels beyond that at atmospheric pressure. The temporal fluorescence waveforms and the high-pressure saturation curves also suggest a depletion of the laser-coupled levels. The extent to which the laser-coupled levels continue to deplete with increased pressure is uncertain,

and in applying the method to high-pressure flames, it is best to calibrate under conditions similar to the ones of interest. Nonetheless, we have shown that at moderately high pressures, the LSF method, when applied to the OH molecule, can give reasonably accurate number densities, even when calibrating at conditions significantly different from the conditions of interest. We anticipate that given a reasonable estimate for the finite sensitivity to Q_{eff} (i.e., accuracy within ±10% for the estimated f_Q), fluorescence measurements accurately calibrated at 1 atm can be applied to flames at ~10 atm with absolute errors within ±50%.

CHAPTER 7

QUENCHING-INDEPENDENT SATURATED FLUORESCENCE MEASUREMENTS OF THE HYDROXYL RADICAL IN LAMINAR HIGH-PRESSURE $C_2H_6/O_2/N_2$ FLAMES

7.1 Introduction

Measurements of flame species by optical methods, such as laser-induced fluorescence (LIF), have proved valuable in elucidating chemical and physical processes occurring in combustion environments (Eckbreth, 1988). Fluorescence measurements are relevant to the study of a broad range of practical combustion topics including turbulent flames, engine knock, pollutant formation, and flame stability. Linear fluorescence methods are particularly useful for turbulent flames, where 2-D images of *relative* species concentrations can yield insight into the complex interaction between chemistry and the flow field. In comparison, laser-saturated fluorescence (LSF), which is currently limited to point-wise or perhaps 1-D measurements, is attractive because it can provide reliable *absolute* species concentrations. Moreover, unlike linear fluorescence, LSF measurements are insensitive to the rate coefficients for both laser excitation and collisional de-excitation. As a consequence, *in situ* calibration of the fluorescence signal is not necessary: a calibration factor determined in one flame (through techniques such as Rayleigh scattering or absorption) can more easily be applied to other flames where calibration is more difficult or perhaps impossible [e.g., turbulent or sooting flames (Lucht et al., 1984, 1985; Drake et al., 1984, 1985)].

Since LSF was first proposed as a combustion diagnostic (Piepmeier, 1972a; Daily, 1977), it has been used to detect the diatomics C_2 (Baronavski and McDonald, 1977; Mailander, 1978), MgO (Pasternack et al., 1978), CN (Bonczyk and Shirley, 1979; Verdieck and Bonczyk, 1981), CH (Mailander, 1977; Bonczyk and Shirley, 1979; Verdieck and Bonczyk, 1981; Kohse-Hoinghaus et al., 1983, 1984; Takubo et al., 1983), OH (Lucht et al., 1978, 1983, 1984, 1985; Kohse-Hoinghaus, 1983, 1984, 1986; Drake et al., 1984, 1985; Salmon and Laurendeau, 1985a, 1985b) and NH (Salmon et al., 1984) in both subatmospheric and atmospheric flames. Initial experiments (Pasternack et al., 1978; Bonczyk and Shirley, 1978; Verdieck and Bonczyk, 1981) showed significant disagreement

between fluorescence and independent absorption measurements. Later, however, Lucht et al. (1983) and Salmon and Laurendeau (1985a) compared LSF measurements of OH concentration (calibrated using Rayleigh scattering) with independent absorption measurements in low-pressure (72 torr) laminar $H_2/O_2/Ar$ flames and demonstrated that saturation can be used to obtain accurate number densities (±15-25%) under these conditions.

Because of the lower intensity in the wings of the laser spatial irradiance profile, the fluorescence signal will always have a finite sensitivity to laser power and quenching. When the transition is well saturated along the central core of the beam, the sensitivity will be dominated by the fraction of energy in the wings of the spatial profile. Hence, some error is always incurred when applying a calibration factor determined in a different collisional environment; the greater the difference in the effective quenching rate coefficient between the calibration flame and the one of interest, the greater will be this error.

In this chapter, we describe experimental results using an alternate method first suggested by Cottereau (1986). This method involves the use of two fluorescence collection geometries for making quenching-independent measurements using saturated fluorescence. We have applied the Cottereau approach for concentration measurements of hydroxyl in laminar high-pressure $C_2H_6/O_2/N_2$ flames.

7.2 Theory

During laser excitation, the population of the directly-excited rotational level peaks and steady-state conditions apply. From the rate equation describing the population of the upper laser-coupled level, we have

$$\frac{N_u}{N_l} = \frac{1}{g_l/g_u + Q_{eff}/W_{lu}} \quad , \tag{7.1}$$

where N_u and N_l are the respective populations of the upper and lower laser-coupled rotational levels, g_u and g_l are the respective degeneracies of levels l and u, and W_{lu} is the rate coefficient for absorption. Q_{eff}, the effective rate coefficient for collisional depopulation of the directly-excited level, includes contributions from rotational and vibrational energy transfer, electronic quenching and spontaneous emission. In general, the population N_u can be related to N_l^0, the unperturbed population of level l, by

$$N_u + N_l = (1 - \gamma)N_l^0 \tag{7.2}$$

where $1 - \gamma$ is the fraction of the original population remaining in the laser-coupled levels, and N_i^0 is related to the species number density through the Boltzmann fraction. When the rates of transfer into and out of the laser-coupled levels are balanced at the observation time τ,

$$\int_0^\tau (R_{in} - R_{out})dt \approx 0 \quad , \tag{7.3}$$

then $1 - \gamma \approx 1$, and the so-called balanced cross-rate model (Lucht et al., 1980, 1983) is valid. We note that for OH molecules with $X^2\Pi(v''=0) \rightarrow A^2\Sigma^+(v'=0)$ excitation, a likely scenario for depletion of the laser-coupled levels includes population of the $v'' > 0$ levels through (1) quenching from the $^2\Sigma^+(v'=0)$ to the $^2\Pi(v''>0)$ levels and (2) slow vibrational transfer to $v'' = 0$ (Rensberger et al., 1989; Wysong et al., 1989).

The influence of depletion on quantitative LSF measurements has been treated theoretically and experimentally in Chapters 3 [see also Campbell (1984a)] and 6, respectively. In an experiment described in Chapter 6, we calibrated fluorescence measurements at high pressure in a flat laminar atmospheric $C_2H_6/O_2/N_2$ flame using absorption; we then compared calibrated fluorescence profiles with absorption profiles in $C_2H_6/O_2/N_2$ flames at 3 and 6 atm. In the 3-atm flame, the two measurements showed good agreement, while at 6 atm the fluorescence measurements were ~25% below the absorption measurements. Since the fluorescence values were corrected for their finite sensitivity to quenching, the ~25% disparity at 6 atm presumably arises from a loss of population from the laser-coupled levels. The saturation curves and the temporal fluorescence profiles were also found to display qualitative behavior consistent with partial depletion of the laser-coupled levels.

Combining Eqs. (7.1) and (7.2) gives

$$N_u = \frac{g_u}{g_l + g_u} N_i^0 (1 - \gamma)\alpha_{sat} \quad , \tag{7.4}$$

where α_{sat}, the degree of saturation, can be defined in terms of the saturation parameter, $W' \equiv W_{lu}/Q_{eff}$, by

$$\alpha_{sat} \equiv \frac{W'}{W' + g_u/(g_l + g_u)} \quad , \tag{7.5}$$

or

$$\alpha_{sat} = \frac{W'/W_p'}{W'/W_p' + g_u/[W_p'(g_l + g_u)]} \quad , \tag{7.6}$$

where $W_p{'}$ is the center-line saturation parameter.

The observed fluorescence signal is given by the integral of the local excited-state population over the imaged volume; i.e.,

$$S_f = \frac{hc\nu_f A_f}{4\pi}(\eta\Omega)\int_v N_u(x,y,z)dV \quad .\tag{7.7}$$

where ν_f (cm^{-1}) is the frequency of the observed transition, A_f (s^{-1}) is the Einstein coefficient for spontaneous emission, η (V/W) is the net efficiency of the fluorescence detection system, and Ω is the solid angle defined by the collection optics. For geometry A (Fig. 7.1), when the image of the slit width (W_A) is small compared to variations in the local excited-stated number density, then $\int N_u dV = W_A\int N_u dA_c$, where A_c is the cross-sectional area of the laser probe. The measured fluorescence signal is therefore given by

$$S_{fA} = \frac{hc\nu_f A_f}{4\pi}(\eta_A W_A \Omega_A)\int_{A_c} N_u(x,y)dA_c \quad .\tag{7.8}$$

Likewise for geometry B (Fig. 7.1), when the dimensions of the slit imaged on the laser beam, H_B and W_B, are small compared to variations in the local excited-state number density, then $\int N_u dV = H_B W_B \int N_u dx$. The measured fluorescence signal is thus

$$S_{fB} = \frac{hc\nu_f A_f}{4\pi}(\eta_B H_B W_B \Omega_B)\int_d N_u(x)dx \quad .\tag{7.9}$$

If N_i^0 is constant throughout the probe volumes, the ratio of the signals is

$$\frac{S_{fA}}{S_{fB}} = \frac{\eta_A W_A \Omega_A \int_{A_c}(1-\gamma)\alpha_{sat}dA_c}{\eta_B H_B W_B \Omega_B \int_d(1-\gamma)\alpha_{sat}dx} \quad .\tag{7.10}$$

When the depletion of the laser-coupled levels is small ($\gamma \approx 0$) and the spatial dependence of the saturation parameter corresponds to that of the laser irradiance (i.e., Q_{eff} does not vary within the imaged volume),

$$\frac{W'(x,y)}{W_p{'}} \approx \frac{I_L(x,y)}{I_L^p} \quad .\tag{7.11}$$

then we can write

$$\frac{S_{fA}}{S_{fB}} \approx f\left\{W_p{'};\frac{I_L}{I_L^p};K\right\} \quad .\tag{7.12}$$

130
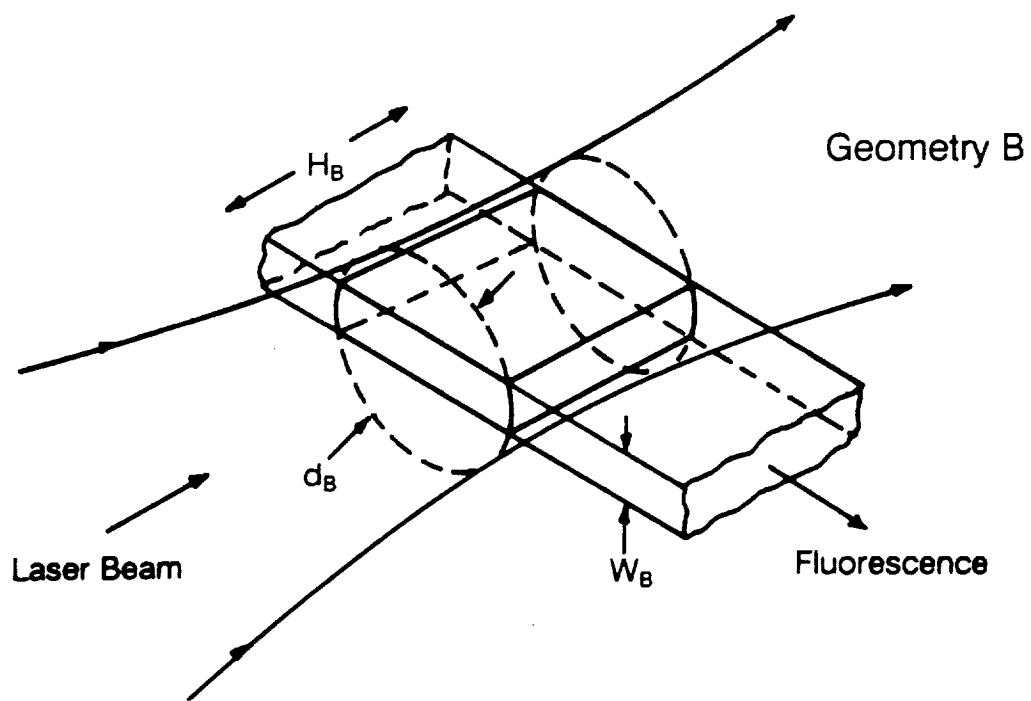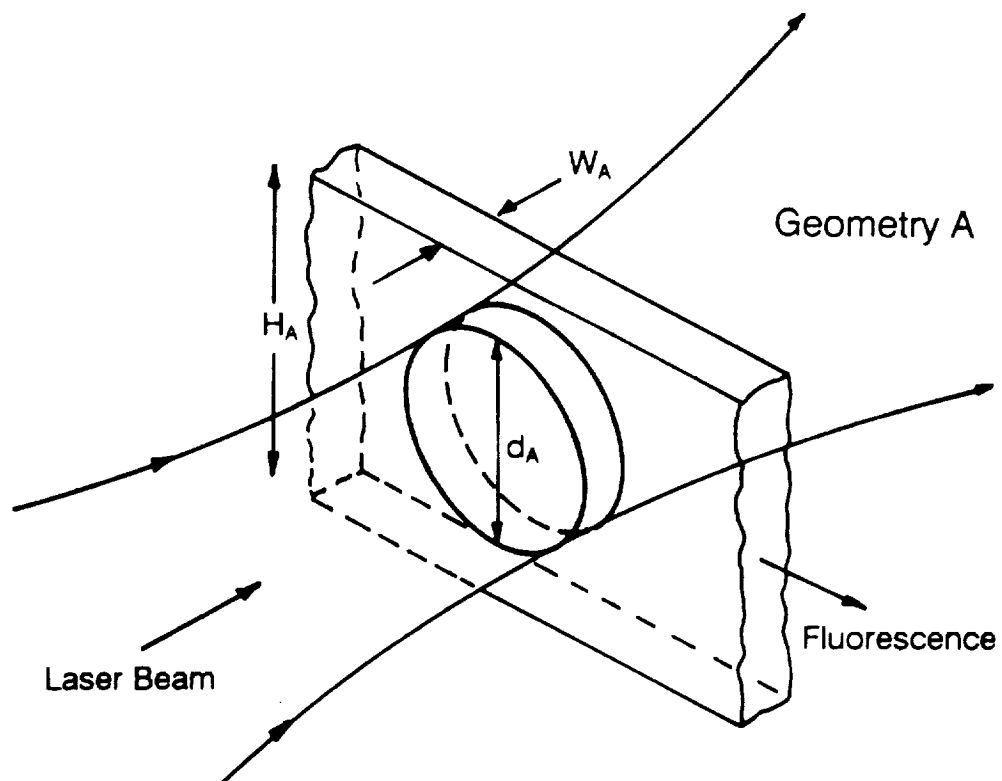
Figure 7.1   Fluorescence collection geometries: top, geometry A; bottom, geometry B.

Thus, the ratio of the two signals is a function of the center-line saturation parameter, the spatial dependence of the laser irradiance, and K, the ratio of detection parameters for the two geometries. Insofar as the detection parameters and the spatial dependence of the laser irradiance are invariant, the ratio S_{fA}/S_{fB} will depend only on W_p'. This being the case, the curve of S_{fA}/S_{fB} versus laser power defines the relative saturation parameter,

$$W_r' = f\left(\frac{S_{fA}}{S_{fB}}\right) \ , \qquad (7.13)$$

which acts as a quenching calibration function, since $S_{fg} = N_i^0 \cdot f_g(W_r')$ for g = A, B.

The Cottereau technique is then applied using the following steps.

1. Select a flame and calibrate the fluorescence signals from both geometries (with measurements from absorption spectroscopy or Rayleigh scattering, for example).

2. In the calibration flame, generate saturation curves for the two geometries by varying the laser irradiance, being careful not to change the spatial dependence of I_L. Since the relative laser irradiance is approximately equivalent to the relative saturation parameter, W_r', when Q_{eff} is constant, the curve S_{fA}/S_{fB} versus I_L defines the calibration function $W_r'(S_{fA}/S_{fB})$. This function should be defined over the range of expected values of W_r'.

3. At the condition of interest, measure S_{fA} and S_{fB}; from the calibration curve $W_r'(S_{fA}/S_{fB})$ determine the value of W_r'. With this value and either saturation curve $S_{fA}(W_r')$ or $S_{fB}(W_r')$, determine the fractional change in fluorescence intensity due to the change in the relative saturation parameter. This value (for geometry A or B) is then used to correct the fluorescence signal (from geometry A or B) for any change in the saturation parameter between the calibration flame and the flame of interest.

Thus, at the condition of interest, the total number density N_T can be described by

$$N_T = S_f f_c f_Q \cdot \prod_i f_i \ , \qquad (7.14)$$

132

where f_c (cm^{-3}/V) is the calibration factor (determined in step 1), f_Q is the *quenching correction factor*, which accounts for the fractional change in W_r', and the f_i are additional correction factors (accounting for variations in the Boltzmann fraction, etc.). To illustrate this technique, we consider Fig. 7.2, where the squares and triangles represent measurements in the calibration flame and the flame of interest, respectively. In the flame of interest, the measurement of $S_{fA}/S_{fB} = 0.70$ (relative to $S_{fA}/S_{fB} = 1.0$ in the calibration flame) gives $W_r' = 0.22$. From the saturation curves, $W_r' = 0.22$ corresponds to quenching correction factors ($f_Q \equiv 1/S_f$ for these normalized saturation curves) of 2.13 and 1.49 for geometries A and B, respectively.

7.3 Experimental Apparatus

Our high-pressure combustion facility includes the following: (1) a pressure vessel constructed from standard stainless steel piping components; (2) an electronic gas delivery system, which is interfaced to a microcomputer; (3) a sintered bronze water-cooled flat-flame burner (2.5 cm in diameter) surrounded by a guard ring; and (4) an internal x-y burner translation system employing stepper motors. The range of movement of the vertical and horizontal translation mechanisms is about 11 and 2.8 cm, respectively, while the associated single-step resolution is about 2 and 1 μm. The motors are stepped through a microcomputer, and thus we can accurately position the burner. Because flow instabilities in the burnt-gas region of the flame increased with increasing pressure (Chapter 5), we attached a screen to the burner housing ~8 mm above the burner surface. This provided a significant improvement in flame stability. Further details of the combustion facility are given in Chapter 4.

The optical layout for the fluorescence measurements is shown in Fig 7.3. The second harmonic (at 532 nm) of a Quanta-Ray DCR-3G Nd:YAG laser is used to pump a PDL-2 dye laser, which includes transversely-pumped oscillator and preamplifier stages along with a longitudinally-pumped amplifier stage. The output of the dye laser is frequency doubled in the Quanta-Ray Wavelength Extender (WEX-1), and the visible and UV beams are then dispersed with a Pellin-Broca prism; though not shown exactly in Fig. 7.3, a portion of the visible beam is then used to trigger the detection electronics. For this experiment we employed ~18 mJ/pulse of UV energy. The UV beam was raised to the appropriate height with a beam steering assembly; the resulting polarization of the radiation was vertical. The beam was attenuated when necessary with Pyrex plates, and an aperture placed before the focussing lens was used to block scattered radiation.
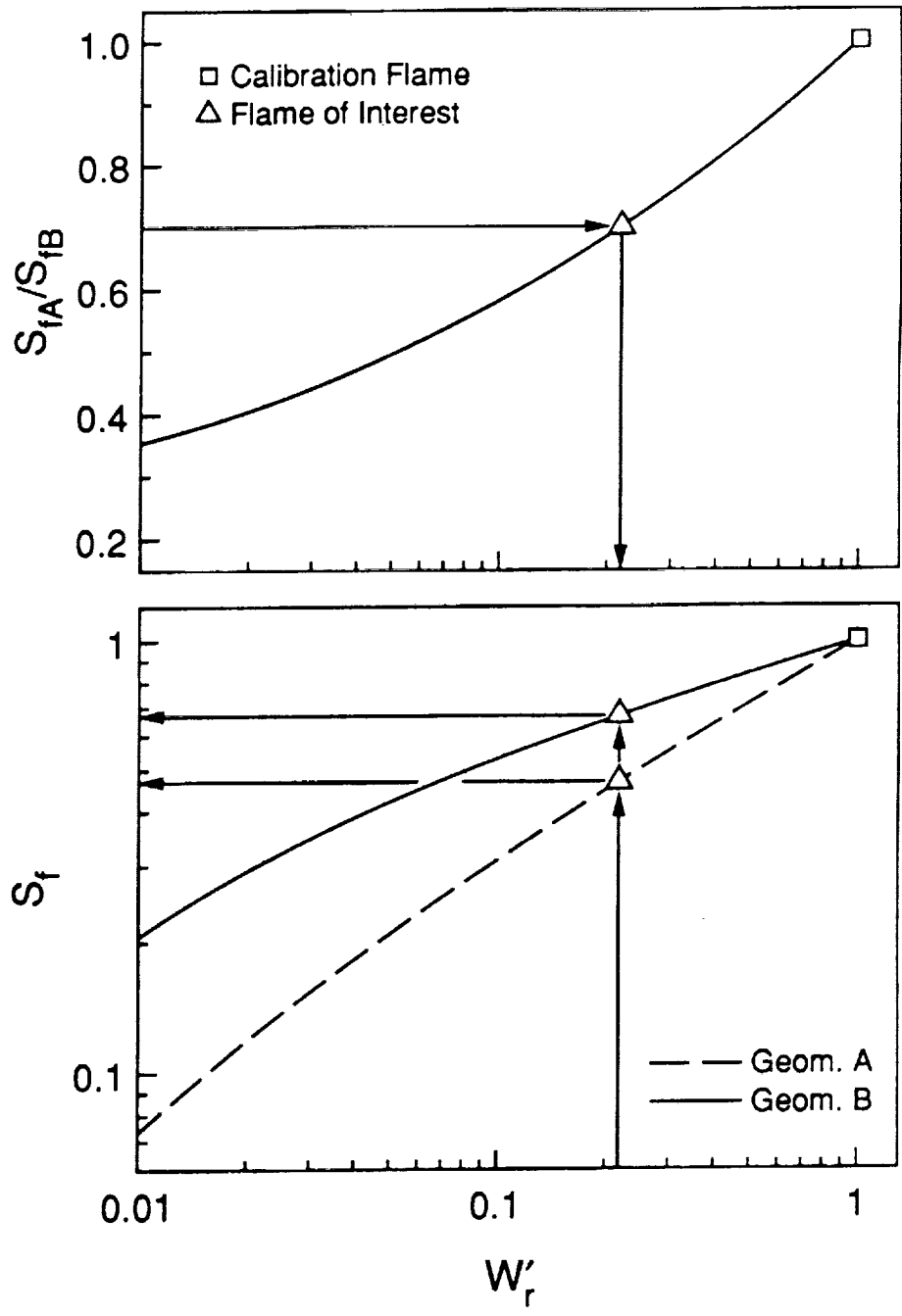
Figure 7.2   Hypothetical saturation curves and the corresponding quenching calibration curve.

Figure 7.3   Schematic for LSF experiments. Components: A - aperture; BD - beam dump; BS - beam splitter; BSA - beam steering assembly; FB - fluorescence block; L - lens; MA - image rotating mirror assembly; PD - photodiode; PMT - photomultiplier tube; PP - Pyrex plate(s); PV - pressure vessel.

135

We used a 250-mm focal-length fused silica lens to focus the beam over the burner and a second 250-mm focal-length lens to collimate the beam after the exit port. At the exit port, the vessel window is fixed at a 10° angle so that light reflected from the window surfaces is directed away from the laser probe volume. Finally, a portion of the beam was directed to a silicon UV-sensitive PIN photodiode (Hamamatsu S1 7722-02), which monitored the shot-to-shot fluctuations of the UV beam energy.

Fluorescence was collimated with a 250-mm focal-length lens, and was split with a UV beam-splitting plate. The fluorescence transmitted by the plate was focused on the entrance slit of monochromator A. The beam-splitting plate, which had a transmission and reflectance of ~30%, also acted as the first reflector of the image rotating assembly, which rotated by 90° the fluorescence image; the fluorescence was then focused on the entrance slit of monochromator B. This arrangement--rather than one with monochromators on either side of the flame--was used so that the two fluorescence signals would be affected equally by self absorption, which was evident in our flames. For monochromator A (a Spex 1700), which employed a grating blazed at 1 μm (and was used in third order), we used an entrance (and exit) slit width and height of 300 μm and 1.2 mm, respectively. The imaged volume is the disk defined by the width of 500 μm and the diameter d_A of the laser probe (as *seen* by geometry A). Though the beam width was measured to be about 0.1 mm (see Chapter 4), with saturation, the apparent probe diameter can be much larger (Salmon and Laurendeau, 1985a). For monochromator B (a Spex 1800-II), which employed a grating blazed at 300 μm (and was used in first order), we used an entrance slit width and height of 30 μm and 2 mm, respectively, and the associated spatial resolution was 42 μm x 2.9 mm x d_B. To increase the signal for this geometry, we used an exit slit width of 60 μm; this also decreased the sensitivity of the signal to variations in line broadening concomitant with pressure variations (and noticeable especially at high pressures). For measurements close to the burner surface, we blocked the lower half of the fluorescence beam prior to the image rotating mirror assembly; thus we could probe close to the burner without vignetting the fluorescence profile. The monochromators employed specially-wired RCA 1P28B photomultiplier tubes (Harris et al., 1976) each with a 1000 V supply voltage for detection of the spectrally resolved fluorescence signals.

The PMT and photodiode signals were recorded with Stanford Research Systems equipment; the two fluorescence signals were resolved with the 200 ps sampling gates of two SR255 fast samplers, which were set at the peak of the respective fluorescence pulses using SR200 gate
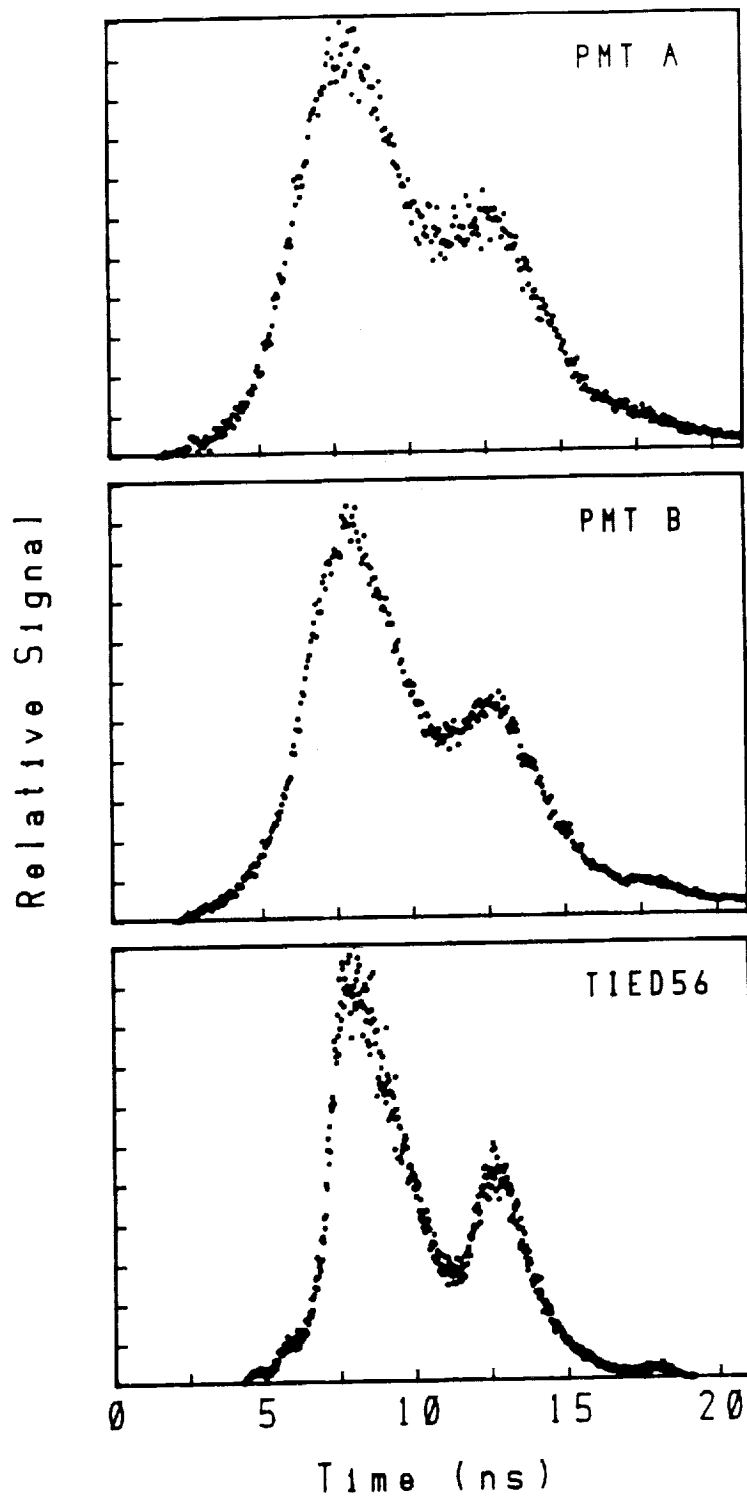
Figure 7.4 Average temporal irradiance of the UV beam measured with the TIED56 avalanche photodiode and the photomultiplier tubes for monochromators A and B using Rayleigh scattering.

scanners. The measured voltages from the fast samplers were digitized and stored with the SR245 computer interface module and the SR265 software package. Typically, for this experiment we averaged the fluorescence signal for 600 to 1200 laser shots. For the PIN photodiode we used a 10 ns gate of the SR250 gated integrator and boxcar averager. We note that on the average, only a small number of fluorescence photons were collected for each laser shot; however, with increases in focussed beam width, the collection solid angle ($\Omega \approx 0.006$ sr for our experiment), and the efficiency of some of the optical components (e.g., the beam splitter), single-shot measurements would be possible.

In Fig. 7.4, the average temporal responses of the PMTs using Rayleigh scattering are compared to the average intensity profile obtained with a silicon avalanche photodiode (Texas Instruments TIED56), which has a temporal response of ~200 ps (Harris et al., 1980). These waveforms, which were taken consecutively rather than simultaneously, were recorded by repetitively scanning in time over the signal, using the 200 ps sampling gate of the fast sampler (SR255), and a scanning voltage supplied by the SR245 computer interface module. The PMTs show good temporal resolution, though the convolution of the detector response and the true temporal profile does result in some distortion of the profile features.

7.4 Results and Discussion

For the fluorescence experiments, we used the $Q_1(8)/P_1(9)$ excitation/detection line pair. These lines are suitable since they are isolated from neighboring lines; in addition, the population of the $N'' = 8$ level varies by only ~10% from 1100 to 2600 K. To attenuate the laser irradiance, we used Pyrex plates of different thickness; these plates were calibrated against neutral density filters (inserted in the fluorescence optical train) by using Rayleigh scattering with geometry A, since the detected signal with this geometry should be insensitive to beam steering caused by the plates. (We note that Pyrex is not the ideal attenuating material for $\lambda \simeq 310$ nm because the transmission is a strong function of wavelength.) To account for possible variations in transmission with position, we *keyed* the plates, and thus we could put them in the same orientation each time. Because the plates steer the laser beam to different locations in the flame, the fluorescence focusing lens for monochromator B, L_{fB} (see Fig. 7.3), was positioned to maximize the signal with each change of attenuation; the lens for monochromator A required no adjustment since the probe diameter was smaller than the slit height. In addition, for lens L_{fB}, a dial gage was used to measure the relative

displacement of this lens, which equals (when multiplied by the system magnification) the displacement of the beam in the flame. Using the vertical fluorescence profile, the saturation curves could then be corrected for beam displacement. Although the saturation curves are affected by beam steering, the ratio of the signals S_{fA}/S_{fB} is not affected insofar as Q_{eff} does not vary over the region probed by the beam.

Because of saturation, the fluorescence signal can also be adversely affected by scattered or reflected radiation. To block some of this radiation, we placed an iris diaphragm directly before the laser focussing lens, with the iris opened just wide enough to allow the beam to pass. In addition, with detection geometry A, we noticed a significant improvement in the vertical resolution of the atmospheric fluorescence measurements when the window at the laser entry port was removed; this indicates that the effective probe diameter was increased by the scattered and reflected radiation from the window. Consequently, we were careful to keep this window clean, thus minimizing the scattered radiation. This situation could be ameliorated further with anti-reflection coatings on the windows.

Table 7.1   Description of $C_2H_6/O_2/N_2$ flames used in experiments.

Flame	Pressure (atm)	Equivalence Ratio	Dilution Ratio	Flow Rate (slpm)
A	0.98	0.77	3.0	3.15
A′	0.98	0.91	3.0	3.2
B	3.1	0.76	3.1	4.6
C	6.1	0.91	3.1	6.45
D	9.2	0.92	3.1	8.2

The $C_2H_6/O_2/N_2$ flames used in these experiments are listed in Table 7.1. The saturation curves obtained at atmospheric pressure are shown in Fig. 7.5. *Partial* saturation is achieved over a large range of laser powers with both geometries; this is especially evident on the log-log scale where the sensitivity of the fluorescence signal to laser power is shown to be approximately constant over two orders of magnitude of I_L. Because of the large effective probe diameter for geometry A and the large vertical gradient in OH concentration, some spatial averaging in the vertical fluorescence profile was evident in flame A with this geometry. Consequently, to generate the atmospheric saturation curves (and the quenching calibration curve) we used a richer flame (flame A′), where the OH concentration gradient was less than for flame A.
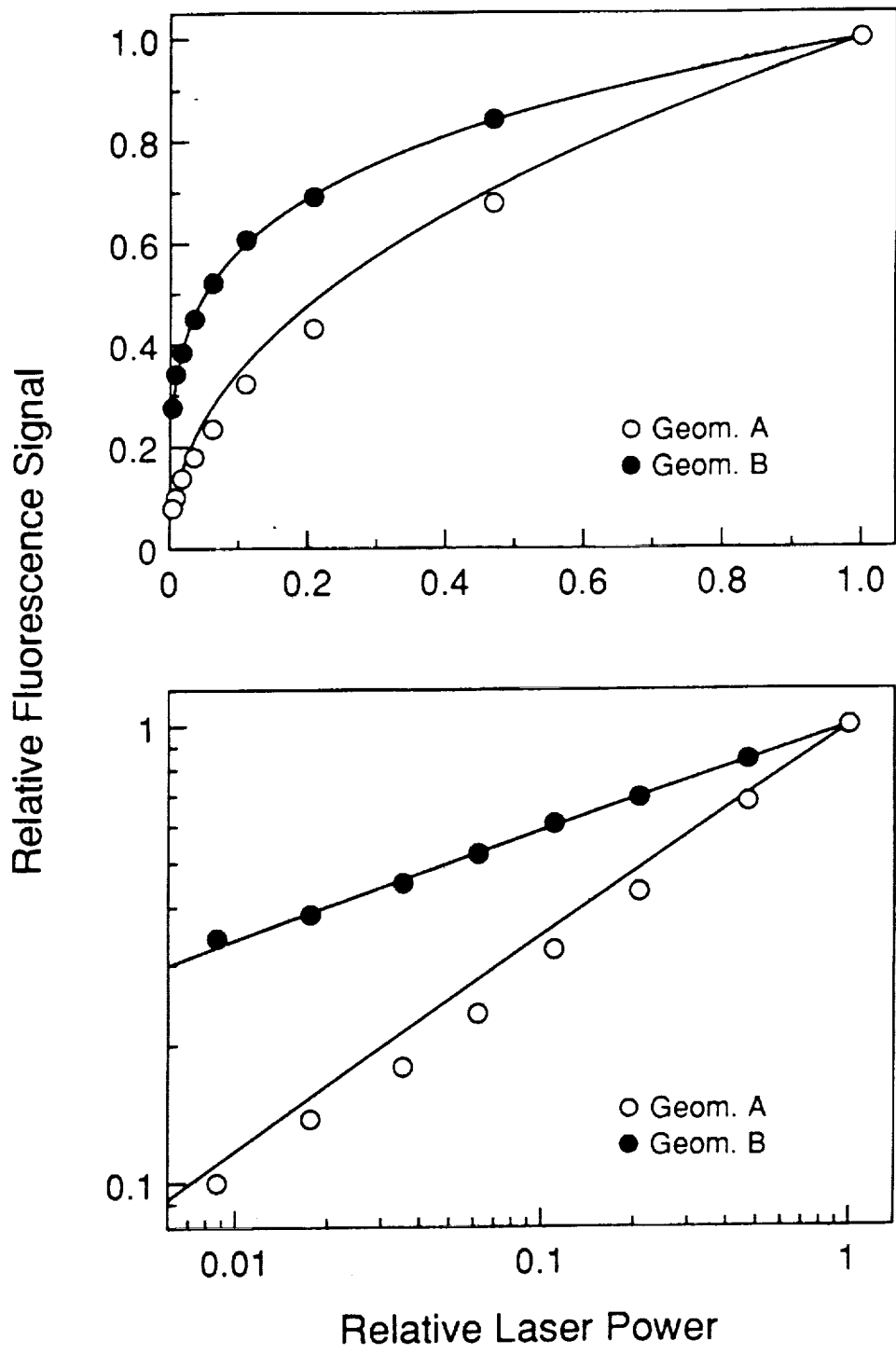
Figure 7.5   Saturation curves in an atmospheric $C_2H_6/O_2/N_2$ flame (flame A' in Table 7.1). The solid lines show the saturation behavior for a simple two-level model using a spatial irradiance function described by Eq. (7.16). For geometry A, we assume that the spatial irradiance function is axisymmetric.

Table 7.2   Parameters describing laser excitation and
            collisional quenching.[a,b]

E	15 mJ
P_L	3.3×10^6 W
I_L^P	2.6×10^{10} W/cm^2
W_{lu}^P	4.2×10^{13} s^{-1}
ν_0	32328 cm^{-1}
A_{lu}	6.399×10^5 s^{-1}
Q_{eff}	2.9×10^9 s^{-1}
$\Delta\nu_L$	0.5 cm^{-1}
$W_p{}'$	15×10^3

[a] The energy used in the calculation is the value estimated to reach the burner, accounting for optical losses, when starting with 18 mJ/pulse.

[b] $\Delta\nu_L$ denotes the laser spectral width (FWHM).

Using a simple two-level model ($\gamma = 0$), the predicted relative saturation curve from Eqs. (7.4) and (7.7) becomes

$$\frac{S_f}{S_{f,m}} = \frac{\int_V \alpha_{sat}\,dV}{\int_V \alpha_{sat,m}\,dV} \quad , \tag{7.15}$$

where $S_{f,m}$ refers to the fluorescence signal at maximum laser power. For geometry B, good agreement between the theoretical and experimental saturation curves results when using the spatial excitation function

$$W_{lu}(r) = \frac{W_{lu}^P}{[\,1 + (r/w)^2\,]^{2.2}} \quad , \tag{7.16}$$

where W_{lu}^P is the absorption rate coefficient at the beam center line, r is the radial position, and w

is the beam halfwidth. Calculation of the maximum center-line rate coefficient, W_{lu}^P, is summarized in Table 7.2; the resulting maximum saturation parameter is 15×10^3. Estimation of W_{lu}^P and $W_p{}'$ from the laser parameters in Table 7.2 is discussed in detail in Chapter 6. To model the saturation behavior of geometry A, we again use Eq. (7.16) with the assumption that the excitation profile is axisymmetric (though we did observe some asymmetry in the beam profile). The resulting saturation curve (Fig. 7.5) is in reasonable agreement with the experimental data for geometry A.
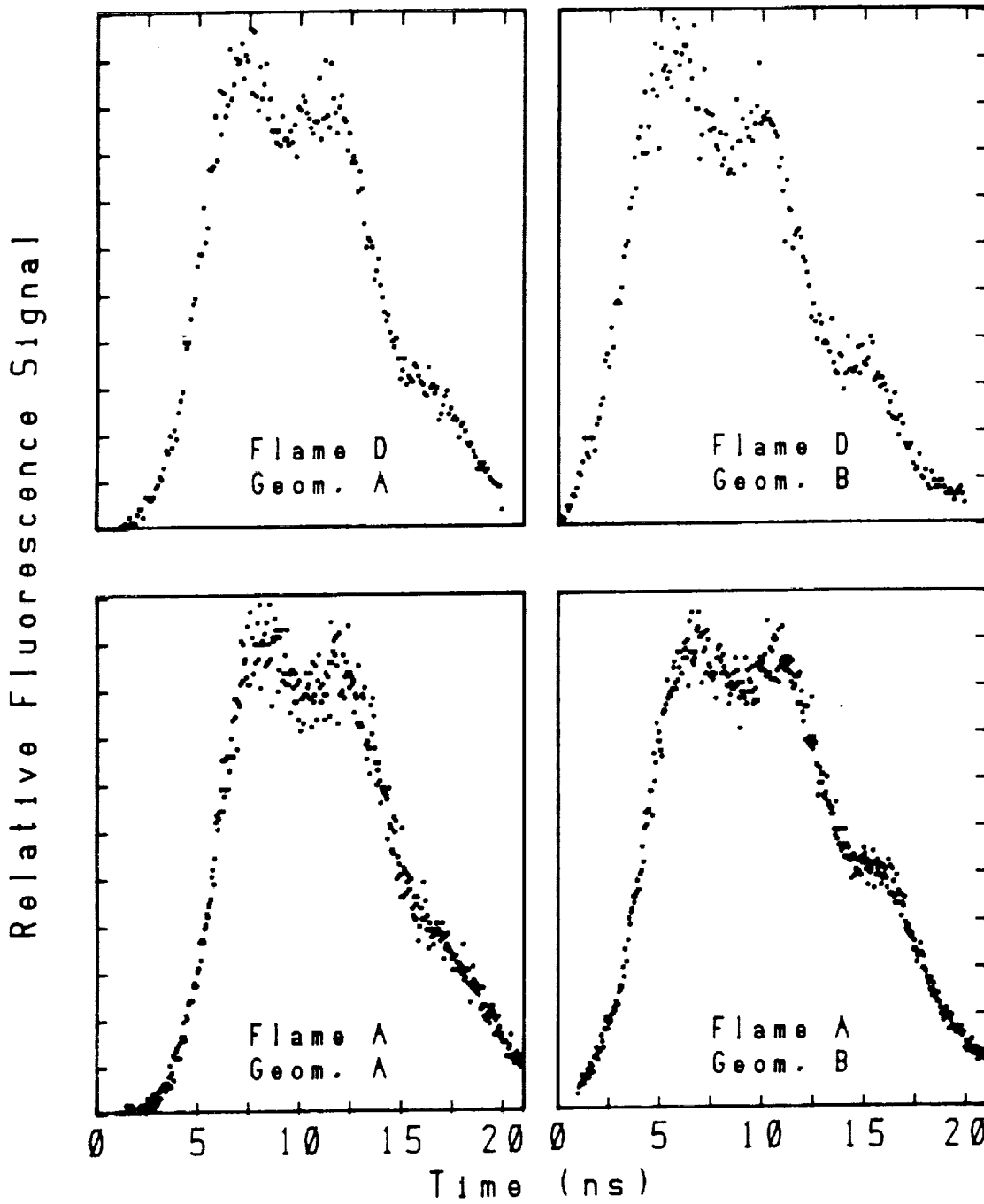
Figure 7.6   Average temporal intensity of fluorescence signal for flames A (30 scans) and D (80 scans).
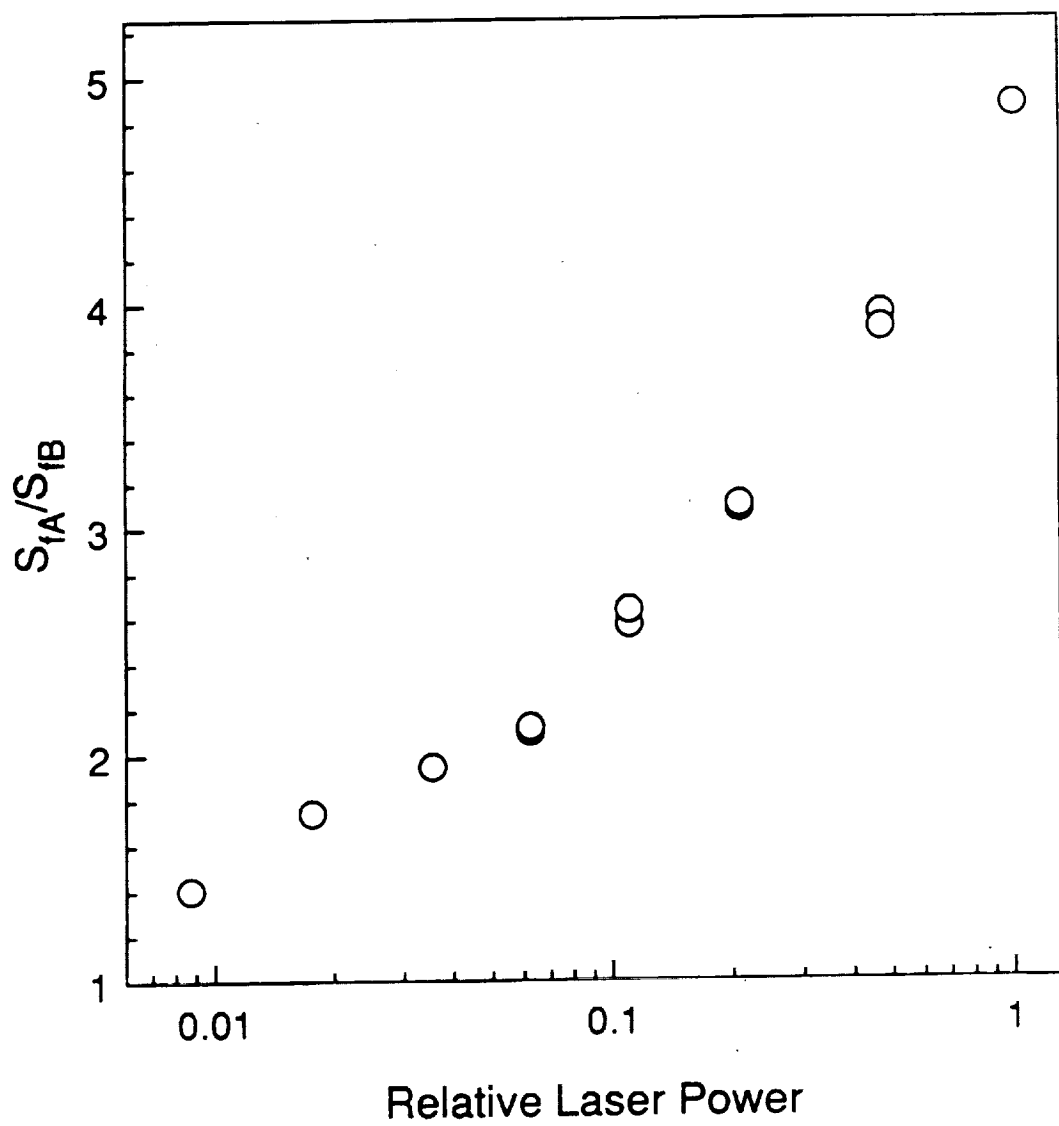
Figure 7.7   Quenching calibration curve derived from the atmospheric saturation curves (Fig. 7.5) in flame A' (see Table 7.1). Multiple data points at the same laser power are repeated measurements.

Figure 7.6 shows temporal fluorescence profiles for the two geometries taken at 1 and 9.2 atm (flames A and D). As discussed in Chapter 6, depletion of the laser-coupled levels can be observed (at the second temporal lobe relative to the first) when comparing profiles at 1 and 9.2 atm. This is especially evident with geometry B, where we expect a larger spatially-averaged depletion of the laser-coupled levels.

In Fig. 7.7, we show S_{fA}/S_{fB} versus relative laser power obtained from the atmospheric saturation curves. Though we refer to this curve as the quenching calibration curve, we emphasize that the corrections derived from the curve take into account variations in laser power as well as the effective quenching rate coefficient. We now make two observations regarding the quenching correction curve. First, any depletion of the laser-coupled levels will result in a larger S_{fA}/S_{fB}, since geometry B (with a smaller contribution from the wings of the fluorescence profile) will show a larger spatially-averaged depletion than geometry A. Consequently, the measured S_{fA}/S_{fB} yields an underestimate of the true quenching correction, since a smaller S_{fA}/S_{fB} ratio corresponds to a larger Q_{eff}. Second, the coupling between the laser and the OH molecules depends on (1) the spectral width of the absorption line relative to that of the laser line and (2) the mode structure of the UV beam. As the absorption line broadens with increasing pressure (from increased collisional broadening) and overtakes the spectral width of the laser beam, the molecules will, on the average, absorb less laser energy (i.e., the coupling between the laser and the transition will become less efficient). An important consequence is that while the saturation curves describe the sensitivity of the fluorescence signal to laser power, they show only approximately the sensitivity to collisional environment. To investigate this difference, we have modelled the excitation process with rate equations for levels l and u using an approach similar to the one taken by Piepmeier (1972a, 1972b); we have also included the effect of the spatial excitation profile using Eq. (7.16). With this model, we calculated the sensitivity of the fluorescence signal to both laser power and pressure. The results suggest that the Cottereau method provides a good estimate of the quenching correction factor, f_Q, which accounts for variations in coupling efficiency as well as quenching and laser power (Appendix D).

The fluorescence voltages for geometries A and B were calibrated at atmospheric pressure using flame A by comparing the relative OH fluorescence profiles with a profile of absolute OH number density derived from absorption measurements (Fig. 7.8). To minimize the effect of self absorption on the profiles, fluorescence was collected at the near edge of the burner; comparison
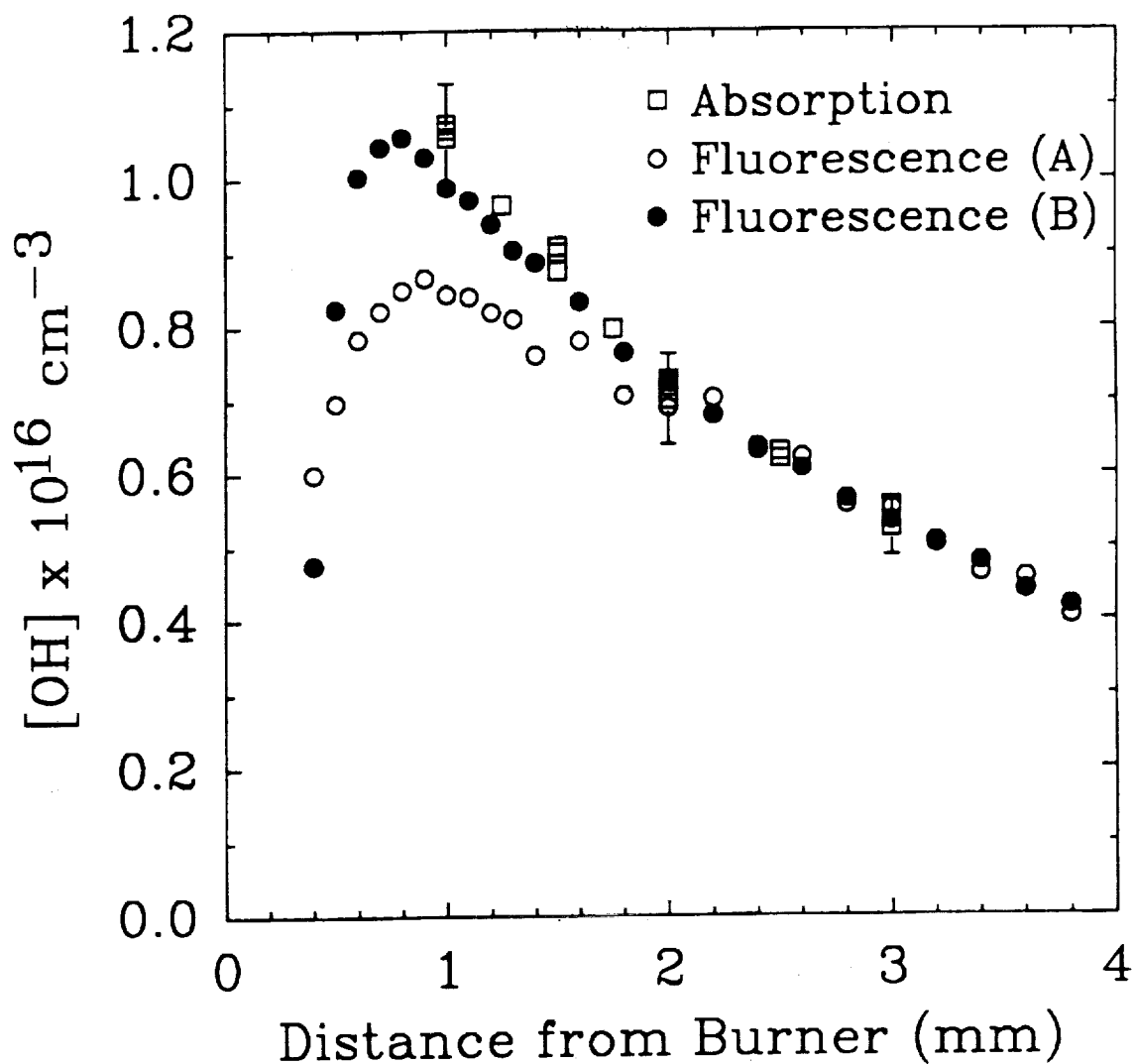
Figure 7.8   Calibration of relative OH fluorescence measurements using absorption measurements in an atmospheric-pressure $C_2H_6/O_2/N_2$ flame (flame A in Table 7.1). Multiple data points (for absorption) at the same height represent measurements made on different days.

of the absorption profile with the relative fluorescence profile from geometry B demonstrates that the fluorescence signal is not measurably affected by self absorption. Comparing the ratios of S_{fA}/S_{fB} in flames A and A' (see Table 7.3) indicates a slightly larger Q_{eff} for flame A' (relative to A); consequently, we extrapolated the quenching calibration curve (Fig. 7.7) to obtain the reference value of W_r' in flame A (where we calibrated the fluorescence voltages with absorption). The effect of spatial averaging when using geometry A is evident in Fig. 7.8; near the burner, where the OH concentration varies strongly with position, the fluorescence profiles A and B deviate significantly. Profile B, because of the small vertical dimension of the sampling volume $(42 \mu m)$, is not significantly affected by spatial averaging.

The absorption measurements in Fig. 7.8 were performed with a 150-W xenon arc lamp, and the effective absorption path length was calculated from horizontal fluorescence scans across the burner (see Chapter 6). For the absorption measurements in flames A and B, we typically used 10 or more absorption lines and the curve-of-growth method (Lucht et al., 1978) to calculate the total OH number density. In a few of the absorption measurements at 3.1 atm and all the measurements at 6.1 atm, we repetitively scanned over the $Q_1(6)$ [and the satellite $Q_{12}(6)$] line. This approach was used because flame jitter (which increased with pressure) and subsequent beam steering reduced the signal-to-noise ratio of the individual spectral absorption profiles. With the repetitive scans, we increased the signal-to-noise of the integrated absorption, since the $Q_1(6)$ line had the largest absorption of the lines analyzed. A significant feature of this approach is that scans affected by severe noise (e.g., those resulting from arc-lamp fluctuations) can be easily eliminated from the average. To extract the total number density from the integrated absorption, we used temperatures derived from silica-coated thermocouple measurements. The uncertainty in the absorption measurements denoted in Fig. 7.8 reflect uncertainty contributions from (1) the integrated absorption (cm^{-1}), (2) temperature (3) the collisional linewidths, and (4) the effective absorption path-length (see Appendix C). In cases where 10 or more lines were used to obtain the total number density, we calculated the 95% confidence interval, which includes uncertainties from the calculated temperature and the variation in concentration calculated from the individual lines.

To calculate the number densities N_T at a higher pressure P, we used the relation

Table 7.3   Quenching calibration parameters at maximum laser power.[a,b]

Flame	S_{fA}/S_{fB}	W_r'	$1/[W_r']$
A	5.02	1	1
A'	4.87	0.95	1.05
B	3.96	0.42	2.4 (3.2)
C	2.88	0.14	6.9 (6.7)
D	2.24	0.062	16 (10.2)

[a] We define $W_r' \equiv 1$ in flame A.

[b] The $1/W_r'$ values in parentheses are estimated from experimental data describing electronic quenching (Garland and Crosley, 1986) and rotational energy transfer (Zizak et al., 1986; Lucht et al., 1986). See Chapter 6 for a description of the calculation of this quantity.

Table 7.4   Correction factors for flames B, C, and D.[a,b]

Flame	f_B	Geometry A		Geometry B	
		f_Q	f_e	f_Q	f_e
B	1.00	1.57	1.0	1.21 (1.30)	1.05
C	1.00	2.69	1.0	1.56 (1.56)	1.08
D	1.00	4.17	1.0	1.90 (1.70)	1.09

[a] The f_{QB} in parentheses are the quantities derived from the estimated $1/W_r'$ (see note b for Table 7.3).

[b] The fluorescence calibration factors from flame A are $f_{cA} = 0.556 \pm 0.028 \times 10^{16}$ cm^{-3}/V and $f_{cB} = 2.79 \pm 0.14 \times 10^{16}$ cm^{-3}/V.

$$N_T(P) = f_c f_B f_Q(P) f_e(P) \cdot S_f(P) \quad , \qquad (7.17)$$

where the correction factors f_B and f_e describe changes in the fluorescence signal due to variations in the Boltzmann fraction and the fluorescence collection efficiency, respectively. The factor f_e accounts for the decrease in detected fluorescence accompanying increased collisional broadening; i.e., with increased collisional broadening more fluorescence will fall outside the spectral detection window. For geometry A, with the larger spectral width, we assumed f_e to be

constant; for geometry B, we measured the fluorescence signal as a function of exit slit width in flames A-D, and the factor f_e represents the ratio of signals at 60 μm and 90 μm, compared at pressure P and 1 atm (flame A); i.e.,

$$f_e = \frac{[S_f(60\ \mu m)/S_f(90\ \mu m)]_1}{[S_f(60\ \mu m)/S_f(90\ \mu m)]_P} \quad . \tag{7.18}$$

Because of the finite slit width W_B = 90 μm, this is an underestimate of the correction factor. We also note that S_{fA}/S_{fB} was calculated subsequent to correcting S_{fB} for increased collisional broadening. In addition, for all the flames, the quenching correction factor was derived from an average of several S_{fA}/S_{fB} values in the burnt-gas region, where the variation in Q_{eff} should be small. Averaging these values was not necessary, but it did improve the signal-to-noise ratio of the S_{fA}/S_{fB} measurement. As discussed above, once S_{fA}/S_{fB} has been calculated, W_r' (see Table 7.3) can be found from the quenching calibration curve (Fig. 7.7), and the f_Q can then be determined from the saturation curves (Fig. 7.5). Values for f_B, f_Q, and f_e for flames B, C, and D are listed in Table 7.4.

The resulting vertical OH concentration profiles for flames B, C and D are shown in Figs. 7.9-7.11. As expected from the measurements described in Chapter 6, the fluorescence and absorption measurements compare well at 3.1 atm (Fig. 7.9). As at atmospheric pressure, fluorescence profile A is distorted near the burner surface where the OH concentration is a strong function of position. At 6.1 atm, the calibrated fluorescence measurements are ~25% below the absorption measurements. This is also the result obtained in Chapter 6, and as we noted above, it is apparently due to the spatially-averaged depletion of the laser-coupled levels beyond that at atmospheric pressure. For the measurements at 9.2 atm (Fig. 7.11), we derived f_{cA} and f_{cB} from the comparison of fluorescence and absorption in flame C (rather than in flame A); the other correction factors were also referenced to those in flame C. This approach was taken for flame D, because of the depletion of the laser-coupled levels observed at 6.1 atm.

In addition to the *measured* W_r' in Table 7.3, we also include the corresponding values estimated from data describing electronic quenching (Garland and Crosley, 1986) and rotational energy transfer (Zizak et al., 1986; Lucht et al., 1986; see Chapter 6 for details). The apparent errors in the estimated W_r' are probably due to (1) uncertainties in the calculation of rotational energy transfer and (2) omission of the coupling efficiency between the laser and the transition. We also note that the quenching calibration curve (i.e., S_{fA}/S_{fB} versus laser power) and thus the *measured* W_r' may be affected slightly by some spatial averaging (with geometry A) in flame A'. Nevertheless,

148
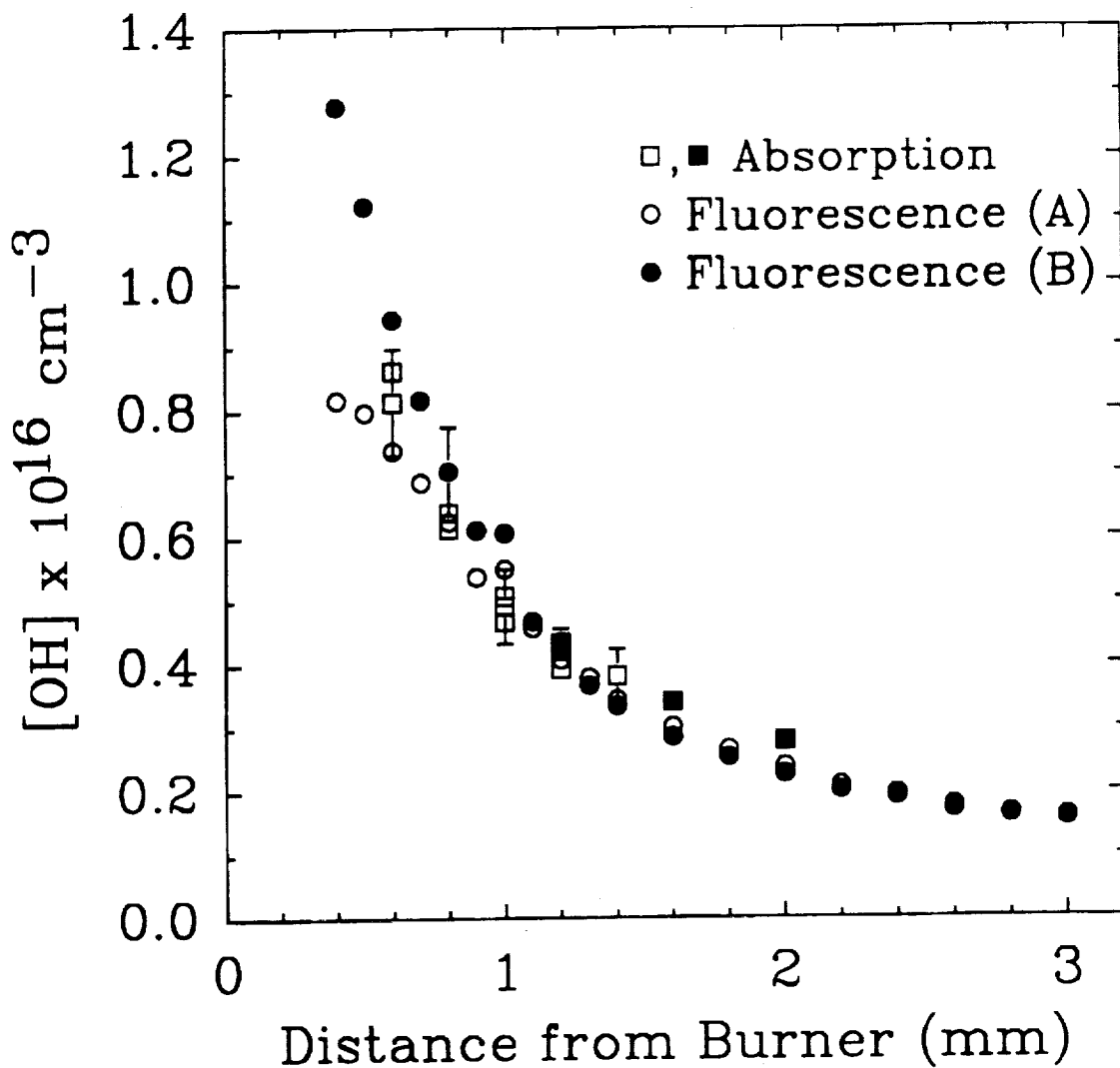
Figure 7.9   Comparison between relative OH fluorescence measurements and absorption measurements in 3.1 atm $C_2H_6/O_2/N_2$ flame (flame B in Table 7.1). The closed squares represent absorption measurements using the $Q_1(6)$ and $Q_{12}(6)$ lines.
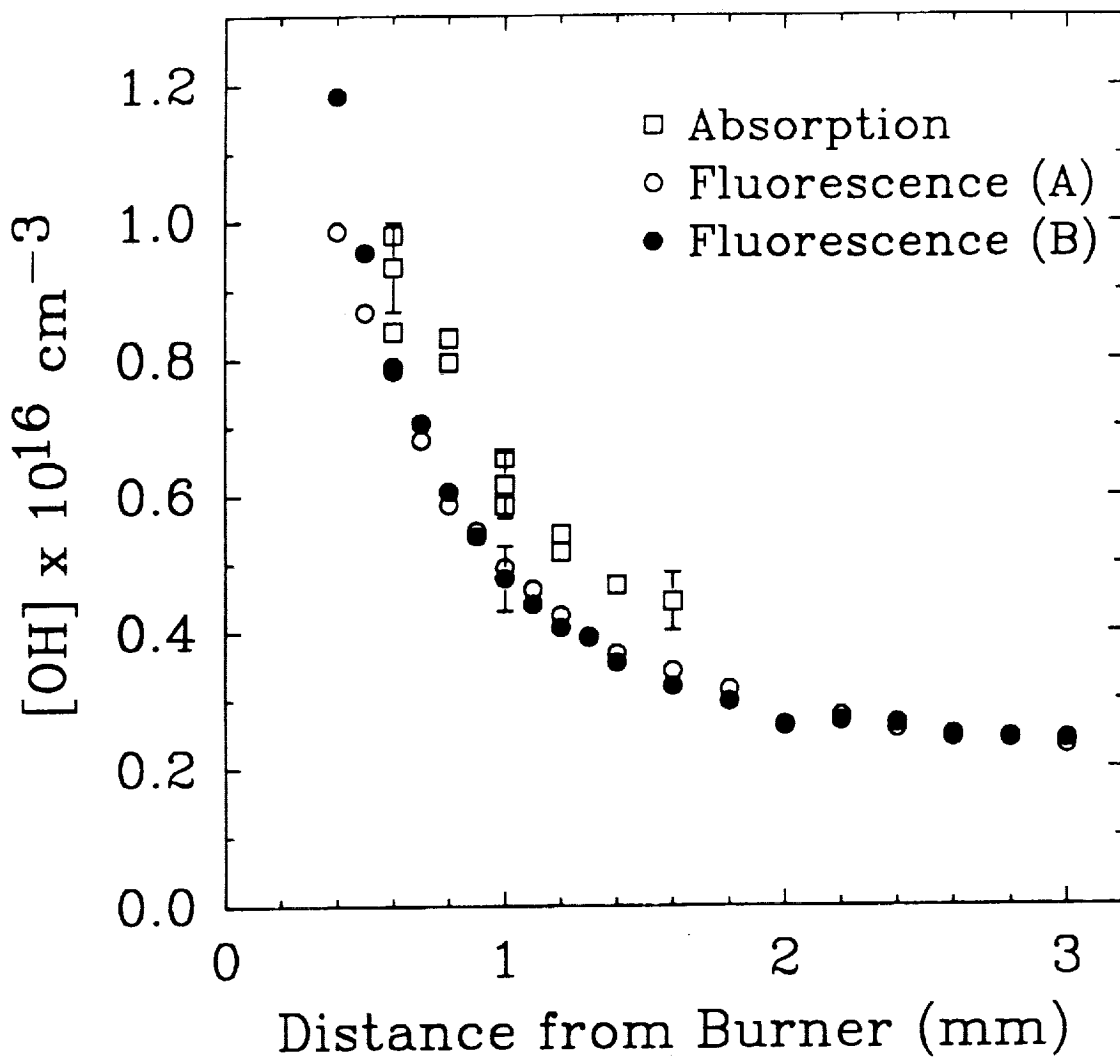
Figure 7.10 Comparison between relative OH fluorescence measurements and absorption measurements in 6.1 atm $C_2H_6/O_2/N_2$ flame (flame C in Table 7.1). The absorption measurements were made using multiple scans of the $Q_1(6)$ and $Q_{12}(6)$ lines.
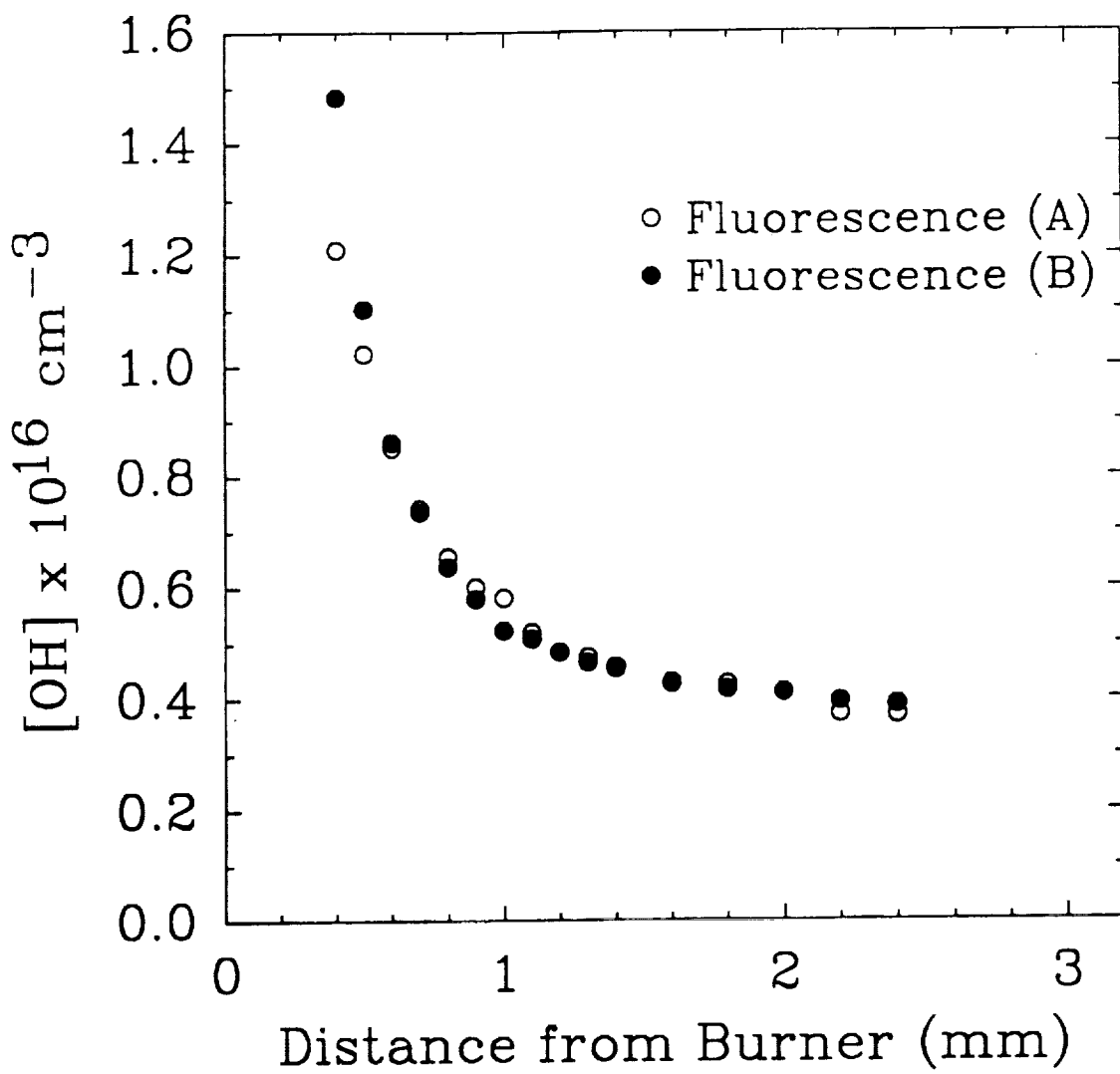
Figure 7.11   OH fluorescence measurements in a 9.2 atm $C_2H_6/O_2/N_2$ flame (flame D in Table 7.1). The fluorescence calibration factor was derived from a comparison of LSF and absorption measurements in flame C (see Table 7.1).

though the difference in the estimated and measured W_r' may be large, the difference in f_Q is small due to saturation (see Tables 7.3 and 7.4). Thus, in some cases one may prefer to apply a quenching correction factor based solely on the estimated ratio of saturation parameters (which in this case is close to the pressure ratio). We also note that the Cottereau method is a potential alternative to the procedure described by Barlow et al. (1989a, 1989b) for absolute concentration measurements of OH. With this approach, Barlow et al. used two lasers to measure simultaneously (1) the relative OH concentration using LIF and (2) H_2, O_2, N_2, and H_2O concentrations using vibrational Raman scattering. With the measured concentrations of the OH-collision partners (i.e., H_2, O_2, N_2, and H_2O) the OH fluorescence voltages were corrected for variations in the electronic quenching rate coefficient in a nonpremixed turbulent jet flame (on a shot-by-shot basis) using quenching cross sections recommended by Garland and Crosley (1986). The Cottereau approach has the advantages of greater simplicity and an *in situ* measurement of the quenching correction factor; however, this method is limited by the accuracy of (1) the balanced cross-rate model and (2) the saturation and quenching calibration curves.

7.5 Conclusions

We have successfully employed a method for making quenching-independent LSF measurements of hydroxyl concentration in high-pressure laminar $C_2H_6/O_2/N_2$ flames. With this technique, one uses two fluorescence detection geometries; the ratio of the two fluorescence signals is a function of the quenching rate coefficient and the spatial dependence of the laser irradiance. As long as the laser spatial irradiance profile is invariant, the ratio of the two fluorescence signals depends only on (1) the center-line saturation parameter and (2) the coupling efficiency between the laser and the transition. Using the Cottereau method, the fluorescence signals from either geometry, which have been calibrated at one condition, can be corrected for their finite sensitivity to quenching via this *in situ* measurement. At atmospheric pressure, we have calibrated the fluorescence signals with absorption measurements; we have also generated the quenching correction function from the corresponding saturation curves in an atmospheric flame. The fluorescence voltages from the flames at 3.1, 6.1 and 9.2 atm have been adjusted for changes in quenching relative to the atmospheric flame, using the experimentally-determined relative quenching rate coefficients; with this procedure, we have obtained absolute concentration profiles of OH in high-pressure flames. The Cottereau method is still affected by the inaccuracy of the

balanced cross-rate model; moreover, the fluorescence profiles from imaging geometry A are adversely affected by scattered and reflected light. Nonetheless, use of this method can further reduce uncertainty in calibrated fluorescence measurements, especially when attempting to obtain absolute number densities under flame conditions significantly different than the calibration condition.

CHAPTER 8

CONCLUSIONS AND RECOMMENDATIONS

8.1 Conclusions

In this report, we have focused on the efficacy of the LSF method for measurement of OH concentration in high-pressure flames. We have investigated theoretically and experimentally the validity of the *balanced cross-rate* model (Lucht et al., 1980, 1983), which relates the measured quantity N_u to the unperturbed number density N_l^0. In essence, the model states that the laser-coupled levels experience approximately no net depletion; i.e.,

$$N_u + N_l \approx N_l^0 \quad . \tag{8.1}$$

The utility of this model is that it requires no knowledge of the collisional environment; consequently, fluorescence measurements can be related more easily to the desired species number density. When this relationship cannot be used due to depletion of the laser-coupled levels and this depletion cannot be accurately measured, LSF can lose much of its attractiveness over linear fluorescence methods.

In the course of this work, we have developed a high-pressure combustion facility, which will be used in future high-pressure combustion studies employing spectroscopic methods. This facility includes the following: (1) a pressure vessel constructed from standard stainless-steel piping components; (2) an internal x-y burner translation system employing inexpensive stepper motors and translation mechanisms; (3) two flat flame burners; and, (4) an electronic gas control system, which is interfaced to a microcomputer. Though the vessel was designed to accommodate turbulent flames, we have used only premixed laminar flames for the present study. To test the facility, we used the laser-induced fluorescence method to measure relative concentrations of OH in lean premixed $C_2H_6/O_2/N_2$ flames at 3.2, 6.3, 9.5, and 12.6 atm. By employing a range of flow rates of the combustible mixture, we demonstrated that the reaction zone can be probed at these pressures. In comparison to atmospheric flames, the reaction zone was small and accordingly, the [OH] gradient was large; we also observed large gradients in the OH recombination zone.

154

We have also performed a theoretical feasibility study on the application of LSF to the measurement of OH concentration in high-pressure flames. Using a numerical model for the collisional dynamics of the OH molecule under nonuniform laser excitation, we investigated the effect of pressure on the validity of the balanced cross-rate model and the sensitivity of the depopulation of the laser-coupled levels to the ratio of rate coefficients describing (1) electronic quenching to the ground-state vibrational levels for which $v'' > 0$ and (2) vibrational relaxation from $v'' > 0$ to $v'' = 0$. At sufficiently high pressures under near-saturated conditions, the total population of the laser-coupled levels reaches an asymptotic value, which is insensitive to the degree of saturation. When the ratio of electronic quenching to vibrational relaxation is small and the rate coefficients for rotational transfer in the ground and excited electronic states are nearly the same, the balanced cross-rate model remains a good approximation for all pressures. When the above ratio is large, depopulation of the laser-coupled levels becomes significant at high pressures, and thus the balanced cross-rate model no longer holds. Under these conditions, however, knowledge of the depletion of the laser-coupled levels could be used to correct the balanced cross-rate model.

We have performed experiments to evaluate the efficacy of LSF for OH concentration measurements in high-pressure combustion environments. First, we demonstrated that saturation is possible in high-pressures $C_2H_6/O_2/N_2$ flames by generating saturation curves at pressures as high as $\sim$12 atm; these curves suggest that partial saturation can be achieved at pressures > 20 atm. To evaluate the limits of the balanced cross-rate model, we compared absorption and calibrated LSF measurements at 3.1 and 6.1 atm. The fluorescence measurements were calibrated with absorption measurements in an atmospheric flame and corrected for their finite sensitivity to quenching with an estimated quenching rate coefficient. In this way, we compared the *spatially-averaged* depletion of the laser-coupled levels (and the effective deviation from the balanced cross-rate model) at 3.1 and 6.1 atm, to the value at atmospheric pressure. While the absorption and calibrated fluorescence measurements compare well at 3.1 atm, the OH fluorescence values are $\sim$25% below the concentrations from absorption at 6.1 atm, indicating an effective error of $\sim$25% in the balanced cross-rate model beyond that in the atmospheric flame. We anticipate that with a reasonable estimate of the quenching correction factor, one can measure OH concentrations within $\pm$50% up to pressures of $\sim$10 atm. We have also presented absolute OH concentration profiles for lean laminar flames at 1, 3.1, 6.1, 9.2 and 12.3 atm; to our knowledge, these are the first high-pressure absolute concentration measurements of OH performed with LIF.

Finally, we have employed a method for making quenching-independent LSF measurements in our $C_2H_6/O_2/N_2$ flames. With this technique, one uses two fluorescence detection geometries; the ratio of the two fluorescence signals is a function of the quenching rate coefficient and the spatial dependence of the laser irradiance. As long as the laser spatial profile is invariant, the ratio of the two fluorescence signals depends only on the relative quenching rate coefficient. Thus, the fluorescence signals from either geometry, which have been calibrated at one condition, can be corrected for their finite sensitivity to quenching from this *in situ* measurement. In this work, we calibrated the fluorescence signals with absorption measurements at 1 atm and generated the requisite quenching correction function from saturation curves. The fluorescence voltages from flames at 3.1, 6.1 and 9.2 atm were adjusted for changes in quenching relative to the atmospheric flame, using the experimentally-determined correction factor. The resulting absolute OH concentration profiles agreed well with those determined by the standard LSF methodology.

8.2 Recommendations

For the high-pressure combustion facility, we make the following recommendations for an improved design.

1. Using the condenser and water trap on the exhaust line, the water was effectively eliminated from the exhaust system; however, for the pressure vessel a drainage system should be designed to direct the water collecting on the interior surfaces to the trap beneath the bottom flange. This would ensure that the accumulation of water does not interfere with the operation of the burner or the electronic components.

2. Though the optical translation stage used for horizontal movement is adequate for most purposes, it does exhibit significant side-play; for more accurate positioning of the burner, the current translation stage should be replaced by a system with reduced side-play (for instance a Newport model M-425-1S stage or a linear bearing/shaft arrangement).

3. The width of the burner guard ring (Fig. 4.4) should be reduced to allow a higher velocity of guard flow for the equivalent volumetric flow of gas. This becomes increasingly important at high pressures, since gas consumption can be large. Finally, for modelling purposes (i.e., providing a tractable boundary condition), the grain size of the sintered bronze flameholder ($\sim$100 μm) should be reduced, since this dimension should be small compared to the flame stand-off distance.

We also note that with LSF (where only a small amount of the total fluorescence is observed), single-shot measurements using our facility were not possible for OH number densities $\leq 10^{16}$ cm^{-3}, because of the small solid angle of fluorescence collection afforded by placing the fluorescence collection lens outside the pressure vessel. However, single-shot measurements would be more feasible by mounting the fluorescence collection lens inside the vessel on the window-housing flange; this could result in a 10 to 20-fold increase in signal. An additional increase in signal can be obtained by opening the monochromator exit slit; the maximum width, of course, is limited by the requirement for spectral isolation of the detected transition. This approach also has the advantage of decreasing the sensitivity of the fluorescence signal to collisional broadening.

Improved flame stability for the flat flame burner would allow absorption measurements at pressures higher than 6 atm. Consequently, one could further characterize the depletion of the laser-coupled levels as a function of pressure; this would be useful when trying to apply LSF for OH measurements at pressures to 20 atm, for example. As noted in Chapter 6, one can potentially estimate the spatially-averaged depletion of the laser-coupled levels from the temporal fluorescence profile. This would require an OH dynamic model, albeit a simpler one (using perhaps only a few energy states) than that described in Chapters 3 and 6. This modelling is of course made easier when the temporal pulse is distinctive (i.e., containing two or more temporal lobes, which for the Quanta-Ray Nd:YAG is obtainable through the setting of the Q-switch delay). The necessary input to the model would include descriptions of the laser temporal and spatial profiles and a rough estimate of the center-line laser irradiance; the spatial profile could perhaps be obtained from a saturation curve (as we did in Chapter 6). The spatially-averaged depletion could then be found by matching the experimental temporal profile with the computational profile for a specific spatially-averaged depletion.

Finally, for the quenching-independent measurements employing the two detection geometries (Chapter 7), we expect a significant improvement in spatial resolution upon reducing reflected UV radiation from the windows. This could be accomplished with the appropriate anti-reflection coatings for the laser entry and exit windows. For the high-pressure facility, an anti-reflection coating is preferable to a Brewster-angle window, because of the large displacement of the laser beam accompanying insertion of a Brewster window (thus making the optical alignment more difficult). In addition, the Cottereau method would be improved with the use of volume-absorbing neutral density filters appropriate for the UV. This would eliminate much of the uncertainty in the quenching calibration and saturation curves. With good spatial resolution and accurate quenching calibration and saturation curves, the Cottereau method is a good alternative to the method used by Barlow et al. (1989a, 1989b; see also Chapter 2), potentially offering greater accuracy and reduced complexity for absolute concentration measurements of OH in turbulent flames.

LIST OF REFERENCES

Abramowitz, M. and Stegun, I.A. (1968). *Handbook of Mathematical Functions,* Dover Publications, New York.

Alkemade, C.Th.J., (1985). Anomalous saturation curves in laser-induced fluorescence. *Spectrochim. Acta* **40B**, 1331.

Altkorn, R. and Zare, R.N. (1984). Effects of saturation on laser-induced fluorescence measurements of population and polarization. *Ann. Rev. Phys. Chem.* **35**, 265.

Andresen, P., Bath, A., Groger, W., Lulf, H.W., Meijer, G., and ter Meulen, J.J. (1988). Laser-induced fluorescence with tunable excimer lasers as a possible method for instantaneous temperature field measurements at high pressures: checks with an atmospheric flame. *Appl. Opt.* **27**, 365.

Armstrong, B.H. (1967). Spectrum line profiles: the Voigt function. *JQSRT* **17**, 61.

Barlow, R.S., Dibble, R.W., Chen J.Y., Lucht, R.P. (1989). Effect of Damkohler Number on superequilibrium OH concentration in turbulent nonpremixed jet flames. AIAA-89-0061.

Barlow, R.S., Dibble, R.W., Lucht, R.P. (1989). Simultaneous measurement of Raman scattering and laser-induced OH fluorescence in nonpremixed turbulent jet flames. *Opt. Lett.* **14**, 263.

Baronavski, A.P. and McDonald, J.R. (1977). Measurement of C_2 concentrations in an oxygen-acetylene flame: an application of saturation spectroscopy. *J. Chem. Phys.* **66**, 3300.

Bonczyk, P.A. and Shirley, J.A. (1979). Measurement of CH and CN concentration in flames by laser-induced saturated fluorescence. *Combust. Flame* **34**, 253.

Bradley, D. and Matthews K.J. (1968). Measurement of high gas temperatures with fine wire thermocouples. *J. Mech. Eng. Sci.* **10**, 299.

Breene, R.G. (1961). *The Shift and Shape of Spectral Lines,* Pergamon, New York.

Campbell, D.H. (1984a). Collisional effects on laser-induced fluorescence measurements of hydroxide concentration in a combustion environment. 1: effects for v'=0 excitation. *Appl. Opt.* **23**, 689.

Campbell, D.H. (1984b). Collisional effects on laser-induced fluorescence measurements of hydroxide concentration in a combustion environment. 2: effects for v'=1 excitation. *Appl. Opt.* **23**, 1319.

Carlone, C. and Dalby, F.W. (1969). Spectrum of the hydroxyl radical. *Can. J. Phys.* **47**, 1945.

Carter, C.D., Salmon, J.T., King, G.B., and Laurendeau, N.M. (1987). Feasibility of hydroxyl concentration measurements by laser-saturated fluorescence in high-pressure flames. *Appl. Opt.* **26**, 4551.

Carter, C.D., King, G.B., and Laurendeau, N.M. (1989). A combustion facility for high-pressure flame studies by spectroscopic methods. *Rev. Sci. Instrum.* **60**, 2606.

Chan, C. and Daily, J.W. (1980). Laser excitation dynamics of OH in flames. *Appl. Opt.* **19**, 1357.

Chao, B.H. and Law, C.K. (1988). Duality, pulsating instability, and product dissociation in burner stabilized flames. *Combust. Sci. Tech.* **62**, 211.

Copeland, R.A., Dyer, M.J., and Crosley, D.R. (1985). Rotational-level-dependent quenching of $A^2\Sigma^+$ OH and OD. *J. Chem. Phys.* **82**, 4022.

Cottereau, M.J. (1986). Single-shot laser-saturated fluorescence measurements: a new method. *Appl. Opt.* **25**, 744.

Daily, J.W. (1977). Saturation effects in laser induced fluorescence spectroscopy. *Appl. Opt.* **16**, 568.

Daily, J.W. (1978). Saturation of fluorescence in flames with a Gaussian laser beam. *Appl. Opt.* **17**, 225.

Dieke, G.H. and Crosswhite, H.M. (1962). The ultraviolet bands of OH. *JQSRT* **2**, 97.

Dimpfl, W.L. and Kinsey, J.L. (1979). Radiative lifetimes of $OH(A^2\Sigma)$ and Einstein coefficients for the A-X system of OH and OD. *JQSRT* **25**, 111.

Doherty, R.M. and Crosley, D.R. (1984). Polarization of laser-induced fluorescence in an atmospheric pressure flame. *Appl. Opt.* **23**, 713.

Drake, M.C. and Pitz, R.W. (1985). Comparison of turbulent diffusion flame measurements of OH by planar fluorescence and saturated fluorescence. *Experiments in Fluids* **3**, 283.

Drake, M.C., Pitz, R.W., Lapp, M., Fenimore, C.P., Lucht, R.P., Sweeney, D.W., and Laurendeau, N.M. (1984). Measurements of superequilibrium hydroxyl concentrations in turbulent nonpremixed flames using saturated fluorescence. *Twentieth Symposium (International) on Combustion*, The Combustion Institute, Pittsburgh, 327.

Eckbreth, A.C. (1988). *Laser Diagnostics for Combustion Temperature and Species*, Abacus Press, Cambridge.

Elzinga, P.A., Kneisler, F.J., Lytle, F.E., Jiang, Y. King, G.B., and Laurendeau N.M. (1987). Pump/probe method for fast analysis of visible spectral signatures utilizing asynchronous optical sampling. *Appl. Opt.* **26**, 4303.

Engleman, R. (1969). Collision broadening of transient absorption spectra. *JQSRT* **9**, 391.

Edwards, T., Weaver, D.P., Adams, R., Hulsizer, S., and Campbell, D.H. (1985). High-pressure combustor for the spectroscopic study of solid propellant combustion chemistry. *Rev. Sci. Instrum.* **56**, 2131 (1985).

Edwards, T., Weaver, D.P., and Campbell D.H. (1987). Laser-induced fluorescence in high pressure solid propellant flames. *Appl. Opt.* **26**, 3496.

Fairchild, P.W., Smith, G.P., and Crosley, D.R. (1983). Collisional quenching of $A^2\Sigma^+$ OH at elevated temperatures. *J. Chem. Phys.* **79**, 1795.

Felton, P.G., Mantzaras, J., Bomse, D.S., and Woodin, R.L. (1988). Initial two-dimensional laser-induced fluorescence measurements of OH radicals in an internal combustion engine. *SAE Technical Series Paper 88163.*

Fiechtner, G.J., Jiang, Y., King, G.B., Kneisler, R.J., and Lytle, F.E. (1988). Determination of relative number density and decay rate for atomic sodium in an atmospheric premixed flame by asynchronous optical sampling. *Twenty-Second Symposium (International) on Combustion*, The Combustion Institute, Pittsburgh, 1915.

Fiechtner, G.J. (1989). Measurements of atomic sodium in flames by asynchronous optical sampling. Ph.D. Thesis, School of Mechanical Engineering, Purdue University, West Lafayette, Indiana.

Flower, W.L. and Bowman, C.T. (1984). Measurement of the structure of sooting laminar diffusion flames at elevated pressures. *Twentieth Symposium (International) on Combustion*, The Combustion Institute, Pittsburgh, 1035.

Flower, W.L. (1986). The effect of elevated pressure on the rate of soot production in laminar diffusion flames. *Combust. Sci. Tech.* **48**, 31.

Flower, W.L. and Bowman, C.T. (1986). Soot production in axisymmetric laminar diffusion flames at pressures from one to ten atmospheres. *Twenty-first Symposium (International) on Combustion*, The Combustion Institute, Pittsburgh, 1115.

Flower, W.L. (1986). An investigation of soot formation in axisymmetric turbulent diffusion flames at elevated pressure. Western States Section/The Combustion Institute, Paper WSS/CI 88-29, Salt Lake City, Utah.

Garland, N.L. and Crosley, D.R. (1986). On the collisional quenching of electronically excited OH, NH, and CH in flames. *Twenty-First Symposium (International) on Combustion*, The Combustion Institute, Pittsburgh, 1693.

German, K.R. (1976). Collision and quenching cross sections in the $A^2\Sigma^+$ state of OH and OD. *J. Chem. Phys.* **64**, 4065.

Harris, J.M., Lytle, F.E., and McCain, T.C. (1976). Squirrel-cage photomultiplier base design for measurement of nanosecond fluorescence decays. *Anal. Chem.* **48**, 2095.

Harris, J.M., Barnes, Jr., W.T., Gustafson, T.L., Bushaw, T.H., and Lytle, F.E. (1980). Simple, inexpensive photodetector for subnanosecond sources. *Rev Sci. Instrum.* **51**, 988.

Harris, M.M. (1985). Effects of temperature and hydroxyl concentration on incipient soot formation in premixed flames. M.S. Thesis, Purdue University, W. Lafayette, Indiana.

Herzberg, G. (1950). *Spectra of Diatomic Molecules*, Van Nostrand Reinhold, New York, 405-435.

Hinze, J.O. (1975). *Turbulence*, McGraw-Hill, New York, 85-91.

Hjima, T. and Takeno, T. (1986). Effects of temperature and pressure on burning velocity. *Combust. Flame* **65**, 35.

Hui, A.K., Armstrong, B.H., and Wray, A.A. (1978). Rapid computation of the Voigt and complex error functions. *JQSRT* **19**, 509.

Humlicek, J. (1979). An efficient method for evaluation of the complex probability function: the Voigt function and its derivatives. *JQSRT* **21**, 309.

Jeffries, J.B., Kohse-Hoinghaus, K., Smith, G.P., Copeland, R.A., and Crosley, D.R. (1988). Rotational-level-dependent quenching of OH($A^2\Sigma^+$) at flame temperatures. *Chem. Phys. Lett.* **152**, 160.

Kohse-Hoinghaus, K., Perc, W., and Just, Th. (1983). Laser-induced saturated fluorescence as a method for determination of radical concentrations in flames. *Ber. Bunsenges. Phys. Chem.* **87**, 1052.

Kohse-Hoinghaus, K., Perc, W., and Just, Th. (1984). Determination of absolute OH and CH concentrations in a low pressure flame by laser-induced saturated fluorescence. *Nineteenth Symposium (International) on Combustion*, The Combustion Institute, Pittsburgh, 1177.

Kohse-Hoinghaus, K., Koczar, P., and Just, Th. (1986). Absolute concentration measurements of OH in low-pressure hydrogen-oxygen, methane-oxygen, and acetylene-oxygen flames. *Twenty-First Symposium (International) on Combustion*, The Combustion Institute, Pittsburgh, 1719.

Kohse-Hoinghaus, K., Jeffries, J.B., Copeland, R.A., Smith, G.P., and Crosley, D.R. (1988). The quantitative LIF determination of OH concentrations in low-pressure flames. *Twenty-Second Symposium (International) on Combustion*, The Combustion Institute, Pittsburgh, 1857.

Korn, A.K. and Korn, T.M. (1968). *Mathematical Handbook for Scientists and Engineers*, McGraw-Hill, New York.

Kramers, H. (1946). Heat transfer from spheres to flowing media. *Physica* **12**, 61.

Laurendeau, N.M., Goldsmith, J.E.M. (1989). Comparison of hydroxyl concentration profiles using five laser-induced fluorescence methods in a lean subatmospheric-pressure $H_2/O_2/Ar$ flame. *Combust. Sci. Tech.* **63**, 139.

Lee, M.P., Paul, P.H., and Hanson, R.K. (1986). Laser-fluorescence imaging of O_2 in combustion flows using an ArF laser. *Opt. Lett.* **11**, 7.

Lengel, R.K. and Crosley, D.R. (1977). Energy transfer in $A^2\Sigma^+$ OH. I. rotational. *J. Chem. Phys.* **67**, 2085.

Lengel, R.K. and Crosley, D.R. (1978). Energy transfer in $A^2\Sigma^+$ OH. II. vibrational. *J. Chem. Phys.* **68**, 5309.

Lucht, R.P., Peterson, R.C., and Laurendeau, N.M. (1978). Fundamentals of absorption spectroscopy for selected diatomic flame radicals. Report PURDU-CL-78-06, School of Mechanical Engineering, Purdue University, West Lafayette, Indiana.

Lucht, R.P., Sweeney, D.W., and Laurendeau, N.M. (1980a). In *Laser probes for combustion chemistry*. D.R. Crosley (Ed.), American Chemical Society, ACS Symposium Series, Washington, D.C., **134**, 145.

Lucht, R.P., Sweeney, D.W., and Laurendeau, N.M. (1980b). Balanced cross-rate model for saturated fluorescence in flames using a nanosecond pulse length laser. *Appl. Opt.* **19**, 3295.

Lucht, R.P. (1981). Experimental and theoretical investigations of laser-saturated OH fluorescence in flames. Ph.D. Thesis, School of Mechanical Engineering, Purdue University, West Lafayette, Indiana.

Lucht, R.P., Sweeney, D.W., and Laurendeau, N.M. (1982). Temperature measurements by two-line laser-saturated fluorescence in flames. *Appl. Opt.* **21**, 3729.

Lucht, R.P., Sweeney, D.W., and Laurendeau, N.M. (1983). Laser-saturated fluorescence measurements of OH concentration in flames. *Combust. Flame* **50**, 189.

Lucht, R.P., Sweeney, D.W., Laurendeau, N.M., Drake, M.C., Lapp, M., and Pitz, R.W. (1984). Single-pulse, laser-saturated fluorescence measurements of OH in turbulent flames. *Opt. Lett.* **9**, 90.

Lucht, R.P., Sweeney, D.W., and Laurendeau, N.M. (1985). Laser-saturated fluorescence measurements of OH in atmospheric pressure $CH_4/O_2/N_2$ flames under sooting and non-sooting conditions. *Combust. Sci. Tech.* **42**, 259.

Lucht, R.P., Sweeney, D.W., and Laurendeau, N.M. (1986). Time-resolved fluorescence investigation of rotational transfer in $A^2\Sigma^+$ (v=0) OH. *Appl. Opt.* **25**, 4086.

Macomber, J.D. (1968). A bibliography of transient effects in resonant elastic response of matter to an intense light pulse. *IEEE J. Quant. Elec.* **QE-9**, 1.

Mailander, M. (1978). Determination of absolute transition probabilities and particle densities by saturated fluorescence excitation. *J. Appl. Phys.* **49**, 1256.

Matsumoto, R., Nakajima, T, Kimoto, K. Noda, S., and Maeda, S. (1982). An experimental study on low frequency oscillation and flame-generated turbulence in premixed/diffusion flames. *Combust. Sci. Tech.* **27**, 103.

Pasternack, L., Baronavski, A.P., and McDonald, J.R. (1978). Application of saturation spectroscopy for measurement of atomic Na and MgO in acetylene flames. *J. Chem. Phys.* **69**, 4830.

Penner, S.S. (1959). *Quantitative Molecular spectroscopy and Gas Emissivities*, Addison-Wesley, Reading, Mass.

Peterson, R.C. (1981). Kinetics of hydrogen-oxygen-argon and hydrogen-oxygen-argon-pyridine combustion using a flat flame burner. Ph.D. Thesis, School of Mechanical Engineering, Purdue University, West Lafayette, Indiana.

Peterson, R.C. and Laurendeau, N.M. (1985). The emittance of yttrium-beryllium oxide thermocouple coating. *Combust. Flame.* **60**, 279.

Piepmeier, E.H. (1972a). Theory of laser saturated atomic resonance fluorescence. *Spectrochim. Acta* **27B**, 431.

Piepmeier, E.H. (1972b). Influence of non-quenching collisions upon saturated resonance fluorescence. *Spectrochim. Acta* **27B**, 445.

Press, W.H., Flannery, B.P., Teukolsky, S.A., and Vetterling, W.T. (1986). *Numerical Recipes: The Art of Scientific Computing*, Cambridge University Press, Cambridge.

Rea, E.C., Chang, A.Y., and Hanson, R.K. (1987). Shock tube study of pressure broadening of the $A^2\Sigma^+$-$X^2\Pi$ (0,0) band of OH by Ar and N_2. *JQSRT* **37**, 117.

Rea, E.C., Chang, A.Y., and Hanson, R.K. (1989). Collisional broadening of the $A^2\Sigma^+ \leftarrow X^2\Pi$ (0,0) band of OH by H_2O and CO_2 in atmospheric-pressure flames. *JQSRT* **41**, 29

Rensberger, K.J., Jeffries, J.B., and Crosley, D.R. (1989). Vibrational relaxation of OH ($X^2\Pi_i$, v=2). *J. Chem. Phys.* **90**, 2174.

Salmon, J.T., Lucht, R.P., Sweeney, D.W., and Laurendeau, N.M. (1984). Laser-saturated fluorescence measurements of NH in a premixed subatmospheric $CH_4/N_2O/Ar$ flame. *Twentieth Symposium (International) on Combustion*, The Combustion Institute, Pittsburgh, 1187.

Salmon, J.T. and Laurendeau, N.M. (1985a). Calibration of laser-saturated fluorescence measurements using Rayleigh scattering. *Appl. Opt.* **24**, 65.

Salmon, J.T. and Laurendeau, N.M. (1985b). Analysis of probe volume effects associated with laser-saturated fluorescence measurements. *Appl. Opt.* **24**, 1313.

Salmon, J.T. (1986a). Quantitative fluorescence measurements of atomic hydrogen in flames via two-photon absorption. Ph.D. Thesis, School of Mechanical Engineering, Purdue University, West Lafayette, Indiana.

Salmon, J.T. (1986b). Private communication.

Schofield, K. (1979). Rate constants for reactions of excited species. *J. Phys. Chem. Ref. Data,* **8**, 763.

Schwarzwald, R., Monkhouse, P., and Wolfrum, J. (1987). Picosecond fluorescence lifetime measurement of the OH radical in an atmospheric pressure flame. *Chem. Phys. Lett.* **142**, 15.

Schwarzwald, R., Monkhouse, P., and Wolfrum, J. (1988). Fluorescence studies of OH and CN radicals in atmospheric pressure flames using picosecond excitation. *Twenty-Second Symposium (International) on Combustion*, The Combustion Institute, Pittsburgh, 1413.

Smith, G.P. and Crosley, D.R. (1981). Quantitative laser-induced fluorescence in OH: transition probabilities and the influence of energy transfer. *Eighteenth Symposium (International) on Combustion.* The Combustion Institute, Pittsburgh, 1511.

Smith, G.P. and Crosley, D.R. (1983). Vibrational energy transfer in $A^2\Sigma^+$ OH in flames. *Appl. Opt.* **22**, 1428.

Stepowski, D. and Cottereau, M.J. (1979). Direct measurement of local OH concentration in a flame from the fluorescence induced by a single laser pulse. *Appl. Opt.* **18**, 354.

Stepowski, D. and Cottereau, M.J. (1981). Study of the collisional lifetime of hydroxyl ($^2\Sigma^+$, $v'=0$) radical in flames by time-resolved laser-induced fluorescence. *Combust. Flame* **40**, 65.

Takubo, Y., Yano, Matsuoka, H., and Shimazu, M. (1983). Saturation behavior of laser-induced CH fluorescence in a propane-air flame. *JQSRT* **30**, 163.

Varghese, P.L. and Hanson, R.K. (1984). Collisional narrowing effects on spectral line shapes measured at high resolution. *Appl. Opt.* **23**, 2376.

Verdieck, J.F. and Bonczyk, P.A. (1981). Laser-induced saturated fluorescence investigations of CH, CN, and NO in flames. *Eighteenth Symposium (International) on Combustion,* The Combustion Institute, Pittsburgh, 1559.

Wang, C.C., Killinger, D.K., and Huang, C. (1980). Rotational dependence in the linewidth of the ultraviolet transitions of OH. *Phys. Rev. A* **22**, 188.

Williams, F.A. (1985). *Combustion Theory,* The Benjamin/Cummings Publishing Co., Menlo Park, California, 130.

Wysong, I.J., Raiche, G.A., Jeffries, J.B., and Crosley, D.R. (1989). Quenching and energy transfer in OH. Western States Section/The Combustion Institute, Paper WSS/CI 89-43, Livermore, California.

Zizak, G., Lanauze, J.A., and Winefordner, J.D. (1986). An experimental study of the excited state rotational population of OH in flames using laser induced fluorescence. *Combust. Flame* **65**, 203.

Appendix A - Flow Control Routine

In this appendix, we include a listing of the flow control program described in Chapter 4. The routine has four major sections, the purposes of which are as follows: (1) the main routine, which handles the selection of menu options; (2) the display package, which initializes and updates the primary display (including the flow rates) and handles some I/O functions; (3) the communications package, which controls RS232 communications with the Linde Readout-and-Control (ROC) box, including conversion between ASCII strings and floating-point numbers; and (4) the package for scaling the flow rates with changes in pressure (see Chapter 4). The routine automatically detects the graphics display adaptor and will thus work on most IBM PC compatibles. The package was written using Turbo C and may employ some library functions which are unique to this product.

```
/*******************************************************************/
/*                                                               */
/* Section 1                                                     */
/*******************************************************************/


/*******************************************************************/
/*    ROUTINE MAIN()                                             */
/*                                                               */
/*    PURPOSE:  To control the ROC box                           */
/*******************************************************************/
#include <stdio.h>
#include <conio.h>
#include <math.h>
#include <stdlib.h>
#include <dos.h>

#define LINE       23
#define NORM        7
#define REVERSE   112
#define ESC       0x1b
#define ON    1
#define OFF        0
#define INC        1
#define DEC        0
#define ETHNOX   3.5

struct text_info initial;
float      flow[] = {0.0, 0.0, 0.0, 0.0, 0.0, 0.0, 0.0, 0.0};
float      flow_tmp[] = {0.0, 0.0, 0.0, 0.0, 0.0, 0.0, 0.0, 0.0};

int  ioroc(char, char []);
void cstring(char [], float []);
void led(float []);
void pled(float);
void adpres_int(int);
void adpres(float *);
void myput(int, int, int, char []);
int  mygets(char []);
void increment(int, float);
void fspd_rd(int *);
void fspd_cal(float, float, float *, float *);
void fspd_cl();
int  cursor(int);
```

```c
main()
{
    FILE  *frec;
    char  key, s[100], buf[80*25*2];
    int   i, j, direction, fspeed_file, frec_file, chan,
          channel[5], power = OFF;
    float pressure, pressure_old;
    float inc, k0, k1, k2, rf0, rf2, phi, phi_trg, phi_stp;

    static    char  menu[5][85] = {
{" MAIN:     <B>    <H>    <M>    <P>    <Q>    <R>    <S>    <T>    <V>    <Z>     "},
{" SET LOOP:      <1>      <2>      <3>      <4>     <H>      <R>       <ESC>  "},
{" TWEAK LOOP: <1>  <2>  <3>  <4>  <5>  <6>  <H>  <I>  <D>  <R>  <ESC> "},
{" MIXTURE LOOP:              <H>            <ESC>                       "},
{" PRESSURE LOOP:             <H>            <ESC>                       "}
    };
    static    char  label[19][85] = {
{"(1)FUEL  (2)OXYGEN  (3)DILUENT  (4)BATH                                 "},
{"(1)FUEL  (2)OXYGEN  (3)DILUENT  (4)BATH  (5)FUEL/OX  (6)OX/DIL  (7)FUEL/OX/DIL  "},
{"(1)FUEL                                                                 "},
{"         (2)OXYGEN                                                      "},
{"                   (3)DILUENT                                           "},
{"                              (4)BATH                                   "},
{"                                       (5)FUEL/OX                       "},
{"                                                   (6)OX/DIL            "},
{"                                                         (7)FUEL/OX/DIL "},
{"+ + + + + + + + + + + + + + + + + + + + + + + + + + + + + + + + + + + + "},
{"- - - - - - - - - - - - - - - - - - - - - - - - - - - - - - - - - - - - "},
{"                 READ THE CONTROL VALVE FLOW RATES                      "},
{"   ERROR:  A/D CHANNEL FOR PRESSURE SIGNAL HAS NOT BEEN SPECIFIED -> REBOOT  "},
{"               TARGET EQUIVALENCE RATIO HAS BEEN REACHED                "},
{"                     PRESSURIZE THE VESSEL                              "},
{"                 ZERO THE CONTROL VALVE FLOW RATES                     "},
{"                   BOOT UP THE CONTROL PROGRAM                         "},
{"                    VENT THE PRESSURE VESSEL                           "},
{"          PRESSURE CHANGE TOO LARGE -> VENT THE PRESSURE VESSEL        "}
    };
/***********************************************************************/
/*   Begin the loop for control of the flow rates                    */
/***********************************************************************/
    gettextinfo(&initial);
    gettext(1, 1, 80, 25, buf);
    display();
    window(1, 1, 80, 25);
    myput(1, 1, REVERSE, menu[0]);
    for(;;){
        key = getch();
/***********************************************************************/
/*        If 'Q' or 'q' has been entered QUIT the program            */
/***********************************************************************/
        if(key == 'Q' || key == 'q'){
            clrscr();
            puttext(1, 1, 80, 25, buf);
            gotoxy(initial.curx, initial.cury);
            cursor(ON);
            break;
        }
/***********************************************************************/
/*        If 'B' or 'b' has been entered BOOT up the program         */
/***********************************************************************/
```

```c
          if(key == 'B' || key == 'b'){
              ioroc('R', s);
              cstring(s, flow);
              led(flow);
              myput(LINE, 1, REVERSE, label[16]);
/*****************************************************************************/
/*              Get the channel for the pressure transducer              */
/*****************************************************************************/
              myput(LINE+2, 1, NORM, "Pressure signal channel (1-6):  ");
              if(mygets(s) == ON){
                  chan = atoi(s);
                  if(chan >= 1 && chan <= 6) {
                      power = ON;
                      adpres_int(chan);
                      adpres(&pressure);
                      pled(pressure);
                  }
              }
          }
/*****************************************************************************/
/*         If 'R' or 'r' has been entered, read and display the          */
/*         set and measured flow rates and pressure                      */
/*****************************************************************************/
          else if(key == 'R' || key == 'r') {
              ioroc('R', s);
              cstring(s, flow_tmp);
              for(i=5; i <= 8 ;i++)
                  flow[i-1] = flow_tmp[i-1];
              led(flow);
/*****************************************************************************/
/*              Read and display the pressure (if POWER = ON)            */
/*****************************************************************************/
              if(power == ON){
                  adpres(&pressure);
                  pled(pressure);
              }
          }
/*****************************************************************************/
/*         If 'S' or 's' has been entered, set the flow rate             */
/*****************************************************************************/
          else if(key == 'S' || key == 's'){
              myput(1, 1, REVERSE, menu[1]);
/*****************************************************************************/
/*              Get the character and set the CHANNEL[] array            */
/*****************************************************************************/
              for(;;){
                  myput(LINE, 1, REVERSE, label[0]);
                  for(i=1; i <= 4 ;i++)
                      channel[i] = OFF;
                  key = getch();
                  if(key >= '1' && key <= '4'){
                      gotoxy(1,25);
                      clreol();
                      if(key == '1'){
                          channel[1] = ON;
                          myput(LINE, 1, REVERSE, label[2]);
                      }
                      else if(key == '2'){
                          channel[2] = ON;
                          myput(LINE, 1, REVERSE, label[3]);
                      }
```

167

```
                        else if(key == '3'){
                                channel[3] = ON;
                                myput(LINE, 1, REVERSE, label[4]);
                        }
                        else if(key == '4'){
                                channel[4] = ON;
                                myput(LINE, 1, REVERSE, label[5]);
                        }
/******************************************************************************/
/*                      Get and set the flow rates                          */
/******************************************************************************/
                        myput(LINE+2, 1, NORM, "FLOW RATE (LPM):  ");
                        if( mygets(s) == ON){
                                for(i=1; i <= 4 ;i++){
                                        if(channel[i] == ON){
                                                flow[i-1] = atof(s);
                                                increment(i, flow[i-1]);
                                        }
                                }
                                led(flow);
                        }
                        gotoxy(1,25);
                        clreol();
                }
/******************************************************************************/
/*              If 'R' or 'r' has been input read the                       */
/*              flow rates and pressure                                     */
/******************************************************************************/
                else if(key == 'R' || key == 'r'){
                        ioroc('R', s);
                        cstring(s, flow_tmp);
                        for(i=5; i <= 8 ;i++)
                                flow[i-1] = flow_tmp[i-1];
                        led(flow);
                        if(power == ON){
                                adpres(&pressure);
                                pled(pressure);
                        }
                }
/******************************************************************************/
/*              If ESC is hit, escape from the SET loop                     */
/******************************************************************************/
                else if(key == ESC){
                        myput(1, 1, REVERSE, menu[0]);
                        break;
                }
        }
}
/******************************************************************************/
/*         If 'T' or 't' has been entered TWEAK the control valves          */
/******************************************************************************/
        else if(key == 'T' || key == 't'){
                myput(1, 1, REVERSE, menu[2]);
                for(i=0; i <= 4 ;i++)
                        channel[i] = OFF;
/******************************************************************************/
/*              Get the increment character string                          */
/******************************************************************************/
```

168

```c
                myput(LINE+2, 1, NORM,"FLOW RATE INCREMENT (1.0 > INC > 0.0):  ");
                if( mygets(s) == ON){
                        inc = atof(s);
                        if(inc < 0 || inc > 1.0)
                                break;
                        myput(LINE, 1, REVERSE, label[1]);
/******************************************************************/
/*                      Begin increment loop                      */
/******************************************************************/
                for(;;){
                        key = getch();
/******************************************************************/
/*                      If "1" through "7" has been input         */
/*                      set the logic array CHANNEL               */
/******************************************************************/
                        if(key >= '1' && key <= '7'){
                                for(i=1; i <= 4 ;i++)
                                        channel[i] = OFF;
                                if(key == '1'){
                                        channel[1] = ON;
                                        myput(LINE, 1, REVERSE, label[2]);
                                }
                                else if(key == '2'){
                                        channel[2] = ON;
                                        myput(LINE, 1, REVERSE, label[3]);
                                }
                                else if(key == '3'){
                                        channel[3] = ON;
                                        myput(LINE, 1, REVERSE, label[4]);
                                }
                                else if(key == '4'){
                                        channel[4] = ON;
                                        myput(LINE, 1, REVERSE, label[5]);
                                }
                                else if(key == '5'){
                                        channel[1] = ON;
                                        channel[2] = ON;
                                        myput(LINE, 1, REVERSE, label[6]);
                                }
                                else if(key == '6'){
                                        channel[2] = ON;
                                        channel[3] = ON;
                                        myput(LINE, 1, REVERSE, label[7]);
                                }
                                else if(key == '7'){
                                        channel[1] = ON;
                                        channel[2] = ON;
                                        channel[3] = ON;
                                        myput(LINE, 1, REVERSE, label[8]);
                                }
                        }
/******************************************************************/
/*                      If 'R' or 'r' has been input             */
/*                      read the flow rates and pressure         */
/******************************************************************/
                        else if(key == 'R' || key == 'r'){
                                myput(LINE+1, 1, REVERSE, label[11]);
                                ioroc('R', s);
                                cstring(s, flow_tmp);
                                for(i=5; i <= 8 ;i++)
                                        flow[i-1] = flow_tmp[i-1];
                                led(flow);
```

169

```
                        if(power == ON){
                                adpres(&pressure);
                                pled(pressure);
                        }
                }
/*********************************************************************/
/*                      If 'I' or 'i' has been input increment the */
/*                      flows                                       */
/*********************************************************************/
                else if(key == 'I' || key == 'i'){
                        myput(LINE+1, 1, REVERSE, label[9]);
                        for(i=1; i <= 4 ;i++){
                                if(channel[i] == ON){
                                        flow[i-1] = flow[i-1]*(1 + inc);
                                        increment(i, flow[i-1]);
                                }
                        }
                        led(flow);
                }
/*********************************************************************/
/*                      If 'D' or 'd' has been input decrement the */
/*                      flows                                       */
/*********************************************************************/
                else if(key == 'D' || key == 'd'){
                        myput(LINE+1, 1, REVERSE, label[10]);
                        for(i=1; i <= 4 ;i++){
                                if(channel[i] == ON){
                                        flow[i-1] = flow[i-1]*(1 - inc);
                                        increment(i, flow[i-1]);
                                }
                        }
                        led(flow);
                }
/*********************************************************************/
/*                      If ESC is hit, escape from the loop        */
/*********************************************************************/
                else if(key == ESC){
                        myput(1, 1, REVERSE, menu[0]);
                        break;
                }
            }
        }
    }
/*********************************************************************/
/*      If 'M'or 'm' has been entered, change the equivalence ratio */
/*********************************************************************/
        else if(key == 'M' || key == 'm') {
            if(flow[1] == 0.0 || flow[0] == 0.0){
                myput(LINE+1, 27, REVERSE,
                    "FLOW RATES CANNOT BE ZERO");
                delay(1000);
                break;
            }
            if(power == OFF) {
                myput(LINE, 1, REVERSE, label[12]);
                delay(1000);
                break;
            }
            fspd_rd(&fspeed_file);
            if(fspeed_file == OFF){
                myput(LINE, 24, REVERSE,
                    "FLAME DATA FILE CANNOT BE OPENED");
```

170

```c
                break;
        }
        myput(1, 1, REVERSE, menu[3]);
/************************************************************************/
/*              Check if the A/D channels have been specified          */
/*              properly.  If not, break from the loop                 */
/************************************************************************/
        phi_stp = 0.0005;
        phi = (flow[0]/flow[1]) * ETHNOX;
        sprintf(s, "Equivalence ratio %4.2f; target value:  ", phi);
        myput(LINE, 1, NORM, s);
        if( mygets(s) == OFF)
                break;
        phi_trg = atof(s);
        if(phi_trg <= 0)
                break;
        if(phi_trg > phi)
                direction = INC;
        else
                direction = DEC;
        adpres(&pressure);
        fspd_cal(pressure, phi, &rf0, &rf2);
        k0 = flow[0]/rf0;
        k1 = flow[1]/rf0;
        k2 = flow[2]/rf2;
        phi = phi + phi_stp;
        for(;;) {
/************************************************************************/
/*              If ESC is hit, exit from MIXTURE option                */
/************************************************************************/
                if(kbhit() && getch() == ESC) {
                        fspd_cl();
                        myput(1, 1, REVERSE, menu[0]);
                        break;
                }
/************************************************************************/
/*              Execute the logic sequence to step the                 */
/*              equivalence ratio                                      */
/************************************************************************/
                if(direction == INC) {
                        if(phi >= phi_trg) {
                                myput(LINE, 1, REVERSE, label[13]);
                                myput(1, 1, REVERSE, menu[0]);
                                break;
                        }
                        else if(phi + phi_stp > phi_trg)
                                phi = phi_trg;
                        else if(phi + phi_stp <= phi_trg)
                                phi = phi + phi_stp;
                }
                else {
                        if(phi <= phi_trg) {
                                myput(LINE, 1, REVERSE, label[13]);
                                myput(1, 1, REVERSE, menu[0]);
                                break;
                        }
                        else if(phi - phi_stp < phi_trg)
                                phi = phi_trg;
                        else if(phi - phi_stp >= phi_trg)
                                phi = phi - phi_stp;
                }
```

171

```c
/*******************************************************************/
/*              Determine the flame speed ratio for the           */
/*              pressure and equivalence ratio.  Update            */
/*              the flow array                                     */
/*******************************************************************/
                fspd_cal(pressure, phi, &rf0, &rf2);
                flow[0] = rf0 * k0;
                flow[1] = flow[0] * ETHNOX/phi;
                flow[2] = flow[1] * k2/k1;
                for(i=1; i <= 3; i++)
                        increment(i, flow[i-1]);
                led(flow);
                pled(pressure);
                k1 = flow[1]/(flow[0] + flow[1] + flow[2]);
                k2 = flow[2]/(flow[0] + flow[1] + flow[2]);
                delay(100);

        }
    }
/*******************************************************************/
/*        If 'P' or 'p' has been entered, pressurize the vessel   */
/*******************************************************************/
        else if(key == 'P' || key == 'p'){
            if(flow[0] == 0.0 || flow[1] == 0.0){
                myput(LINE+1, 27, REVERSE,
                        "FLOW RATES CANNOT BE ZERO");
                break;
            }
            fspd_rd(&fspeed_file);
            if(fspeed_file == OFF){
                myput(LINE+1, 24, REVERSE,
                        "FLAME DATA FILE CANNOT BE OPENED");
                delay(1000);
                break;
            }
            if(power == OFF) {
                myput(LINE+1, 1, REVERSE, label[12]);
                delay(1000);
                break;
            }
            myput(1, 1, REVERSE, menu[4]);
            if( (frec = fopen("flame.rec", "a") ) == NULL){
                frec_file = OFF;
                myput(LINE, 1, REVERSE,
                        "RECORD FILE CANNOT BE OPENED");
                delay(2000);
            }
            else
                frec_file = ON;
            fprintf(frec, "Pressure   fuel   Oxygen  Diluent   rf0   rf2\n");
            myput(LINE, 1, REVERSE, label[14]);
/*******************************************************************/
/*              Begin the loop for incrementing the flow rates    */
/*******************************************************************/
            adpres(&pressure);
            phi = flow[0]/flow[1] * ETHNOX;
            fspd_cal(pressure, phi, &rf0, &rf2);
            k0 = flow[0]/rf0;
            k1 = flow[1]/rf0;
            k2 = flow[2]/rf2;
            pressure_old = pressure;
            for(;;){
                if(kbhit()){
```

```
                                 if( (key=getch() ) == ESC){
                                     fspd_cl();
                                     if(frec_file == ON)
                                         fclose(frec);
                                     myput(1, 1, REVERSE, menu[0]);
                                     break;
                                 }
                                 else if(key == 'R' || key == 'r'){
                                     ioroc('R', s);
                                     cstring(s, flow_tmp);
                                     for(i=5; i <= 8 ;i++)
                                         flow[i-1] = flow_tmp[i-1];
                                     led(flow);
                                 }
                             }
                         adpres(&pressure);
/***************************************************************************/
/*                     Vent if pressure change is 1 atm or more         */
/***************************************************************************/
                         if(pressure-pressure_old >=  1.0 ||
                            pressure-pressure_old <= -1.0){
                             myput(LINE, 1, REVERSE, label[18]);
                             for(i=1; i <= 3 ;i++){
                                 flow[i-1] = 0.0;
                                 increment(i, flow[i-1]);
                             }
                             ioroc('R', s);
                             cstring(s, flow_tmp);
                             for(i=5; i <= 8 ;i++)
                                 flow[i-1] = flow_tmp[i-1];
                             led(flow);
                             break;
                         }
                         if(pressure-pressure_old >=  0.1 ||
                            pressure-pressure_old <= -0.1){
                             fspd_cal(pressure, phi, &rf0, &rf2);
                             flow[0] = (rf0 * k0);
                             flow[1] = (rf0 * k1);
                             flow[2] = (rf2 * k2);
                             for(i=1; i<= 3; i++)
                                 increment(i,flow[i-1]);
                             led(flow);
                             pled(pressure);
                             pressure_old = pressure;
                             if(frec_file == ON)
                                 fprintf(frec,
                                 "%7.4f  %7.4f  %7.4f  %7.4f  %7.4f  %7.4f\n",
                                 pressure,flow[0],flow[1],flow[2],rf0,rf2);
                         }
                     }
                 }
/***************************************************************************/
/*         If 'V' or 'v' has been entered vent the pressure vessel      */
/***************************************************************************/
             else if(key == 'V' || key == 'v'){
                 myput(LINE, 1, REVERSE, label[17]);
                 for(i=1; i <= 3 ;i++){
                     flow[i-1] = 0.0;
                     increment(i, flow[i-1]);
                 }
                 ioroc('R', s);
                 cstring(s, flow_tmp);
                 for(i=5; i <= 8 ;i++)
```

```
                        flow[i-1] = flow_tmp[i-1];
                led(flow);
                delay(500);
            }
/*****************************************************************/
/*          If 'Z' or 'z' has been entered, zero the control valves    */
/*****************************************************************/
            else if(key == 'Z' || key == 'z'){
                myput(LINE, 1, REVERSE, label[15]);
                for(i=1; i <= 4 ;i++){
                        flow[i-1] = 0.0;
                        increment(i, flow[i-1]);
                }
                ioroc('R', s);
                cstring(s, flow_tmp);
                for(i=5; i <= 8 ;i++)
                        flow[i-1] = flow_tmp[i-1];
                led(flow);
                delay(500);
            }
/*****************************************************************/
/*          Reset the screen                                     */
/*****************************************************************/
            window(1, LINE, 80, 25);
            clrscr();
            window(1, 1, 80, 25);
        }
/*****************************************************************/
/*    End of routine MAIN                                        */
/*****************************************************************/

}


/*****************************************************************/
/* Section 2                                                     */
/*****************************************************************/


#include <conio.h>
#include <stdio.h>
#include <stdlib.h>
#include <dos.h>
#define ON        1
#define OFF       0
#define    ESC    0x1b
#define NDEC      5             /* Number of significnat digits */
#define COLUMN   1
#define    START 3             /* Starting column            */
#define WIDTH     4             /* Width of channel info      */
#define NORM      7             /* Normal attribute           */
#define MAX       80            /* Maximum label length       */
#define FULL      219           /* Full square character      */
#define HALF      221           /* Half square character      */
#define BLANK     ' '           /* Blank square character     */
#define ZERO      222

void myput(int, int, int, char []);
/*****************************************************************/
/*    ROUTINE DISPLAY()                                          */
/*                                                               */
/*    PURPOSE: To Initialize the display                         */
/*****************************************************************/
```

```c
void display()
{
    int   i, v_mode, line;
    char  s[10];
/*************************************************************************/
/*   Define the initialization character strings                       */
/*************************************************************************/
    static    char   label[5][MAX+1] = {
("FUEL      0       0.2      0.4      0.6      0.8      1.0      1.2       "),
("OXYGEN    0       0.5      1.0      1.5      2.0      2.5      3.0       "),
("DILUENT   0       2        4        6        8        10       12     14"),
("BATH      0       5        10       15       20       25       30     35"),
("PRESSURE  0                5                 10                15        ")
    };
    static    char   tick[2][MAX+1] = {
("(LPM)     .........  .........  .........  .........  .........  .........  ......... "),
("(ATM)     .........  .........  .........  .........  .........  .........  ......... ")
    };
    cursor(OFF);
    clrscr();
    window(1, 1, 80, 25);
/*************************************************************************/
/*   Print out header character strings                                */
/*************************************************************************/
    for(i=0, line=START; i <= 4 ;i++, line=line+WIDTH)
        myput(line, COLUMN, NORM, label[i]);
/*************************************************************************/
/*   Print out tick marks                                              */
/*************************************************************************/
    for(i=1; i <= 8 ;i++)
        tick[0][(10*i)-1] = 31;
    for(i=1; i <= 8 ;i++)
        tick[1][(10*i)-1] = 31;
    for(i=0; i <= 4 ;i++){
        line = (START + 1) + (i * WIDTH);
        if(i<=3)
            myput(line, COLUMN, NORM, tick[0]);
        else
            myput(line, COLUMN, NORM, tick[1]);
    }
/*************************************************************************/
/*   End of routine display                                            */
/*************************************************************************/
}
/*************************************************************************/
/*   INT MYGETS(CHAR S[])                                              */
/*                                                                     */
/*   PURPOSE: To fill a character array until the RETURN key is        */
/*            entered. All characters input are echoed on the          */
/*            screen until the RETURN key is hit.                      */
/*************************************************************************/
int mygets(char s[])
{
    unsigned char     i, key;
    struct text_info initial;
    gettextinfo(&initial);
/*************************************************************************/
/*   Get the character string from the key board                       */
/*************************************************************************/
```

```c
        cursor(ON);
        for(i=0; i < MAX ; ){
                if( (key=getch() ) == ESC){      /* if escape return     */
                        cursor(OFF);
                        return(OFF);
                }
                else if(key == '\b'){            /* if backspace backup   */
                        if(i >= 1){
                                putch('\b');
                                putch(' ');
                                gotoxy(initial.curx + --i, initial.cury);
                        }
                        else
                                key = '\0';
                }
                else if(key == '\r'){            /* if return finished    */
                        s[i] = '\0';
                        cursor(OFF);
                        if(i==0)
                                return(OFF);
                        return(ON);
                }
                else{                            /* else store character  */
                        putch(key);
                        s[i] = key;
                        ++i;
                }
        }
/****************************************************************************/
/*    End of routine MYGETS()                                            */
/****************************************************************************/
}
/****************************************************************************/
/*    VOID MYPUT(INT LINE, INT COLUMN, INT ATTRIB, CHAR S[])            */
/*                                                                      */
/*    PURPOSE:  To direct the cursor position and then write            */
/*              information to the CRT display                          */
/****************************************************************************/
void myput(int line, int column, int attrib, char s[])
{
        int    i;
        gotoxy(column, line);
        textattr(attrib);
        cputs(s);
/****************************************************************************/
/*    End of routine MYPUT                                              */
/****************************************************************************/
        textattr(NORM);
}
/****************************************************************************/
/*    VOID LED(FLOAT FLOW)                                              */
/*                                                                      */
/*    PURPOSE:  To construct the character strings representing the      */
/*              flow readings and settings                             */
/****************************************************************************/
void led(float flow[])
{
        int    i, j, k, line, x, bar_st[4], bar_rd[4];
        char   temp[10], s[4][MAX+1];
        static      float scale[4] = {100, 40, 10, 4};
```

```
/*****************************************************************/
/*   Convert the flow rates to character strings and put the strings   */
/*   into the display string, S                                        */
/*****************************************************************/
     for(i=0, line=START+2; i <= 3; i++, line=line+WIDTH){
          s[i][0] = 'S';
          s[i][1] = ':';
          gcvt( (double) flow[i], NDEC, temp);
          for(j=0; j < NDEC; j++){
               if(temp[j] == '\0')
                    break;
               s[i][j+2] = temp[j];
          }
          for(k=j; k < NDEC+2; k++)
               s[i][k+2] = ' ';
          s[i][9] = ZERO;
          bar_st[i] = flow[i] * scale[i];              /*scale flow[i]    */
          bar_rd[i] = flow[i+4] * scale[i];
/*****************************************************************/
/*        Construct the flow rate charcter strings given the          */
/*        scaled flow rates                                            */
/*****************************************************************/
          for(j=10; j <= 79 ;j++){
               x = 2*j - 17;
/*****************************************************************/
/*             Execute logic for displaying the measured flow         */
/*****************************************************************/
               if (bar_rd[i] < x && bar_rd[i] >= (x-1) )
                    s[i][j] = HALF;
               else if(bar_rd[i] < x)
                    s[i][j] = BLANK;
               else if(bar_rd[i] >= x)
                    s[i][j] = FULL;
/*****************************************************************/
/*             Execute logic for displaying the set flow rates        */
/*****************************************************************/
               if (bar_st[i] < x && bar_st[i] >= (x-2) )
                    s[i][j] = HALF;
          }
/*****************************************************************/
/*   Write the string to the screen                                   */
/*****************************************************************/
          s[i][80] = '\0';
          gotoxy(COLUMN, line);
          for(j=0; j <= MAX-1 ;j++)
               putch(s[i][j]);
     }
/*****************************************************************/
/*   End of routine LED                                               */
/*****************************************************************/
}
/*****************************************************************/
/*   VOID PLED(FLOAT PRESSURE)                                        */
/*                                                                    */
/*   PURPOSE:  To construct the character string representing the      */
/*            pressure                                                 */
/*****************************************************************/
```

```
void pled(float pressure)
{
    float scale = 8;
    int   i, j, k, x, bar;
    char  temp[10], s[MAX+1];
/***********************************************************************/
/*    Initialize the character string for the pressure              */
/***********************************************************************/
    s[0] = 'R';
    s[1] = ':';
    gcvt( (double) pressure, NDEC, temp);
    for(j=0; j < NDEC; j++){
        if(temp[j] == '\0')
            break;
        s[j+2] = temp[j];
    }
    for(k=j; k < NDEC+2; k++)
        s[k+2] = ' ';
    s[9] = ZERO;
    bar = pressure * scale;
/***********************************************************************/
/*    Construct the pressure charcter string given the scaled value  */
/***********************************************************************/
    for(i=10; i <= 79 ;i++){
        x = 2*i - 17;
        if(bar < x && bar >= (x-1) )
            s[i] = HALF;
        else if(bar < x)
            s[i] = BLANK;
        else if(bar >= x)
            s[i] = FULL;
    }
    s[80] = '\0';
    gotoxy(COLUMN, START+18);
    for(i=0; i <= MAX-1 ;i++)
        putch(s[i]);
/***********************************************************************/
/*    End of routine PLED                                            */
/***********************************************************************/
}
/***********************************************************************/
/*    INT CURSOR(INT TOGGLE)                                         */
/*                                                                   */
/*    PURPOSE:  To turn the cursor on and off                        */
/***********************************************************************/
#define VIDEO    0x10
#define TOP      6
#define BOT      7
int cursor(int toggle)
{
    union REGS regs;
    regs.h.ah = 1;
    if(toggle == ON){
        regs.h.ch = TOP;
        regs.h.cl = BOT;
    }
    else if(toggle == OFF){
        regs.h.ch = -TOP;
        regs.h.cl = -BOT;
    }
```

```
          else
                return;
          int86(VIDEO, &regs, &regs);
/****************************************************************/
/*   End of routine cursor                                    */
/****************************************************************/
}


/****************************************************************/
/* Section 3                                                  */
/****************************************************************/



#include <stdio.h>
#include <conio.h>
#include <stdlib.h>
#include <math.h>
#define THR       0x3f8 /* Transmitter Holding Register address */
#define RBR       0x3f8 /* Receiver Buffer Register address   */
#define MCR       0x3fc    /* Modem Control Register address      */
#define LSR       0x3fd /* Line Status Register address        */
#define MAX       80
#define WAIT      2000
int ioroc(char, char []);
/****************************************************************/
/*    VOID CSTRING(CHAR S[], FLOAT *P_FLOW)                   */
/*                                                            */
/*    PURPOSE:  To convert the character string of numbers    */
/*              (terminated by a \0) to a floating point array. */
/****************************************************************/
cstring(char s[], float *p_flow)
{
     int    i, j, k, l;
     char   temp[5];
     static      float scale[8] = (0.001, 1, 1, 1, 0.001, 1, 1, 1);
/****************************************************************/
/*   Begin the loop to convert the character string to numbers */
/****************************************************************/
     for(i=0, j=0, l=0; ;i++){
            if(s[i] == '\0')            /* Break if end of string */
                 break;
/****************************************************************/
/*         If character s[i] is a period or a number store in  */
/*         character string TEMP                               */
/****************************************************************/
            else if(s[i] == '.' || (s[i] >= '0' && s[i] <= '9') ){
                 temp[j] = s[i];
                 j++;
            }
/****************************************************************/
/*         When S is a comma or a carriage return, then it has a */
/*         complete number.  Convert the character string TEMP  */
/*         to an integer, INTGR                                */
/****************************************************************/
            else if(s[i] == ',' || (s[i] == '\n' && (l == 3 || l == 7) ) ){
                 temp[j] = '\0';
                 *p_flow = atof(temp) * scale[l];
                 p_flow++;
                 j=0;
```

179

```c
                    i++;
                }
        }
/****************************************************************/
/*    End of routine CSTRING                                  */
/****************************************************************/

}
/****************************************************************/
/*    ROUTINE INCREMENT(INT I, FLOAT FLOW)                     */
/*                                                             */
/*    PURPOSE: To take channel CHAN and flow rate set-point FLOW*/
/*             convert them into ASCII characters, and send them*/
/*             to the ROC box                                  */
/****************************************************************/

void increment(int chan, float flow)
{
    char  s[10], in[100];
    int   i, pad;
    static      float scale[4] = (1000, 100, 100, 100);
/****************************************************************/
/*    Send the control character 'C' and the channel number   */
/****************************************************************/

    ioroc('C', in);
    itoa(chan, s, 10);
    ioroc(s[0], in);
/****************************************************************/
/*    Send the control character 'S' and the new flow rate set-points */
/****************************************************************/

    ioroc('S', in);
    itoa((int) (flow*scale[chan-1]), s, 10);
    for(i=0; s[i] >= '0' && s[i] <= '9' ;i++)
            ;
    pad = 4 - i;
    for(i=0; i < pad ; i++)
            ioroc('0', in);
    for(i=0; i <= (3-pad) ;i++)
            ioroc(s[i], in);
/****************************************************************/
/*    End of Routine INCREMENT                                 */
/****************************************************************/

}
/****************************************************************/
/*    INT IOROC(CHAR PROMPT, CHAR RESPONSE[])                  */
/*                                                             */
/*    PURPOSE: To send the ROC control character and retrieve the ROC */
/*             response through the COM1 port.                 */
/****************************************************************/

int ioroc(char prompt, char response[])
{
    int   i, j;
/****************************************************************/
/*    Send the character to the ROC box                        */
/****************************************************************/

    outportb(MCR, 0x01);                        /* Send the lo RTS signal */
    while( (inportb(LSR) & 0x20) != 0x20 )      /* Wait for hi THRE signal*/
            ;
    outportb(THR, prompt);
    while( (inportb(LSR) & 0x60) != 0x60 )      /* wait for hi THRE & TSRE*/
            ;
```

```c
/**********************************************************************/
/*   Get the character(s) sent in response by the ROC box          */
/**********************************************************************/
      outportb(MCR, 0x03);              /* Send the hi RTS signal */
      for(i=0; i < MAX ;i++){

/**********************************************************************/
/*        Wait for complete character from ROC box before proceding  */
/**********************************************************************/
          for(j=0; (inportb(LSR) & 0x01) != 0x01; j++){
                if(j > WAIT){
                       outportb(MCR, 0x01);
                       response[i] = '\0';
                       return(i);
                }
          }
          response[i] = inportb(RBR);
      }
/**********************************************************************/
/*   End of routine ioroc                                           */
/**********************************************************************/

}
/**********************************************************************/
/*     Function adget(int channel, float *pvalue)                   */
/*                                                                  */
/*   Purpose:  To get values from the MetraByte A to D converter.   */
/*             The syntax of the calling statement should be        */
/*                                                                  */
/*   adget(channel, &value);                                        */
/*                                                                  */
/*   where channel  is the channel (0-15) of the A/D               */
/*         pvalue   is the pointer to value                         */
/**********************************************************************/
#include <dos.h>
#define    ADC_LO 0x300
#define    ADC_HI 0x301
#define STATUS 0x302

void adget(int chan, float *pvolt)

{
/**********************************************************************/
/*   Start A/D conversion process.  A/D conversion will be complete */
/*   when the value of the MSB of the status register is low        */
/**********************************************************************/
      outportb(STATUS, chan);
      outportb(ADC_HI, 0x00);
      while( (inportb(STATUS) & 0x80) == 0x80)
            ;
/**********************************************************************/
/*   Get the low and high bytes describing the voltage signal.      */
/**********************************************************************/
      *pvolt = (float) ( ( (inportb(ADC_HI) << 4) & 0xff0) +
                    ( (inportb(ADC_LO) >> 4) & 0x00f) );
      *pvolt = 10.0 * (*pvolt/4096) - 5.0;
/**********************************************************************/
/*   End of function adget                                          */
/**********************************************************************/

}
```

```
/***********************************************************************/
/* Section 4                                                           */
/***********************************************************************/


#include <conio.h>
#include <stdlib.h>
#include <stdio.h>
#include <math.h>
#define    ON    1
#define OFF       0
float      amax, a[2], b[2], c[2];
FILE       *fdat;
/***********************************************************************/
/*    ROUTINE FSPD_RD(INT *P_FSPEED_FILE)                             */
/*                                                                     */
/*    PURPOSE:  To read the flame speed data file                     */
/***********************************************************************/
void fspd_rd(int *p_fspeed_file)
{
    char  s[80];
/***********************************************************************/
/*    Read the data file FLAME.DAT                                    */
/***********************************************************************/

    *p_fspeed_file = ON;
    if( (fdat = fopen("flame.dat", "r")) == NULL){
        *p_fspeed_file = OFF;
        return;
    }
    fgets(s, 80, fdat);
    sscanf(s, " %f %f %f ",&a[0], &a[1], &amax);
    fgets(s, 80, fdat);
    sscanf(s, " %f %f ",&b[0], &b[1]);
    fgets(s, 80, fdat);
    sscanf(s, " %f %f ",&c[0], &c[1]);
/***********************************************************************/
/*    End of routine FSPD_RD                                          */
/***********************************************************************/
}
/***********************************************************************/
/*    ROUTINE FSPD_CL()                                               */
/*                                                                     */
/*    PURPOSE:  To close flame speed data file                        */
/***********************************************************************/
void fspd_cl()
{
    fclose(fdat);
/***********************************************************************/
/*    End of routine FSPD_CL                                          */
/***********************************************************************/
}
/***********************************************************************/
/*    ROUTINE FSPD_CAL(FLOAT PRESSURE, FLOAT PHI, FLOAT *PF0, FLOAT *PF2)*/
/*                                                                     */
/*    Purpose:  Calculate the fuel and oxydant flow rates             */
/***********************************************************************/
void fspd_cal(float pressure, float phi, float *pf0, float *pf2)
{
    float xsqr, xcbe, phat;
    double      exp(double);
```

```
/******************************************************************************/
/*    Calculate the various parameters and the fuel/oxygen float rate    */
/******************************************************************************/

      xsqr = (phi-amax) * (phi-amax);
      xcbe = (phi-amax) * xsqr;
      *pf0 = 1.0 - a[0] * xsqr - a[1] * xcbe;
      phat = b[1] * (1.0 - pressure);
      *pf0 = *pf0 * (1.0 + (b[0] - 1) * (1 - exp( (double) phat ) ) );

/******************************************************************************/
/*    Calculate the diluent flow rate                                    */
/******************************************************************************/

      phat = c[1] * (1.0 - pressure);
      *pf2 = 1.0 + (c[0] - 1) * (1 - exp( (double) phat) );

/******************************************************************************/
/*    End of routine FSPD_CAL                                            */
/******************************************************************************/

}
```

Appendix B - Absorption Theory and Sensitivity Analysis for Collisional Linewidths

B.1 Introduction

In this appendix, we first present the theory for absorption measurements. We then discuss collisional broadening of OH at flame temperatures, and we compile data on the broadening of $A^2\Sigma^+ \leftarrow X^2\Pi$ (0,0) transitions of OH based on recent measurements by Rea et al. (1986, 1989). This data base was used to calculate number densities from absorption measurements in the flames we described in Chapters 6 and 7. In the final section, we present calculations of the sensitivity of absorption number densities to line broadening. These calculations were performed for simulated flames at 1, 3, 6, and 12 atm, with the input parameters based on the $C_2H_6/O_2/N_2$ flames in Chapters 6 and 7.

B.2 Theory

The spectral absorption at the exit slit of the monochromator, A_ν, is given by (Penner, 1959)

$$A_\nu = 1 - \frac{\int_{v-\Delta v^*}^{v+\Delta v^*} I_v(L) \cdot g(|v' - v|) dv'}{\int_{v-\Delta v^*}^{v+\Delta v^*} I_v(0) \cdot g(|v' - v|) dv'} \quad . \tag{B.1}$$

where $\Delta \nu^*$ (cm^{-1}) is the spectral width of the exit slit, $I_\nu(0)$ and $I_\nu(L)$ are the respective spectral irradiances entering and leaving the absorbing medium, and $g(|\nu' - \nu|)$ is the normalized slit function for which

$$\int_{-\infty}^{\infty} g(|v' - v|) dv' = 1 \quad . \tag{B.2}$$

With broad-band excitation, $I_\nu(0)$ is approximately constant over the limits of integration, and therefore

$$A_\nu = 1 - \int_{-\Delta v^*}^{\Delta v^*} \exp\left[-\int_0^L k(\tau + v) ds\right] g(\tau) d\tau \quad , \tag{B.3}$$

where $\tau \equiv \nu' - \nu$ and L is the path length. The spectral absorption coefficient $k(\nu)$ is related to the normalized line profile $Y(\nu)$ and the population in the coupled levels, N_l and N_u, by

$$k(v) = \left(\frac{hv_0}{c}\right) Y(v)[N_l B_{lu} - N_u B_{ul}] \quad , \tag{B.4}$$

184

where ν_0 (cm⁻¹) is the central frequency of the transition and B_{lu} and B_{ul} (cm³-cm⁻¹/J-s) are the respective Einstein coefficients for absorption and stimulated emission. Note that the absorption coefficient $k(\nu)$ is integrated over the absorption path to account for variations in the population and linewidth; also, for electronic transitions under conditions of local thermodynamic equilibrium, $N_u \simeq 0$. At higher pressures, $Y(\nu)$ results from a convolution of the collisional and Doppler broadening profiles; thus, in terms of the nondimensional frequency $\zeta \equiv 2 \sqrt{(\ln 2)} (\nu - \nu_0)/\Delta\nu_D$

$$Y(\zeta) = \frac{2\sqrt{\ln 2}}{\sqrt{\pi}\,\Delta v_D}\, V(\zeta;a)$$

$$= \frac{2\sqrt{\ln 2}}{\sqrt{\pi}\,\Delta v_D}\frac{a}{\pi}\int_{-\infty}^{\infty}\frac{\exp(-y^2)dy}{a^2 + (\zeta - y)^2} \quad . \qquad (B.5)$$

Here, the Doppler linewidth (FWHM), $\Delta\nu_D$, is given by

$$\Delta v_D = 2v_0 \cdot \left(\frac{2kT\ln 2}{mc^2}\right)^{1/2} \quad , \qquad (B.6)$$

where k is the Boltzmann constant, T is the translational temperature, and m is the mass of the absorbing species; $V(\zeta;a)$ is known as the Voigt function and also the real part of the complex error function (Abramowitz and Stegun, 1968; Armstrong, 1967; Hui et al., 1978; Humlicek, 1979).

The broadening parameter,

$$a = \sqrt{\ln 2}\,\frac{\Delta v_N + \Delta v_C}{\Delta v_D} \quad , \qquad (B.7)$$

describes the relative influences of the two homogeneous processes, natural and collisional broadening, and the inhomogeneous process, Doppler broadening. The natural linewidth, $\Delta\nu_N$, is the broadening of the transition due to spontaneous emission, while the collisional linewidth, $\Delta\nu_C$, is the broadening of the transition due to dephasing collisions; at 1 atm and above for the hydroxyl radical, collisional broadening is much greater than natural broadening. The collisional broadening is expressed as a sum of the contributions of the gas constituents; i.e.,

$$\Delta v_C = P\sum_i x_i \cdot (2\gamma_i) \quad . \qquad (B.8)$$

where P is the total pressure, and x_i and $2\gamma_i$ (cm⁻¹/atm) are the mole fraction and broadening coefficient, respectively, of the i-th constituent. Finally, note that at higher pressures, with the increased contribution from collisional narrowing, the Voigt profile may not adequately describe the linewidth (Varghese and Hanson, 1984; Rea et al. 1986).

The effect of the slit function is to spread the profile over a wider range of frequencies; thus

$$A = \int_{\nu_1}^{\nu_2} A_\nu \, d\nu = \int_{\nu_1}^{\nu_2} \left\{ 1 - \int_{-\Delta\nu'}^{\Delta\nu'} \exp\left[-\int_0^L k(\tau + \nu) ds \right] g(\tau) d\tau \right\} d\nu \quad . \quad (B.9)$$

where the limits of integration, ν_1 and ν_2, are chosen to be sufficiently large to include most of the line but not adjacent lines. The total energy absorbed, though, remains constant (Penner, 1959), and hence, for a particular transition, integration over the line profile gives

$$A = \int_{\nu_1}^{\nu_2} \left\{ 1 - \exp\left[-\int_0^L k(\nu) ds \right] \right\} d\nu \quad . \quad (B.10)$$

Thus, as long as one integrates over the broadened line, knowledge of the slit function is unnecessary.

The curve-of-growth method represents the solution of Eq. (B.10) for the parameter K (Lucht et al., 1978)

$$K = \frac{k(\zeta)L}{V(\zeta; a)} = \left(\frac{h\nu_0}{c} \right) N_l B_{lu} \frac{2\sqrt{ln2} \, L}{\sqrt{\pi} \Delta\nu_D} \quad , \quad (B.11)$$

as a function of the total absorption and the broadening parameter; if the temperature is known, the total number density, $N_T = N_l/F_{lB}$, can then be found from K. If the total absorption from two or more energy levels is known, then both the rotational temperature and the total number density can be calculated by comparing the measured spectra with the spectra calculated from the curve-of-growth method (Salmon, 1986a). We note that for weak absorption, $\int_0^L k(\nu) ds \ll 1$, the integrated absorption A is insensitive to a; however, when $\int_0^L k(\nu) ds > 1$, accurate determination of N_T is limited by the uncertainty in a.

B.3 Collisional Broadening of OH

The principal difficulty in calculating the parameter a lies in determining the temperature dependence of the linewidth $\Delta\nu_C$ for interactions with the main collision partners. In a room-temperature experiment at subatmospheric pressure, Engleman (1969) measured broadening of the $A^2\Sigma^+\leftarrow X^2\Pi$ (0,0) transitions of OH and found similar linewidths for collisions with molecules such as O_2, N_2, and CO_2. Moreover, unlike interactions of OH with these collision partners, those with H_2O showed a dependence on OH rotational level. In a later high-temperature experiment (T $\approx$ 1300 K), Wang et al. (1980) measured the homogeneous linewidths for collisions with O_2 and H_2O at subatmospheric pressures, again finding a dependence on OH rotational level for interactions with H_2O. This behavior, they concluded, is the result of rotational transitions of

C-3

H_2O in near resonance with those of OH. Recently, Rea et al. (1986, 1989) measured collisional broadening of the electronic transitions of OH by Ar, N_2, H_2O, and CO_2, and fit the temperature behavior of the broadening coefficients to the exponential relation,

$$2\gamma_i = 2\gamma_o \left(\frac{T_{ref}}{T}\right)^n \quad , \qquad\qquad (B.12)$$

which follows from a simple hard-sphere collision model where the exponent is 1/2.

Table B.1 Summary of the reference linewidth coefficients and temperature exponents [from Rea et al. (1986, 1989)].

J	H_2O (T_{ref}=1620 K)		CO_2 (1680 K)		N_2 (2000 K)		O_2 (2000 K)	
	$2\gamma_0$	n	$2\gamma_0$	n	$2\gamma_0$	n	$2\gamma_0$	n
1.5	0.155	0.9	0.108	1.2	0.050	0.8	0.033	0.8
2.5	0.160	1.0	0.092	1.2	0.047	0.8	0.033	0.8
3.5	0.160	0.9	0.067	1.2	0.045	0.8	0.032	0.8
4.5	0.165	0.7	0.060	1.2	0.043	0.8	0.032	0.8
5.5	0.160	0.6	0.054	1.2	0.042	0.8	0.032	0.8
6.5	0.145	0.4	0.050	1.2	0.040	0.8	0.032	0.8
7.5	0.125	0.35	0.048	1.2	0.039	0.8	0.032	0.8
8.5	0.115	0.35	0.048	1.2	0.038	0.8	0.032	0.8
9.5	0.110	0.35	0.048	1.2	0.037	0.8	0.032	0.8
10.5	0.105	0.25	0.048	1.2	0.037	0.8	0.032	0.8
11.5	0.100	0.2	0.048	1.2	0.037	0.8	0.032	0.8
12.5	0.095	0.1	0.048	1.2	0.037	0.8	0.032	0.8
13.5	0.095	0.1	0.048	1.2	0.037	0.8	0.033	0.8
14.5	0.090	0.0	0.048	1.2	0.037	0.8	0.033	0.8
15.5	0.090	0.0	0.050	1.2	0.037	0.8	0.034	0.8

Table B.2 Relative (ϵ) and absolute (δ) uncertainties in the broadening coefficient for J = 5.5 at a flame temperature of 1800 K [from Rea et al. (1986, 1989)].

Collision Partner	ϵ (2γ)	δ (2γ) (cm^{-1}/atm)
CO_2	0.17	0.0085
H_2O	0.08	0.012
N_2	0.12	0.0053
O_2	0.20	0.0070

The linewidths resulting from OH-Ar and OH-N_2 collisions were first measured in a shock tube over a temperature range of 1400 to 4100 K. A rapid-tuning frequency-doubled ring dye laser was used to resolve lineshapes behind reflected shock waves in weak mixtures of H_2 and O_2 diluted with N_2 or Ar; these measurements show a small dependence on rotational level, though this dependence is within the uncertainty of the measurements. For broadening by H_2O and CO_2, Rea et al. (1989) used a flat flame burner and a diffusion burner to assess the low and high-temperature behavior, respectively, of the collisional linewidths. To estimate the contribution from O_2, Rea et al. assumed that O_2 and Ar broaden the OH transitions by the same amount. This hypothesis was based on the measurements of Engleman (1969) and Shirinzadeh et al. (1985) and was tested using the measured linewidths and temperature exponent for Ar; the two values compared well and Rea et al. used the linewidth data for Ar to calculate the small contribution from O_2 in their lean flames.

The $2\gamma_i$ of the principal collision partners for our lean $C_2H_6/O_2/N_2$ flames are listed in Table B.1. These values are based on the measurements of Rea et al. (1986, 1989); the broadening behavior of O_2 was assumed to be the same as that for Ar. Table B.2 lists the approximate uncertainties in the $2\gamma_i$ values, which are based on reported uncertainties for the J = 5.5 rotational level. Though $2\gamma(O_2)$ was not measured, we have assigned a relative uncertainty of 20%; nonetheless, the total uncertainty is insensitive to this value since the concentration of O_2 is small in the burnt-gas region.

Table B.3   Total and partial uncertainties in the collisional linewidth for J = 5.5 and the flames A, B, and C described in Chapters 6 and 7. The collisional linewidth and the associated total uncertainty [calculated from Eq. (B.13)] are listed under the column labeled $\Delta\nu_C$.

P (atm)	$\Delta\nu_C$ (cm^{-1})	$P\{\Sigma[x_i \ \delta(2\gamma_i)]^2\}^{1/2}$ (cm^{-1})	$P\Sigma\delta x_i \ (2\gamma_i)$ (cm^{-1})	$\delta P\Sigma x_i \ (2\gamma_i)$ (cm^{-1})
0.98 ± 0.01	0.0592 ± 0.0046	0.0041	0.002	0.0006
3.1 ±0.14	0.184 ± 0.017	0.013	0.006	0.0083
6.1 ±0.20	0.383 ± 0.032	0.0264	0.012	0.0126

In addition to the uncertainties in Table B.2, uncertainties in the pressure and species concentrations also contribute to the total uncertainty in $\Delta\nu_C$. Thus, the total uncertainty is

$$\delta(\Delta v_c) = \left\{ P^2 \sum_i [x_i \cdot \delta(2\gamma_i)]^2 + \left[P \sum_i \delta x_i \cdot (2\gamma_i) \right]^2 + \left[\delta P \sum_i x_i \cdot (2\gamma_i) \right]^2 \right\}^{1/2} . \qquad (B.13)$$

Since the mole fractions are correlated (i.e., the sum must equal unity), they cannot be handled individually, as if they were random errors. Instead, to estimate the uncertainty in $\Delta\nu_C$ due to uncertainties in the mole fractions, we have calculated the term $P\Sigma\delta x_i \cdot (2\gamma_i)$ for the case where $x(CO_2)$ and $x(H_2O)$ are 10% below their expected equilibrium values, and we have assumed that the unknown species making up this deficit broaden the OH transitions weakly as does Ar. In estimating the total uncertainty in the collisional linewidth, we have used flames A, B, and C described in Chapters 6 and 7. This result and the summary of the terms in Eq. (B.13) are shown in Table B.3. The values are calculated for the pressure and mole fractions in the absorption measurements. These calculations for the $J = 5.5$ rotational level show that the net uncertainty in the collisional linewidth is $< 10\%$. In general, we expect an uncertainty of $\sim 10\%$ in the calculation of $\Delta\nu_C$ for the lines we have used for absorption measurements in our $C_2H_6/O_2/N_2$ flames.

B.4 Calculations

For the calculations described below, Eqs. (B.3) and (B.10) were integrated with FORTRAN routines, which employ Romberg integration and are based on algorithms suggested by Press et al. (1986). For accurate integration with an infinite limit, the variable transformation $x \equiv 1/\nu$ was used to map infinity into zero. Consequently, for integration over the range of zero to infinity, we have used the relation

$$\int_0^\infty f(v)dv = \int_0^1 f(v)dv + \int_0^1 \frac{1}{x^2} f\left(\frac{1}{x}\right)dx . \qquad (B.14)$$

In Figs. B.1-B.4, we show the calculated spectral absorption profiles at pressures of 1, 3, 6, and 12 atm. The spectral profiles are calculated using Eq. (B.3) with (1) infinite spectral resolution (i.e., $\Delta\nu^* = 0$) and (2) the triangular slit function,

Table B.4   Values of K and A (as functions of pressure) for three transitions assuming $N_T = 8 \times 10^{15}$ cm^{-3}. The broadening parameter is calculated using data of Rea et al. (1986, 1989) and the equilibrium distribution of species in a lean (equivalence ratio = 0.8, dilution ratio = 3.1) $C_2H_6/O_2/N_2$ flame at 1800 K.

Line	K	a/P (atm^{-1})	A (cm^{-1})			
			1 atm	3	6	12 atm
$P_1(2)$	0.6916	0.236	0.149	0.159	0.165	0.170
$Q_1(6)$	1.538	0.201	0.274	0.310	0.337	0.360
$Q_1(13)$	0.3836	0.171	0.087	0.090	0.093	0.094

$$g(\tau) = T(\tau) = \begin{cases} 0 & -\Delta v^* > \tau > \Delta v^* \\ (\Delta v^* + \tau)/(\Delta v^*)^2 & -\Delta v^* < \tau < 0 \\ (\Delta v^* - \tau)/(\Delta v^*)^2 & 0 < \tau < \Delta v^*. \end{cases} \qquad (B.15)$$

Here, we use a slit width (FWHM) $\Delta v^* = 1$ cm^{-1}, which is approximately the value measured from experimental lines. For all cases, the spectral absorption for the $Q_1(6)$ and $Q_1(13)$ lines is simulated using $N_T = 8.0 \times 10^{15}$ cm^{-3}. This OH number density is consistent with values measured experimentally, and the $Q_1(6)$ and $Q_1(13)$ lines were, in general, the strongest and weakest lines, respectively, used to calculate the total number density. In addition, the broadening parameter was calculated using T = 1800 K and the collisional coefficients of Rea et al. (1986, 1989); the information for these lines and the additional $P_1(2)$ line is summarized in Table B.4. In each case, the integrated absorption [A (cm^{-1})] evaluated from Eq. (B.10) is also shown; we note that one consequence of the increased collisional broadening is an increase in the integrated absorption.

In Figs. B.5-B.8, we show $\epsilon N_T(\Delta v_C)$, the relative uncertainty in N_T, due to uncertainties in Δv_C of 10% and 20%. These curves are calculated as a function of K since experimentally one has control over this parameter through choice of the absorption line or through variation of the total flow rate of the combustible mixture. As the latter is increased (while holding constant the equivalence and dilution ratios), the flame temperature in the burnt-gas region will also increase (Ferguson and Keck, 1979; Chao and Law, 1988), resulting in a greater OH concentration. As expected, the relative error increases with increasing K. One surprising result, however, is that for constant K, the relative error at 12 atm is less than that at 6 atm. For our purposes, the important conclusion is that for the range of concentrations in our $C_2H_6/O_2/N_2$ flames at 1, 3.1, and 6.1 atm, the uncertainty in N_T due to the uncertainty in Δv_C is small ($\leq$ 2%).

Finally, we note that one source of uncertainty in N_T which we have not included is absorption in the wings of the profile that cannot be resolved due to noise. At higher pressures, the influence of collisional broadening increases, resulting in a larger value for the broadening parameter and thus a broader line, with a greater fraction of the absorbed energy in the wings. Consequently, for a constant value of the parameter K, the uncertainty in N_T increases, because of a decrease in the effective signal-to-noise ratio of the profile. From calculations performed by Penner (1959), however, we expect this contribution to be small for our flames.
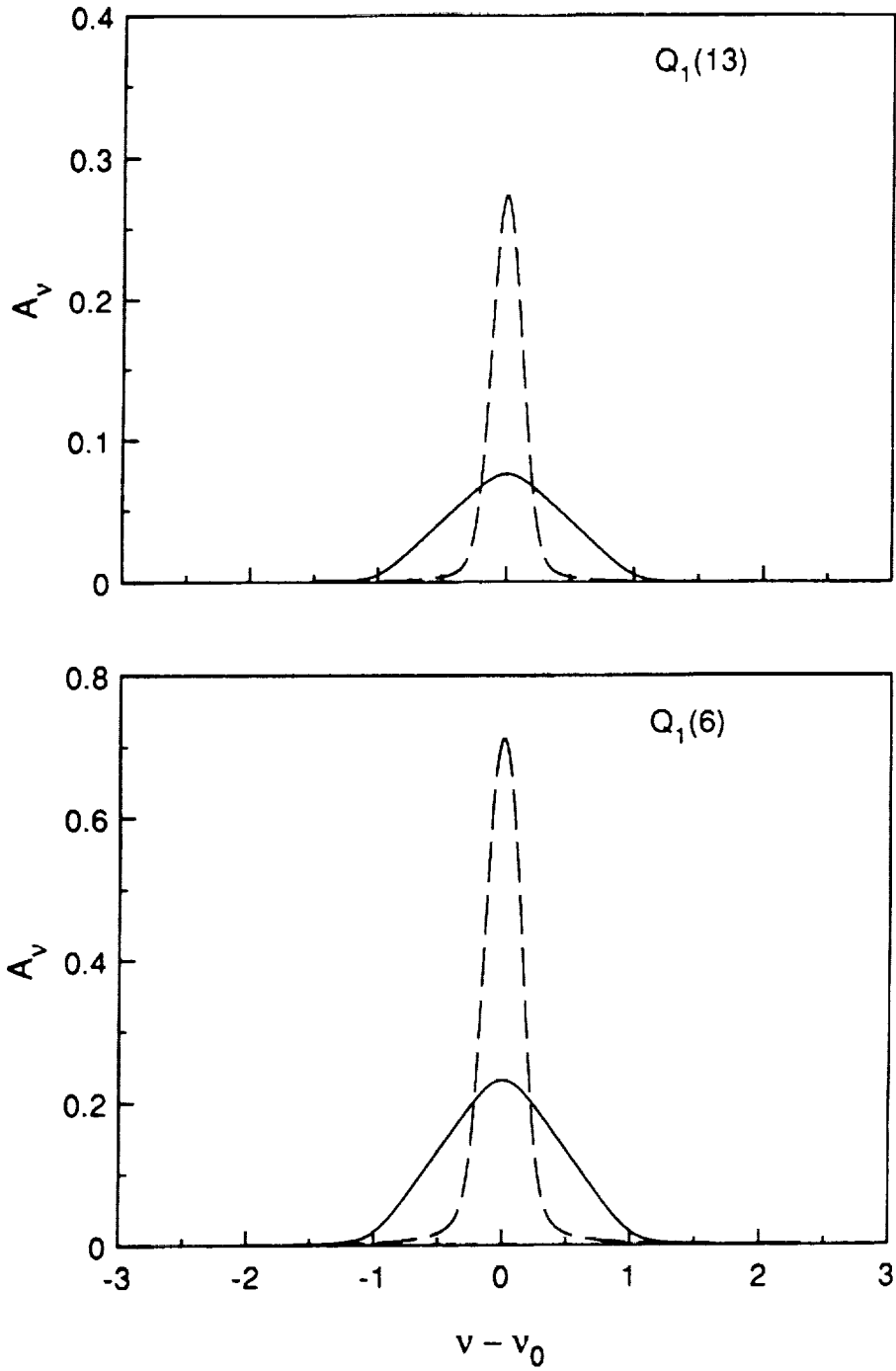
Figure B.1   Spectral absorption profiles for the $Q_1(6)$ (bottom) and $Q_1(13)$ (top) lines for $P \simeq 1$ atm, T = 1800 K, and $N_T = 8 \times 10^{15}$ cm⁻³. The solid curve is the convolution of the true spectral absorption, which is represented by the dashed curve, and a triangular slit function ($\Delta\nu^* = 1$ cm⁻¹).
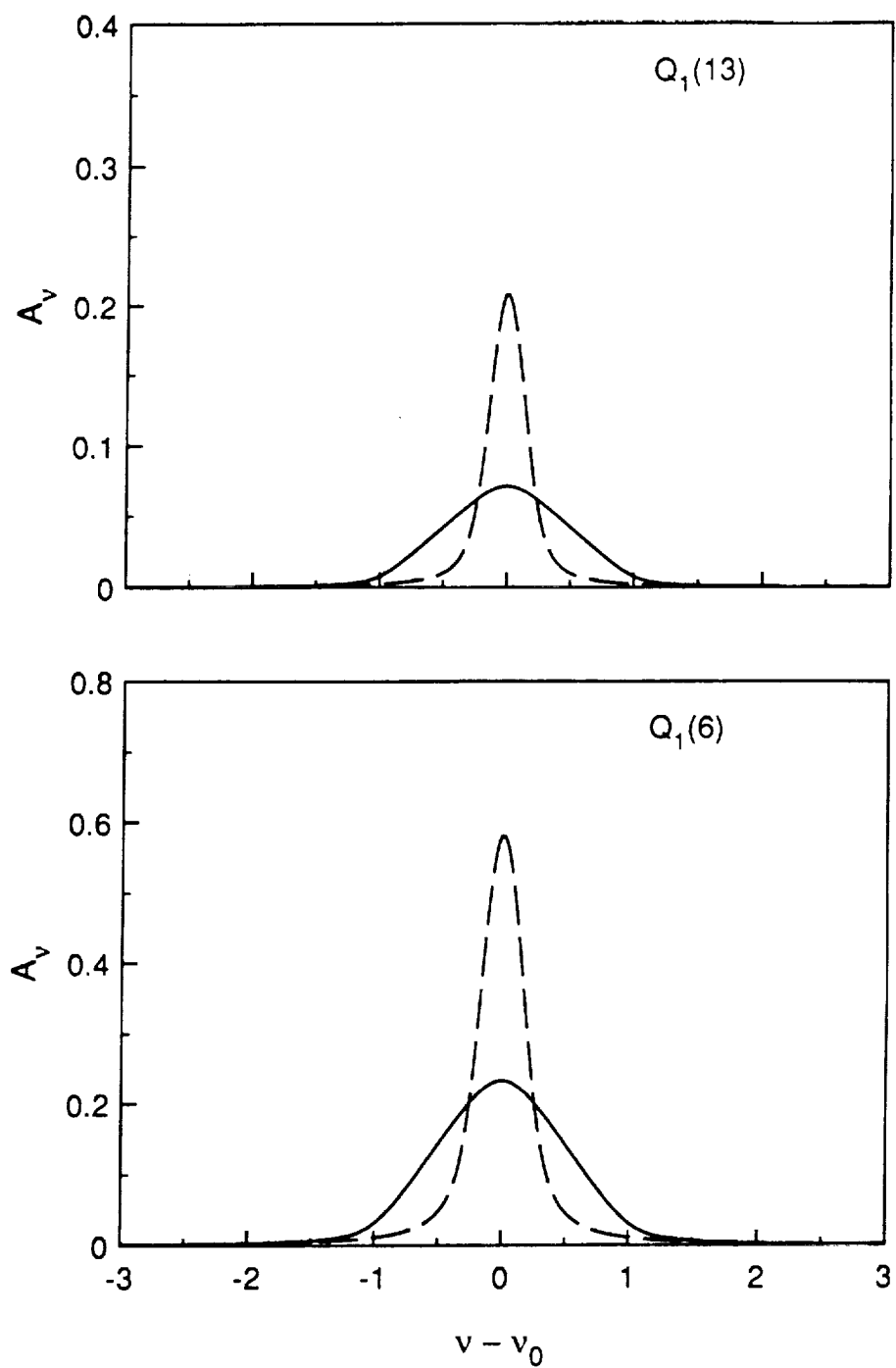
Figure B.2   Spectral absorption profiles for the $Q_1(6)$ (bottom) and $Q_1(13)$ (top) lines for $P \simeq 3$ atm, $T = 1800$ K, and $N_T = 8 \times 10^{15}$ cm^{-3}. The solid curve is the convolution of the true spectral absorption, which is represented by the dashed curve, and a triangular slit function ($\Delta\nu^* = 1$ cm^{-1}).
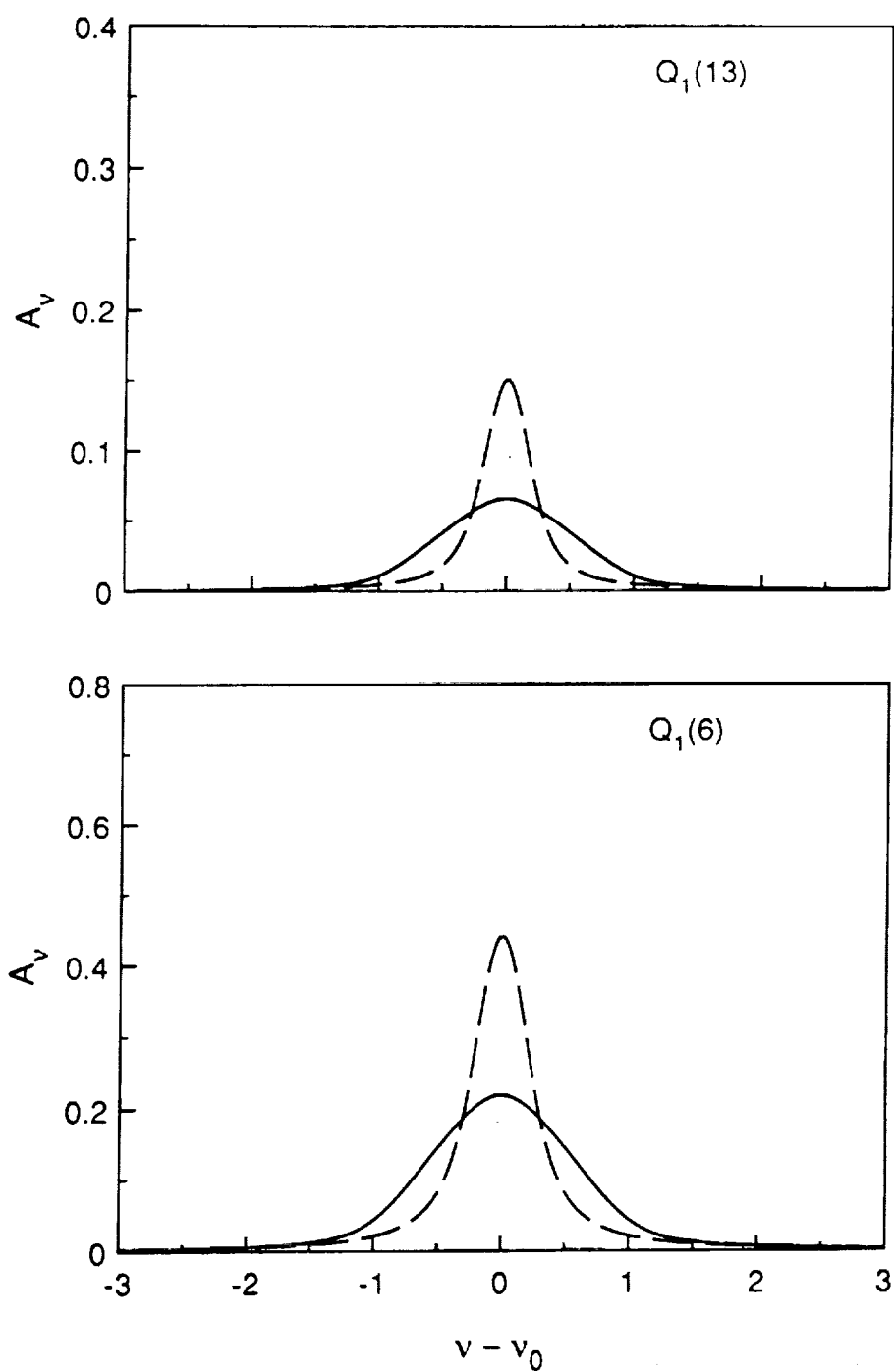
Figure B.3 Spectral absorption profiles for the $Q_1(6)$ (bottom) and $Q_1(13)$ (top) lines for $P \simeq 6$ atm, $T = 1800$ K, and $N_T = 8 \times 10^{15}$ cm^{-3}. The solid curve is the convolution of the true spectral absorption, which is represented by the dashed curve, and a triangular slit function ($\Delta \nu^* = 1$ cm^{-1}).
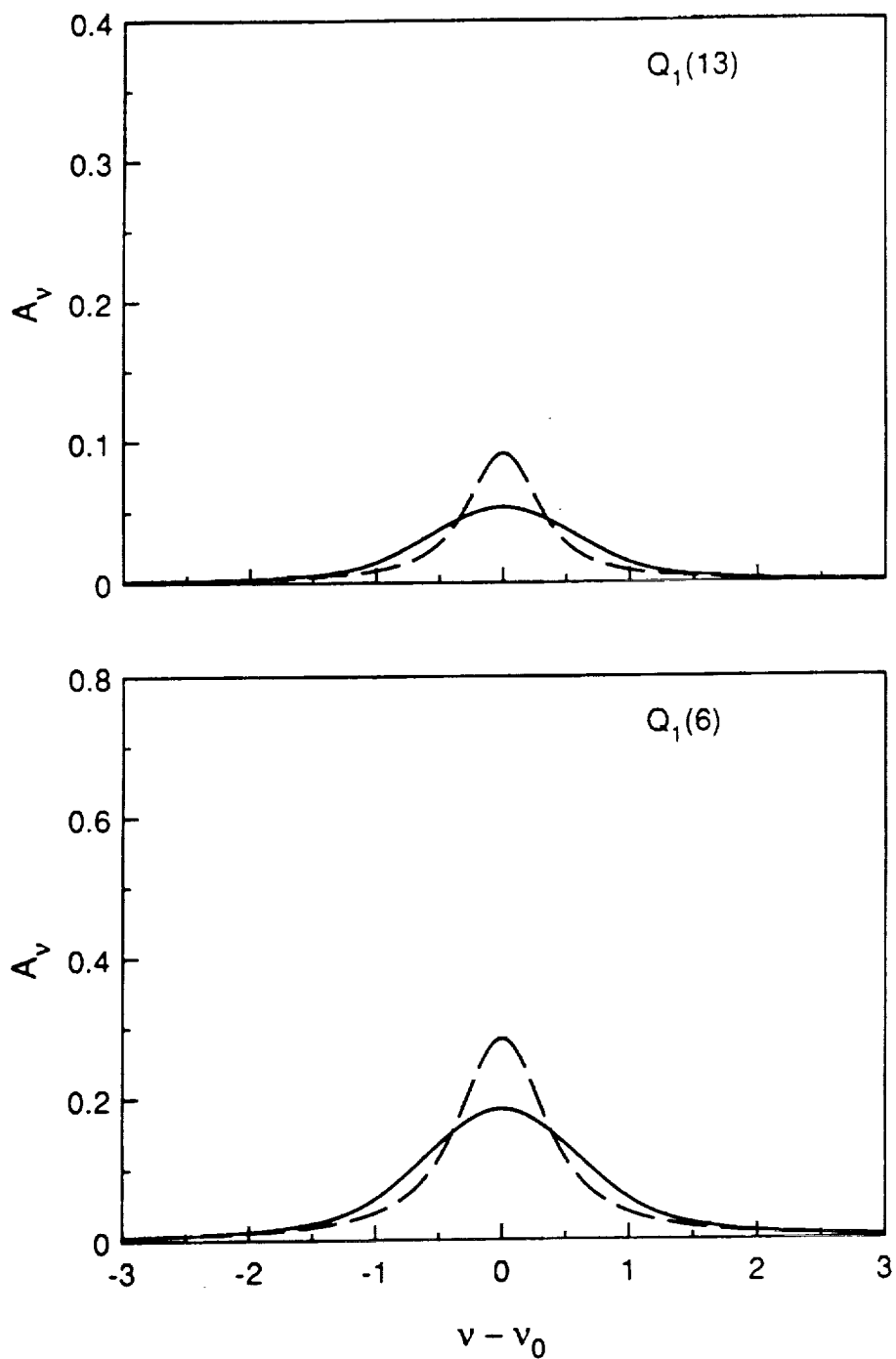
Figure B.4   Spectral absorption profiles for the $Q_1(6)$ (bottom) and $Q_1(13)$ (top) for $P \simeq 12$ atm, $T = 1800$ K, and $N_T = 8 \times 10^{15}$ cm^{-3}. The solid curve is the convolution of the true spectral absorption, which is represented by the dashed curve, and a triangular slit function ($\Delta \nu^* = 1$ cm^{-1}).
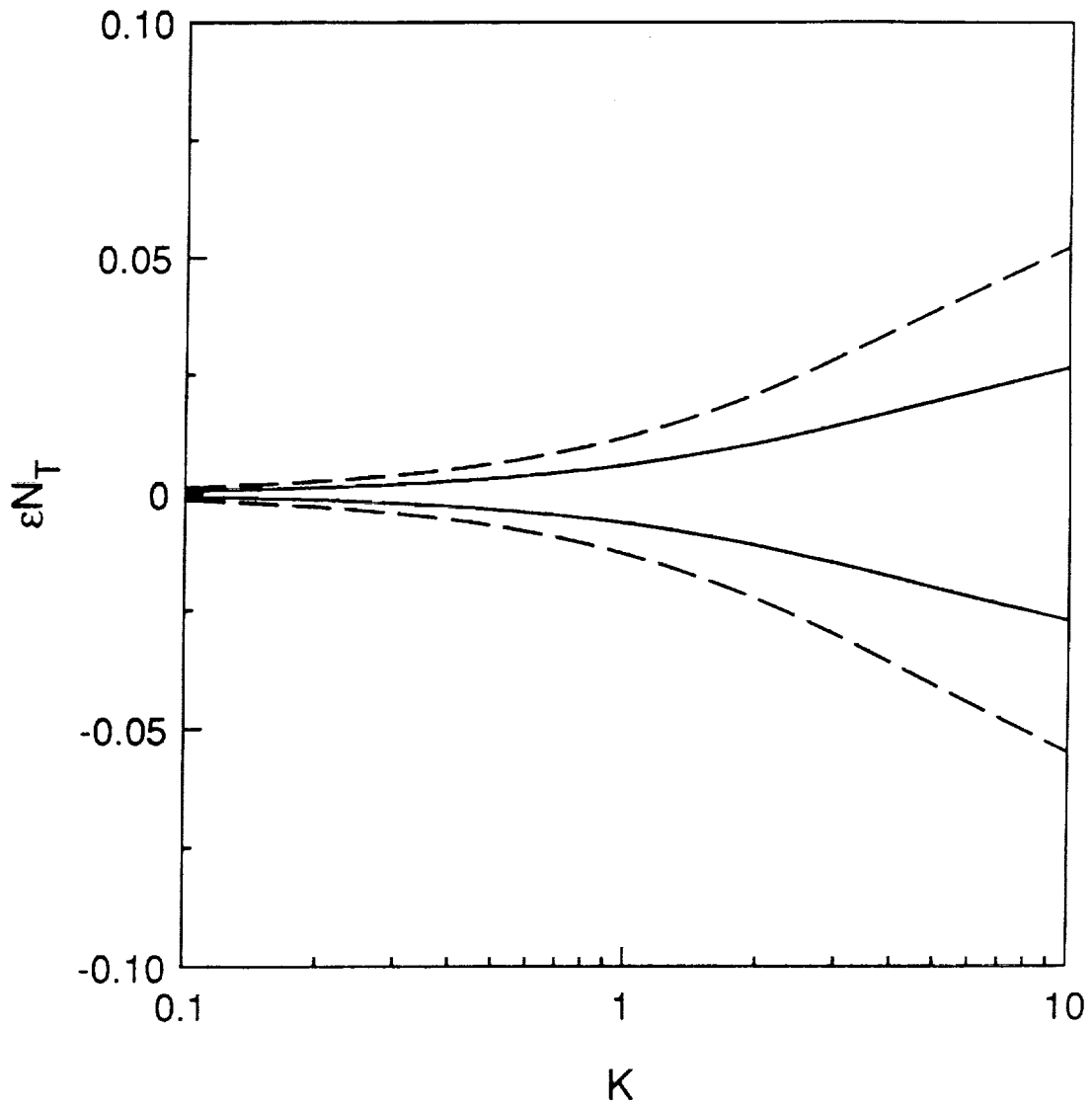
Figure B.5   Uncertainty in N_T for $a = 0.2$ ($P \simeq 1$ atm) due to an uncertainty in $\Delta\nu_C$ of $\pm 10\%$ (solid curve) and $\pm 20\%$ (dashed curve).
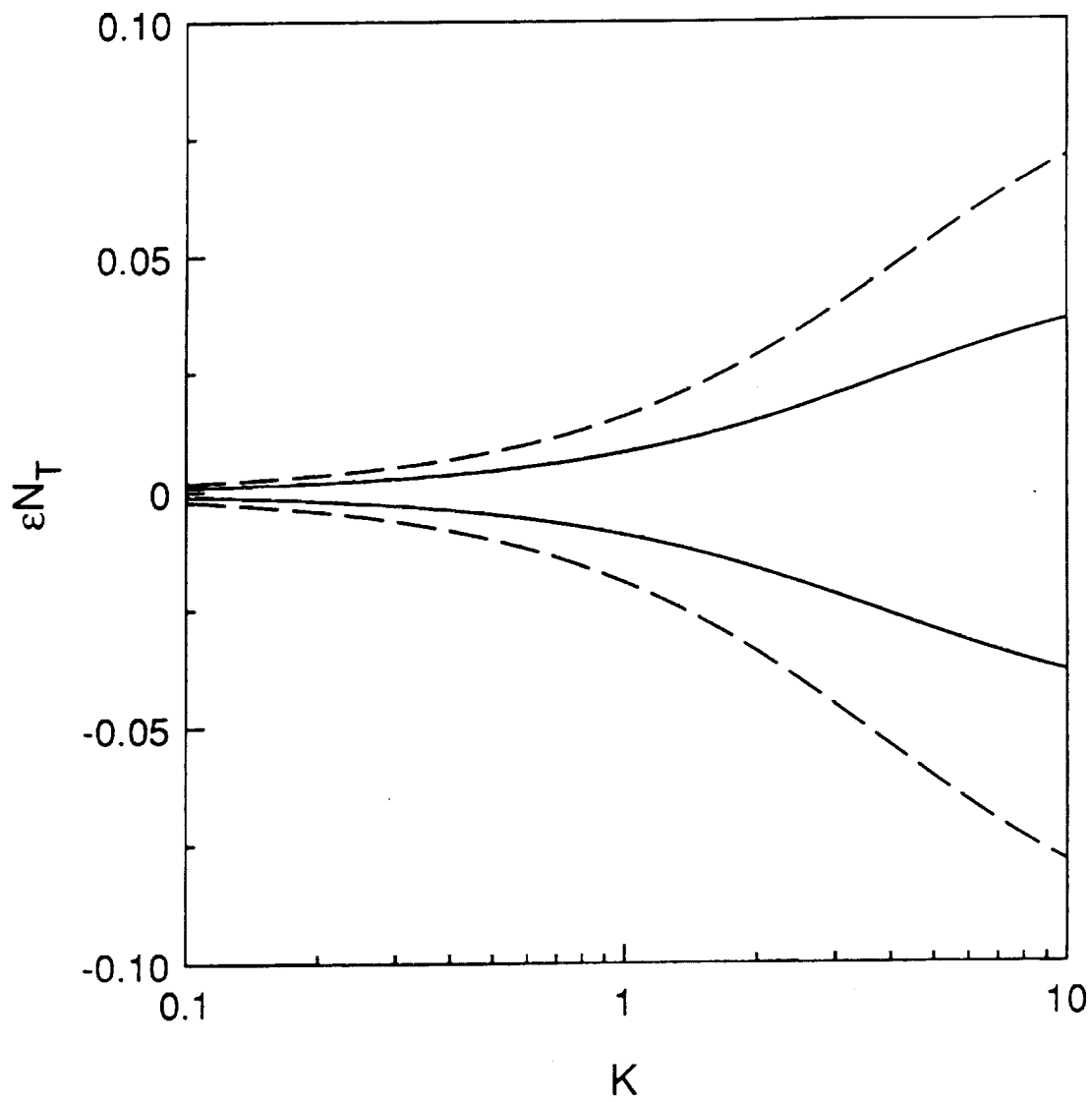
Figure B.6   Uncertainty in N_T for $a = 0.6$ ($P \simeq 3$ atm) due to an uncertainty in $\Delta\nu_C$ of $\pm10\%$ (solid curve) and $\pm20\%$ (dashed curve).
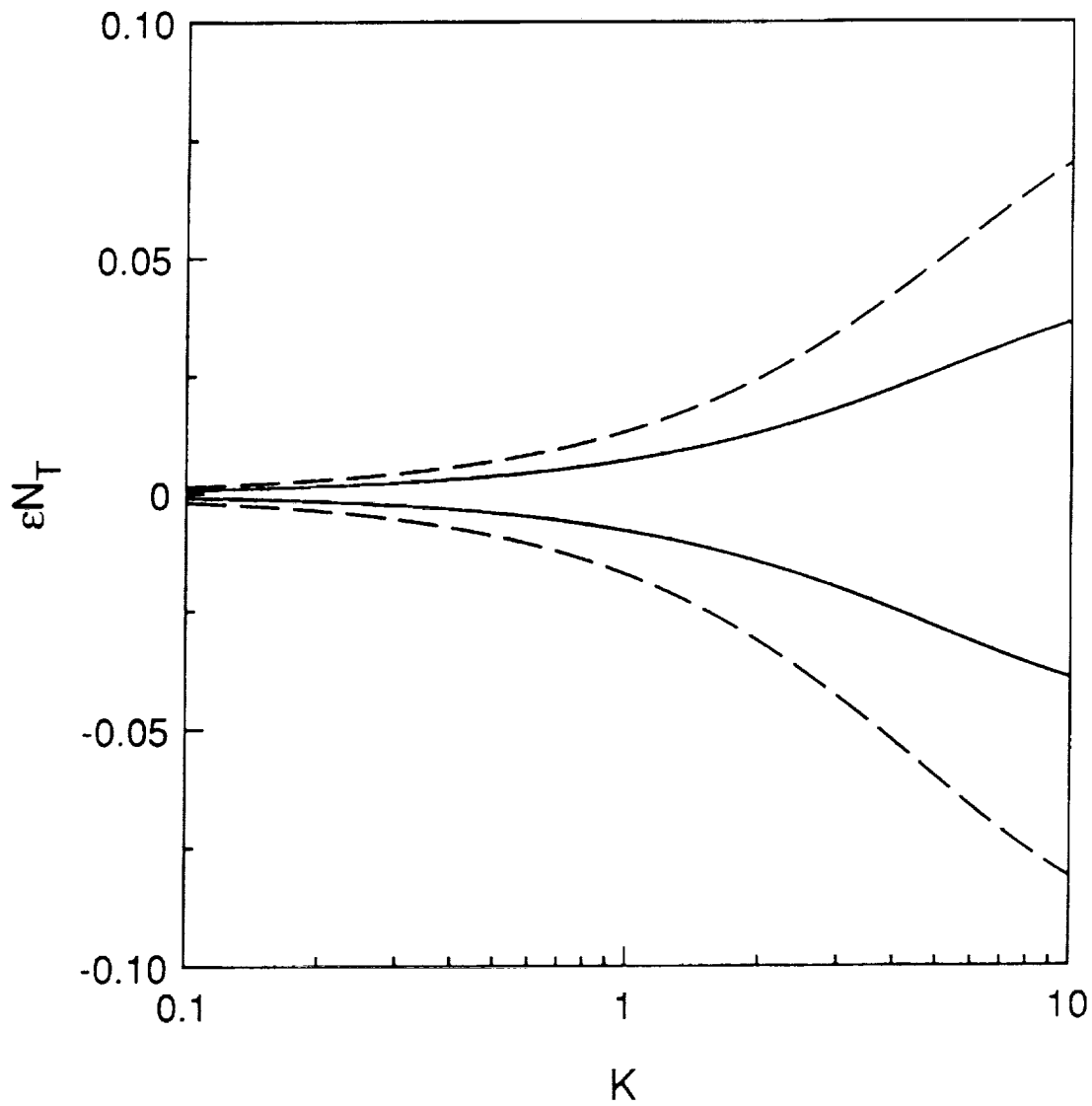
Figure B.7   Uncertainty in N_T for $a = 1.2$ ($P \simeq 6$ atm) due to an uncertainty in $\Delta\nu_C$ of $\pm 10\%$ (solid curve) and $\pm 20\%$ (dashed curve).
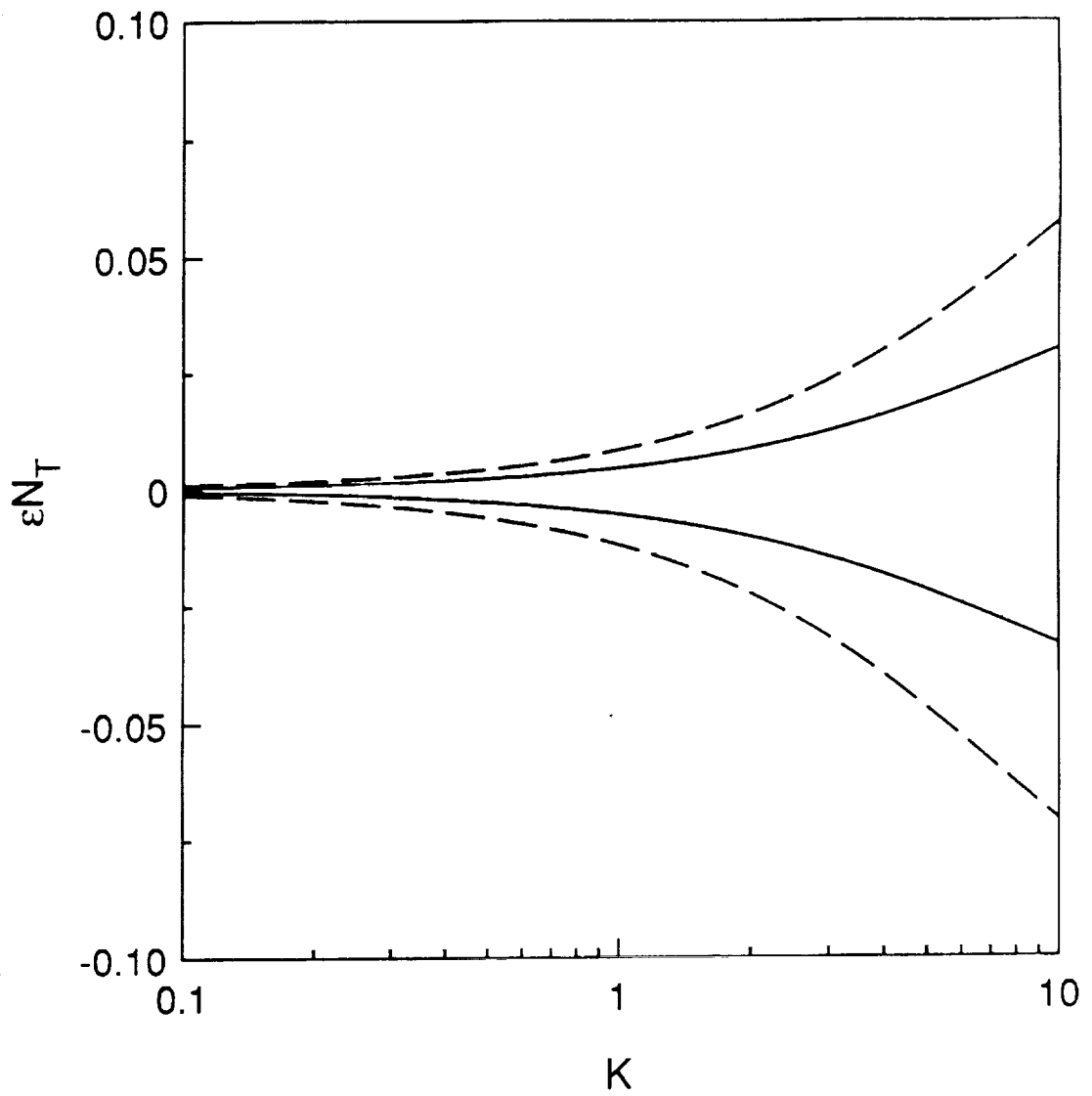
Figure B.8   Uncertainty in N_T for $a = 2.4$ ($P \simeq 12$ atm) due to an uncertainty in $\Delta\nu_C$ of $\pm10\%$ (solid curve) and $\pm20\%$ (dashed curve).

199

Appendix C - Error Analysis of Absorption Measurements

The uncertainties in the absorption concentration measurements reflect uncertainties from (1) the calculation of the integrated absorption (cm^{-1}) from the measured profile, (2) temperature (3) the line broadening parameter (see Appendix B), and (4) the path-length measurement. In cases where multiple lines ($\geq$ 10) are used to calculate the total number density, a statistical analysis is performed by the absorption program; the 95% confidence interval calculated by the program includes uncertainties from the calculated temperature and the variation in concentrations of individual lines. When the OH concentration is derived from scans of only the $Q_1(6)$ and the $Q_{12}(6)$ lines, the uncertainty in the integrated absorption was estimated from the signal-to-noise ratio of the profile and baseline.

The temperatures were measured subsequent to the OH absorption and fluorescence measurements using silica-coated thermocouples above the burner center (rather at the burner edge where the fluorescence measurements were taken). We note that even at high pressures, evidence of catalytic reactions was observed when uncoated thermocouples were used. The temperatures were corrected for radiative losses using an emissivity for silica of 0.22 and the Nusselt number correlation recommended by Bradley and Matthews (1968); this correlation, which is used to model convective heat transfer from hot wire anemometers and is described by Hinze (1975) and Kramers (1946), is given by

$$Nu = 0.42\, Pr^{0.2} + 0.57\, Pr^{0.33}\, Re^{0.50} \quad , \tag{C.1}$$

where Pr is the Prandtl number and Re is the Reynolds number. The thermocouple is thus modelled as a cylinder in cross flow, with a diameter equal to that of the thermocouple bead; a computer program developed by Harris (1985) was used to obtain the corrected temperatures. While the thermocouple measurements at 3.1 atm employed a thermocouple with a diameter of ~170 μm, the values at 1, 6.1, and 9.1 atm employed a thermocouple with a ~100 μm diameter. To make these measurements, we also removed the flame stabilization screen which was fixed about 8 mm above the burner. The uncertainty in these temperatures is estimated to be $\pm$50 K for all the flames.

For the effective path length for absorption, we estimate the uncertainty to be $\pm$1 mm; typically, the effective path length was ~24 mm. This uncertainty accounts for possible errors due to effects such as beam steering, laser wavelength drift (during the absorption path-length measurement), and the fluorescence signal-to-noise ratio. Finally, we include the uncertainty in N_T from an uncertainty in the collisional linewidth, $\Delta \nu_C$, of $\pm$10% (see Appendix B).

200

Table C.1   Total absorption uncertainty (molecules/cm³) from the partial values due to uncertainties in (1) the integrated absorption [$\delta N_T(A)$], (2) temperature [$\delta N_T(T)$], when not included in the absorption calculation], (3) path length [$\delta N_T(L^x_{eff})$], and (4) the collisional linewidth [$\delta N_T(\Delta\nu_C)$]. The total concentration and associated uncertainty are listed under the column labeled N_T.

Pressure (atm)	Position (mm)	N_T	$\delta N_T(A)$	$\delta N_T(T)$ 10^{16} cm^{-3}	$\delta N_T(L^x_{eff})$	$\delta N_T(\Delta\nu_C)$
0.98	1.0	1.057 ± 0.072	±0.055	--	∓0.045	∓0.014
	2.0	0.702 ± 0.061	±0.053	--	∓0.029	∓0.005
	3.0	0.526 ±0.037	±0.028	--	∓0.024	∓0.003
3.1	0.6	0.813 ± 0.083	±0.074	--	∓0.037	∓0.008
	1.0	0.492 ± 0.063	±0.059	--	∓0.023	∓0.003
	1.2	0.434 ± 0.022	±0.010	±0.008	∓0.018	∓0.003
	1.4	0.382 ± 0.042	±0.038	--	∓0.017	∓0.002
6.1	0.6	0.934 ± 0.065	±0.044	±0.018	∓0.040	∓0.019
	1.0	0.616 ±0.048	±0.037	±0.011	∓0.027	∓0.009
	1.6	0.445 ±0.042	±0.037	±0.007	∓0.019	∓0.004

Finally, for selected OH absorption measurements, the partial uncertainties for the four sources listed above have been added in quadrature to obtain the total uncertainty in N_T. For the flames at 1, 3.1 and 6.1 atm, the uncertainties (shown in Figs. 6.9-6.11) are summarized in Table C.1.

Appendix D - Saturation of an Inhomogeneously-Broadened $A^2\Sigma^+ \leftarrow X^2\Pi$ (0,0) Transition of OH

In this appendix, we examine the saturation behavior of an $A^2\Sigma^+ \leftarrow X^2\Pi$ (0,0) transition of the hydroxyl molecule at flame temperatures as a function of pressure. We have modelled the excitation process with rate equations using an approach similar to the one taken by Piepmeier (1972a, 1972b). Because $\int \alpha_{sat} dV$ (where V is the imaged volume) is of principal interest, one need consider only the two laser-coupled energy levels u and l. Since the rate coefficient for excitation can vary over the absorption profile, the distribution of molecules among the Doppler intervals will also vary with frequency. One must then define $n_u(\nu)$ and $n_l(\nu)$, the spectral population in energy levels u and l, respectively, where

$$N_u = \int_0^\infty n_u(\nu) d\nu \qquad (D.1)$$

and

$$N_l = \int_0^\infty n_l(\nu) d\nu \quad . \qquad (D.2)$$

Accompanying the variation of W_{lu} over the absorption profile is a deviation from the Maxwell-Boltzmann velocity distribution in the excited state, and thus a net population transfer between the Doppler intervals of level u is possible. The rate of transfer out of the Doppler interval of interest is simply Q_D, the rate coefficient of velocity-changing *non-quenching* collisions, times the population $n_u(\nu)d\nu$. The rate of transfer into this Doppler interval is equal to $Q_D[N_u - n_u(\nu)d\nu]$, the total rate at which velocity-changing non-quenching collisions occur with molecules outside the interval, times the probability that a collision will transfer the molecule into the interval. This probability is given by $n_l^0(\nu)d\nu/N_l^0$, where $n_l^0(\nu)$ and N_l^0 are the respective unperturbed spectral and unperturbed total populations of level l. The ratio of these populations (times $d\nu$) is simply the fraction of the total population in the interval $d\nu$, which for a Maxwell-Boltzmann velocity distribution, is given by the normalized Gaussian function,

$$\frac{n_l^0(\nu)}{N_l^0} = G(\nu - \nu_0; \Delta\nu_D) \qquad (D.3)$$

$$= \frac{2}{\Delta\nu_D}\left(\frac{ln2}{\pi}\right)^{1/2} \exp\{-ln2[2(\nu - \nu_0)/\Delta\nu_D]^2\} \quad .$$

where $\Delta \nu_D$ (cm^{-1}) is the Doppler width (FWHM). Thus, the net rate of transfer into the frequency interval ν to $\nu + d\nu$ is

$$n_l^0(\nu)(N_u/N_l^0)Q_D - n_u(\nu)Q_D \quad , \qquad (D.4)$$

where the second-order differential has been dropped. The rate equation for the excited-state population density $n_u(\nu)$ is then given by

$$\frac{dn_u(\nu)}{dt} = Q_D n_l^0(\nu)N_u/N_l^0 + n_l(\nu)W'_{lu}(\nu) - \qquad (D.5)$$

$$n_u(\nu)[Q_{eff} + W'_{ul}(\nu) + Q_D] \quad .$$

With the spectral population fraction, $1 - \gamma(\nu)$, equal to one, population densities in levels u and l are related by

$$n_l(\nu) + n_u(\nu) = n_l^0(\nu) \quad ; \qquad (D.6)$$

this equation implies that laser excitation does not change the velocity of the molecule. As in Chapter 3, the peak fluorescence signal is of principal interest. Thus, setting Eq. (D.5) to zero and solving for $n_u(\nu)$ using Eq. (D.6) gives

$$n_u(\nu) = n_l^0(\nu) \left\{ \frac{(Q_D/Q_{eff})(N_u/N_l^0) + W'_\nu}{1 + Q_D/Q_{eff} + [1 + (g_l/g_u)]W'_\nu} \right\} \quad . \qquad (D.7)$$

Note that in setting Eq. (D.5) to zero, we implicitly assume that each n_u reaches steady state at the same time. For each Doppler interval, W'_ν, the spectral saturation parameter, is given by a convolution of the spectral energy density, ρ_ν (J/cm^3-cm^{-1}), and the homogeneous absorption profile; i.e.,

$$W'_\nu = \frac{W'_{lu}(\nu)}{Q_{eff}} = \frac{B_{lu}}{Q_{eff}} \int_0^\infty \rho_{\nu'} \cdot \frac{\Delta \nu_C}{2\pi(\nu - \nu')^2 + \pi \Delta \nu_C^2/2} d\nu' \quad , \qquad (D.8)$$

where $\Delta \nu_C$ (cm^{-1}) is the collisional linewidth (FWHM) and B_{lu} (cm^3-cm^{-1}/J-sec) is the Einstein coefficient for absorption. When the rate coefficient for excitation is independent of frequency ν, the population $n_u(\nu)$ will also be independent of frequency, and Eqs. (3.4) and (D.7) will then be equivalent.

One can now solve for the desired quantity, namely N_u, by integrating Eq. (D.7) after substitution from Eq. (D.3); thus,

$$N_u = \left(\frac{g_u}{g_u + g_l} \right) N_l^0 \frac{\left(\frac{g_u + g_l}{g_u} \right) \int_0^\infty \frac{G(\nu - \nu_0; \Delta \nu_D)W'_\nu}{1 + Q_D/Q_{eff} + [1 + (g_l/g_u)]W'_\nu} d\nu}{1 - (Q_D/Q_{eff}) \int_0^\infty \frac{G(\nu - \nu_0; \Delta \nu_D)}{1 + Q_D/Q_{eff} + [1 + (g_l/g_u)]W'_\nu} d\nu} \quad . \qquad (D.9)$$

Comparing Eqs. (3.4) and (D.9), we observe that α_{sat}, the degree of saturation, is

$$\alpha_{sat} = \frac{\dfrac{g_u \cdot g_l}{g_u} \displaystyle\int_{-\infty}^{\infty} \dfrac{(1/\sqrt{\pi})\exp(-y^2)W_y{}'}{1 + Q_D/Q_{eff} \cdot [1 + (g_l/g_u)]W_y{}'} \, dy}{1 - (Q_D/Q_{eff}) \displaystyle\int_{-\infty}^{\infty} \dfrac{(1/\sqrt{\pi})\exp(-y^2)}{1 + (Q_D/Q_{eff}) \cdot [1 + (g_l/g_u)]W_y{}'} \, dy} \quad , \qquad (D.10)$$

where $y \equiv 2\sqrt{(\ln 2)}\,(\nu - \nu_0)/\Delta\nu_D$ is the nondimensional frequency. Note that when $W_y{}' \ll 1$, Eq. (D.10) reduces to

$$\alpha_{sat} \approx \frac{g_u + g_l}{g_u} \int_{-\infty}^{\infty} (1/\sqrt{\pi})\exp(-y^2)W_y{}' \, dy \quad . \qquad (D.11)$$

Although the dependence on velocity-changing collisions has disappeared, the degree of saturation still depends on the integral of the saturation parameter times the transition Doppler profile.

Since we are interested in the spatially-integrated degree of saturation, we have solved the equation

$$\int_V \alpha_{sat} \, dV = \int_V \left\{ \frac{\dfrac{g_u \cdot g_l}{g_u} \displaystyle\int_{-\infty}^{\infty} \dfrac{(1/\sqrt{\pi})\exp(-y^2)W_y{}'}{1 + Q_D/Q_{eff} \cdot [1 + (g_l/g_u)]W_y{}'} \, dy}{1 - (Q_D/Q_{eff}) \displaystyle\int_{-\infty}^{\infty} \dfrac{(1/\sqrt{\pi})\exp(-y^2)}{1 + (Q_D/Q_{eff}) \cdot [1 + (g_l/g_u)]W_y{}'} \, dy} \right\} dV \qquad (D.12)$$

using a 2-D Romberg integration routine, which is similar to the 1-D version employed in Appendix B and is based on an algorithm suggested by Press et al. (1986). We model the spatial dependence of the spectral energy density with the axisymmetric function (see Chapters 6 and 7)

$$\rho_\nu(r) = \frac{\rho_\nu(0)}{[1 + (r/w)^2]^{2.2}} \quad , \qquad (D.13)$$

where r is the radial position, w is the beam halfwidth, and $\rho_\nu(0)$ is the spectral energy density at the laser beam center line. For the imaged volume, we consider the following two cases (see Fig. 7.1): (1) geometry A, which yields the disk with the differential volume $dV = 2\pi W_A \, r dr$; (2) geometry B, which yields the slab with the differential volume $dV = W_B H_B \, dr$.

To model the spectral distribution of energy in the laser pulse of the Quanta-Ray dye laser, we have used a series of monochromatic modes (i.e., ρ_ν described with a series of δ-functions) separated by $\Delta\nu_{Lm}$; the relative intensity of the modes is given by a Lorentzian function, with a spectral FWHM $\Delta\nu_L = 0.5$ cm^{-1}. Thus we have

$$\rho_\nu = \frac{\rho_0}{[2(\nu - \nu_{lc})/\Delta\nu_L]^2 + 1} \cdot \sum_{m=-M}^{M} \delta(\nu - \nu_{Lm}) \quad , \qquad (D.14)$$

with

$$v_{Lm} = v_{Lc} + (m \cdot \Delta v_{Lm}) \quad . \tag{D.15}$$

Here, ρ_0 (J/cm^{-3}) is the energy density of the central mode, which is located at v_{Lc} (cm^{-1}), and v_{Lm} (cm^{-1}) is the frequency of the m-th of 2M+1 modes. The energy density of the m-th mode is thus given by

$$\rho_m = \int_m \left\{ \frac{\rho_0}{[2(v - v_{Lc})/\Delta v_L]^2 + 1} \cdot \delta(v - v_{Lm}) \right\} dv \tag{D.16}$$

$$= \frac{\rho_0}{[2(m \cdot \Delta v_{Lm})/\Delta v_L]^2 + 1}$$

or

$$\rho_m = \frac{\rho_0}{[2(m \cdot \Delta y_{Lm})/\Delta y_L]^2 + 1} \tag{D.17}$$

in terms of the nondimensional frequency [again using the normalization constant $\Delta v_D/2\sqrt{(\ln 2)}$]. Note that this model for saturation is least accurate for small Δv_C, since the actual nonzero width of the modes will act to increase the degree of saturation. In addition, a dye laser has a homogeneously-broadened line profile; consequently, mode competition results in fewer axial modes than are possible (from the cavity length) being active on each laser pulse. Effects such as vibration prevent complete mode competition (i.e., the elimination of all but a single mode on each laser shot). We note that for our laser, the mode spacing determined from the cavity length is estimated to be 0.038 cm^{-1}.

From Eq. (D.8), the spectral saturation parameter is given by

$$W_v' = \frac{B_{lu}\rho_0}{Q_{eff}} \int_0^\infty \left\{ \frac{\sum_{m=-M}^{M} \delta(v' - v_{Lm})}{[2(v' - v_{Lc})/\Delta v_L]^2 + 1} \cdot \frac{\Delta v_c}{2\pi(v - v')^2 + \pi \Delta v_c^2/2} \right\} dv' \tag{D.18}$$

or in nondimensional form

$$W_y' = \frac{2\sqrt{\ln 2}}{\pi \Delta v_D} \cdot \frac{B_{lu}\rho_0}{Q_{eff}} \int_{-\infty}^{\infty} \left\{ \frac{\sum_{m=-M}^{M} \delta(y' - y_{Lm}')}{[2(y' - y_{Lc})/\Delta y_L]^2 + 1} \cdot \frac{a}{(y' - y)^2 + a^2} \right\} dy' \tag{D.19}$$

$$= \frac{2\sqrt{\ln 2}}{\pi \Delta v_D} \cdot \frac{B_{lu}\rho_0}{Q_{eff}} \sum_{m=-M}^{M} \left\{ \frac{1}{[2(m \cdot \Delta y_{Lm})/\Delta y_L]^2 + 1} \cdot \frac{a}{[y - (y_{Lc} + m \cdot \Delta y_{Lm})]^2 + a^2} \right\} \quad .$$

205

where $a \equiv \sqrt{(ln2)} \, \Delta\nu_C/\Delta\nu_D$ is the broadening parameter (when the contribution from natural broadening is negligible) and $y_{Lc} \equiv 2\sqrt{(ln2)} \, (\nu_{Lc} - \nu_0)/\Delta\nu_D$ goes to zero when the central frequencies of the transition and the laser spectral profile match. We note that Eqs.(D.18) and (D.19) describe a series of Lorentzian-shaped modes under the envelope of the laser spectral energy distribution (assumed to be a Lorentzian in this case). As a function of the spectral energy density, the laser irradiance is given by

$$I_L = c \cdot \int_0^\infty \rho_\nu \, d\nu \qquad (D.20)$$

$$= \rho_0 \cdot c \sum_{m=-M}^{M} (\rho_m/\rho_0) \quad .$$

Finally, the spectral saturation parameter in terms of the laser irradiance is

$$W_y'(r) = \frac{\sqrt{ln2}\,(g_u/g_l)A_{ul}}{(4\pi^2 c^2 \Delta\nu_D)\nu_0^3 Q_{eff}} \cdot \frac{I_L(r)}{\displaystyle\sum_{m=-M}^{M} \frac{1}{[2(m \cdot \Delta y_{Lm})/\Delta y_L]^2 + 1}} \qquad (D.21)$$

$$\cdot \sum_{m=-M}^{M} \left\{ \frac{1}{[2(m \cdot \Delta y_{Lm})/\Delta y_L]^2 + 1} \cdot \frac{a}{[y - (y_{Lc} + m \cdot \Delta y_{Lm})]^2 + a^2} \right\} \quad ,$$

where we have used the identity

$$B_{lu} = \frac{(g_u/g_l)A_{ul}}{8\pi h \nu_0^3 c} \qquad (D.22)$$

to cast the equation in terms of the Einstein A-coefficient.

To calculate the Doppler and collisional linewidths (see Appendix B), we use a temperature of 1750 K and the Einstein A-coefficient and frequency of the $Q_1(8)$ line. In addition, we estimate the ratio Q_D/Q_{eff} by comparing the dephasing collision frequency with the *quenching* collision frequency. Here, we assume that collisions which *quench* the molecule (i.e., change its energy state) also dephase the molecule. The collision frequency is given by the sum of the rate coefficients for electronic quenching and vibrational plus rotational energy transfer. Since the rate coefficient for vibrational energy transfer will be small in the $A^2\Sigma^+(v=0)$ state, the net frequency for quenching collisions is $Q_e + Q_r$, the sum of rate coefficients for electronic quenching and rotational relaxation. Using the procedure described in Chapter 6, we find $Q_e \approx 0.45 \times 10^9$ s^{-1}, $Q_r \approx 3.8 \times 10^9$ s^{-1}, and $Q_{eff} \approx 2.9 \times 10^9$ s^{-1} for the burnt gas region of an atmospheric $C_2H_6/O_2/N_2$ flame at T = 1750 K.

In comparison, the dephasing collision frequency is $f_C = \pi c \Delta \nu_C \simeq 5.3 \times 10^9$ s^{-1} (see Appendix B). Thus we have $Q_D/Q_{eff} = [f_C - (Q_e + Q_r)]/Q_{eff} \approx 0.25$. The relevant modelling parameters are summarized in Table D.1.

Table D.1   Modelling parameters for the
$Q_1(8)$ line at 1750 K.[a]

$I_L(0)$	2.6×10^{10} W/cm^2
a/P	0.20 atm^{-1}
$\Delta \nu_D$	0.235 cm^{-1}
ν_0	32328 cm^{-1}
Q_e/P	0.45×10^9 s^{-1} atm^{-1}
Q_r/P	3.8×10^9 s^{-1} atm^{-1}
Q_{eff}/P	2.9×10^9 s^{-1} atm^{-1}
Q_D/Q_{eff}	0.25

[a] We use the symbol P for pressure.

Figure D.1 shows curves describing the variation in the relative fluorescence signal (which is proportional to the spatially-integrated degree of saturation in the absence of depletion of the laser-coupled levels) for the two imaging geometries, versus the broadening parameter. We consider three cases for the laser spectral energy density: (1) the profile contains 41 modes with a separation of $\Delta \nu_{Lm} = 0.038$ cm^{-1} (which is approximately the value calculated from the cavity length of the dye laser); (2) the profile contains 11 modes with $\Delta \nu_{Lm} = 0.152$ cm^{-1}; (3) the profile contains 5 modes with $\Delta \nu_{Lm} = 0.38$ cm^{-1}. We note that for our flames, the range $a = 0.02$ to 4 corresponds approximately to a range of pressures of 0.1 to 20 atm. The spectral saturation parameter was calculated from Eq. (D.21) using a center-line irradiance of $I_L(0) = 2.6 \times 10^{10}$ W/cm^2. In addition, a ratio of Q_{eff}/P of 2.9×10^9 s^{-1}atm^{-1} was employed to describe the variation of the quenching rate coefficient with pressure (using $a/P = 0.20$ atm^{-1}). For these saturation curves to follow those shown in Chapter 7 (Fig. 7.7), the coupling efficiency between the transition and the laser must remain constant. However, when (1) the homogeneous linewidth is much narrower than the separation of the modes and (2) the frequency of Doppler-changing collisions is smaller than the frequency of quenching collisions, $n_u(\nu)$ retains much of the nonuniformity of the laser spectral energy distribution, and as a consequence, the coupling efficiency is poor. With increasing $\Delta \nu_C$, $n_u(\nu)$ retains less of the nonuniform distribution of the laser; the coupling efficiency can therefore increase with increasing pressure. We therefore expect that the relative fluorescence signal will exhibit a smaller sensitivity to pressure than would be obtained when the coupling efficiency is

constant and only Q_{eff} changes. This is shown in Fig. D.1 for small **a**. However, as $\Delta\nu_C$ increases further, this effect is offset by a decrease in the absorption at frequencies near ν_0, causing a decrease in the coupling efficiency with increasing pressure; consequently, the sensitivity of the fluorescence signal becomes larger than would be observed solely with increased quenching. In addition, we note that the relative saturation profile is insensitive to the specific shape of the energy density spectral profile (e.g., Gaussian or Lorentzian), the width of this profile, and the ratio Q_D/Q_{eff} (especially with larger **a**).

In Fig. D.2, we compare the saturation curves (for imaging geometries A and B) calculated by varying (1) pressure (i.e., the broadening parameter and the quenching rate coefficient) and (2) the laser irradiance, while holding constant the broadening parameter and the quenching rate coefficient. For case (1), we have employed the model with 5 axial modes and $\Delta\nu_{Lm} = 0.38$ cm^{-1}; in addition, we have used $a/P = 0.20$ atm^{-1}, $Q_{eff}/P = 2.9 \times 10^9$ s^{-1}atm^{-1} and $I_L = 2.6 \times 10^{10}$ W/cm^2 to simulate the saturation curve that would be obtained by exciting the $Q_1(8)$ line in our $C_2H_6/O_2/N_2$ flames and varying the pressure from 1 to 20 atm. For comparative purposes, we used the model employing only 5 modes, since of the three models studied (see Fig. D.1), it is the least like the saturation curve generated by varying the laser irradiance. For case (2), we used $a = 0.20$, $Q_{eff} = 2.9 \times 10^9$ s^{-1}, and $I_L \times P = 2.6 \times 10^{10}$ W-atm/cm^2 to simulate the saturation curve that would be obtained by varying the laser irradiance at atmospheric pressure. The resulting curves for case (2) are almost identical to the ones used in Chapters 6 and 7, where we assumed the that the relative fluorescence signal is independent of collisional broadening (see Eq. 6.14).

Of particular interest, given the variation in the coupling efficiency with pressure, is the accuracy with which one can calculate the fluorescence correction factor, f_Q--which accounts for changes in the laser irradiance, the quenching rate coefficient, and the coupling efficiency--from S_{fA}/S_{fB}, the ratio of the fluorescence signals from the two imaging geometries. With the Cottereau method (1986), which is discussed in detail in Chapter 7, one uses saturation curves derived by varying the laser irradiance at constant pressure to generate the *quenching correction curve*, S_{fA}/S_{fB} versus the relative saturation parameter (W_r). The measurement of S_{fA}/S_{fB} under some other condition is used to calculate W_r', which can then be used to calculate f_Q from the saturation curve (for either geometry A or B). In the bottom part of Fig. D.2, we show the quenching correction curves which result from the saturation curves shown in the top part of the figure. The solid curve represents the dependence of the ratio S_{fA}/S_{fB} on pressure, while the dashed curve represents the dependence of S_{fA}/S_{fB} on W_r'. Using Fig. D.2, we can compare the f_Q calculated from the two sets of curves with

the following procedure: (1) for an arbitrary value of S_{fA}/S_{fB} determine the corresponding pressure, P_s (P_d) from the solid curve (dashed curve); (2) with P_s (P_d), determine from the solid curves (dashed curves) of the top graph the value of f_Q (where $f_Q = 1/S_f$) from the curve describing either geometry. For the Cottereau method to work effectively, the dashed curves should give approximately the same correction factor (for the same geometry) as the solid curves, which give the true dependence of the fluorescence signal on pressure. We have carried out this comparison for several values of S_{fA}/S_{fB}, and the results are listed in Table D.2. This comparison shows that the Cottereau method can yield a good estimate of f_Q, even though the two sets of saturation curves differ significantly.

Table D.2   Comparison of f_Q calculated from the saturation functions where (1) pressure [f(P)] and (2) the laser irradiance [f(I_L)] are varied (see Fig. D.2). The f_Q shown below are the values for geometry A.[a]

S_{fA}/S_{fB}	f(P) (solid curve)		f(I_L) (dashed curve)		$\epsilon(f_Q)$
	P (atm)	f_Q	P (atm)	f_Q	
0.80	2.34	1.50	2.66	1.57	0.041
0.70	3.62	1.94	4.78	2.05	0.059
0.60	5.75	2.63	9.39	2.80	0.065
0.50	9.58	3.80	20.8	4.05	0.066

[a] $\epsilon(f_Q)$ is the relative error in the fluorescence correction factor from using the constant-pressure saturation curves (and the corresponding quenching correction curve).
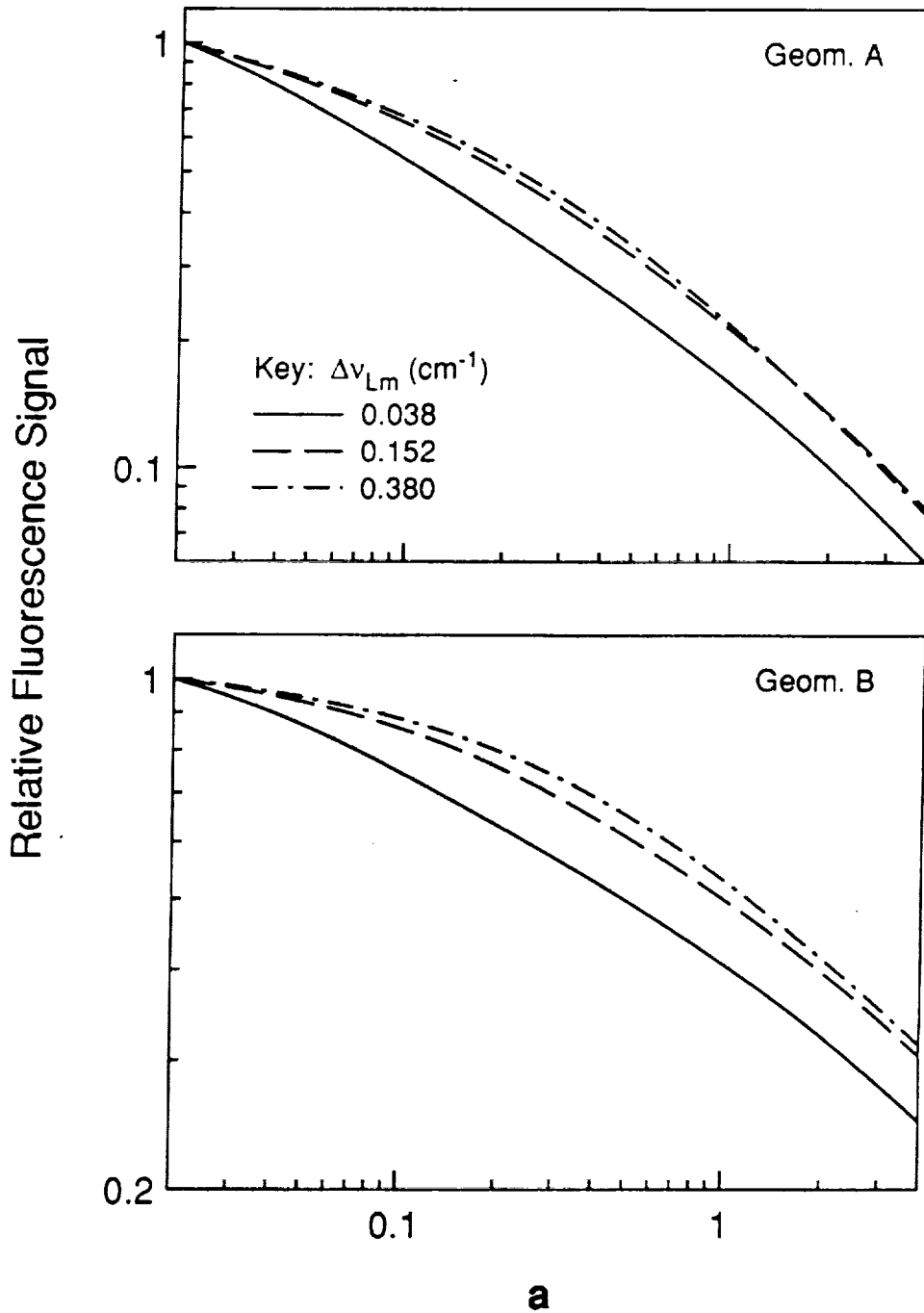
Figure D.1   Relative fluorescence signal versus the broadening parameter. The top and bottom graphs show the variation of the signal for geometries A and B, respectively, when the spectral laser profile contains (1) 41 modes (separated by 0.038 cm⁻¹), (2) 11 modes (separated by 0.152 cm⁻¹), and (3) 5 modes (separated by 0.38 cm⁻¹).
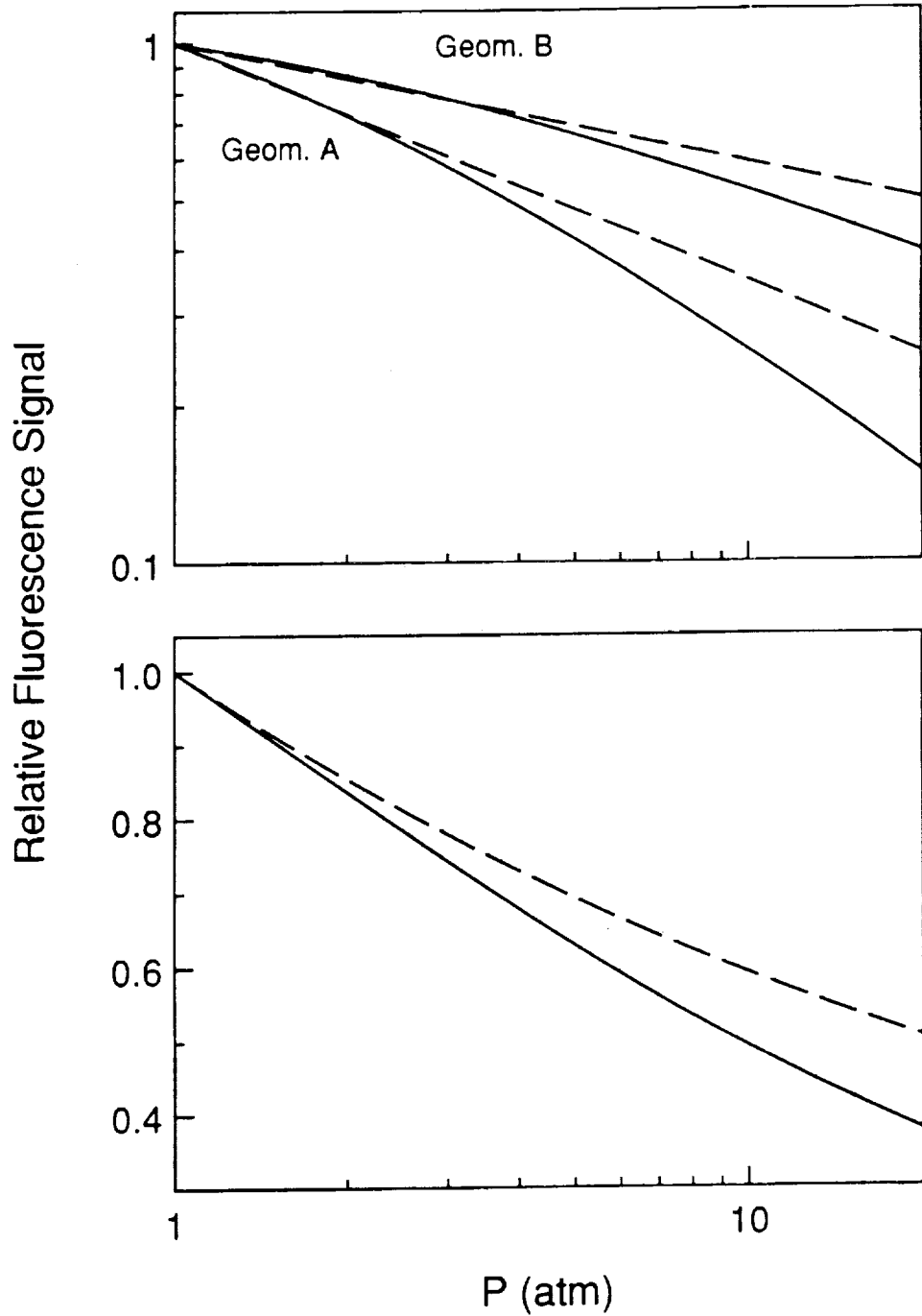
Figure D.2   Relative fluorescence signals (top) and their ratios (bottom) for geometries A and B versus pressure. For the solid and dashed curves, we use a laser spectral profile containing 5 modes (and $\Delta\nu_{Lm}$ = 0.38 cm^{-1}). The solid curves were calculated by varying the pressure, while the dashed curves were calculated by varying the laser irradiance.

Appendix E - Gaussian Quadrature Formula for the Weighting Function W(x) = 1/(1 + x²)

Listed in Table E.1 are the abscissa (x_i) and weights (v_i) of a 20-th order Gaussian quadrature formula for the integral (Salmon, 1986b)

$$\int_{-\infty}^{\infty} \frac{f(x)}{1 + x^2} dx \quad , \qquad (E.1)$$

where $1/(1 + x^2)$ is the weighting function, W(x), and f(x) is some *smooth* function. Integration of a function $g(x) \equiv W(x)f(x)$ is then given by

$$\int_{-\infty}^{\infty} g(x) dx \approx \sum_{i=1}^{N} v_i g(x_i) \quad . \qquad (E.2)$$

For example, with the weights and abscissa listed in Table E.1 and the function $g(x) = 1/[(1 + x^2)^2]$, the error in the integral is $\sim 4 \times 10^{-4}$. A general discussion of quadrature formulas, as well as a routine for calculation of the weights and abscissa for Gauss-Legendre integration is given by Press et al. (1986).

Table E.1   Abscissa and weights for the
Gaussian quadrature formula
describing Eq. (E.1).

x_i	v_i
±0.12079	0.24345
±0.37390	0.26708
±0.66524	0.32198
±1.03474	0.42833
±1.55437	0.63422
±2.37541	1.06355
±3.87244	2.09242
±7.20763	5.21265
±17.65124	19.93440
±92.64416	237.50059

NASA
National Aeronautics and Space Administration

Report Documentation Page

1. Report No. NASA CR-185218	2. Government Accession No.	3. Recipient's Catalog No.
4. Title and Subtitle Saturated Fluorescence Measurements of the Hydroxyl Radical in Laminar High-Pressure Flames		5. Report Date February 1990
		6. Performing Organization Code
7. Author(s) Campbell D. Carter, Galen B. King, and Normand M. Laurendeau		8. Performing Organization Report No. None
		10. Work Unit No. 506-42-51
9. Performing Organization Name and Address Purdue University School of Mechanical Engineering West Lafayette, Indiana 47907		11. Contract or Grant No. NAG3-351
		13. Type of Report and Period Covered Contractor Report Final
12. Sponsoring Agency Name and Address National Aeronautics and Space Administration Lewis Research Center Cleveland, Ohio 44135-3191		14. Sponsoring Agency Code

15. Supplementary Notes

Project Manager, Valerie J. Lyons, Space Propulsion Technology Division, NASA Lewis Research Center.

16. Abstract

We have investigated theoretically and experimentally the efficacy of laser-saturated fluorescence (LSF) for OH concentration measurements in high-pressure flames. Using a numerical model describing the interaction of hydroxyl with nonuniform laser excitation, we have studied the effect of pressure on the validity of the balanced cross-rate model and the sensitivity of the depopulation of the laser-coupled levels to the ratio of rate coefficients describing (1) electronic quenching to $^2\Sigma^+(v'' > 0)$ and (2) vibrational relaxation from $v'' > 0$ to $v'' = 0$. At sufficiently high pressures and near-saturated conditions, the total population of the laser-coupled levels reaches an asymptotic value, which is insensitive to the degree of saturation. When the ratio of electronic quenching to vibrational relaxation is small and the rate coefficients for rotational transfer in the ground and excited electronic states are nearly the same, the balanced cross-rate model remains a good approximation for all pressures. When the above ratio is large, depopulation of the laser-coupled levels becomes significant at high pressures, and thus the balanced cross-rate model no longer holds. Under these conditions, however, knowledge of the depletion of the laser-coupled levels can be used to correct the model. A combustion facility for operation up to 20 atm was developed to allow LSF measurements of OH in high-pressure flames. Using this facility, we achieved partial saturation in laminar high-pressure (≤ 12.3 atm) $C_2H_6/O_2/N_2$ flames. To evaluate the limits of the balanced cross-rate model, we compared absorption and calibrated LSF measurements at 3.1 and 6.1 atm. The fluorescence voltages were calibrated with absorption measurements in an atmospheric flame and corrected for their finite sensitivity to quenching with (1) estimated quenching rate coefficients and (2) an in situ measurement from a technique employing two fluorescence detection geometries. While the absorption and calibrated fluorescence measurements compare well at 3.1 atm, the OH fluorescence values are ~25% below the absorption measurements at 6.1 atm, indicating an effective error of ~25% in the balanced cross-rate model. We anticipate that with atmospheric-pressure fluorescence calibration and a measurement or a reasonable estimate of the quenching correction factor, one can measure OH concentrations within ±50% at pressures up to 10 atm.

17. Key Words (Suggested by Author(s)) Diagnostics Flames Combustion Laser fluorescence	18. Distribution Statement Unclassified – Unlimited Subject Category 35

19. Security Classif. (of this report) Unclassified	20. Security Classif. (of this page) Unclassified	21. No. of pages 221	22. Price* A10

NASA FORM 1626 OCT 86   *For sale by the National Technical Information Service, Springfield, Virginia 22161